Development of a New Generation of Inoculants for Ti-Al Alloys

Jacob Roman Kennedy

Development of a New Generation of Inoculants for Ti-Al Alloys

Thèse

Pour l'obtention du titre de:

Docteur de l'Université de Lorraine

Sciences des Matériaux

Science et Ingénierie des Matériaux et Métallurgie

Présentée Par:

Jacob Roman Kennedy

17-07-2018

Président :	A. HAZOTTE	Professeur - Université de Lorraine
Rapporteurs :	J. LACAZE	Directeur de Recherche, CIRIMAT - Toulouse
	M. THOMAS	Directeur de Recherche, ONERA - Paris
Examinateurs :	F. KARGL	Professeur, DLR – Cologne
	U. HECHT	Chercheur, ACCESS – Aachen
Directeur de thèse	E. BOUZY	Professeur - Université de Lorraine
Co-Directeur de thèse	J. ZOLLINGER	Maitre de Conférences - Université de Lorraine

Abstract

Ti-Al alloys are an important material for aerospace applications. In order to implement them in more applications it is important to develop a method of grain refinement which can avoid precipitates. A new method of inoculation called isomorphic inoculation was developed where inoculant particles act as direct centers of growth rather than nucleation sites, avoiding the energy barrier required for nucleation. Three inoculant alloys were tested, two which balanced lattice matching between the inoculant and bulk alloy and the inoculant stability in the liquid melt, Ti-10Al-25Nb and Ti-25Al-10Ta, and one which prioritized stability, Ti-47Ta. Casting trials were carried out which showed the balanced alloys sucessfully grain refined the as-cast structure without leaving any heterogeneous particles in the structure. The binary Ti-Ta alloy was not successful due to its high density which caused the particles to settle to the bottom of the ingots where they could not participate in solidification. The inoculants were found to have an efficiency greater than one, meaning each particle was responsible for more than one new grain forming in the cast structure. This was attributed to the polycrystalline nature of the partciles which may break up into multiple particles by preferential dissolution or wetting of the grain boundaries during interaction with the melt. Calculations showed that taking into account particle break up and dissolution the efficiencies approached one, indicating this mechanism is responsible for the anomalously high efficiencies observed.
Keywords: Solidification, Inoculation, Ti-Al

Résumé

Les alliages Ti-Al sont depuis peu utilisés industriellement dans le domaine aéronautique. Il est nécessaire d'affiner les grains dans ces alliages en évitant la formation des précipités. Une nouvelle méthode d'inoculation appelée inoculation isomorphe a été développée où les particules agissent comme des sites de croissance plutôt que comme des sites de germination, évitant ainsi la barrière d'énergie pour la germination. Trois alliages inoculants ont été développés, les deux premiers, Ti-10Al-25Nb et Ti-25Al-10Ta, allient une bonne cohérence du paramètre de maille avec l'alliage de base et une bonne stabilité dans le liquide. Le troisième, Ti-47Ta, met en avant l'aspect stabilité. Les coulées ont montré que les premiers deux alliages ont affiné les grains sans laisser de particules hétérogènes. L'alliage binaire Ti-Ta a une densité trop importante et les particules ont sédimentées dans le lingot où elles n'ont pas pu jouer leur rôle. L'efficacité des inoculants est supérieure à l'unité, chaque particule étant responsable de la formation de plus d'un nouveau grain. Ce dernier effet est attribué à la polycristallinité des inoculants qui peuvent se fragmenter par dissolution préférentielle aux joints de grains. Les calculs prenant en compte la fragmentation et la dissolution indiquent des efficacités proches de l'unité, ce qui confirme les valeurs expérimentales d'efficacité anormalement élevées.

Mots Clés: Solidification, Inoculation, Ti-Al

Acknowledgements

This work was carried out through the LabEx DAMAS, both at Institut Jean Lamour in Nancy and the LEM3 in Metz. Thanks to Theirry Belmont, Eric Gaffet, El Mostafa Daya and Laszlo Toth for hosting me in their laboratories.

Special thanks to Jaques Lacaze and Marc Thomas for taking the time to review and report on this manuscript. Thanks as well to the other members of the jury Florian Kargl, Ulrike Hecht and Alain Hazotte for attending my defense and for all of your thoughtful questions.

I would like to thank my supervisors Julien Zollinger and Emmanuel Bouzy for their support and guidance. You were both a constant support, always willing to help both within the framework of work as well as life in general. I have learned an immense amount from both of you.

Thanks as well to Herve Combeau head of the research group “solidification” for his leadership and management of our team. I would also like to thank Dominique Daloz for his input and counsel through this work. As well thanks to Miha Zoloznik and Bernard Rouat for always being available to help me with whatever I needed.

Thanks to the researchers and students in group 302, and department 3, Rayan Bhar, Edgar Castro, Lea Decultot, Manoj Joshi, Rapheal Marin, Savya Sachi, Ilia Ushakov, Benjamin Gerin, Yuze Li, Antonio Olmedilla, Kartik Jeyabalan, my office mates Marvin Gennesson, Soufiane Guernaoui, Bassem Ben Yahia, my lunch buddies Kanika Anand, Martín Cisternas, Nicole Reilly and Suresh Kumar Pillai, and everyone else at Institute Jean Lamour and LEM3, as well as Mark Park for his assistance with the experimental work for TiTa. Special thanks to Julien Jourdan for your friendship and willingness to try any crazy plan. I could not have done this without all of you. I would also like to thank Jaime, for moving across the planet and being beside me for every new challenge we’ve faced.

A final thanks to the French State for funding this thesis through the program "Investment in the future" operated by the National Research Agency (ANR) and referenced by ANR-11-LABX-0008-01 (LabEx DAMAS) and to the Region Lorraine.

À plus dans le bus!

Do not try to do extraordinary things but do ordinary things with intensity.
-Emily Carr

To move to a new place -- that's the greatest excitement. For a while you believe you carry nothing with you -- all is canceled from before, or cauterized, and you begin again and nothing will go wrong this time."
—Margaret Laurence, The Stone Angel

Résumé étendu

Les alliages Ti-Al sont très utiles pour les cas industriels, spécifiquement dans le domaine aérospatial. Depuis les années 1990 beaucoup d'études ont été conduites sur ces alliages, spécialement pour des applications à haute température. Ces alliages sont intéressants pour ces applications parce qu'ils sont résistants à l'oxydation, au fluage et en fatigue, en ayant une bonne résistance spécifique. Malheureusement ils ont une faible ductilité à température ambiante. Cela rend leur fabrication difficile. Ces alliages sont très réactifs, ce qui complique leur élaboration et augmente les coûts associés. Une comparaison de leur résistance spécifique par rapport à d'autres matériaux en fonction de la température et l'évolution de la contrainte à rupture avec la température est présentée sur la Figure 1.

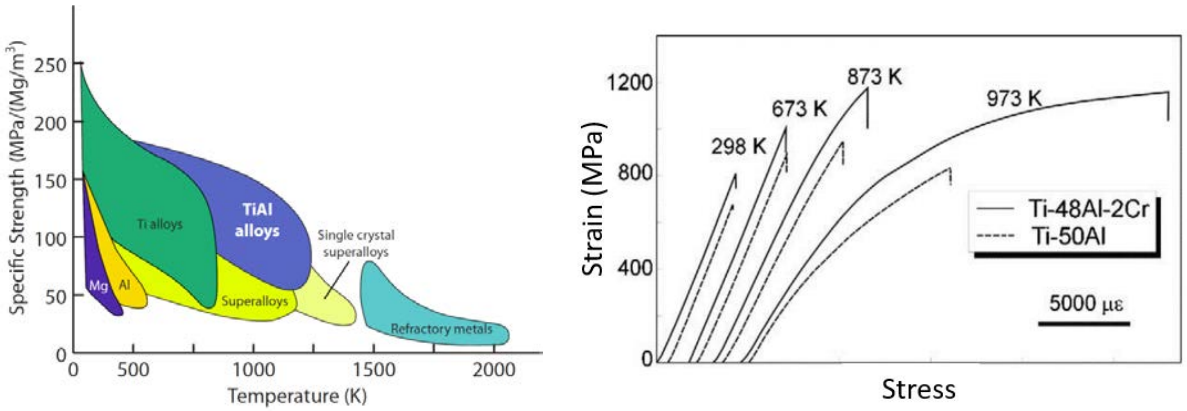

(A) (B)

Figure 1: (A) Résistance spécifique pour une sélection de matériaux [**1**] et (B) courbes issues d'essais de traction pour deux alliages de Ti-Al à différentes températures [**2**].

Aujourd'hui, ces alliages sont utilisés dans les aubes de turbines basse pression dans le dernier étage des moteurs de SAFRAN, le LEAP et GE, le GeNX, et aussi dans les turbocompresseurs et les soupapes d'échappement de certaines voitures. Les alliages intéressants pour des applications industrielles, sont sur le plateau péritectique à environ 40 à 50 at% Al. Sur ce plateau il y a trois phases qui peuvent se former, α, β, et γ. La phase α a une structure hexagonale compacte (HC), la phase β a une structure cubique centrée (CC) et la phase γ a une structure quadratique mais comme le rapport c/a est proche de 1, on la considèrera le plus souvent comme ayant une pseudo-symétrie cubique à faces centrées (CFC). Ces trois phases possèdent des relations d'orientation. Une possibilité pour augmenter leur faible ductilité à basse température est l'affinage de la taille de grains dans la microstructure. Normalement, le fait d'avoir des grains fins est un facteur défavorable pour le fluage mais dans les aubes des turbines le mode de rupture est complexe, et il faut un compromis entre propriétés en fluage, en oxydation et en fatigue. Dans ce cas particulier, un affinage des grains est plutôt une bonne solution. Aujourd'hui, le contrôle de la microstructure s'effectue principalement au cours de traitements thermomécaniques et pas ou peu lors de l'élaboration par fonderie. L'objectif de ce travail est de développer une méthode d'affinage de la microstructure lors de l'étape de solidification.

Pour faire un affinage des grains pendant la fonderie il est nécessaire de comprendre le procédé de solidification. La solidification est une étape très importante pour la fabrication des alliages métalliques, la plupart des alliages industriels sont fabriqués avec un procédé qui comprend une étape où l'alliage est à l'état liquide. Ce peut être pour la fabrication d'un gros lingot qui subira ensuite d'autres procédés de mise en forme ou pour la fonderie d'un produit proche de la forme finale. Dans tous les cas le procédé de solidification comprend deux étapes, la germination et la croissance. La germination correspond à la formation d'un « germe » de solide dans le liquide. Si le germe a une taille suffisante il va croître, sinon il va redevenir liquide. La taille critique dépend de beaucoup de paramètres comme la température du liquide, l'existence de particules dans le liquide sur lesquelles la germination peut se faire etc. Ces paramètres sont importants parce qu'ils déterminent la barrière d'énergie à franchir pour éviter la refusion et donc permettre la croissance. Si le nombre des germes augmentent, avec une taille supérieure ou égale à la taille critique, il y aura davantage de grains dans le matériau après solidification et donc les grains seront plus fins.

Une des méthodes pour augmenter le nombre de germes est l'inoculation. Cela peut se faire selon deux modes. Le premier consiste à ajouter directement les particules solides dans le liquide. Le deuxième consiste à ajouter des éléments dans le liquide qui vont réagir avec le liquide et former des particules. Les deux modes sont utilisés dans l'industrie. Chaque particule ne donne pas lieu à la formation d'un germe mais lorsque c'est le cas, elles permettent de diminuer la barrière d'énergie pour former un germe. Celle-ci dépend des relations entre le liquide, les particules et le solide qui va se former. Il existe plusieurs théories. Si le mouillage entre la particule et le solide est faible, la théorie, dite classique, où le germe forme un hémisphère sur la surface de la particule, fonctionne bien. Si, au contraire, le mouillage entre la particule et le solide est fort, cette théorie ne fonctionne plus et d'autres théories comme celles de l'adsorption ou du mouillage seront utilisées. Dans le cas des alliages Ti-Al, les inoculants utilisés traditionnellement sont les borures de titane. Ils permettent de bien affiner la microstructure. Cependant, ils forment de longs précipités fragiles dans la structure de solidification qui vont réduire la ductilité. Il est donc nécessaire de trouver de nouveaux inoculants pour les alliages de Ti-Al qui ne réduisent pas la ductilité.

Dans le cadre de l'inoculation traditionnelle, les particules permettent de diminuer la barrière d'énergie mais celle-ci existe encore. Nous proposons un nouveau concept d'inoculation dans lequel les particules ne donnent pas lieu à la formation de germes mais sont elles-mêmes des germes. Cette inoculation est dite inoculation isomorphe parce que les particules appartiennent à la même phase que le solide qui croît à partir d'elles. Avec ces particules, il n'y a plus de barrière d'énergie correspondant à l'étape de germination puisque les germes existent déjà et que le solide ne fait que croître à partir de ces derniers. Une comparaison entre l'inoculation traditionnelle et l'inoculation isomorphe se trouve sur le schéma de la Figure 2. Contrairement à l'inoculation traditionnelle, dans l'inoculation isomorphe, chaque particule participe à la solidification et contribue à la formation d'un nouveau grain. Pour qu'une inoculation isomorphe puisse se faire de manière efficace, nous proposons quatre critères. Le premier critère correspond à un bon accord de phase et de paramètres réticulaires entre les particules et la phase solide qui se forme de façon à ce qu'il n'y ait pas de germination du solide mais une

croissance directe à partir des particules d'inoculant. Le deuxième critère correspond à une bonne stabilité thermique et diffusive des particules dans le liquide. En effet, si les particules ne sont pas stables dans le liquide, elles vont fondre ou se dissoudre dans le liquide et donc ne participeront pas à la solidification. Le troisième critère correspond à la facilité à mettre en œuvre l'inoculation isomorphe. Ainsi, il faut prendre en compte la différence de densité entre les particules et le liquide pour que le mélange se fasse de manière homogène, ou la facilité à fabriquer des particules etc. Le dernier critère est impératif, il consiste à ne pas diminuer les propriétés mécaniques de l'alliage après solidification, et donc à éviter la formation de phases fragiles.

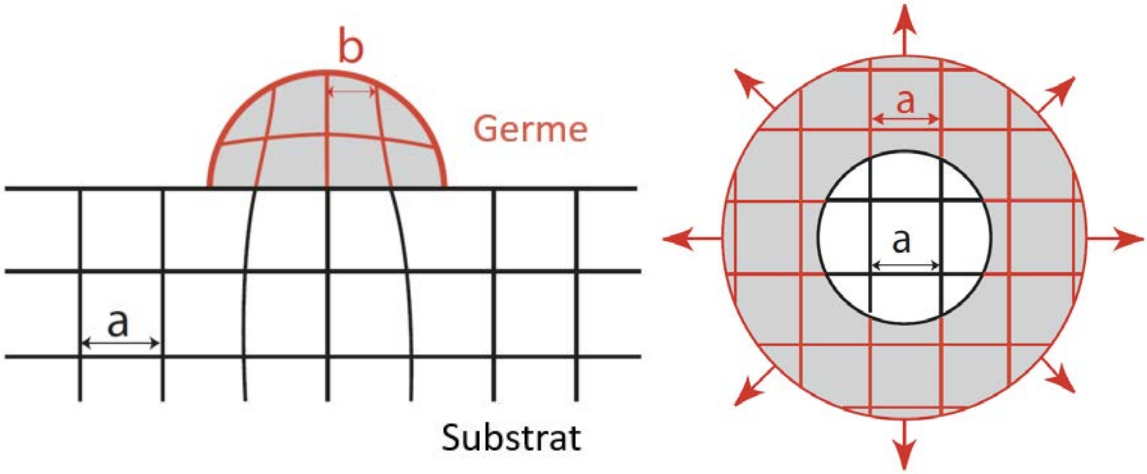

Figure 2: Schéma d'inoculation traditionnelle (à gauche) et d'inoculation isomorphe (à droite) avec les particules d'inoculant en blanc et le solide qui se forme en gris.

Les alliages constituant les inoculants ont été choisis selon ces quatre critères. L'alliage de base à inoculer a pour composition chimique Ti-46Al (at%). Les compositions chimiques des alliages constituant les inoculants ont été choisies parmi deux systèmes ternaires : Ti-Al-Nb et Ti-Al-Ta et un système binaire Ti-Ta. En ce qui concerne le système ternaire Ti-Al-Nb, Nb est un élément qui stabilise la phase β Ti [**3**] avec un haut point de fusion : 2415 ºC [**4**]. Un compromis entre la stabilité et le bon accord des phases et des paramètres réticulaires entre l'inoculant et l'alliage de base a été trouvé. L'alliage choisi a la composition chimique Ti-10Al-25Nb (at%). A haute température, il est constitué de la phase β jusqu'à sa température de fusion (1800ºC [**5**]) qui se situe bien au-delà de celle de l'alliage de base (1550°C), de plus, il a un faible désaccord paramétrique avec l'alliage de base, moins de deux pour cent, et le Nb devrait augmenter sa stabilité vis-à-vis de la diffusion. A signaler toutefois, la densité de cet alliage est supérieure de 40% à celle de l'alliage de base. Le second système étudié est le ternaire Ti-Al-Ta. Ta a une température de fusion plus élevée que celle du Nb (3000ºC [**4**]) mais il est aussi plus dense. Un compromis a été trouvé entre la stabilité et le bon accord des phases et des paramètres réticulaires et un alliage de composition chimique Ti-25Al-10Ta a été choisi. Comme pour Ti-Al-Nb il y a un faible désaccord paramétrique avec l'alliage de base (2%), le Ta devrait augmenter sa stabilité vis-à-vis de la diffusion et il a une température de fusion (1725ºC) plus élevée que celle de l'alliage de base. Le dernier système étudié est le binaire Ti-Ta. Il a été choisi parce que l'on voulait placer la priorité davantage sur la stabilité thermique

et diffusive que sur le bon accord des phases et des paramètres réticulaires. L'alliage retenu a la composition chimique : Ti-47Ta, ce qui correspond au maximum de Ta possible sans risque de formation de la phase fragile σ. Cet alliage (Ti-47Ta) a un désaccord paramétrique avec l'alliage de base plus élevé que les deux autres inoculants mais il reste toutefois inférieur à cinq pour cent. Il a la plus haute température de fusion (2200°C) de tous les inoculants et plus de Ta, ce qui accroît sa stabilité vis-à-vis de la diffusion. Il est à noter que c'est l'inoculant qui a la plus grande densité, deux fois plus élevée que celle de l'alliage de base. Cela pourra poser un problème pour la mise en œuvre de cet inoculant. Les propriétés importantes de ces trois alliages sont résumées dans le Table 0.1.

Table 0.1:Propriétés des alliages inoculants (à 1540°C)

Alliage	α Paramètre cristallin (nm)	T_m (°C)	ρ (g/cm^3)		Espèce qui diffuse le plus lentement	D (cm^2/s) (traceur) [**6**]	D (cm^2/s) (interdiffusion)
			25 °C	1540 °C			
Ti-46Al	0.330	1540	3.71	3.55			
Ti-10Al-25Nb	0.335	1800	5.25	5.02	Nb	$1.40\text{x}10^{-8}$	$1.02\text{x}10^{-8}$ [**7**]
Ti-25Al-10Ta	0.336	1725	5.13	4.91	Ta	$5.63\text{x}10^{-9}$	$1.22\ \text{x}10^{-8}$ [**8**]
Ti-47Ta	0.345	2200	10.14	8.95	Ta	$5.63\text{x}10^{-9}$	$2.34\ \text{x}10^{-10}$ [**8**]

Pour utiliser ces alliages pour l'inoculation isomorphe, il est nécessaire d'élaborer les alliages puis de les réduire en poudres de façon à pouvoir les ajouter à l'alliage de base. Les alliages ont été fabriqués à l'aide d'une sole froide chauffée par induction à partir d'éléments purs (pureté>99%). Chaque élément a été ajouté en commençant par l'élément avec la plus haute température de fusion et ainsi de suite. Un lingot de chaque alliage été produit puis des tournures ou des copeaux ont été obtenus par tournage ou par forage, ils ont ensuite été réduits en poudres par cryo-broyage. Le procédé de cryo-broyage a été choisi parce qu'il rend les alliages plus fragiles et de ce fait, permet de réduire la taille des poudres et de prévenir leur agglomération. Le cryo-broyage a été effectué pour des temps allant de 90 minutes à 11 heures de manière à disposer de différentes distributions de tailles de poudres à inoculer. Les poudres ont été caractérisées selon deux méthodes, l'analyse d'images faites avec un MEB (microscope électronique à balayage) et DLS (diffusion dynamique de la lumière). Les deux méthodes permettent de caractériser la taille des poudres, avec le MEB par la méthode numérique et avec la DLS par la méthode volumétrique. Les résultats obtenus à l'aide des deux méthodes se trouvent dans le Table 0.2. Enfin la microstructure des poudres a été caractérisée par la méthode TKD (transmission Kikuchi diffraction) pour les poudres de Ti-Al-Nb après trois et neuf heures de cryo-broyage. Après trois heures, la microstructure se présente sous forme de grains de phase β aplatis comme des crêpes d'épaisseur d'environ 50 nm et après neuf heures, comme des grains de phase β plus ou moins équiaxes de taille d'environ 50 nm car le processus de subdivision des grains se poursuit pendant le broyage.

Table 0.2: Taille des particules de poudres

	D50 (μm)										
	MEB					DLS					
Alliage	1.5	3	6	9	11	1.5	3	6	9	11	Atmosphère
Ti-Al-Nb	-	191	163	113	48	-	282	267	205*	137	Air
Ti-Al-Ta	-	56	38	20*	-	-	125	110	100	-	Air
Ti-Ta	70	35	22	20	-	98	39	31	20*	-	Ar
Ti-Al-Nb	-	233	-	-	-	-	339	-	-	-	Ar
	D99 (μm)										
	MEB					DLS					
Alliage	1.5	3	6	9	11	1.5	3	6	9	11	Atmosphère
Ti-Al-Nb	-	775	561	440	282	-	478	420	370*	337	Air
Ti-Al-Ta	-	567	390	267*	-	-	410	387	299	-	Air
Ti-Ta	334	160	73	56	-	430	208	156	108*	-	Ar
Ti-Al-Nb	-	607	-	-	-	-	522	-	-	-	Ar

Pour tester les inoculants, des lingots de ~40g de Ti-Al ont été produits avec et sans inoculants et les tailles de grains après solidification ont été comparées. Les poudres sont introduites sous forme de pastilles obtenues par pression à froid d'une moitié de poudres d'inoculant et d'une moitié de poudres d'Al pur. L'Al a été ajouté pour lier les particules de poudres d'inoculant entre elles. Les pastilles sont maintenues au-dessus de l'alliage de base au bout d'une tige par aspiration du vide. Lorsque l'alliage a fondu, le vide de la tige est cassé et la pastille tombe dans l'alliage fondu. La pastille reste en contact avec le métal liquide pendant une période de 20 s de façon à ce que les poudres atteignent équilibre thermique et commencent à interagir avec le liquide. Après cette période, le four est coupé et la solidification commence. Pour l'analyse métallographique, une attaque chimique avec le réactif de Kroll est faite sur une coupe transversale de chacun des lingots. Les inoculants ternaires (Ti-Al-Nb et Ti-Al-Ta) sont comparés avec l'alliage de base préparé pour chaque expérience à partir des éléments purs mais les inoculants binaires (Ti-Ta) sont testés avec l'alliage de base provenant d'un gros lingot préparé pour toutes les expériences. Les images caractéristiques de la structure à l'échelle microscopique (par MEB) et à l'échelle macroscopique (par microscope optique) des lingots préparés avec les inoculants Ti-Al-Nb, Ti-Al-Nb et Ti-Ta et d'un lingot préparé sans inoculant se trouvent sur la Figure 3. Enfin, un autre lingot a été préparé, pour voir quel est l'effet de l'élément Nb lorsqu'il est ajouté non pas sous forme d'inoculant mais en solution dans le métal liquide dans les expériences avec Ti-Al-Nb. Les résultats des expériences d'inoculation avec la taille des grains réduite par rapport à ce qu'elle est sans inoculation, se trouvent dans le Tableau 3.

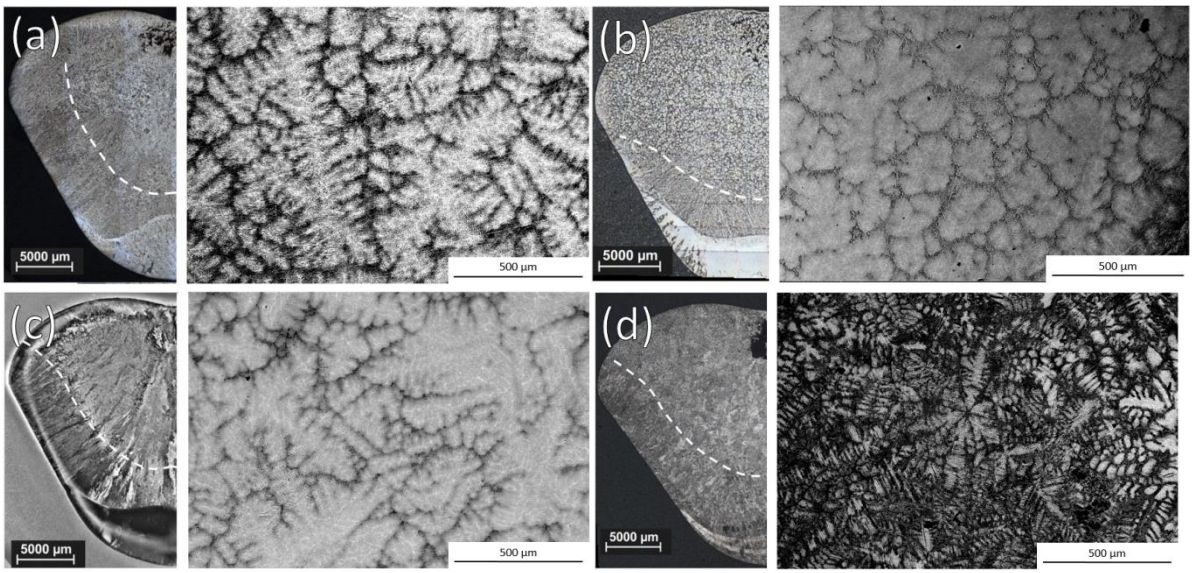

Figure 3: Images optiques de la coupe transversale des lingots et images BSE par MEB de la zone equiaxe (a) sans inoculation et après inoculation avec des poudres cryo-broyées pendant 3 heures de (b) Ti-Al-Nb, (c) Ti-Al-Ta et (d) Ti-Ta.

Table 0.3: taille des grains et fraction équiaxe avec et sans inoculation

Alliage	Temps de broyage (hrs)	Taille des Grains (µm)	Fraction Equiaxe	Composition Al (at%)
Reference		696	0.3	46.1
Nb en sol. solide		587	0.31	45.1
Ti-Al-Nb	0	403	0.69	45.6
	3 (Ar)	397	0.68	45.5
	3	336	0.63	45.5
	6	446	0.64	44.4
	9	337	0.64	45.4
	11	188	0.42	45.1
Ti-Al-Ta	3	335	0.52	45.7
	9	308	0.64	45.8

Les particules de Ti-Ta ont été introduites parce qu'elles avaient la meilleure stabilité dans le liquide, mais aucune des expériences avec ces particules n'a permis de réduire la taille des grains dans les lingots. En fait, les particules de Ti-Ta se trouvent au fond des lingots et non pas dans la zone équiaxe, elles ne sont donc pas utiles pour la solidification. Elles se trouvent au fond des lingots parce qu'elles présentent une grande différence de densité avec le liquide. De plus, la phase qui solidifie dans ces lingots n'est pas la phase β-Ti mais la phase α-Ti. En effet, les dendrites ont six bras comme dans une structure hexagonale et non pas quatre comme dans une structure cubique. Ce peut être dû au fait que le gros lingot de Ti-Al utilisé pour l'alliage de base pour ces expériences ait été contaminé par l'oxygène. En effet, une légère augmentation de l'oxygène peut changer la phase primaire de solidification de β à α.

Pour les inoculants Ti-Al-Nb et Ti-Al-Ta, les expériences ont été couronnées de succès en ce sens qu'elles ont permises de réduire la taille de grain. Sur la Figure 4, on peut voir comment la taille des grains après solidification varie avec la taille ou le nombre des particules d'inoculant introduites. Si la taille des particules ajoutées diminue, la taille des grains equiaxes diminue aussi. Si le nombre de particules ajoutées augmente, la taille des grains equiaxes diminue. En fait, il y a une relation entre la taille et le nombre de particules ajoutées car tous les essais se sont fait à masse d'inoculant constante et donc, plus la taille des particules diminue et plus leur nombre augmente.

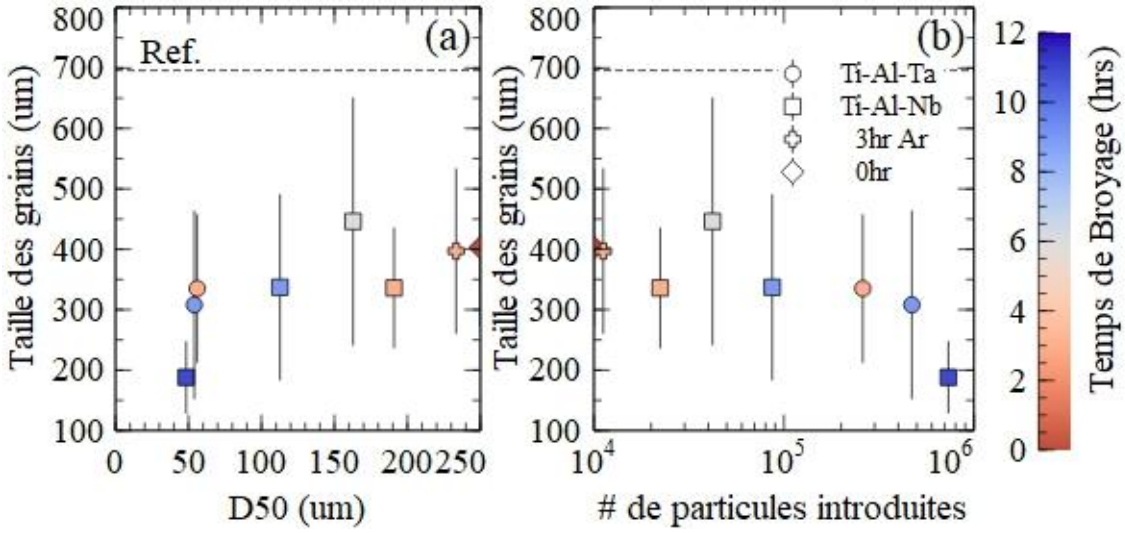

Figure 4: Effet des particules ajoutées sur la taille des grains par (a) taille des particules et (b) nombre de particules introduites

Dans le cas de l'inoculation classique, il est nécessaire d'ajouter beaucoup plus de particules qu'il n'y a de grains qui se forment. Il est intéressant de voir sur la Figure 5(a) que dans chacune des expériences avec les particules de Ti-Al-Nb, plus d'un grain été formé pour chaque particule ajoutée. Dans le cas des particules de Ti-Al-Ta il y a environ un grain qui se forme pour chaque particule ajoutée. En comparaison, dans l'inoculation classique ce ratio est beaucoup plus faible [**9**,**10**]. L'augmentation drastique de ce ratio entre l'inoculation classique et l'inoculation isomorphe s'explique par le fait que les mécanismes sont différents. Dans l'inoculation isomorphe, il n'est pas besoin de former un nouveau germe de solide comme dans l'inoculation classique, le solide peut simplement croître à partir de l'inoculant qui constitue un germe préexistant. Ainsi, chaque particule peut former au moins un grain. On peut voir sur la Figure 5b) que les particules les plus grosses, qui ont été ajoutées en plus petit nombre puisque l'ajout se fait à masse constante, forment plus de grains par particule. Cela peut s'expliquer par un phénomène de fragmentation des particules en plusieurs petites particules. En effet, pendant leur temps de maintien à haute température (20s), il y a une dissolution spécifique au niveau des joints de grains dans les particules d'inoculants [**11**]. Chaque petite particule peut alors être responsable de la croissance d'un nouveau grain dans le lingot. Comme les grosses particules peuvent se fragmenter en plus de parties que les petites particules, elles permettent de former plus de grains que les petites.

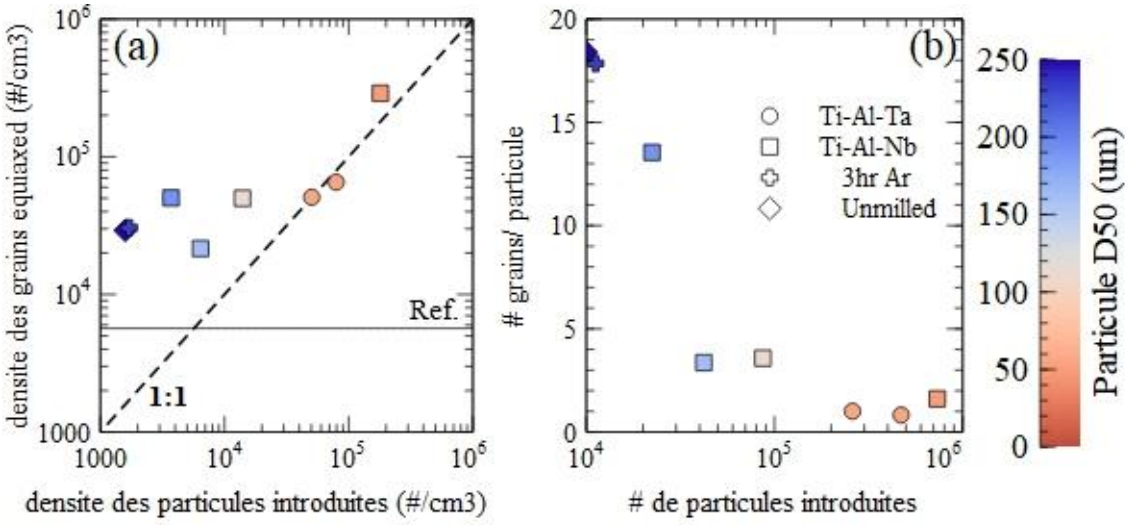

Figure 5 : (a) effet du nombre de particules par unité de volume sur le nombre de grains par unité de volume dans le lingot et (b) relation entre le nombre de particules introduites et le nombre de grains formé par chaque particule

Un cas de fragmentation d'une grosse particule a été observé dans un lingot inoculé avec des particules Ti-Ta, comme on peut le voir sur la Figure 6 avec le schéma correspondant. On voit nettement la dissolution qui se fait au niveau des joints de grain et qui aboutit à la fragmentation de la particule en plusieurs. Cette fragmentation des particules va entraîner un changement de la distribution des particules dans le liquide pendant l'inoculation. Par ailleurs, les plus petites particules peuvent se dissoudre totalement dans le liquide. Ainsi, le nombre de particules introduites n'est pas le nombre réel de particules présentes pendant solidification car les petites particules se dissolvent et les grosses particules se fragmentent. Pour cette raison, le nombre des particules introduites est simplement indicatif du nombre de particules présentes pendant la solidification.

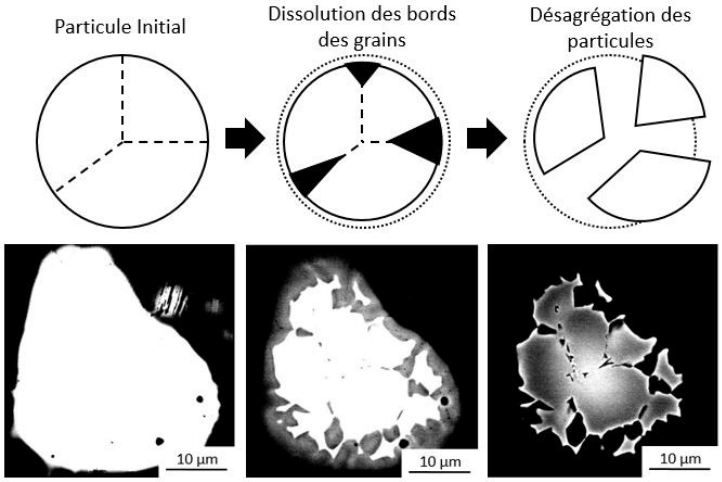

Figure 6: Schéma du processus de fragmentation des particules par dissolution préférentielle au niveau des joints de grains et images d'une particule de Ti-Ta dans un lingot solidifié pendant un tel processus de fragmentation .

Une expérience a été menée dans laquelle une tige de Ti-Al-Nb est trempée dans un liquide de Ti-Al pendant 20s puis solidifiée. Il est intéressant d'examiner l'interface tige/liquide pour savoir si un germe solide se forme sur Ti-Al-Nb ou bien s'il y a une simple croissance à partir de Ti-Al-Nb. Une partie de cette interface se trouve sur la Figure 7 avec les relations d'orientations entre les phases correspondantes. La tige correspond à la phase β (bleue) en haut des images avec en dessous une bande de α (jaune). De la tige au liquide, il y a une partie où il est possible de voir la transition de β à α et γ. les orientations des phases obéissent aux relations d'orientations entre phases habituelles. Ce qui indique qu'il n'y a pas germination mais bien croissance à partir de l'inoculant.

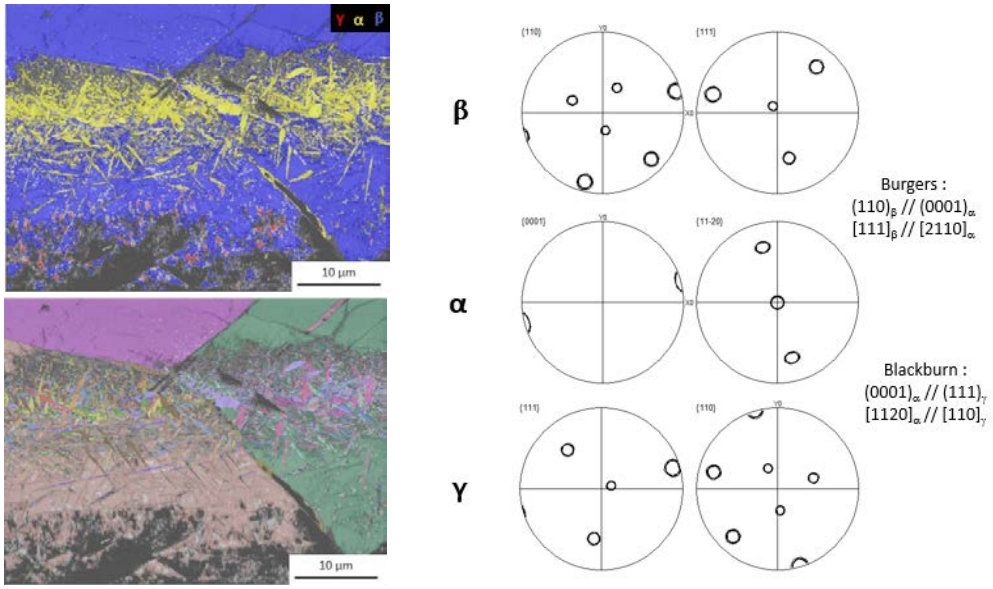

Figure 7: Images de la tige et de l'interface Ti-Al-Nb / Ti-Al liquide et orientations correspondantes des différentes phases

Table of Contents

Abstract I
Acknowledgements II
Résumé étendu IV
List Of Figures XVIII
List of Tables XXIV
Introduction 1
Chapter 1 Titanium Aluminium Alloys 3
1.1 Introduction to Ti-Al 3
1.2 The Ti-Al Binary System 5
1.2.1 Ti-Al Phase Diagram 5
1.1.4 Microstructures 8
1.3 Casting and Processing 11
1.4 Mechanical Properties 12
1.4.1 Creep 13
1.4.2 Fatigue 14
1.4.3 Fracture 14
1.5 Summary 15
Chapter 2 Solidification, Grain Refinement, and Isomorphic Self Inoculation 17
2.1 Solidification of Metallic Alloys 17
2.1.1 Overview of the Solidification process 17
2.1.2 Nucleation Theories 19
2.1.3 Solutal Growth Restriction 24
2.1.4 Summary 25
2.2 Inoculation of Metallic Alloys 25
2.2.1 Inoculation in The Ti-Al System 28
2.3 Development of Isomorphic Self Inoculation 30
2.3.1 ISI Criteria I: Phase and Lattice Matching 31
2.3.2 ISI Criteria II: Stability in the Melt 32
2.3.3 ISI Criteria III: Usability Factors 34
2.3.4 ISI Criteria IV: No Negative Effects on Final Cast Product 34
2.4 Summary 34
Chapter 3 Inoculant Alloy Selection, Production, and Characterization 37
3.1 Inoculant Alloy Selection 37
3.1.1 Selection and Description of the Bulk Base Alloy 37
3.1.2 Selection and Description of the Inoculant Alloys 41

3.1.3 Summary of Inoculant and Bulk Alloy Properties 52
3.2 Powder Production 52
3.2.1 Bulk Alloys 52
3.2.2 Powder Milling 54
3.3 Powder Characterization 55
3.3.1 Size Characterization 56
3.3.2 Microstructure Characterization 62
3.3.3 Effects on Milling 65
3.4 Summary 72
Chapter 4 Isomorphic Self-Inoculation Casting Trials 75
4.1 Inoculation Procedure 75
4.1.1 Inoculant Preparation 75
4.1.2 Number of Inoculant Particles 76
4.1.3 Ingot Preparation 78
4.1.4 Inoculation 79
4.2 Ingot Analysis Procedure 81
4.2.1 Sample Preparation 81
4.2.2 Measurement of Ingot Equiaxed Area 82
4.2.3 Grain Size Measurement 83
4.3 Individual Bulk Alloy Ingot Trials 84
4.3.1 Ti-Al-Nb Trials 84
4.3.2 Ti-Al-Ta Trials 92
4.3.3 Summary of Individual Ingot Trials 94
4.4 Ti-Ta Trials 94
4.4.1 Ti-Ta Collective Bulk Alloy Trials 95
4.4.2 Individual Bulk Alloy Ingot Trial 100
4.4.3 Summary 101
4.5 Conclusions 102
Chapter 5 Influence of Inoculant Alloys and Their Processing Parameters 103
5.1 Anomalous Ti-Ta Results 103
5.1.1 Density Effects 104
5.1.2 Oxygen Content 104
5.1.3 Superlarge Particles 105
5.1.4 Individual Bulk Alloy Trial 106
5.1.5 Summary 107
5.2 Ti-Al-Nb and Ti-Al-Ta Grain Refinement 107
5.2.1 Distribution Effects 107

5.2.2 Particle Break Up 111
5.3 Particle-Melt Interactions 112
5.3.1 Effect of Particle Size and Density on Velocity in the Melt 112
5.3.2 Diffusion between Particles and Molten Alloy 114
5.4 Conclusions 117
Chapter 6 Inoculant-Melt Interactions 118
6.1 Inoculant Alloy Interaction with Melt 118
6.1.1 Rod Dipping Procedure 118
6.1.2 Dissolution of Rod in Melt 119
6.2 Influence of Thermal Effects on Particle Grain Size 121
6.2.1 Particle annealing 121
6.2.2 As-Milled Particle Microstructure 121
6.2.3 Recreating Particle Thermal Treatment 123
6.3 Particle Dissolution in Liquid Melt 126
6.3.1 Influence of Fluid Flow 126
6.3.2 Application of the Model to Different Particle Sizes 131
6.4 Repercussions on Isomorphic Inoculation Trials 133
6.4.1 Number of Grains Present During Solidification 133
6.5 Conclusions 137
Chapter 7 Conclusions and Recommendations 139
7.1 Conclusions 139
7.2 Recommendations 141
7.2.1 Ti-Al Applications 141
7.2.2 Mechanism of Isomorphic Inoculation 141
References 143
Appendix A –Particle Size Distributions ..... A
A.1 SEM Image Characterization ..... A
A.1.1 Ti-Al-Nb SEM Particle Size Analysis ..... A
A.1.2 Ti-Al-Ta SEM Particle Size Analysis ..... B
A.1.3 Ti-Ta SEM Particle Size Analysis C
A.2 Differential Laser Scattering Characterization ..... E
A.2.1 Ti-Al-Nb DLS Particle Size Analysis ..... E
A.2.2 Ti-Al-Ta DLS Particle Size Analysis ..... F
A.2.3 Ti-Ta DLS Particle Size Analysis ..... G
A.3 Trends in Particle Distributions with Grinding Time I
A.3.1 Ti-Al-Nb I
A.3.2 Ti-Al-Ta ..... J

A.3.3 Ti-Ta ..... K
A.4 Comparison of SEM and DLS ..... K
Appendix B – Calculation of the Effect of Al Content on Grain Size ..... M
Appendix C - Effect of interaction time on Unsuccessful Ti-Ta Trials ..... U
C.1 Nine Hour Milled Ti-Ta 20s Interaction Time ..... U
C.2 6 Hour Milled Ti-Ta ..... W
C.3 Summary ..... Y
Appendix D – Rod Manufacture and Further Analysis ..... AA
D.1 Manufacturing of Ti-Al-Nb Rod ..... AA
D.2 Rod Microstructure and Grain Size CC
D.3 Chemical Analysis to Determine Interface Temperature ..... EE
D.4 Orientation Relationship Between Rod and Bulk ..... FF
Appendix E - Particle Heat Treatment II
E.1 Extended Time Heat Treatment Procedure II
E.2 Short Time Particle Thermal Treatment ..... JJ
E.3 Chemical Analysis ..... JJ
Abstract LL

List Of Figures

FIGURE 1: (A) RESISTANCE SPECIFIQUE POUR UNE SELECTION DE MATERIAUX [**1**] ET (B) COURBES ISSUES D'ESSAIS DE TRACTION POUR DEUX ALLIAGES DE TI-AL A DIFFERENTES TEMPERATURES [**2**]. IV
FIGURE 2: SCHEMA D'INOCULATION TRADITIONNELLE (A GAUCHE) ET D'INOCULATION ISOMORPHE (A DROITE) AVEC LES PARTICULES D'INOCULANT EN BLANC ET LE SOLIDE QUI SE FORME EN GRIS. VI
FIGURE 3: IMAGES OPTIQUES DE LA COUPE TRANSVERSALE DES LINGOTS ET IMAGES BSE PAR MEB DE LA ZONE EQUIAXE (A) SANS INOCULATION ET APRES INOCULATION AVEC DES POUDRES CRYO-BROYEES PENDANT 3 HEURES DE (B) TI-AL-NB, (C) TI-AL-TA ET (D) TI-TA..... IX
FIGURE 4: EFFET DES PARTICULES AJOUTEES SUR LA TAILLE DES GRAINS PAR (A) TAILLE DES PARTICULES ET (B) NOMBRE DE PARTICULES INTRODUITES X
FIGURE 5 : (A) EFFET DU NOMBRE DE PARTICULES PAR UNITE DE VOLUME SUR LE NOMBRE DE GRAINS PAR UNITE DE VOLUME DANS LE LINGOT ET (B) RELATION ENTRE LE NOMBRE DE PARTICULES INTRODUITES ET LE NOMBRE DE GRAINS FORME PAR CHAQUE PARTICULE..... XI
FIGURE 6: SCHEMA DU PROCESSUS DE FRAGMENTATION DES PARTICULES PAR DISSOLUTION PREFERENTIELLE AU NIVEAU DES JOINTS DE GRAINS ET IMAGES D'UNE PARTICULE DE TI-TA DANS UN LINGOT SOLIDIFIE PENDANT UN TEL PROCESSUS DE FRAGMENTATION XI
FIGURE 7: IMAGES DE LA TIGE ET DE L'INTERFACE TI-AL-NB / TI-AL LIQUIDE ET ORIENTATIONS CORRESPONDANTES DES DIFFERENTES PHASES..... XII
FIGURE 1.1: CROSS SECTION OF TYPICAL TURBINE WITH COMMON BLADE MATERIALS AND OPERATING TEMPERATURES FOR EACH REGION [**13**] 3
FIGURE 1.2: LOW PRESSURE TURBINE OF GENX ENGINE WITH TIAL BASED 6TH AND 7TH STAGES [**14**]..... 4
FIGURE 1.3: (A) SPECIFIC STRENGTH WITH TEMPERATURE SHOWING BENEFIT OF TIAL ALLOYS [**1**] AND (B) CORRESPONDING ELONGATIONS BEFORE FRACTURE [**16**]. 4
FIGURE 1.4: EVOLUTION OF TI-AL PHASE DIAGRAM OVER TIME (A) 1951 BY OGDEN ET.AL. [**19**] (B) 1988 BY MURRAY [**21**]..... 5
FIGURE 1.5: PHASE DIAGRAMS EVALUATED WITH THE HELP OF CALPHAD (A) 2006 BY SCHUSTER AND PALM [**22**] AND (B) 2008 BY WITUSCIEWICZ ET.AL. [**23**]..... 6
FIGURE 1.6: TITANIUM ALUMINIUM BINARY PHASE DIAGRAM AND TRANSFORMATION PATH FOR HYPO-PERITECTIC ALLOY 6
FIGURE 1.7: TI-AL B_0 PHASE CRYSTAL STRUCTURE [**30**] 7
FIGURE 1.8: Ti_3Al A_2 PHASE CRYSTAL STRUCTURE [**30**] 8
FIGURE 1.9: TI-AL Γ PHASE CRYSTAL STRUCTURE [**30**]..... 8
FIGURE 1.10: AS CAST DENDRITE MORPHOLOGIES OBSERVED WITH PRIMARY SOLIDIFICATION PHASE (A) ALPHA [**34**] AND (B) BETA [**35**]..... 9
FIGURE 1.11: FULLY LAMELLAR (A) AND DUPLEX (B) MICROSTRUCTURES OF TI-47.5AL-2.5V-1CR [**36**] 10
FIGURE 1.12: MICROGRAPHS OF THE DIFFERENT MICROSTRUCTURES OF TI-48AL-2CR: (A) NEAR-Γ; (B) DUPLEX; (C) NEARLY LAMELLAR; AND (D) FULLY LAMELLAR [**37**]. 10
FIGURE 1.13: TIAL STRESS STRAIN CURVES AT VARIOUS TEMPERATURES [**2**]..... 13
FIGURE 1.14: CREEP STRAIN OVER TIME FOR LAMELLAR TI-45AL-2MN-2NB ALLOY AT DIFFERENT TEMPERATURES AND APPLIED STRESSES [**64**]..... 13
FIGURE 2.1: TEMPERATURE VS. TIME FOR SOLIDIFICATION 17
FIGURE 2.2: 2D SCHEMATIC OF INGOT STRUCTURE..... 19
FIGURE 2.3: HETEROGENEOUS NUCLEATION OF A SPHERICAL CAP ON FLAT SUBSTRATE..... 19
FIGURE 2.4: EFFECT OF SUBSTRATE GEOMETRY ON HETEROGENEOUS NUCLEATION FROM (A) CAVITY REDRAWN FROM [**92**] AND (B) SPHERE REDRAWN FROM [**97**]..... 20
FIGURE 2.5: SCHEMATIC AND EQUATIONS FOR NUCLEATION BY WETTING OF A SPHERICAL SUBSTRATE [**102**]. 22
FIGURE 2.6: CRITICAL VOLUME FOR NUCLEATION BY PARTICLE WETTING REDRAWN FROM [**102**]..... 22
FIGURE 2.7: RELATION BETWEEN LIQUID QUASICRYSTALS AND SOLID, REDRAWN FROM [**111**]. 23
FIGURE 2.8: SCHEMATIC OF SOLIDIFICATION WITH INOCULATION SHOWING (A) INOCULANT INTRODUCTION (B) NUCLEATION (C) GROWTH AND (D) FULLY SOLIDIFIED. 26
FIGURE 2.9: SCHEMATIC OF HETEROGENEOUS NUCLEATION ON INOCULANT SUBSTRATE 27
FIGURE 2.10: SOLUTE DIFFUSION DIFFUSION FIELD FOR (A) SINGLE PARTICLE AND (B) MULTIPLE OVERLAPPING PARTICLES FROM: [**146**]..... 28
FIGURE 2.11: EVIDENT GRAIN REFINEMENT OF TIAL BY BORON ADDITION (A) TI-45AL AND (B) TI-45AL-0.5B [**159**]. 29
FIGURE 2.12: DETRIMENTAL BORIDE MORPHOLOGIES IN TIAL (A) NEEDLE [**152**] AND (B) FLAKE [**157**] 29
FIGURE 2.13: SCHEMATIC OF SOLID GROWTH BY ISOMORPHIC SELF INOCULATION..... 31

FIGURE 2.14: SCHEMATIC OF SOLIDIFICATION BY ISOMORPHIC SELF INOCULATION SHOWING (A) PARTICLE ADDED TO MELT, (B) SOLID GROWING FROM PARTICLE (C) CONTINUED GROWTH OF PARTICLE AND (D) FINAL MICROSTRUCTURE WITHOUT HETEROGENEOUS REMNANTS OF INOCULANTS. 32
FIGURE 2.15: ISI PARTICLE SIZE EVOLUTION (A) AS INTRODUCED TO MELT (B) INTERACTION WITH MELT AND REACHING EQUILIBRIUM (C) ON SOLIDIFICATION 33
FIGURE 3.1: TI-AL BINARY PHASE DIAGRAM SHOWING BULK ALLOY COMPOSITION [**173**] 38
FIGURE 3.2: CALCULATED DIFFUSION RATES FOR SOME REFRACTORY METALS IN HIGH TEMPERATURE B-TI [**6**]. .. 39
FIGURE 3.3: CALCULATED EVOLUTION OF BASE ALLOY (TI-46AL) LATTICE PARAMETER WITH TEMPERATURE. 40
FIGURE 3.4: CALCULATED EVOLUTION OF BASE ALLOY (TI-46AL) DENSITY WITH TEMPERATURE. 41
FIGURE 3.5: LIQUIDUS SURFACE MAP FOR THE TI-AL-NB SYSTEM [**118**] 42
FIGURE 3.6: CALCULATED TI-AL-NB TERNARY PHASE DIAGRAMS USING THERMOCALC AT (A) 900K AND (B) 1900K SHOWING THE INOCULANT (BLUE X) AND REFERENCE ALLOY (RED X) COMPOSITIONS 43
FIGURE 3.7: DIFFUSION OF NB IN B-TI [**7**]. TI-AL-NB ALLOY AT BULK ALLOY MELTING TEMPERATURE INDICATED. 43
FIGURE 3.8: LATTICE PARAMETER EVOLUTION FOR TI-10AL-25NB FROM 750-1750^{o}C AND CORRESPONDING LATTICE MISMATCH WITH TI-46AL 44
FIGURE 3.9: CALCULATED EVOLUTION OF TI-AL-NB DENSITY WITH TEMPERATURE AND COMPARISON WITH BASE ALLOY (TI-46AL) 45
FIGURE 3.10: LIQUIDUS SURFACE MAP FOR THE TI-AL-TA SYSTEM [**119**] 46
FIGURE 3.11: CALCULATED TI-AL-TA TERNARY PHASE DIAGRAMS USING THERMOCALC AT (A) 900K AND (B) 1800K SHOWING THE INOCULANT (BLUE X) AND REFERENCE ALLOY (RED X) COMPOSITIONS 46
FIGURE 3.12: DIFFUSION OF TA IN B-TI [**8**]. TI-25AL-10TA AT 1540^{o}C INDICATED. 47
FIGURE 3.13: LATTICE PARAMETER EVOLUTION FOR TI-25AL-10TA FROM 750-1750^{o}C AND CORRESPONDING LATTICE MISMATCH WITH TI-46AL 47
FIGURE 3.14: CALCULATED TI-AL-TA DENSITY WITH TEMPERATURE AND COMPARISON WITH TI-46AL 48
FIGURE 3.15: BINARY TI-TA PHASE DIAGRAM [**177**] 49
FIGURE 3.16: TERNARY TI-AL-TA PHASE DIAGRAM SHOWING Σ FORMING REGIONS, BASE ALLOY COMPOSITION (RED X) AND INOCULANT COMPOSITION (BLUE X) 49
FIGURE 3.17: DIFFUSION OF TA IN B-TI [**8**]. TI-TA ALLOY AT BULK ALLOY MELTING TEMPERATURE INDICATED. . 50
FIGURE 3.18: LATTICE PARAMETER EVOLUTION FOR TI-47TA FROM 750-1750^{o}C AND CORRESPONDING LATTICE MISMATCH WITH TI-46AL 51
FIGURE 3.19: CALCULATED EVOLUTION OF TI-TA DENSITY WITH TEMPERATURE AND COMPARISON WITH BASE ALLOY (TI-46AL) 51
FIGURE 3.20: SCHEMATIC OF INDUCTION HEATED COLD CRUCIBLE APPARATUS. 53
FIGURE 3.22: EDX MAP AND POINT ANALYSIS FOR SUCCESSFULLY ALLOYED TI-TA 54
FIGURE 3.23: SEM SE IMAGES OF TI-TA DRILLINGS 54
FIGURE 3.24: CRYOMILLING APPARATUS AND SCHEMATIC OF MILLING CONTAINER SHOWING STEEL BALLS (GREY), POWDERS (BLACK) AND LIQUID NITROGEN (BLUE) 55
FIGURE 3.25: EXAMPLE SEM IMAGES AND PROCEDURE FOR POWDER SIZE ANALYSIS, FROM TI-AL-NB POWDER MILLED FOR 3 HOURS UNDER ARGON, SHOWING (A) SE IMAGE (B) BSE IMAGE (C) COMBINED AND EDITED IMAGE (D) BINARIZED IMAGE WITH ERASED AREAS (E) ANALYZED PARTICLES (F) COLOURIZED AND MEASURED PARTICLE AREAS 58
FIGURE 3.26: APPARATUS (A) AND SCHEMATIC (B) OF DLS SETUP 59
FIGURE 3.27: COMPARISON OF SEM (DASHED LINE), DLS (SOLID LINE), AND NUMERICAL (SQUARE POINTS), VOLUMETRIC (CIRCLE POINTS) MEASURED D50 (A) AND D99 (B) FOR TI-AL-NB PARTICLES. 60
FIGURE 3.28: COMPARISON OF SEM (DASHED LINE), DLS (SOLID LINE), AND NUMERICAL (SQUARE POINTS), VOLUMETRIC (CIRCLE POINTS) MEASURED D50 (A) AND D99 (B) FOR TI-AL-TA PARTICLES. 61
FIGURE 3.29: COMPARISON OF SEM (DASHED LINE), DLS (SOLID LINE), AND NUMERICAL (SQUARE POINTS), VOLUMETRIC (CIRCLE POINTS) MEASURED D50 (A) AND D99 (B) FOR TI-TA PARTICLES. 61
FIGURE 3.30: SCHEMATIC OF TKD SETUP (A) AND SAMPLE KIKUTCHI PATTERN FOR B-TI OBTAINED USING ON-AXIS TKD (B) 62
FIGURE 3.31: PROCEDURE FOR OBTAINING TKD SAMPLES. (A) SELECTION OF AN APPROPRIATE PARTICLE (B) MASKING SECTION OF PARTICLE (C) MILLING OF SAMPLE (D) FINAL SAMPLE 63
FIGURE 3.32: 3 HOUR CRYOMILLED TI-AL-NB (A) TKD ORIENTATION MAP AND (B) FSD IMAGE 64
FIGURE 3.33: 3 HOUR CRYOMILLED TI-AL-NB (A) BOUNDARY MAP SHOWING MISORIENTATIONS >15^{o} AS YELLOW AND <15^{o} AS GREEN, RED OR BLUE AND (B) GRAIN MAP 65
FIGURE 3.34: 3 HOUR CRYOMILLED TI-AL-NB (A) GRAIN SIZE AND (B) GRAIN SHAPE (AVERAGES INDICATED) 65
FIGURE 3.35: 9 HOUR CRYOMILLED TI-AL-NB (A) TKD ORIENTATION MAP AND (B) FSD IMAGE 66
FIGURE 3.36: 9 HOUR CRYOMILLED TI-AL-NB (A) BOUNDARY MAP SHOWING MISORIENTATIONS >15^{o} AS YELLOW AND <15^{o} AS GREEN, RED OR BLUE AND (B) GRAIN MAP 67

FIGURE 3.37: 9 HOUR CRYOMILLED TI-AL-NB (A) GRAIN SIZE AND (B) GRAIN SHAPE (AVERAGES INDICATED) 67
FIGURE 3.38: ALL ALLOY SEM PARTICLE DISTRIBUTION CHARACTERISTICS: (A) D50, D99 AND (B) DISTRIBUTION SPAN. 68
FIGURE 3.39: ALL ALLOY DLS PARTICLE DISTRIBUTION CHARACTERISTICS: (A) D50, D99 AND (B) DISTRIBUTION SPAN. 69
FIGURE 3.40: NUMERICAL (BLACK) AND VOLUMETRIC (BLUE) SIZE DISTRIBUTIONS FOR TI-AL-NB ALLOY MILLED FOR 3 HOURS (A) UNDER AIR AND (B) UNDER AR. 69
FIGURE 3.41: 3 HOUR CRYOMILLED AND HEAT TREATED TI-AL-NB (A) TKD ORIENTATION MAP AND (B) FSD IMAGE 70
FIGURE 3.42: TKD ORIENTATION MAPS OF (A) B-TI AND (B) A-TI FOR 3 HOUR CRYOMILLED THEN HEAT TREATED POWDER 70
FIGURE 3.43: 3 HOUR CRYOMILLED + HEAT TREATED TI-AL-NB (A) BOUNDARY MAP SHOWING MISORIENTATIONS $>15^{o}$ AS YELLOW AND $<15^{o}$ AS GREEN, RED OR BLUE AND (B) GRAIN MAP (C) BOUNDARY MAP SHOWING A-TI AS BLACK AND (D) BOUNDARY MAP SHOWING B-TI AS BLACK 71
FIGURE 3.44: 3 HOUR CRYOMILLED + HEAT TREATED TI-AL-NB (A) GRAIN SIZE AND (B) GRAIN SHAPE FOR BOTH B (BLACK) AND A (BLUE) 72
FIGURE 4.1: IMAGE AND SCHEMATIC OF PELLET FABRICATION PRESS 75
FIGURE 4.2: CONVERTED 3 HR MILLED TI-AL-NB SIZE DISTRIBUTIONS OF (A) SEM NUMERICAL TO VOLUME FRACTION AND (B) DLS VOLUME FRACTION TO NUMERICAL (NOTE LOGARITHMIC SCALE) 76
FIGURE 4.3: CALCULATED INOCULANT SIZE DISTRIBUTION FOR 3 HOUR MILLED TI-AL-NB INOCULATION TRIAL . 77
FIGURE 4.4: LARGE INGOT FABRICATION PROCEDURE SHOWING MELTING (LEFT), CASTING IN PROGRESS (CENTRE) AND FINAL INGOT SOLIDIFICATION (RIGHT). 78
FIGURE 4.5: LARGE CAST TI-AL INGOT (A) TOP VIEW (B) SIDE VIEW (C) REMAINING UNCAST ALLOY SOLIDIFIED IN THE CRUCIBLE AND (D) CUT INGOT CROSS SECTION 79
FIGURE 4.6: COLD CRUCIBLE INOCULATION APPARATUS WITH TOP PORT CIRCLED IN WHITE. 80
FIGURE 4.7: SCHEMATIC OF INOCULATION PROCEDURE SHOWING (A) INITIAL SETUP, (B) INOCULANT PELLET HELD AWAY FROM MOLTEN TI-AL, (C) LOWERING OF PELLET CLOSE TO MELT, (D) REMOVAL OF VACUUM AND PELLET DROP INTO THE MELT, (E) INTERACTION TIME BETWEEN INOCULANT AND MELT AND (F) FINAL INGOT SOLIDIFICATION. 81
FIGURE 4.8: INGOT CROSS SECTION PREPARATION SHOWING (A) THE RAW INGOT, (B) CROSS SECTIONED INGOT IN FIRST MOUNTING AND (C) INGOT HALF MOUNTED FOR POLISHING/ETCHING. 82
FIGURE 4.9: OPTICAL IMAGES OF REFERENCE INGOT BY (A) BRIGHT FIELD WITH COLUMNAR/EQUIAXED TRANSITION INDICATED AND (B) DELINEATION BETWEEN COLUMNAR (BOTTOM) AND EQUIAXED (TOP) REGIONS OF SOLIDIFIED INGOT 82
FIGURE 4.10: BSE IMAGE IN EQUIAXED ZONE OF REFERENCE INGOT WITH POST PROCESSED FALSE COLOURED GRAINS 83
FIGURE 4.11: BSE IMAGE OF REFERENCE EQUIAXED DENDRITIC GRAIN OUTLINED IN WHITE WITH NEAR PERPENDICULAR TIP TO TIP MEASUREMENT LINES 84
FIGURE 4.12: EXAMPLE BF INGOT CROSS SECTIONS AND BSE MICROGRAPH OF 3 HR TI-AL-NB INOCULATED MICROSTRUCTURE 86
FIGURE 4.13: EXAMPLE BF INGOT CROSS SECTIONS AND BSE MICROGRAPHS WITH (A) 6 HR, (B) 9 HR AND (C) 11 HR MILLED TI-AL-NB PARTICLES 88
FIGURE 4.14: EXAMPLE BF INGOT CROSS SECTIONS AND BSE MICROGRAPHS WITH (A) UNMILLED, (B) 3 HR AR AND (C) 3 HR HT TI-AL-NB PARTICLES 90
FIGURE 4.15: EXAMPLE BF INGOT CROSS SECTIONS AND BSE MICROGRAPH OF REFERENCE INGOT 91
FIGURE 4.16: EXAMPLE BF INGOT CROSS SECTIONS AND BSE MICROGRAPH SHOWING SOLUTAL EFFECT OF NB ADDITION 92
FIGURE 4.17: EXAMPLE BSE MICROGRAPHS WITH (A) 3 HR AND (B) 9 HR MILLED TI-AL-TA PARTICLES 93
FIGURE 4.18: CONTINUOUS SEM BSE IMAGE OF INGOT INOCULATED WITH 9 HOUR MILLED TI-TA PARTICLES SHOWING COLUMNAR GRAINS PRESENT FROM BOTTOM CAP TO TOP SOLIDIFICATION SHRINKAGE 96
FIGURE 4.19: EXAMPLE BF INGOT CROSS SECTIONS AND BSE MICROGRAPHS WITH (A) 3 HR, (B) 6 HR AND (C) 9 HR MILLED TI-TA PARTICLES 97
FIGURE 4.20: EXAMPLE BF INGOT CROSS SECTIONS AND BSE MICROGRAPH FOR 1.5 HR MILLED TI-TA PARTICLES 98
FIGURE 4.21: EXAMPLE BSE MICROGRAPHS WITH (A) 6 HR, (B) 9 HR MILLED TI-TA PARTICLES AND REDUCED INTERACTION TIME TO 10 SECONDS 99
FIGURE 4.22: EXAMPLE BF INGOT CROSS SECTIONS AND BSE MICROGRAPH OF REMELTED LARGE INGOT 100
FIGURE 4.23: EXAMPLE BF INGOT CROSS SECTIONS AND BSE MICROGRAPH FOR INDIVIDUALLY FABRICATED BULK ALLOY INGOT INOCULATED WITH 1.5 HR MILLED TI-TA PARTICLES 101

FIGURE 4.24: CONTINUOUS SEM BSE IMAGE OF INDIVIDUAL INGOT INOCULATED WITH 1.5 HOUR MILLED TI-TA PARTICLES SHOWING NEARLY TOTAL EQUIAXED STRUCTURE 101
FIGURE 5.1: BSE IMAGES OF BOTTOM REGION OF INGOTS INOCULATED WITH (A) TI-TA, (B) TI-AL-NB AND (C) TI-AL-TA PARTICLES 103
FIGURE 5.2: EDX ANALYSIS OF PARTICLE LOCATED AT THE BOTTOM OF INOCULATED INGOT SHOWING COMPOSITION TO BE TI-TA 104
FIGURE 5.3: SUPERLARGE TI-TA PARTICLE BLOCKING GROWTH OF COLUMNAR GRAINS 106
FIGURE 5.4: GRAIN SIZE EVOLUTION ACROSS INDIVIDUALLY FABRICATED INGOT INOCULATED WITH 1.5HR MILLED TI-TA PARTICLES 107
FIGURE 5.5: INFLUENCE OF (A) PARTICLE SIZE AND (B) NUMBER OF PARTICLES INTRODUCED ON EQUIAXED GRAIN SIZE. THE ERROR BARS CORRESPOND TO THE STANDARD DEVIATION OF GRAIN SIZE MEASUREMENTS. 109
FIGURE 5.6: (A) INFLUENCE INOCULANT PARTICLE DENSITY AND (B) RELATIONSHIP BETWEEN # OF GRAINS FORMED BY EACH INOCULANT AND NUMBER OF PARTICLES INTRODUCED (ONLY IN THE EQUIAXED ZONE). 110
FIGURE 5.7: SEM BSE IMAGES SHOWING REGION OF COLUMNAR ZONE WHERE THE PARTICLE OF INTEREST WAS LOCATED 111
FIGURE 5.8: SCHEMATIC OF PARTICLE BREAKUP PROCESS: WHOLE POLYCRYSTALLINE PARTICLE, PREFERENTIAL GRAIN BOUNDARY DISSOLUTION, PARTICLE BREAKUP AND BSE MICROGRAPHS OF TI-TA PARTICLE IN SOLIDIFIED INGOT DEMONSTRATING PARTICLE BREAKUP BY ADJUSTING IMAGING CONTRAST 112
FIGURE 5.9: TERMINAL SETTLING VELOCITIES OF PARTICLES IN UNSTIRRED MELT. 114
FIGURE 5.10: SEM BSE IMAGES SHOWING (A) REGION OF COLUMNAR ZONE WHERE THE PARTICLE OF INTEREST WAS LOCATED AND 9 HR MILLED TITA PARTICLE AFTER (B) 10S AND (C) 20S INTERACTION TIME 115
FIGURE 5.11: EDX LINE SCAN ACROSS 9 HR CRYOMILLED TITA PARTICLE AFTER 10S INTERACTION TIME 116
FIGURE 5.12: EDX PROFILE SHOWING INTERFACE COMPOSITIONS (HOLLOW POINTS) OF PARTICLE AFTER 10S INTERACTION TIME COMPARED TO ISOTHERMAL SECTION OF THE TI-AL-TA PHASE DIAGRAM AT 1950 K.. 116
FIGURE 6.1: TI-AL-NB ROD IN TI-AL INGOT AND CUTTING PLANES FOR METALLOGRAPHICAL PREPARATION 118
FIGURE 6.2: OPTICAL IMAGE OF CIRCULAR ROD CROSS SECTION (A) SECTION A AFTER DIPPING AND (B) SECTION D WHICH DID NOT CONTACT THE MELT. 119
FIGURE 6.3: RECTANGULAR ROD CROSS SECTIONS ALONG SECTION B AFTER INTERACTION WITH THE MELT 120
FIGURE 6.4: VARIATION OF RADIUS ALONG THE LENGTH OF THE ROD AFTER INTERACTION WITH THE MELT FROM CROSS SECTION WITH PORE (SOLID LINE) AND WITHOUT (DASHED LINE) UNDISSOLVED DIMENSIONS IN GREY. 120
FIGURE 6.5: INTERNAL GRAIN DISORIENTATION MAPS FROM TKD ANALYSIS OF (A) 3HR AND (B) 9 HR MILLED TI-AL-NB POWDER (0° MISORIENTATION DARK BLUE, 15° DARK RED) 122
FIGURE 6.6: GEOMETRICALLY NECESSARY DISLOCATIONS FOR (A) 3 HR AND (B) 9 HR MILLED POWDER 122
FIGURE 6.7: BSE MICROGRAPHS OF 3 HOUR MILLED AND 9 HOUR MILLED TI-AL-NB POWDERS AFTER 5 MIN AND 20S HOLDS AT 1600^{o}C 123
FIGURE 6.8: PARTICLE GRAIN SIZE OF HEAT TREATED 3HR AND 9HR MILLED TI-AL-NB PARTICLES AFTER (A) 5 MINUTES AND (B) 20S AT 1600^{o}C 124
FIGURE 6.9: AVERAGE GRAIN SIZE WITH THERMAL TREATMENT AT 1600OC (A) FITTING EQUATION (6.1) TO THE EXPERIMENTAL DATA FOR 20S (K=68), 300S (K=22) AND THE BEST FIT (K=35) AND (B) FITTING A POWER LAW TREND. 125
FIGURE 6.10: SCHEMATIC OF INTERFACE WITH FLUID FLOW 127
FIGURE 6.11: FORCE BALANCE ON PARTICLE IN MOVING REFERENCE FRAME 127
FIGURE 6.12: VARIATION OF DRAG COEFFICIENT WITH REYNOLDS NUMBER, FROM [**193**] 128
FIGURE 6.13: PARTICLE BOUNDARY AND DISPLACEMENT LAYERS AT POINT R, THE RADIUS OF THE PARTICLE. 129
FIGURE 6.14: DISSOLUTION OF ROD CONSIDERING FLUID FLOW AND FINITE OR INFINITE LIQUID 131
FIGURE 6.15: EFFECT OF PARTICLE SIZE ON RELATIVE VELOCITY AND WIDTH OF BOUNDARY LAYER 131
FIGURE 6.16: EFFECT OF PARTICLE SIZE ON DISSOLUTION LENGTH (A) WITH A CONSTANT VOLUME OF LIQUID AND (B) WITH A CONSTANT VOLUME FRACTION OF PARTICLES 132
FIGURE 6.17: EFFECT OF LIQUID INTERACTION VOLUME (VOLUME FRACTION OF PARTICLES) ON DISSOLUTION LENGTH 132
FIGURE 6.18: METHOD TO DETERMINE NUMBER OF PARTICLES PRESENT DURING SOLIDIFICATION 133
FIGURE 6.19: EVOLUTION OF VOLUME OF THE PARTICLES OF A GIVEN SIZE AND 3HR MILLED PARTICLE SIZE DISTRIBUTION OF PARTICLES BY VOLUME BEFORE AND AFTER DISSOLUTION 134
FIGURE 6.20: EFFECT OF PARTICLE DISSOLUTION ON INOCULATION EFFICIENCY (A) GRAIN AND PARTICLE NUMBER DENSITY COMPARISON, (B) # GRAINS FORMED BY EACH PARTICLE 135
FIGURE 6.21: SCHEMATIC OF CALCULATION METHOD FOR # OF PARTICLE GRAINS REMAINING FOR SOLIDIFICATION 135
FIGURE 6.22: PARTICLE GRAIN DENSITY AND EQUIAXED GRAIN DENSITY FOR PARTICLE GRAINS AND COMPARISON TO TRADITIONAL ALTIB INOCULATION OF AL [**202**] AND TI [**203**]. 136

FIGURE 6.23: RELATIONSHIP BETWEEN # PARTICLES INTRODUCED AND EFFICIENCY FACTOR CONSIDERING THE EXPERIMENTAL RESULTS AND CALCULATIONS 137
FIGURE A0.1: SEM OBTAINED TI-AL-NB GROUND PARTICLE DISTRIBUTIONS AFTER (A) 3 HRS, (B) 6 HRS, (C) 9 HRS, (D) 11 HRS AND (E) 3 HRS UNDER AR. THE CUMULATIVE DISTRIBUTIONS ARE SHOWN AS DASHED LINES AND THE VERTICAL DASHED LINES ARE THE DISTRIBUTION D50 ..... A
FIGURE A0.2: SEM OBTAINED TI-AL-TA GROUND PARTICLE DISTRIBUTIONS AFTER (A) 3 HRS, (B) 6 HRS AND (C) 9 HRS. THE CUMULATIVE DISTRIBUTIONS ARE SHOWN AS DASHED LINES AND THE VERTICAL DASHED LINES ARE THE DISTRIBUTION D50 ..... B
FIGURE A0.3: SEM OBTAINED TI-TA GROUND PARTICLE DISTRIBUTIONS AFTER (A) 1.5 HRS, (B) 3 HRS, (C) 6 HRS AND (D) 9 HRS. THE CUMULATIVE DISTRIBUTIONS ARE SHOWN AS DASHED LINES AND THE VERTICAL DASHED LINES ARE THE DISTRIBUTION D50 ..... D
FIGURE A0.4: SCHEMATIC OF NUMERICAL SIZE DISTRIBUTION DETERMINATION ..... D
FIGURE A0.5: DLS OBTAINED TI-AL-NB GROUND PARTICLE DISTRIBUTIONS AFTER (A) 3 HRS, (B) 6 HRS, (C) 9 HRS, (D) 11 HRS AND (E) 3 HRS UNDER AR. THE CUMULATIVE DISTRIBUTIONS ARE SHOWN AS DASHED LINES AND THE VERTICAL DASHED LINES ARE THE DISTRIBUTION D50 ..... F
FIGURE A0.6: DLS OBTAINED TI-AL-TA GROUND PARTICLE DISTRIBUTIONS AFTER (A) 3 HRS, (B) 6 HRS AND (C) 9 HRS. THE CUMULATIVE DISTRIBUTIONS ARE SHOWN AS DASHED LINES AND THE VERTICAL DASHED LINES ARE THE DISTRIBUTION D50 ..... G
FIGURE A0.7: DLS OBTAINED TI-TA GROUND PARTICLE DISTRIBUTIONS AFTER (A) 1.5 HRS, (B) 3 HRS, (C) 6 HRS AND (D) 9 HRS. THE CUMULATIVE DISTRIBUTIONS ARE SHOWN AS DASHED LINES AND THE VERTICAL DASHED LINES ARE THE DISTRIBUTION D50 ..... H
FIGURE A0.8: SCHEMATIC OF VOLUMETRIC SIZE DISTRIBUTION DETERMINATION I
FIGURE A0.9: TI-AL-NB (A) D50 AND (B) D99 EVOLUTION TRENDS WHEN MEASURED BY SEM (BLUE) AND DLS (BLACK). ..... J
FIGURE A0.10: TI-AL-TA (A) D50 AND (B) D99 TRENDS BY SEM (BLUE) NUMERICAL (SQUARES) AND VOLUMETRIC (CIRCLES) AND DLS (BLACK). ..... J
FIGURE A0.11: TI-TA (A) D50 AND (B) D99 EVOLUTION TRENDS WHEN MEASURED BY SEM (BLUE) AND DLS (BLACK). ..... K
FIGURE A0.12: PARTICLE SIZE DISTRIBUTIONS FOR 3 HOUR MILLED TI-AL-NB POWDER (A) NUMERICAL SIZE DISTRIBUTION OBTAINED BY SEM AND (B) VOLUMETRIC SIZE DISTRIBUTION OBTAINED BY DLS. L
FIGURE B0.1: GRAIN SIZE EVOLUTION WITH ALUMINUM CONTENT ..... M
FIGURE B0.2: COMPARISON OF GRAIN SIZE WITH (A) ALUMINUM CONTENT AND (B) PRO-PERITECTIC B FRACTION. VERTICAL LINES REPRESENT THE ONSET, PERITECTIC POINT, AND END POINT OF THE PERITECTIC PLATEAU. .N
FIGURE B0.3: SCHEIL SOLIDIFICATION CURVES FOR INGOT CONDITIONS WITH NOMINAL COMPOSITION ..... O
FIGURE B0.4: SCHEIL SOLIDIFICATION CURVES FOR INGOT CONDITIONS WITH NO INOCULANT DISSOLUTION ..... O
FIGURE B0.5: (A) CHANGE IN PERITECTIC PLATEAU POINTS (SHOWN AS LINES, SOLID-ONSET, DASHED PERITECTIC POINT AND DOTTED PERITECTIC ENDPOINT) WITH INCREASING NB CONTENT AND (B) GRAIN SIZE CURVES CORRECTED TO TI-AL BINARY ..... P
FIGURE B0.6: FRACTIONAL DISTANCES FROM THE PERITECTIC POINT FOR (A) FULL DISSOLUTION AND (B) NO DISSOLUTION OF INOCULANT PARTICLES. ..... Q
FIGURE B0.7: EFFECT OF FRACTIONAL DISTANCE FROM THE PERITECTIC POINT ON GRAIN SIZE ..... Q
FIGURE B0.8: GRAIN REFINEMENT BY INOCULATION AS PARTICLE GRINDING TIME INCREASES FOR (A) FULL DISSOLUTION AND (B) NO DISSOLUTION OF INOCULANT PARTICLES. ..... R
FIGURE B0.9: INFLUENCE OF (A) PARTICLE SIZE AND (B) NUMBER OF PARTICLES INTRODUCED ON GRAIN SIZE REDUCTION CONSIDERING NO PARTICLE DISSOLUTION (BLACK) AND FULL PARTICLE DISSOLUTION (BLUE) 6HR MILLED PARTICLE RESULTS CIRCLED ..... R
FIGURE B0.10: NUMBER OF GRAINS FORMED BY INOCULANTS COMPARED TO NUMBER OF INOCULANTS INTRODUCED TO THE MELT CONSIDERING NO PARTICLE DISSOLUTION (BLACK) AND FULL PARTICLE DISSOLUTION (BLUE). 1:1 RATIO SHOWN AS DASHED LINE. ..... S
FIGURE C0.1: SEM BSE IMAGES SHOWING (A) REGION OF COLUMNAR ZONE WHERE THE PARTICLE OF INTEREST WAS LOCATED AND (B) 9 HR CRYOMILLED TITA PARTICLE AFTER 20S INTERACTION TIME ..... U
FIGURE C0.2: EDX LINE SCAN ACROSS 9 HR CRYOMILLED TITA PARTICLE AFTER 20S INTERACTION TIME V
FIGURE C0.3: EDX PROFILE SHOWING INTERFACE COMPOSITIONS (HOLLOW POINTS) OF PARTICLE AFTER 20S INTERACTION TIME COMPARED TO ISOTHERMAL SECTION OF THE TERNARY TI-AL-TA PHASE DIAGRAM AT (A) 1950 K AND (B) 1856K. ..... W
FIGURE C0.4: SEM BSE IMAGES SHOWING (A) REGION OF INGOT WHERE THE PARTICLE OF INTEREST WAS LOCATED AND (B) 6 HR CRYOMILLED TITA PARTICLE AFTER 10S INTERACTION TIME ..... W
FIGURE C0.5: SEM (A) BSE AND (B) SE IMAGE OF 6 HR CRYOMILLED TITA PARTICLE AFTER 10S INTERACTION TIME X
FIGURE C0.6: EDX LINE SCAN ACROSS 6 HR CRYOMILLED TITA PARTICLE AFTER 10S INTERACTION TIME X

FIGURE C0.7: EDX PROFILE SHOWING INTERFACE COMPOSITIONS (HOLLOW POINTS) OF 6 HOUR MILLED PARTICLE AFTER 10S INTERACTION TIME COMPARED TO ISOTHERMAL SECTION OF THE TI-AL-TA PHASE DIAGRAM AT (A) 1925 K AND (B) 1950 K.....Y
FIGURE D0.1: SCHEMATIC OF VACUUM PULLING TO FABRICATE TI-AL-NB ROD .....AA
FIGURE D0.2: TI-AL-NB ROD (A) AS CAST AND (B) WELDED TO THREADED ROD ..... BB
FIGURE D0.3: SCHEMATIC OF PROCEDURE FOR TI-AL-NB ROD DIPPING EXPERIMENT ..... BB
FIGURE D0.4: TI-AL-NB ROD IN TI-AL INGOT AND CUTTING PLANES, A, C AND D USED FOR GRAIN SIZE ANALYSIS CC
FIGURE D0.5: MICROSTRUCTURE OF TI-AL-NB ROD AFTER INTERACTION WITH THE MELT (SECTION A) IMAGED WITH BOTH SECONDARY ELECTRONS (SE) AND BACKSCATTERED ELECTRONS (BSE) CC
FIGURE D0.6: MICROSTRUCTURE OF TI-AL-NB ROD AFTER SOME INTERACTION WITH THE MELT (SECTION C) IMAGED WITH BOTH SE AND BSE .....DD
FIGURE D0.7: MICROSTRUCTURE OF TI-AL-NB ROD WHICH DID NOT INTERACT WITH THE MELT (SECTION D) IMAGED WITH BOTH SE AND BSE .....DD
FIGURE D0.8: EDX PROFILE FROM BULK ALLOY (LEFT) INTO ROD (RIGHT) .....EE
FIGURE D0.9: EDX PROFILE SHOWING INTERFACE COMPOSITIONS (HOLLOW POINTS) OF ROD AFTER 20S INTERACTION TIME COMPARED TO ISOTHERMAL SECTION OF THE TERNARY TI-AL-NB PHASE DIAGRAM AT (A) 1950 K AND (B) 1875K.....FF
FIGURE D0.10: LOW RESOLUTION EBSD MAP OF ROD (TOP) / BULK (BOTTOM) INTERFACE ..... FF
FIGURE D0.11: HIGH RESOLUTION EBSD MAPS OF ROD/BULK INTERFACE (A) ORIENTATION MAP (B) PHASE MAP .....GG
FIGURE D0.12: ORIENTATION RELATIONSHIPS BETWEEN ROD (B) AND BULK (Γ) SHOWING EPITAXIAL GROWTH THROUGH INTERMEDIARY A PHASE .....GG
FIGURE E0.1: SCHEMATIC OF TSD APPARATUS AND CRUCIBLE SETUP II
FIGURE E0.2: SHORT TIME HIGH TEMPERATURE PARTICLE TREATMENT SCHEMATIC ..... JJ
FIGURE E0.3: EDX CHEMICAL ANALYSIS OF TI-AL-NB PARTICLE AFTER 5 MIN INTERACTION WITH MOLTEN CAF2 AT 1600^{o}C INCLUDING BSE IMAGE, AL CONTENT, CA, O AND F CONTENT AND TI AND NB CONTENT. .....KK

List of Tables

TABLE 0.1:PROPRIETES DES ALLIAGES INOCULANTS (A 1540°C) VII
TABLE 0.2: TAILLE DES PARTICULES DE POUDRES VIII
TABLE 0.3: TAILLE DES GRAINS ET FRACTION EQUIAXE AVEC ET SANS INOCULATION IX
TABLE 1.1: COMMON ALLOYING ELEMENTS AND THEIR EFFECTS 11
TABLE 2.1: GROWTH-RESTRICTION FACTOR Q CALCULATED FOR BINARY AND MULTICOMPONENT TIAL ALLOYS 25
TABLE 3.1: SELECTED PROPERTIES OF PROPOSED INOCULANT ALLOYS (AT 1540°C) 52
TABLE 3.2: SUMMARY OF POWDER CRYOMILLING CONDITIONS 55
TABLE 3.3: PARTICLE SIZE SUMMARY 73
TABLE 4.1: INOCULANT MASS AND ESTIMATED NUMBER OF PARTICLES INTRODUCED FOR EACH TRIAL 77
TABLE 4.2: TI-AL-NB EXPERIMENTAL CONDITIONS FOR MILLING TIME TRIALS 85
TABLE 4.3: TI-AL-NB EXPERIMENTAL CONDITIONS FOR FURTHER TRIALS 85
TABLE 4.4: TI-AL-TA EXPERIMENTAL CONDITIONS FOR MILLING TIME TRIALS 92
TABLE 4.5: TI-TA EXPERIMENTAL CONDITIONS FOR MILLING TIME TRIALS 94
TABLE 4.6: TI-TA EXPERIMENTAL CONDITIONS FOR FURTHER TRIALS 95
TABLE 7: VARIABLES FOR ROD DISSOLUTION IN FLUID FLOW ASSUMING SOLUTE IS NB 130
TABLE A0.1: SEM OBTAINED TI-AL-NB PARTICLE SIZE DISTRIBUTION CHARACTERISTICS ..... B
TABLE A0.2: SEM OBTAINED TI-AL-TA PARTICLE SIZE DISTRIBUTION CHARACTERISTICS C
TABLE A0.3: SEM OBTAINED TI-TA PARTICLE SIZE DISTRIBUTION CHARACTERISTICS C
TABLE A0.4: DLS OBTAINED TI-AL-NB PARTICLE SIZE DISTRIBUTION CHARACTERISTICS. ..... E
TABLE A0.5: DLS OBTAINED TI-AL-TA PARTICLE SIZE DISTRIBUTION CHARACTERISTICS ..... G
TABLE A0.6: DLS OBTAINED TI-TA PARTICLE SIZE DISTRIBUTION CHARACTERISTICS ..... H

Introduction

TiAl alloys are an important material which are beginning to be used in industry for high temperature applications. Their high specific strength makes them ideal for applications such as turbochargers or turbine blades. In order to further use TiAl alloys in industry their low ductility must be improved, one method of doing this is by inoculation. Current inoculants for TiAl alloys remain as brittle precipitates in the as-cast ingots. This work aims to develop a new generation of ductile inoculants for use in TiAl alloys which will grain refine as-cast ingots without any brittle precipitates remaining in the ingots.

This thesis is divided into seven chapters. Chapter 1 presents an introduction to TiAl alloys and their properties. Chapter 2 gives an overview of the phenomena of solidification and inoculation and intoduces the concept of isomorphic self inoculation developed in this work. Chapter 3 relates to the selection of three suitable alloys to use as isomorphic inoculants and how they were fabricated and processed into powders to be used in inoculation trials. Chapter 4 presents the results of the inoculation trials conducted with the three inoculant alloys. Chapter 5 discusses these results and differences between the alloy behaviours. Chapter 6 delves into the interactions between the inoculants and melt before solidification in order to gain further insight into their behaviour. Chapter 7 then provides the conclusions which can be drawn from the work as well as recomendations for future work on the topic.

Chapter 1 Titanium Aluminium Alloys

Some of the large breadth of research on titanium aluminium (Ti-Al) alloys is presented. Significant work has been done on alloys of this type since the 1990s as interest has grown in their usage for high temperature applications. The overall characteristics of alloys in the system are presented along with their mechanical properties and some information on common processing methods.

1.1 Introduction to Ti-Al

Titanium aluminium alloys are an interesting material for many applications. Their high temperature oxidation resistance, good creep resistance and high specific strength make them particularly promising for use in turbine engines [**12**]. Titanium aluminides have already replaced nickel based superalloys in the two last low pressure stages of the GEnx and LEAP turbine engines. A schematic of a typical turbine engine for aircraft use is shown in Figure 1.1 along with typical materials and operating temperatures for each section of the turbine.

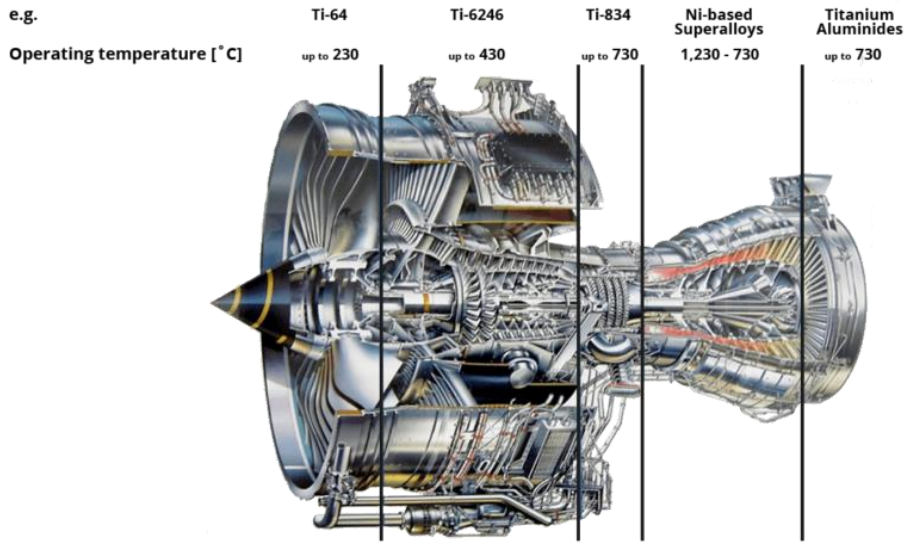

Figure 1.1: Cross section of typical turbine with common blade materials and operating temperatures for each region [**13**]

Reducing the weight of the blades in the last stage of the engine is one of the factors which allows these engines to increase their fuel efficiency. Replacing just the 6th and 7th stages in the GEnx reduced the weight of the engine by nearly 200 kg [**14**]. This region of the GEnx engine is shown in Figure 1.2. Advances in Ti-Al technology which would permit replacing more nickel based blades would further increase fuel efficiency while reducing the overall weight of the engine. In order to be used deeper into turbines their properties must be improved for high temperature (>800ºC) applications. TiAl alloys have also been implemented in automotive applications such as turbocharger wheels used in Porsche automobiles [**15**].

Figure 1.2: Low pressure turbine of GEnx engine with TiAl based 6th and 7th stages [**14**]

The major advantage of TiAl alloys over conventional superalloys is their light weight, a comparison of popular alloy types and their specific strength at a given temperature is shown in Figure 1.3A. It should also however be noted that a major problem for TiAl alloys is their low ductility at room temperature compared to other alloys, as shown in Figure 1.3B. The widely considered minimum elongation for TiAl alloys at room temperature is 1%, however, many cast alloys do not even achieve this ductility [**16**]. The toughness of TiAl can also increase at high temperature, increases have been reported close to 50% at 650ºC compared to room temperature with lamellar type microstructures [**17**]. TiAl alloys are particularly well suited to turbocharger wheels and engine exhaust valves as their low ductility is less of a drawback in the less harsh environments there compared to turbine blades [**18**].

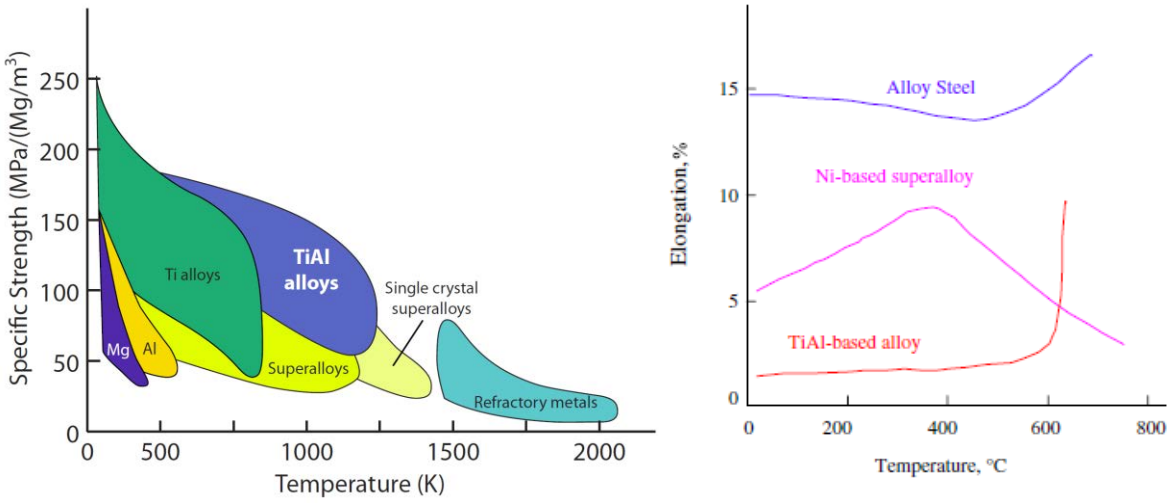

(A) (B)

Figure 1.3: (A) Specific strength with temperature showing benefit of TiAl alloys [**1**] and (B) corresponding elongations before fracture [**16**].

1.2 The Ti-Al Binary System

This section provides an overview on phase and microstructure in the Ti-Al binary alloy system. Particular focus is given to the peritectic region which is of interest for industrial applications in the system.

1.2.1 Ti-Al Phase Diagram

The Ti-Al binary system consists of titanium, aluminum and intermetallic phases. Over time the understanding of the phases formed between the two pure metals has evolved. The first investigation into the full Ti-Al binary not solely concerned with the Al rich region was conducted in 1951 by Ogden, et.al. [**19**]. They established the first phase diagram of the system as can be seen in Figure 1.4A. Their work was continued by Mcpherson and Hansen who's phase diagram was published 1954 [**20**]. Murry combined experimental results with thermodynamic calculations to produce an updated phase diagram in 1988 [**21**], shown in Figure 1.4B.

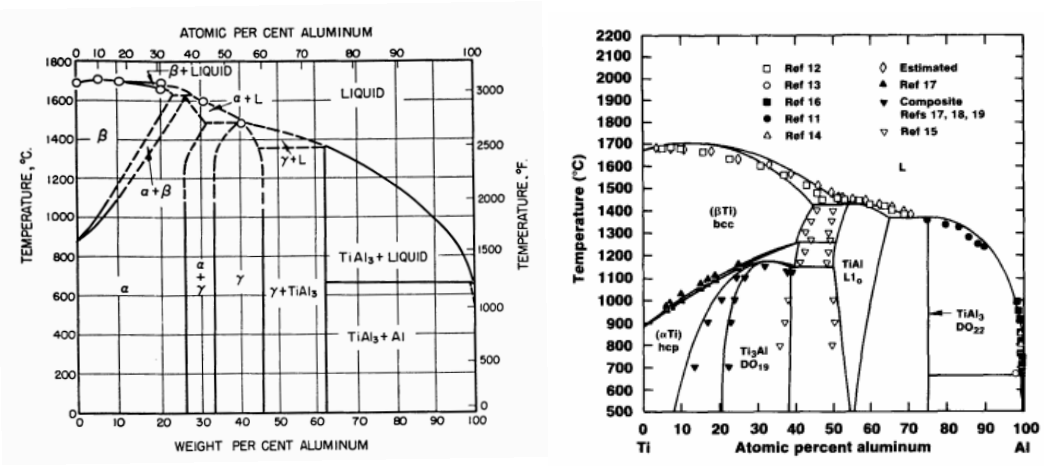

(A) (B)

Figure 1.4: Evolution of Ti-Al phase diagram over time (A) 1951 by Ogden et.al. [**19**] (B) 1988 by Murray [**21**]

In more recent years coupling of experimental data and CALPHAD calculations have been used to update the phase diagram such as done by Schuster and Palm [**22**] or Witusciewicz et.al. [**23**] and Wang et.al. [**24**], Figure 1.4C and D respectively. The most recent work attempts to couple experimental data with both CALPHAD and atomistic modelling [**25**]. In this work the data and phase diagram used is that of Witusciewicz in 2008 [**23**].

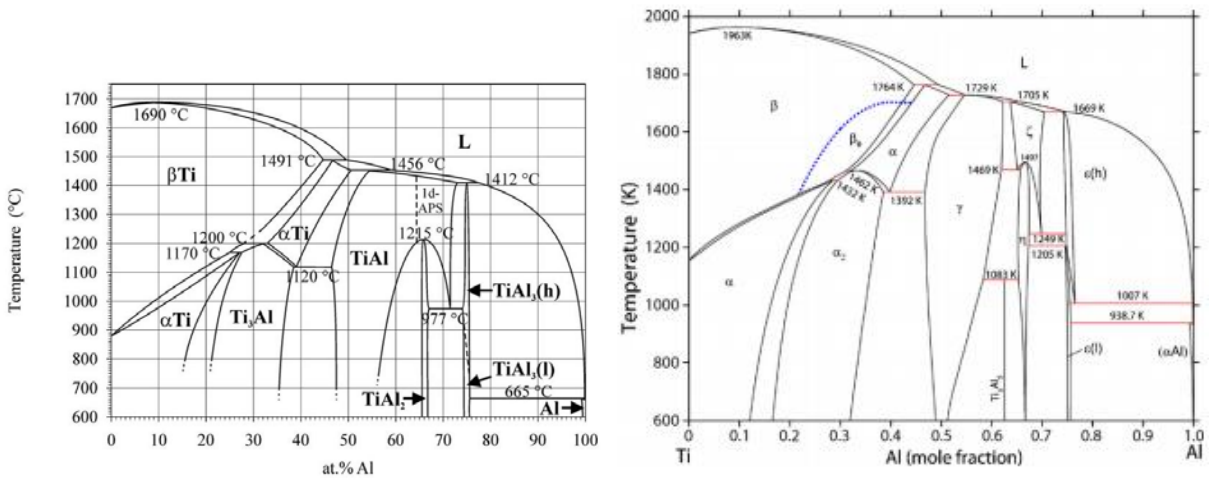

(A) (B)

Figure 1.5: Phase diagrams evaluated with the help of CALPHAD (A) 2006 by Schuster and Palm [**22**] and (B) 2008 by Witusciewicz et.al. [**23**]

Alloys of interest normally consist of less than 50 at% Al around the peritectic plateau at 1503°C and 44-48 at% Al [**26**]. Alloys which are processed from the liquid state in this region can include up to four phase changes from liquid to room temperature [**26**]. These could include the initial solidification of β grains from the liquid, transformation of β grains to α (following Burgers orientation relationship $(110)_\beta$ // $(0001)_\alpha$ [**27**]), α to α and γ (following Blackburn's orientation relationship $(0001)_\alpha$ // $(111)_\gamma$ [**28**]) and finally α and γ to γ and α_2 [**29**]. An example progression from liquide to room temperature can be seen in Figure 1.6.

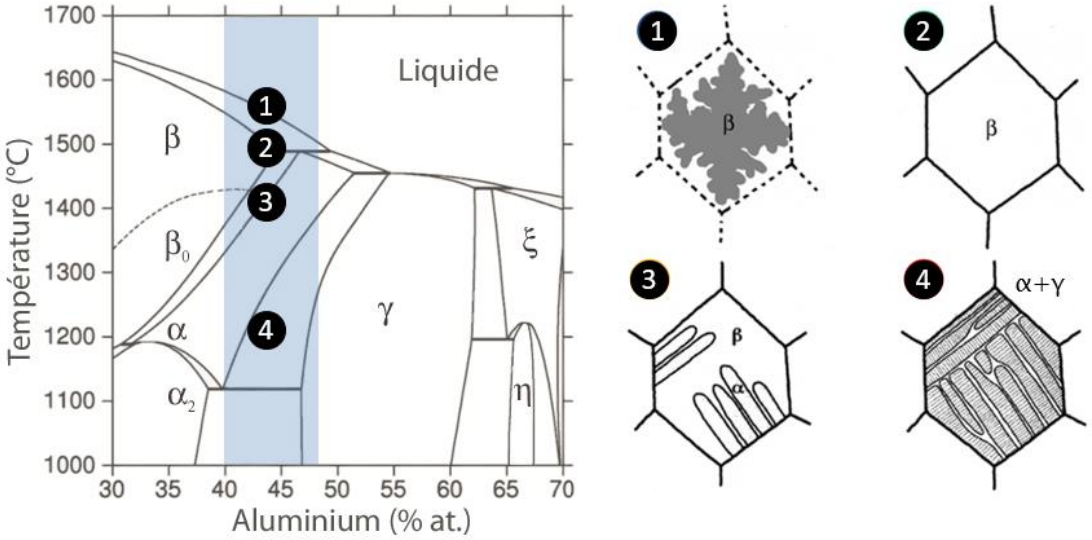

Figure 1.6: Titanium Aluminium binary phase diagram and transformation path for hypo-peritectic alloy

1.2.2 Ti-Al Phases

It can be seen from the phase diagram that there are four main phases of interest for Ti-Al alloys in the peritectic region, β, α, α_2 and γ. This section introduces these phases, their structure and characteristics.

1.2.2.1 β Phase

The solidifying phase of Ti rich alloys in the system is the β phase. The β phase has a body centered cubic structure consisting of eight Ti atoms on the vertices with a single Al atom encapsulated in the centre. Such a lattice can be seen in Figure 1.7.

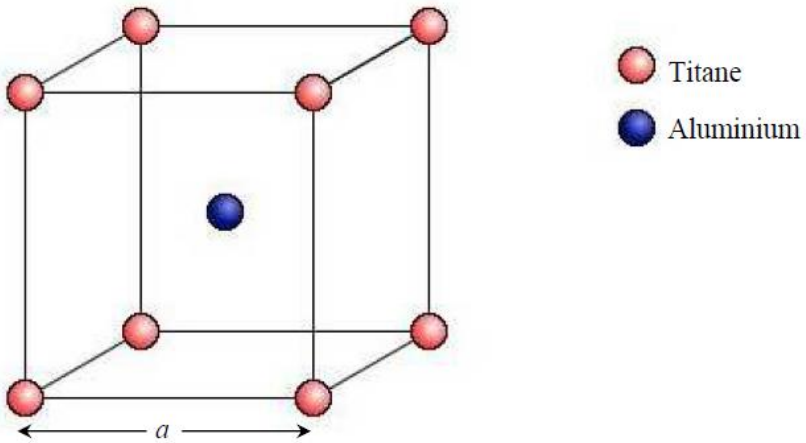

Figure 1.7: Ti-Al β_0 phase crystal structure [**30**]

β solidifying TiAl alloys are ideal to reduce texture, increase hot-workability, limit macro-segregation and increase the homogeneity of the as-cast microstructure [**31**]. The high temperature properties and castability of TiAl was also found to increase when β solidifying alloys were used [**15**]. In alloys designed to be β solidifying the interlamellar spacing of the room temperature structure was decreased, also improving the mechanical properties at room temperature.

1.2.2.2 α and α_2 phases

The α and α_2 phases are similar hexagonal close packed systems with different lattice parameters. The α phase is the natural allotrope of pure Ti at room temperature while α_2 is modified by the addition of Al to the lattice. The aspect ratio of the lattice changes drastically between α and α_2, with α having half the lattice parameter (a) of α_2 while maintaining a similar c value [**32**].The lattice of α_2 is shown in Figure 1.8.

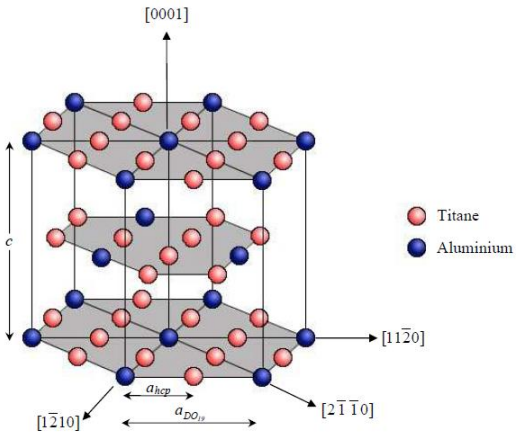

Figure 1.8: Ti_3Al α_2 phase crystal structure [**30**]

1.2.2.3 γ phase

The γ phase is a face centered cubic structure consisting of alternating planes of Ti and Al [**33**]. γ is the intermetallic TiAl phase which exists broadly in the middle of the phase diagram, and can exist from room temperature up until it's melting point near 1450°C. The alternation of planes results is a slight anisotropy between the C and A values of the lattice, however, the c/a ratio remains approximately 1.01-1.02 [**21**]. The Lattice of γ can be seen in Figure 1.9.

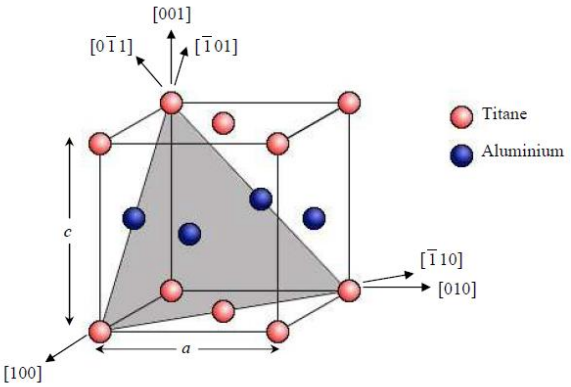

Figure 1.9: Ti-Al γ phase crystal structure [**30**]

1.1.4 Microstructures

A variety of microstructures can be found in TiAl alloys. Of particular interest to this work are the structures which form on solidification of the alloy. Once solidification is complete a number of solid state phase transformations can take place which change the microstructure. Post solidification heat treatment can also be implemented to obtain further microstructures as well.

1.1.4.1 Solidification Microstructures

The two major solidification phases which can form from a TiAl melt near the peritectic plateau are α or β. These are often formed as dendrites from the melt and can be distinguished from one another by their shape, examples of both can be seen in Figure 1.10. Dendrites which are composed of the α phase have six fold symmetry as they have a hexagonal structure [**34**]. They can be easily distinguished as equiaxed dendrites which are seen in perfect cross section should have six primary arms 60° apart from one another with secondary arms also growing from the primary at an angle of 60°. In contrast β dendrites have a cubic structure and as such can be distinguished by their four primary arms growing at right angles and secondary arms perpendicular to the primary. Segregation phases such as γ may also form, especially between the dendrites when the liquid is particularly rich in solutes.

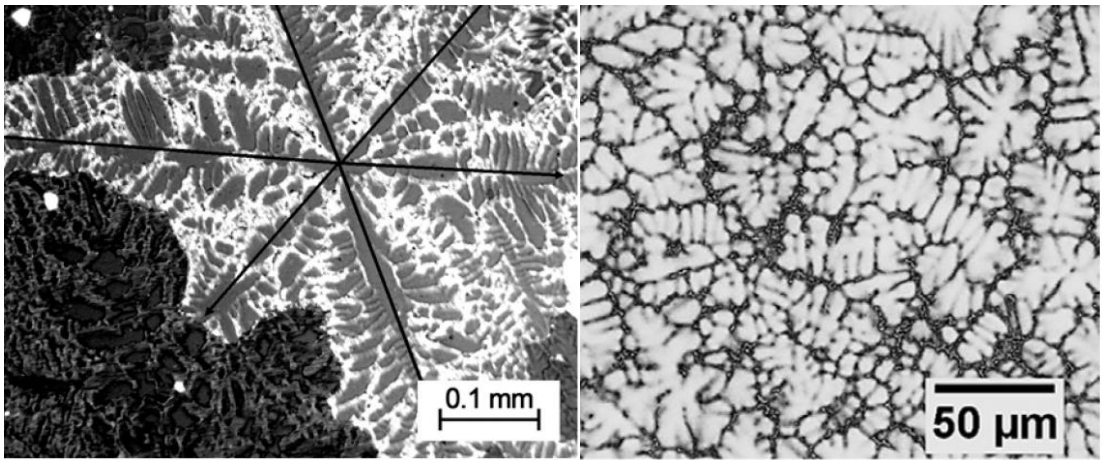

(A) (B)

Figure 1.10: As cast dendrite morphologies observed with primary solidification phase (A) alpha [**34**] and (B) beta [**35**]

1.1.4.2 Heat Treated Microstructures

As previously explained the solidification structure of α or β dendrites no longer exists at room temperature as solid state transformations take place when the alloy cools to room temperature. Example fully lamellar and duplex microstructures produced from the same processed (forged) sample of Ti-47.5Al-2.5V-1Cr can be seen in Figure 1.11 and are typical of room temperature structures. The duplex structure was obtained by annealing at 1250°C for 18h and has lamellar colonies of 100 µm with lamellar spacings of 0.2 µm along with 50 µm equiaxed gamma grains, while the fully lamellar microstructure has colonies of 200 µm with lamellar spacings of 0.5 µm [**36**].

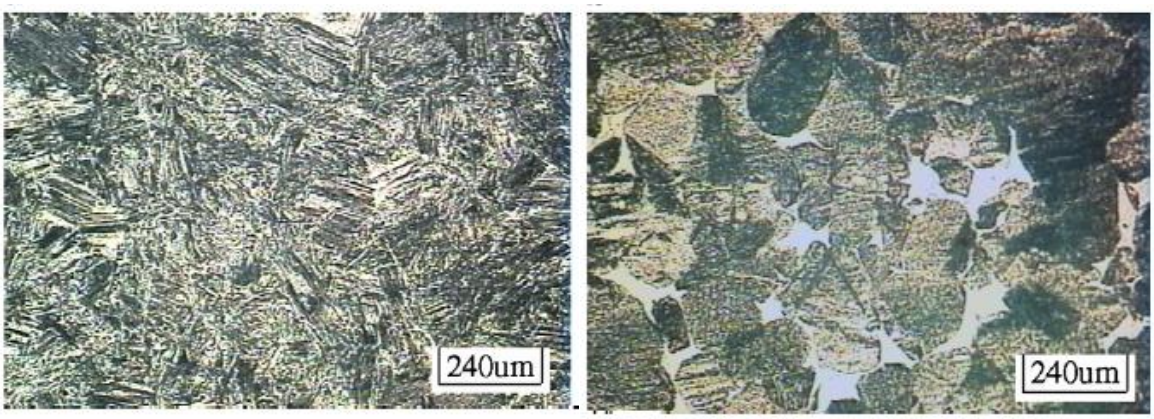

(A) (B)

Figure 1.11: Fully lamellar (A) and duplex (B) microstructures of Ti-47.5Al-2.5V-1Cr [**36**]

Higher resolution micrographs of four such microstructures of a Ti-48Al-2Cr alloy are shown in Figure 1.12 [**37**]. Heat treatment at 1200ºC (75ºC above the eutectic) for two hours led to a Near-γ (NG) structure constituted of γ equiaxed grains with a few α2 grains at grain boundaries and triple junctions (Figure 1.12a). Increasing the heat treating temperature into the (α +γ) field can lead to a DuPlex (DP) structure constituted of a mixture of monolithic γ grains and small lamellar colonies of (α2 + γ) (Figure 1.12b). A Nearly Lamellar (NL) structure mainly constituted of big lamellar colonies and small γ grains (Figure 1.12c) can be formed with a 30 minute heat treatment near the α-transus (1360ºC). Further increasing the heat treatment temperature leads to a Fully Lamellar (FL) structure organized in big lamellar (α2 +γ) colonies (Figure 1.12d).

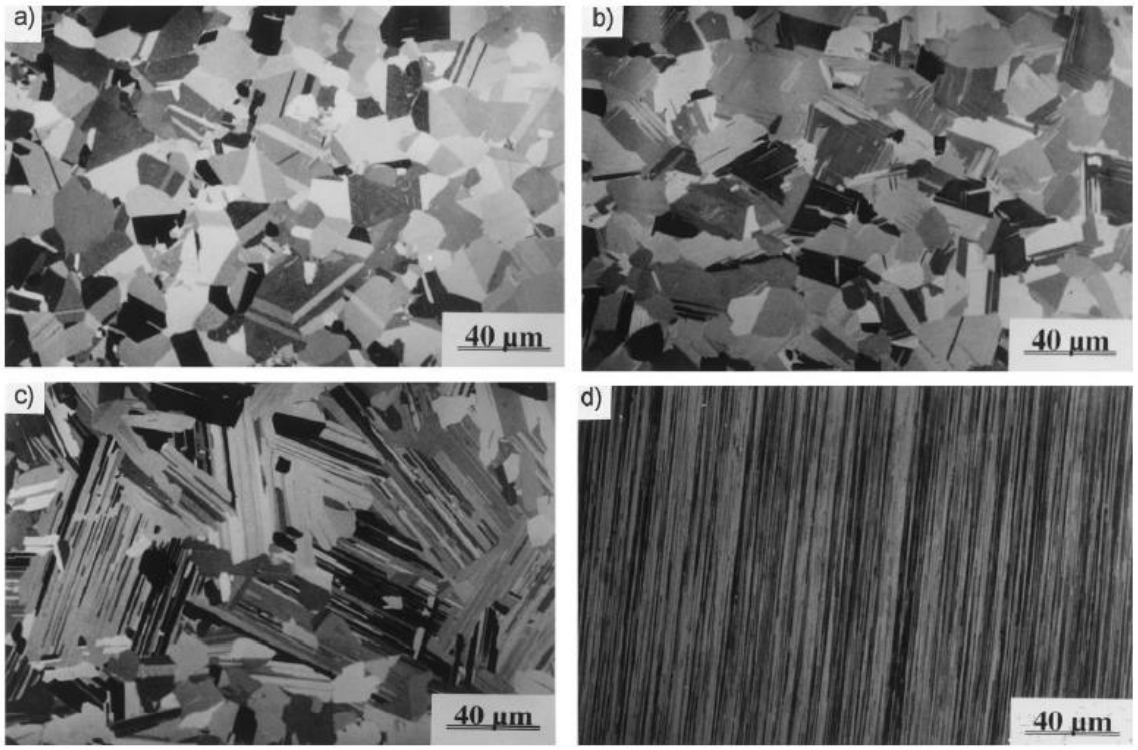

Figure 1.12: Micrographs of the different microstructures of Ti-48Al-2Cr: (a) near-γ; (b) duplex; (c) nearly lamellar; and (d) fully lamellar [**37**].

1.1.4.1 Multi-Component Systems

The TiAl system is often augmented by the addition of other elements such as Cr or Nb as used in the GE alloy. The addition of Nb to TiAl can cause precipitation of a deleterious ω phase at high temperatures, this was found to worsen with Ni additions, however it could be greatly lessened by Mn additions [**38**]. Additions of Y to TiAl were found to cause Y2O3 precipitation as well as Y being located in the α2 and γ solid solutions. These additions assisted grain refinement and increased the strength of the alloys, additionally increasing the oxidation resistance [**39**]. Oxidation resistance was found to decrease with V additions, however oxidation resistance increased with Nb addition even if V was also added, this is attributed to Nb forming a solid solution with TiO_2 and restricting O movement [**40**]. A summary of common alloying elements and their effects is given in Table 1.1.

Table 1.1: Common Alloying Elements and their effects

Element	Alloying Effects [**3**]	Stabilization Phase [**41**]
B	>0.5% Reduces grain size, increases strength, machinability and castability	
C	Increases resitance to creep and fatigue but reduces ductility	α
O	Reduces ductility	α
Si	0.5-1% increases resistance to creep, oxidation and castability	
P	Increases oxidation resistance	
V	1-3% Increases duplex structure ductility, reduces oxidation resistance	β
Cr	1-3% Increases duplex structure ductility, >2% increases machinability and superplastic behaviour, >8% strongly increases oxidation resistance	β
Mn	1-3% Increases duplex structure ductility	β
Fe	Increases castability, Increases hot tearing	β
Ni	Increases castability	
Nb	Increases resistance to creep and oxidation	β
Mo	Increases ductility, fine grain strength, and oxidation resistance	β
Ta	Increases resistance to creep and oxidation, increases hot tearing	β
W	Strongly increases resistance to oxidation and creep	

1.3 Casting and Processing

High cooling rates are beneficial to grain refine since the massively transformed γ grains which form have a significant number of defects which act as nucleation sites for the subsequent α grains which form [**42**]. Additionally higher cooling rates result in reduced γ phase fractions when compared to slower cooling of the same alloys [**43**]. β solidifying alloys have also been found to have reduced casting defects compared to alloys which are richer in Al while maintaining mechanical properties and oxidation resistance [**44**]. Processing is difficult as TiAl is highly reactive with many crucible materials and will even react with Y_2O_3 in the solid state above 1500^{o}C [**45**]. Reactions with crucibles may lead to undesirable effects such as oxygen

pickup making production of critical parts difficult [**46**]. Optimization of crucible structure can lead to improved crucible survivability and a decrease of inclusions in the melt due to the crucible, but inclusions will be introduced regardless [**47**,**48**]. In TiAl products produced by powder metallurgy porosity is a critical variable as there is a near linear relation between decreasing Young's modulus and increasing porosity [**49**]. Other methods being developed for processing also include centrifugal casting with ceramic molds to cast turbochargers [**50**].

Processing which occurs after casting can also have a drastic effect on microstructure, even after forging increasing the annealing temperature from 800°C to 1000°C in a β solidifying alloy can result in microstructure changes from duplex to more lamellar [**51**]. Annealing for short periods at temperatures just into the β-phase field, allowing β stabilizing elements to diffuse homogeneously, can result in fully lamellar microstructures without blocky α grains [**52**]. Hot forging can also be used to homogenize the microstructure of some alloys [**53**]. Processing can also be done to increase fracture toughness, such as applying strains perpendicular to the crack direction [**54**]. Hot working of TiAl is also possible though requires careful control, for example hot working a Ti-45Al-V-Nb-Y alloy must be done at temperatures greater than 1150°C and strains less than 0.01 s^{-1} to avoid defect formation [**55**]. Work is also being done to quantify the effects of TMCP (thermos-mechanically controlled processing) after casting in order to reduce costs and optimize properties [**56**]. These TMCP methods have been able to increase room temperature ductility with elongations in the range of 5-7% [**57**].

1.4 Mechanical Properties

Mechanical properties are of critical importance when implementing materials. TiAl alloys follow the hall petch relation where decreasing grain size increases the strength [**58**]. For high temperature alloys such as turbine blades creep and fatigue are both important. An overview of creep and fatigue behavior of TiAl alloys is presented below. A brief discussion of fracture in turbine blades follows. Reducing grain size in TiAl alloys improves tensile strength and elongation both at room and elevated temperature [**59**]. Stress strain curves for two TiAl alloys at various temperatures are shown in Figure 1.13. It can be seen that the alloys are much more brittle at room temperature than elevated. Reduction of the lamellar spacing or grain size are both effective at improving mechanical properties [**60**]. These mechanical properties as well as creep resistance can be improved by processing the alloys to contain β interlayers between some of the α/γ lamellar colonies [**61**]. Primary dendrite arm spacing and interlamellar spacing are reduced with increased cooling rate, which is also correlated with increasing microhardness and tensile strength of the as-cast alloy [**62**].

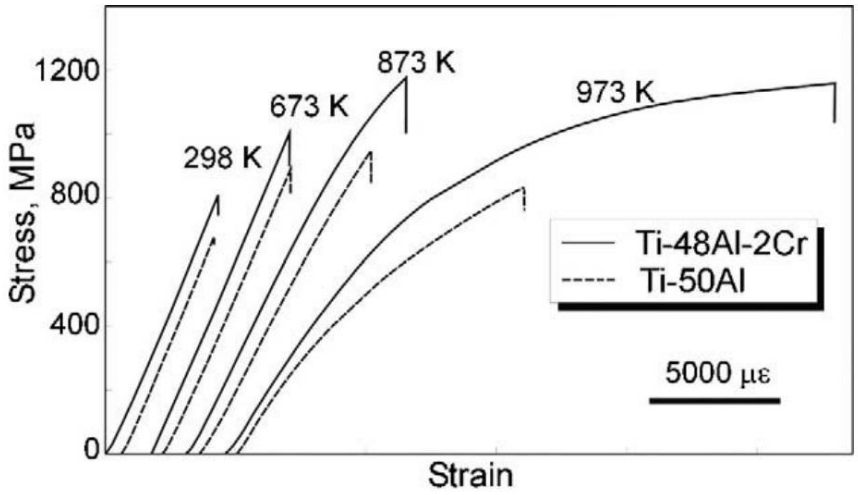

Figure 1.13: TiAl stress strain curves at various temperatures [**2**]

1.4.1 Creep

Creep is the process by which metals deform under applied stress at elevated temperatures [**63**]. This process can be divided into three stages; primary creep, secondary or steady state creep, and tertiary creep. Example creep curves for a TiAl alloy are shown in Figure 1.14.

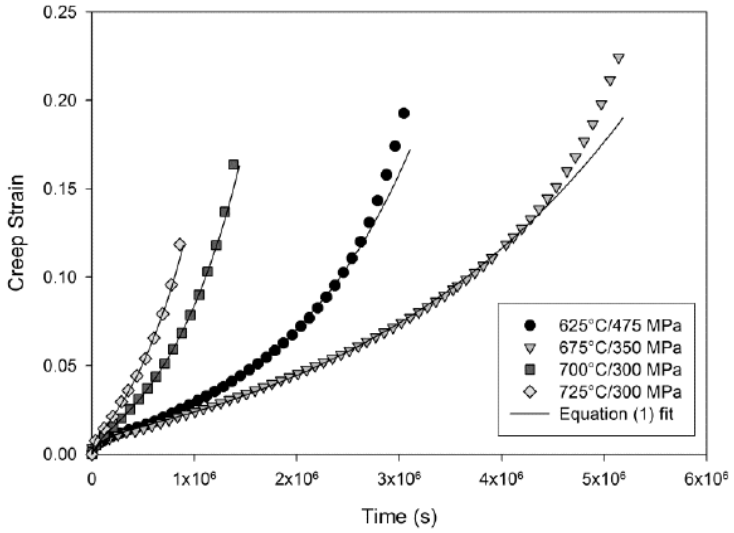

Figure 1.14: Creep strain over time for lamellar Ti-45Al-2Mn-2Nb alloy at different temperatures and applied stresses [**64**]

Primary creep is characterized by an initial high strain rate decreasing to a minima, once this minima is reached creep progresses at this rate in a steady state manner i.e. secondary creep [**63**]. The tertiary creep regime is characterized by rapidly increasing strain rate and fracture of the material. Creep may also progress linearly from initiation, avoiding primary creep, or may never reach a minimum, avoiding secondary creep, depending on the material and loading conditions. Due to the length of the time scale involved in secondary creep compared to primary

and tertiary, it is often the only mechanism considered when designing for creep [**65**]. Creep behavior is highly dependent on the temperature, applied stress and material being investigated. The creep behavior of TiAl alloys can be described in most cases by either dislocation glide/climb or grain boundary sliding [**66**]. Dislocation glide is the movement of dislocations along their slip planes, while dislocation climb is the movement not along the slip planes [**67**]. Since in a real crystal a curved dislocation consists of straight sections connected by kinks and jogs dislocation movement may also be a combination of dislocation glide and climb. The movement of these dislocations results in plastic deformation of the material in dislocation creep. The presence of solute atoms can also have an effect on dislocation glide [**68**]. In low strain creep situations fully lamellar TiAl samples show signs of ductile failure, however when exposed to higher strains the fracture was seen to be more brittle [**69**]. The presence of non-lamellar γ grains has also been found to greatly reduce creep resistance compared to fully lamellar structures [**70**]. This is due to grain boundary sliding occurring rather than the dislocation creep which is impeded by the lamellar structure. In fully lamellar structures the creep behavior is governed by dislocation climb [**71**]. Cyclical heating can also severely decrease the mechanical properties of TiAl alloys, especially decreasing the ductility [**72**]. It has also been seen that some partitioning of elements on solidification, such as Re in interdendritic regions and W in intradendritic, can improve creep resistance [**73**].

1.4.2 Fatigue

The reduction of properties during high temperature fatigue is caused by the lamellar microstructure degrading into single phase regions. The lamellar grain boundaries can stop dislocation movement in their absence intergranular fracture can occur. Although when crack propagation occurs in fatigue the lamellar orientation relative to the crack is critical to the crack propagation speed, this plays relatively little role in the overall behaviour as the cycles to crack initiation account for more than 90% of the fatigue life [**74**]. Small particles of silicides or B2 along lamellar grain boundaries have also been found to increase high strain creep resistance [**75**]. TiAl also shows softening under cyclical loading between 750-800^{o}C, however the stress amplitude still remains high, above 300 MPa [**76**]. TiAl can still maintain good creep and fatigue properties up to temperatures of 850^{o}C [**77**]. While fine grains are good for fatigue they degrade the creep resistance of the alloy [**66**], however in high strain creep situations fine grained lamellar structures have been found to be beneficial.

1.4.3 Fracture

In TiAl Cracks prefer to propagate down α/γ or γ/γ interlamellar boundaries, they prefer less to travel trans-lamellarly [**78**]. Fine grained fully lamellar structures exhibit better fracture behavior than coarser microstructures as the crack must deflect at the many grain boundaries, additionally the roughness of the path results in a high degree of crack closure [**79**]. Duplex structures are less crack resistant due to the equiaxed γ grains which provide an easy path for crack propagation [**36**]. Corresponding with the change from transgranular to intergranular cracking a phase transformation was also observed along the grain boundaries from γ to α due to the induced strain [**80**].

Turbine blade failure can have many causes, from exterior effects such as foreign object strikes material effects such as creep and fatigue. Often creep and fatigue work together to cause failure [**81**], for example small cracks caused by creep (grain boundary sliding) leading to low cycle fatigue failure [**82**]. Predicting the lifetime of components in these situations then requires not only an understanding of the creep behavior of the material but also fatigue and how the two work together to reduce the lifetime [**83**]. Such factors as the direction of stresses are also important as compression and tension may have differing effects and complex models may be required [**84**,**85**]. This applies to turbines of all kinds, not only for aerospace applications [**86**]. The root of the turbine blade near the connection to the hub is critical as often cracks are initiated there [**87**]. Additionally, high temperature oxidation can cause premature blade failure even with Ni-based superalloys when coating defects cause localized oxidation followed again by fatigue failure [**88**]. Wear may also play a role in some blade fracture cases [**89**].

1.5 Summary

TiAl alloys are interesting for high temperature applications due to their good oxidation, creep and fatigue resistance and high specific strength. Their low room temperature ductility and high reactivity makes processing difficult and expensive. Their current applications are limited to low pressure turbine blades, turbocharger wheels and automotive exhaust valves. Industrial alloys normally fall near the peritectic plateau and the phases most commonly formed are BCC β, FCC γ and hexagonal α, all of which have preferential orientation relations between one another. A method to improve the low ductility is to grain refine the microstructure. While finer grains are normally considered detrimental for creep situations the failure mechanisms in parts where the alloy would be implemented are complex, often combinations of oxidation, creep and fatigue working together. Novel processing methods are being investigated to control the microstructure of TiAl alloys including TMCP, and other post-casting treatments in order to improve their properties.

The aim of this work is to increase the ability of TiAl alloys to be used in more applications by providing new processing options to grain refine the alloy directly as the melt solidifies rather than using post casting methods. An overview of the process of solidification and grain refining possibilities as the melt solidifies are next investigated in Chapter 2.

Chapter 2 Solidification, Grain Refinement, and Isomorphic Self Inoculation

In order to grain refine TiAl it is important to understand the process of solidification and how it can be manipulated to affect the grain size. A traditional method of refining the as-cast grain size is by inoculation. This section provides a review of both the process of solidification, including differing theories of nucleation, and the process of inoculation and its applications. Finally, the novel concept of isomorphic self inoculation is presented along with the critical parameters developed for designing a sucessful isomorphic inoculant.

2.1 Solidification of Metallic Alloys

Solidification is the process by which a material changes phase from liquid to solid. The structure which develops when a material solidifies can have drastic effects on the properties of a material even if, as is the case for many TiAl alloys, there are solid state phase transformations after it solidifies [**90**].

2.1.1 Overview of the Solidification process

Solidification can be broken into two steps, nucleation and growth. First clusters of atoms form in the liquid arranged together to be in the solid phase [**91**]. If enough atoms can group together and surpass a critical size they can remain stable in the melt and grow, otherwise they remelt into the liquid. Since there is an energy barrier to nucleation it does not occur exactly at the melting temperature of the alloy but beneath it by a sufficient amount to account for this energy. A schematic of the temperature as time progresses for solidification is shown in Figure 2.1. The temperature the melt reaches below its melting point is called the undercooling (ΔT). Since the process of solidifying is exothermic there is an increase of temperature after nucleation where some remelting may occur called recalescence. After this period the melt cools and the nuclei grow until all the liquid has solidified.

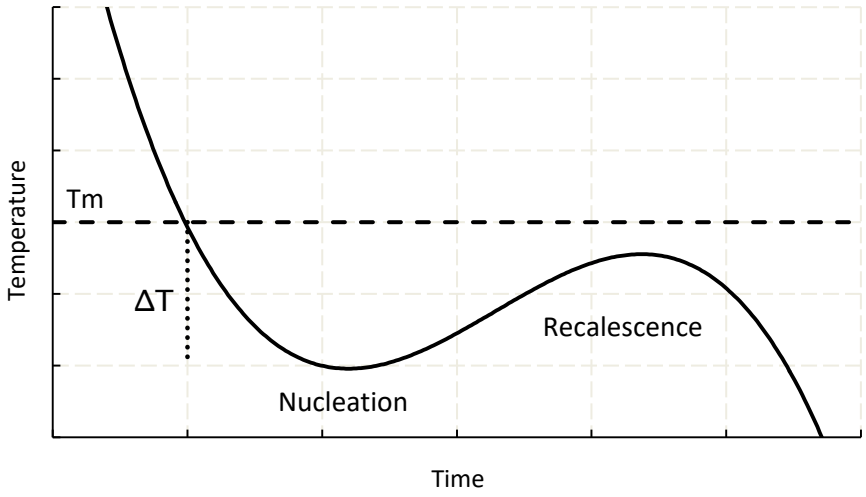

Figure 2.1: Temperature vs. Time for solidification

In order for a stable nucleus to form in the melt without any substrate or impurity atoms it must form homogeneously. A homogeneous nucleus forms from random fluxuations in the melt. If the nucleus which forms is smaller than a critical radius (r*) it remelts back into the liquid. If it is greater than r* it may survive and grow, participating in solidification. This critical radius is determined by the counteraction of the free energy of the surface of the nucleus in contact with the liquid melt (dependent on γ, the interfacial energy between the solid and liquid) and volume of the nucleus. The critical size for a solid nucleus which forms homogeneously in the melt, as determined by the free energy of formation (ΔG*), is given by [**92**]:

$$r^* = \frac{-2\gamma}{\Delta G^*} \qquad (2.1)$$

$$\Delta G^* = \frac{16\pi\gamma^3}{3\Delta G^2} \qquad (2.2)$$

The r* calculated for homogeneus nucleation can be quite large and not representative of that observed experimentally. This is because the energy barrier of formation can be significantly reduced by the presence of impurities or surfaces in the melt, in reality it is extremely difficult to nucleate a metallic melt homogeneously. The presence of these impurities or surfaces leads to solidification by heterogeneous nucleation. Different theories and cases for heterogeneous nucleation are considered in Section 2.1.2.

Once a stable nucleus has formed it can then grow. The nucleus which forms may be solute depleted, depending on the solute partitioning, and form a solute rich layer around it unless diffusion or stirring are significant enough to mix the layer back into the liquid [**91**]. This can have a significant effect on solidification and as such will be further presented in Section 2.1.3. Depending on the processing conditions this growth can occur in different manners depending on the stability of the solid-liquid interface, these are planar front, cellular and dendritic growth [**93**]. This work is not overly concerned with these modes as the majority of structures found are of the dendritic type.

The expected macrostructure of an ingot such as those produced in this work is shown schematically in 2D in Figure 2.2. Solidification begins from the edges of the ingot which are in contact with the crucible since the thermal gradient is strongest here. Grains nucleated here then form columnar dendrites [**94**]. The central region of the ingot is made up of equiaxed dendrites and there exists a region of porosity near the top of the ingot formed by solidification shrinkage since the solid is more dense than the liquid.

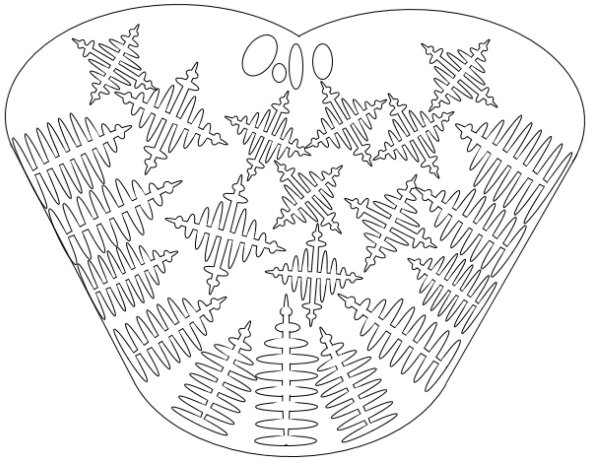

Figure 2.2: 2D Schematic of ingot structure

2.1.2 Nucleation Theories

Nucleation is of critical importance to the process of solidification and thus the structure of a material [**90**]. Since nucleation in metal alloys is at high temperature and metallic melts are often quite reactive it is difficult to observe and analyze the process of nucleatin in-situ in real time. As such multiple theories have been developed in order to describe how nucleation is occuring, such as the spherical cap or classical theory, adsorption, wetting or icosahedral quasi crystal formation [**95**].

2.1.2.1 Nucleation By The Spherical Cap (Classical) Theory

Nucleation via inoculation is commonly represented by the spherical cap heterogeneous nucleation model [**90**]. This model is based on a reduction of activation energy compared to homogenous nucleation caused by the presence of solid surfaces which act as nucleation sites. This reduction of activation energy depends on many factors such as the interfacial energies between the liquid, solid and nucleus [**92**] as well as the shape of the solid (i.e. flat, convex, concave) [**96**]. As discussed previously, in order for a solid to grow a nucleus must form with a critical size of r*. Since the nucleus is forming on a substrate its shape is that of a spherical cap as shown in Figure 2.3.

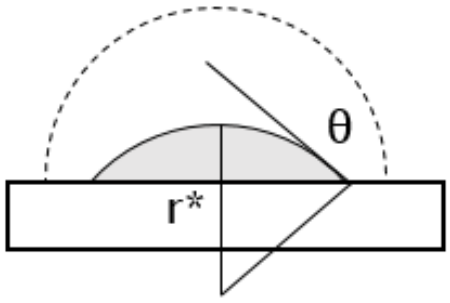

Figure 2.3: Heterogeneous nucleation of a spherical cap on flat substrate

The introduction of the substrate can reduce the free energy needed to form the nuclei and can be calculated by:

$$\Delta G^* = \frac{16\pi\gamma^3 f(\theta)}{3\Delta G^2} \qquad (2.3)$$

where $f(\theta)$ is the shape factor, which has a value <1, a function of θ the contact angle between the substrate and nucleus. In order for this situation to be accurate the substrate must have a size greater than 2r*. If the substrate is smaller other considerations must be taken. The size is particularly important for athermal nucleation, where at a given undercooling all nucleants of a certain size can be active. The situation becomes much more complex when other geometries are considered. The example of nucleation within a crack of a substrate or on the surface of spherical substrate are shown schematically in Figure 2.4.

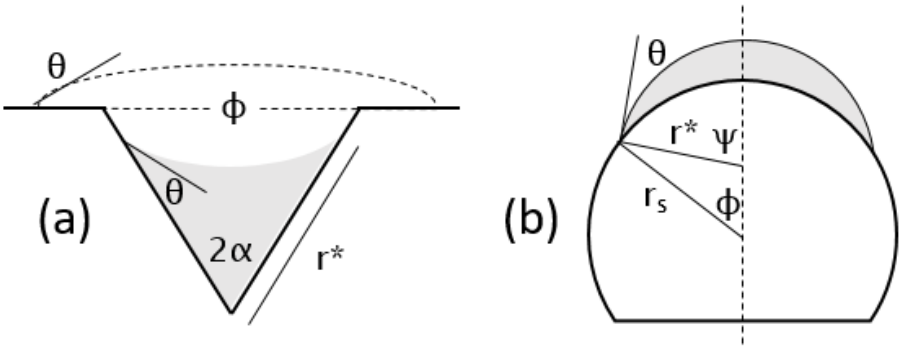

Figure 2.4: Effect of substrate geometry on heterogeneous nucleation from (a) cavity redrawn from [**92**] and (b) sphere redrawn from [**97**].

In the case of nucleation within a cavity, shown in Figure 2.4(a), it is possible for a solid nucleus to form above the melting temperature of the alloy, however it cannot grow unless the temperature drops due to the change in surface curvature required to leave the crack and grow from the surface, this also holds true for cylindrical cavities or holes as well as cracks [**98**]. The free energy (ΔG^{cone}) of the nucleus for a conical cavity is given by [**92**]:

$$\Delta G^{cone} = \frac{4\pi(r^*)^3}{3}\rho(v_s - v_l)f_v + \pi(r^*)^2\gamma_{sl}f_a \qquad (2.4)$$

where v_s and v_l are the volume fraction of the solid and liquid respectively and fv and fa are energy functions related to the area and volume of the nucleus:

$$f_v(\alpha,\theta) = sin^3\alpha\left(\frac{1}{4\tan\alpha} - \frac{f(\alpha+\theta-\frac{\pi}{2})}{cos^3(\alpha+\theta)}\right) \qquad (2.5)$$

$$f_a(\alpha,\theta) = \frac{2sin^2\alpha}{1+\sin(\alpha+\theta)} - \sin\alpha\cos\theta \qquad (2.6)$$

These two functions counteract one another and give a critical size of the nucleus within the cavity/crack at a given temperature above the melting point. This is not a true nucleus however as it cannot grow at the given temperature. The temperature must decrease in order for it to

grow within the crack and further energy is needed for the curvature of its surface to change and allow growth outside of the crack, which is only possible below the melting point when the driving force is increased by undercooling [**92**].

In Figure 2.4(b) r* is again the critical radius for the nucleus and θ the contact angle, r_s is the substrate radius, Φ the angle between the substrate center and nucleus edge, Ψ the angle between the nucleus center and nucleus edge as first given by Fletcher in 1958 [**97**]. The shape factor in this case is given by:

$$f(m,x) = 1 + \left(\frac{1-mx}{g}\right)^3 + x^3\left(2 - 3\left(\frac{x-m}{g}\right) + \left(\frac{x-m}{g}\right)^3\right) + 3mx^2\left(\frac{x-m}{g} - 1\right) \qquad (2.7)$$

$$m = \cos(\theta) \qquad x = r_s/r^* \qquad g = (x^2 - 2mx + 1)^{1/2}$$

Regardless of the geometry of the substrate it can be seen that the fundamental process of nucleation remains unchanged between homogenous and heterogeneous nucleation with the spherical cap theory. A nucleus does not survive unless it is formed at or larger than a critical size, once formed it can grow. An energy barrier still exists to this formation even if it can be significantly reduced by nucleation occuring on a suitable substrate.

2.1.2.2 Nucleation By Adsorption/ Wetting

The spherical cap model of nucleation is very successful at describing nucleation on substrates where there is a significant contact angle between the substrate and nucleus, this model however does not describe highly efficient nucleation catalysis where there is a very small wetting angle between the substrate and nucleus. In this case an alternative model which describes the nucleation as atom by atom adsorption onto the substrate surface to create a nucleus rather than the formation of a spherical cap has been proposed [**99**]. When the contact angle (θ) drops below 20° the size of the spherical cap would be only a few atoms thick and when below 10° it would exist as less than a single monolayer of atoms, the theory of spherical cap nucleation then fails and the shape factor no longer adequately describes the reduction in energy required to form a nucleus. Calculations using the spherical cap theory of nucleation do not agree with experimental results when the interfacial energy between the solid and liquid are very small i.e. very low contact angle [**100**]. It was shown that in these cases the nuclei were more accurately described as a single monolayer made up of atoms which form the solid on the substrate. This mechanism was found to help explain solidification of Sn on substrates with very small undercoolings (less than 7°C) [**101**].

In the case of inoculation with small particles, a nucleation model where the nucleus exists as a thin film encasing the particle may also be possible [**102**]. This can be shown schematically in Figure 2.5 followed by the equations to calculate the chemical potential of the nucleus (b_v).

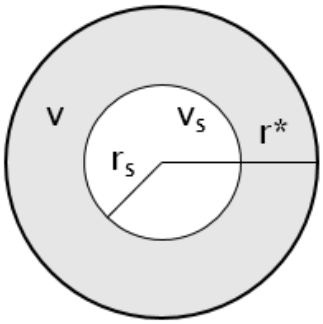

Figure 2.5: Schematic and equations for nucleation by wetting of a spherical substrate [**102**].

$$b_v = \frac{2}{3}\alpha v^{-1/3} + \beta_v \qquad (2.8)$$

$$\alpha = \frac{4\pi\gamma}{kT}\left(\frac{3v_s}{4\pi}\right)^{2/3} \qquad (2.9)$$

$$\beta_v = \frac{-v_s\Pi}{kT} \qquad (2.10)$$

where v is the nucleus volume, v_s the substrate volume, k the boltzman constant , Π the disjoining presure and γ the surface tension of substrate/nucleus interface. The first term is a positive contribution due to the capillary pressure from the curvature of the nucleus surface and β_v is a negative contribution from the disjoining pressure between the nucleus and substrate and the work of wetting the nucleus. Effectively this means you have a critical size for a nucleus in the same manner as for the spherical cap theory. This is shown schematically in Figure 2.6 where the solid line is the evolution of the chemical potential while the dashed line is if there is no particle present (homogenous nucleation). As with spherical cap theory there is then an energy barrier to nucleation which must be overcome in order for solidification to occur.

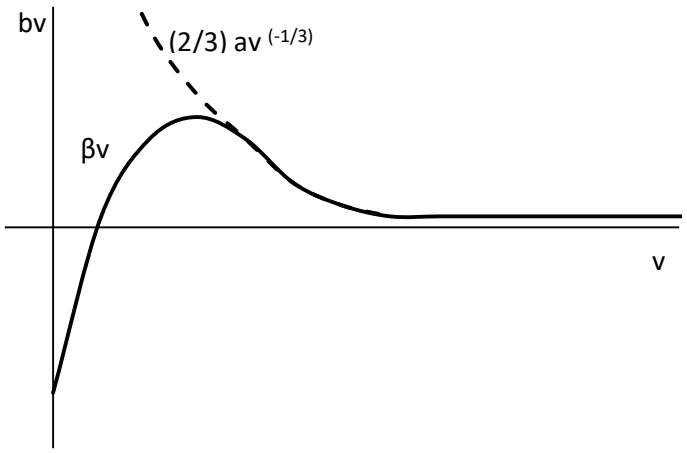

Figure 2.6: Critical volume for nucleation by particle wetting redrawn from [**102**].

2.1.2.3 Nucleation Assisted by Liquid Ordering

Another mechanism of nucleation is the specific case of icosahedral quasi-crystal formation in the liquid melt before solidfication as has been found in such alloy sytems as Mg-Zn-Y [**103**] and Al-Cu-Co/Fe [**104**]. The presence of these quasicrystals in the melt significantly reduces the energy barrier for nucleation [**105**]. The exact mechanism of the formation and growth of these quasi crystals is difficult to quantify though in-situ synchrotron methods indicate interface kinetics play a crucial role [**106**]. The solidification structures have been confirmed to relate to the orientations of these quasi-crystals [**107**]. Similar 5-fold symmetry orientation relationships are shown in the solidified grains as possesed by the quasi-crystals [**108**] along with a significant number of twin-boundaries [**109**]. A rough schematic of this process and the relation between quasi-crystals and solid is shown in Figure 2.7. It is also possible that short range ordering in the liquid can decrease the energy barrier for nucleation even if the mechanism does not exist in the alloy for isocahedral quasi-crystal formation [**110**].

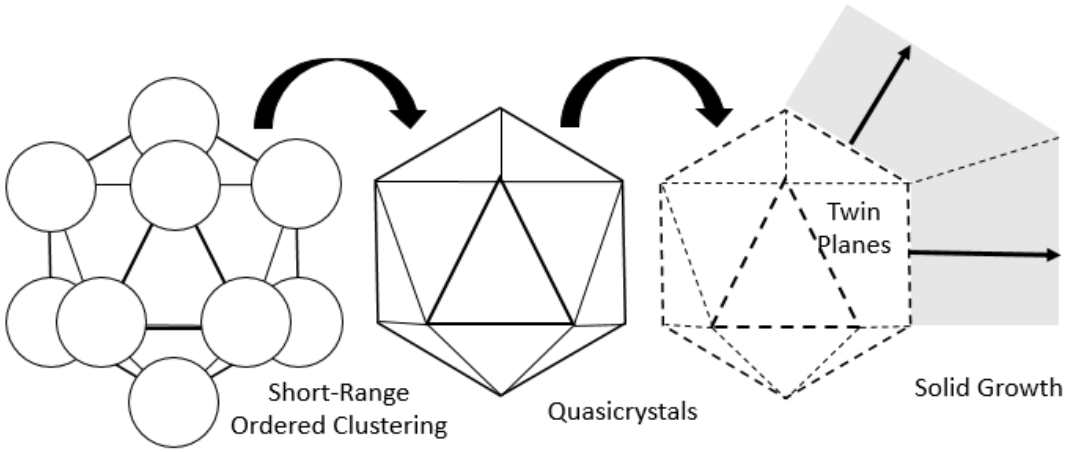

Figure 2.7: Relation between liquid quasicrystals and solid, redrawn from [**111**].

2.1.2.4 Nucleation Summary

Nucleation is a critical first step in solidification. There are multiple theories as to how nucleation can occur depending on the substrate and melt conditions. The classical spherical cap theory of nucleation applies well to substrates which are not perfectly matched to the melt, such as crucible walls, and can be modified for different geometries. When the substrates are a better match for the melt other nucleation modes such as adsorption or particle wetting may occur. In some cases nucleation may even occur from icosahedral quasi-crystals which form in the liquid. In all these cases there is a critical energy barrier a nucleus must cross in order to grow, below which the nucleus will remelt. In each case factors may decrease this energry barrier, and the requisit nucleus size, such as heterogeneous nucleation sites or liquid ordering but the barrier still exists.

2.1.3 Solutal Growth Restriction

Solutal growth restriction is the result of the partitioning/rejection of solute by the growth of the solid. Growth restriction was originally derived by Maxwell & Hellawell [**112**] in the case of a spherical particle growing by diffusion. Assuming dendritic growth and a binary alloy, the growth rate V of the solid phase can be expressed in the form [**113**]:

$$V = \frac{AD_l(\Delta T)^2}{\Gamma m_l(k-1)c_0} \qquad (2.11)$$

where A is a constant, Γ is the Gibbs Thomson parameter, D_l is the solute diffusion coefficient in the liquid, ΔT is the dendrite tip undercooling, c_0 is the solute content and m_l and k are the liquidus slope and the partition coefficient respectively. The growth-restriction factor Q is widely considered to be given by [**114**]:

$$Q = m_l(k-1)c_0 \qquad (2.12)$$

The growth rate V is then inversely proportional to Q, some authors then include the diffusion coefficient in the growth-restricting factor [**115**]. Data is often lacking for the diffusion coefficients of solutes in the liquid phase of metals and alloys so this expression of Q lacking the diffusion coefficients is more easily implemented. Extended to *i*-component alloys, the expression of the growth-restricting factor becomes:

$$Q = \sum_i m_l^i(k^i - 1)c_0^i \qquad (2.13)$$

In some multicomponent alloys the solute additions do not hinder the growth of the solid but have growth enabling effects, so care must be taken in multi component systems [**116**]. Sometimes alloying elements also have effects beyond solutal growth restrictions such as Ti reacting with minute impurity elements to form nucleant particles in Al or peritectic-forming additions which form pro-peritectic particles [**117**].

2.1.3.1 Solutal Growth Restriction in Ti-Al Based Systems

In Ti-Al based systems the growth restriction effect has not been thoroughly investigated. It is difficult to experimentally characterize the solidification structure because of solid state transformations which occur on cooling and no exhaustive thermodynamic databases exist to obtain m_l and k values. Table 2.1 shows some calculated values of Q for different alloys with data taken from Thermocalc calculations using databases from Vitusiewicz et al. [**118**] [**119**] [**120**]. Q_i/C_0^i values are also shown which reflect the growth-restricting effect independent of the alloy composition. This number demonstrates the individual effect of each element. Nb and Ta have an effect on the Q value similar to Al when their composition does not exceed 8 at%. Boron can be as efficient as Al, Nb and Ta with a composition of only 0.2 at%. As mentioned earlier, since usually only the lamellar colony size is measured after solid state transformations,

this growth restricting effect has not been quantified experimentally via measurement of the primary β grain size.

Table 2.1: Growth-restriction factor Q calculated for binary and multicomponent TiAl alloys.

Alloy	Q	Q_i/C_0^i		
		Al	Nb or Ta	B
Ti-43Al	34.35	79	/	/
Ti-46Al	45.04	97	/	/
Ti-46Al-8Nb	83.72	90	528	/
Ti-43Al-8Nb-0.2B	107.96	85	470	16714
Ti-46Al-8Ta	128.58	138	811	/

2.1.4 Summary

Solidification of metallic alloys is their process of transformation from liquid to solid. This occurs in two main steps, nucleation and growth. The first step, nucleation, is the initial formation of small solid regions. These regions must be of a critical size or they rapidly remelt. The critical size and energy to prevent remelting depends on how the regions form, and can be decreased if they form heterogeneously on substrates rather than homogenously in the melt. Depending on the substrate different theories exist as to how the solid nucleation occurs. Once solid nuclei exist they can then grow. Depending on the solute partitioning the nuclei may reject solute and the liquid will become richer. This enrichment may impede the growth of the solid causing it to occur more slowly. This continues until no liquid remains and the material is fully solid.

2.2 Inoculation of Metallic Alloys

Inoculation is the process of grain refinement by increasing heterogeneous nucleation during solidification [**121**]. This can be implemented by adding particles to the melt which act as nucleation sites such as inoculation of Mg by CaO particles [**122**] or by alloying additions which precipitate particles which then act as nucleation sites as Al_3Zr particles nucleating Al after Zr additions [**123**]. In either case the effectiveness of inoculation normally also relies on the presence of other solutes in the melt slowing the growth of the solids, giving more time for nuclei to form [**124**]. The relationship between solid growth and nucleation in inoculated melts can be quantified with the interdependence theory. This relates the effect of constitutional supercooling, from rejected solute, to the size a solid must grow to produce sufficient solute to nucleate a new grain, the distance this occurs from the solid/liquid interface of the growing solid and the distance the nearest inoculant particle is from that interface [**125**]. The grain refinement can be estimated by the empirical relation [**126**]:

$$d = a + b/Q \qquad (2.14)$$

where d is the predicted grain size, Q the growth restriction factor and a and b are factors related to the inoculant selected. The a factor is related to the number density of active inoculants and

the b factor to the potency of the inoculants [**126**]. The process of nucleation is shown schematically in Figure 2.8. First the inoculant particles are introduced, either by precipitation or introduction of heterogeneous particles. Next the active inoculants nucleate new solid, when this occurs depends on the size and potency of the particles. The nucleated solid then grows and finally all the liquid alloy solidifies. The inoculant particles can normally be found in the center of grains.

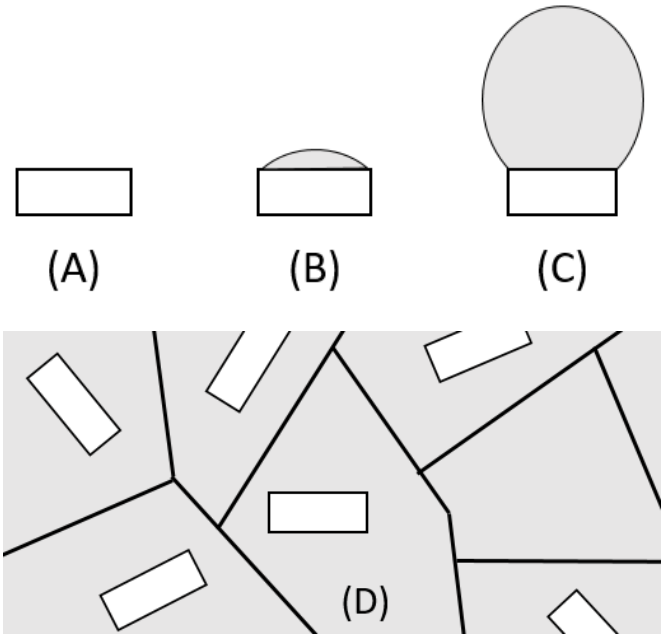

Figure 2.8: Schematic of solidification with inoculation showing (A) inoculant introduction (B) nucleation (C) growth and (D) fully solidified.

Inoculation is particularly common in the light metal systems, such as Al, Ti and Mg, where significant work has been done to design inoculants and determine their mechanisms [**127**]. Inoculation may be an unobvious source of grain refinement, such as Zn inoculation by $MgZn_2$ particles precipitated in binary Zn-Mg alloys where multiple characterization techniques such as EDS, selected area diffraction (SAD) and convergent beam Kikuchi line diffraction patterns were required to identify the precipitates and confirm they were acting as inoculants [**128**]. In some cases, such as Zr inoculation with Ag, the alloying addition functions both to precipitate inoculant particles as well as contributinig significantly to solutal growth restriction [**129**]. Conversely in some cases particles added may result in grain refinement even if they are not acting as inoculants, such as SiC or C in Mg-Al where grain refinement is observed but inoculants are not the added particles but precipitated Al_4C_3 particles made possible by C content from dissolved particles [**130**]. There are also cases where inoculation is responsible for grain refinement only as a function of processing such as in binary Al-Mg alloys where melt sheering can introduce O to the melt, $MgAl_2O_4$ particles then precipititate and act as inoculants [**131**].

Effectiveness of innoculation depends on many criteria, it is not simple to determine if a potential inoculant is ineffective whether the responsibility is from the inoculant itself or if it is

poorly matched to the processing conditions and may be effective in other cases [**132**]. Accordingly an inoculant which is effective for one alloy system, eg Al-B inoculation of Al-Si, may prove to be ineffective in a similar systems, eg Al-B in Al-Zn, Al-Cu, or Al-Mg, or ternaries, Al-B in Al-Si-Mg much more effective than in Al-Cu-Si [**133**]. Similarly, if a specific solute element is removed from an alloy inoculants which may otherwise be ineffective may become viable, eg viability of AlB_3 as an inoculant in Ti free AlSiMg and AlSiCu [**134**]. The addition of a solute element may also poison the inoculants and render them ineffective. It can be difficult to determine the exact mechanism of grain refinement by inoculation, and some discussions occur in the literature as to how certain inoculants affect solidification e.g. Mg refinement by C inoculation being due to C segregation [**135**] or effects of ternary Al additions interacting with the C [**136**].

Nucleation and grain refinement efficiency is closely tied to the misfit between the lattice of the inoculant and the bulk matrix [**137**], smaller lattice mismatches result in more effective inoculants [**138**]. A schematic of the lattice mismatch between an inoculant substrate and nucleated solid can be seen in Figure 2.9. The smaller the lattice misfit between the solids the less undercooling is necessary to nucleate [**139**]. Nucleation can occur at misfits greater than 15%, as acheived with Al nucleation on Al_2O_3 (misfit of 25%) however, this possible only due to an epitaxial layer of microtwins forming between the Al_2O_3 and bulk Al, there was no orientation relationship between the bulk Al and Al_2O_3 [**140**]. In the case of epitaxial nucleation an ordered layer forms on the substrate, this layer is then responsible for the nucleation of the solid phase rather than the substrate itself [**141**].

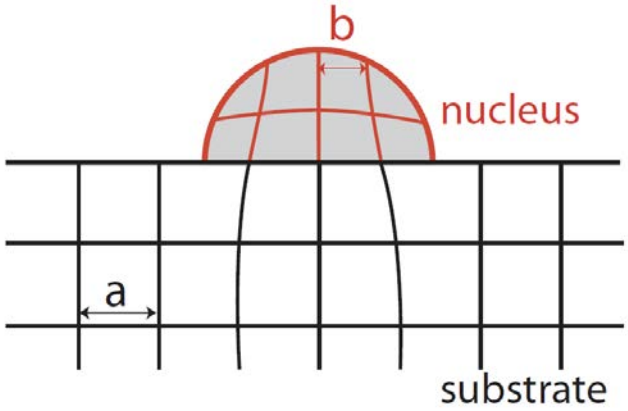

Figure 2.9: Schematic of heterogeneous nucleation on inoculant substrate

Nucleation occurs first on the largest particles as the critical radii (r*) is largest at low undercooling and decreases as undercooling increases, an inoculant distribution containing a single size, very narrow distribution, of larger particles may approach 100% efficiency as they could all nucleate at the same time [**142**]. It is possible to model the grain refinement action of these particles in ideal conditions [**143**]. In the case of TiC inoculation of Al there was found to be an orientation relationship between the large particles (>~1μm) and bulk which they nucleated while smaller particles were found at grain boundaries and were not centres of nucleation [**144**]. It is also possible that some other factors may be responsible for the decrease

in inoculant effeciency as in some cases the constitutional undercooling may be sufficient for nucleation from the vast majority of inoculant particles [**145**].The absolute value of grain refinement may also be effected by impingement of thermal gradients between inoculant particles [**112**] as well as the impingement of solute fields between particles [**146**], shown schematically in Figure 2.10. This means regardless of the number of inoculant particles or their potency there is a theoretical maximum to the grain refinement they can acheive.

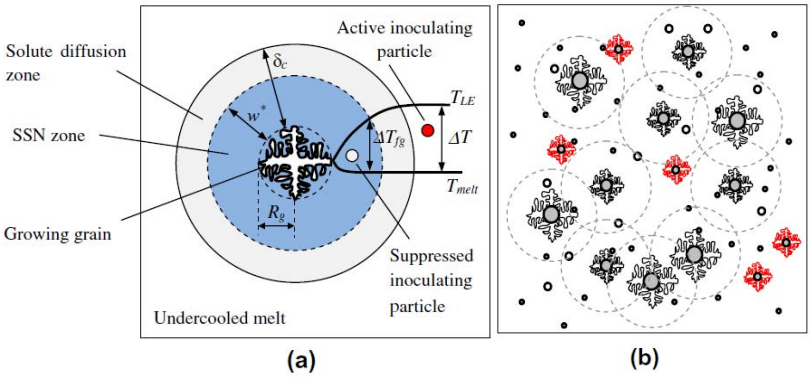

Figure 2.10: Solute diffusion diffusion field for (a) single particle and (b) multiple overlapping particles from: [**146**]

In order to maximize the refinement effect of inoculants both the size and number density of particles must be optimized [**147**]. The amount of time between inoculation and casting is also critical as inoculants may be rendered ineffective if left in the melt for too long, known as inoculant "fading", due to instability in the melt or interaction with other solute atoms (poisoning). Inoculants which function well at low interaction times may require modification to function where longer interaction times are needed [**148**]. It is also possible for multiple inoculant particles to form in the same melt and work together to refine the grains, such as TiB_2 and TiC forming in an Al melt after Al-Ti-B-C master alloy addition [**149**]. Inoculation techniques used for Al alloys inspired similar methods for Mg alloys as well [**150**]. In some cases the inoculant particles may not only participate in grain refinement but their presence in the bulk material may have other positive effects, such as increasing creep resistance of cast Mg-Y alloys by Al_2Y preciptates where inactive inoculants are located on grain boundaries and augment high temperature stability [**151**].

2.2.1 Inoculation in The Ti-Al System

Inoculation by boron additions is the traditional method to grain refine Ti-Al alloys by inoculation [**152**], though some work has also been done investigating grain refinement by other precipitates such as carbides [**153**]. Different forms of boride are stable in the melt such as TiB, TiB_2, and Ti_3B_4 [**154**]. TiB_2 additions can refine the room temperature γ-phase colony size and reduce the interlamellar spacing [**155**]. Boride inoculation works to nucleate both β and α Ti phases, and is particularly useful at refining α grain sizes in interdendritic spaces [**156**]. TiB_2 is a potent inoculant for β but less so for α, existing β grains are preferential nucleation sites for α compared to TiB_2 [**157**]. Increasing the boron content also increases the extent of the grain refinement produced [**158**]. The grain size reduction possible is quite drastic and is evident in

Figure 2.11 where adding 0.5 at% B to a Ti-45Al alloy drastically reduces the grain size [**159**]. Different polymorphs of TiB can form from the melt after B additions depending on the alloying elements in the system [**160**]. Borides have also been found to be useful at refining the microstructure not only during solidification but when found in the interdendritic regions after fast cooling where they could not precipitate before the bulk β they assisted in solid state transformations breaking orientation relations in the β-α transformation [**161**,**162**]. At sufficient addition levels the addition of B to TiAl melts, enough that borides form and nucleate β grains, a significant decrease in segregation is possible [**163**]. Using phase field calculations a boride initiated nucleus in an alpha solidifying alloy was found to impede other nucleation events around it by a volume 40% larger than its maximum size [**164**].

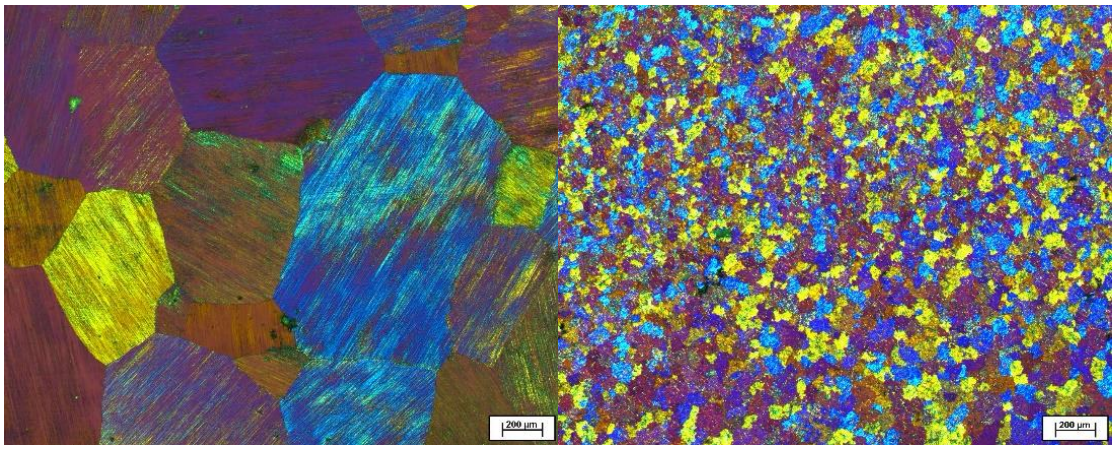

(A) (B)

Figure 2.11: Evident grain refinement of TiAl by boron addition (A) Ti-45Al and (B) Ti-45Al-0.5B [**159**].

However, at higher addition levels the borides which form can have a flake [**157**] or needle like [**152**] morphologies, as shown in Figure 2.12. These morphologies are detrimental to the final mechanical properties of the alloy and can result in decreased creep resistance and tensile strength, leading to brittle fracture in the as-cast state [**165**]. The presence of precipitates of any kind in the final part is also forbidden in certain material specifications. These borides are also commonly found on fracture surfaces when present in TiAl alloys [**166**,**167**].

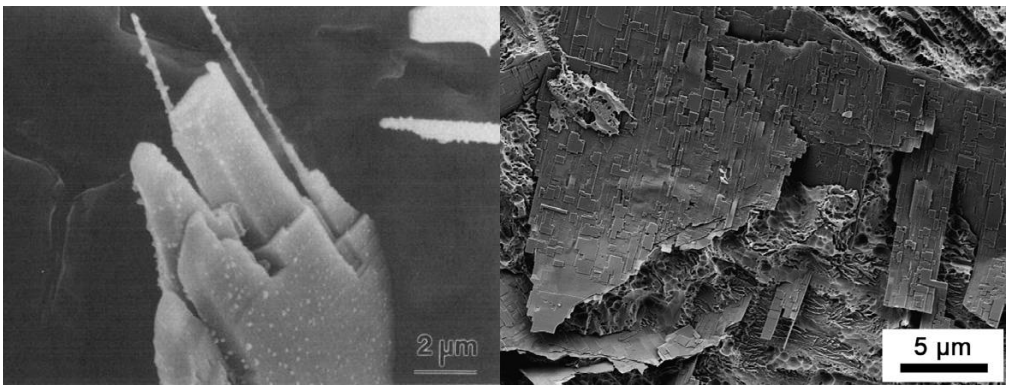

(A) (B)

Figure 2.12: Detrimental boride morphologies in TiAl (A) needle [**152**] and (B) flake [**157**]

Grain refinement using transformations besides the solid/liquid have also been investigated in TiAl systems. Attempts to grain refine by using the γ massive transformation during heat treatment required large cooling rates that resulted in deformations that made applications of the method difficult for manufacturing parts [**168**,**169**]. Grain refinement by ultrasonic vibration has also been successfully applied to a TiAl Alloy, reducing the grain size [**170**]. The pressure induced by the ultrasonic wave has two known effects assisting nucleation first locally increasing the melting point, by the pressure pulse-melting point mechanism, effectively increasing the undercooling for solidification and secondly cavitation induced wetting which increases contact between the melt and heterogeneous surfaces within the melt [**171**].

2.3 Development of Isomorphic Self Inoculation

It can then be seen from the literature that an inoculant is needed which cannot embrittle the bulk alloy, especially important for the Ti-Al system which already suffers from a lack of ductility. This section moves from a review of the literature to the development of a new method of inoculation. It has been shown that even inoculants which are highly efficient still have an energy barrier to nucleation. Only after the new phase nucleates can the solid grow and solidification continue. This energy barrier reduces the efficiency of the inoculants as factors such as insufficient undercooling cause less than the total number of inoculants to ever be active participants in solidification. A novel solution to this problem is proposed where rather than having the inoculants act as centers for nucleation to use particles which can act instead as centres of growth, bypassing the nucleation step and requisit energy barrier. In this case, as there is no energy barrier to surpass for solidification to progress, each particle added can be active in solidification and be the center of a new grain.

A similar method of grain refinement was previously investigated by Bermingham et.al. for a Ti alloy by pouring the melt over pure Ti powders and into a mold [**172**]. This was possible due to the close lattice match between the Ti alloy and pure Ti powder as well as the short interaction time (2-3s) between the powders and the melt before solidification permiting the Ti particles to grow epitaxially. They attribute the grain refinement in their castings to a combination of solutal grow restriction by Cr addition and the heterogeneous nucleation of new solid on the surface of the Ti particles. In contrast here we design inoculants specifically for an alloy which can then be used by direct introduction to the melt before casting, allowing longer interaction times. As well, while they attribute their grain refinement to heterogenous nucleation on the pure Ti particles we suppose the nucleation step can be avoided. Inoculants of this type are here dubbed Isomorphic Self Inoculants (ISI). In order to develop inoculants which function in this manner four design criteria were proposed:

I) Phase and lattice matching
II) Stability in the melt
III) Good Usability factors
IV) No negative effects on final casting

The first two criteria are the phenomenological factors determining if the inoculant can successfully act as an isomorphic inoculant. The final two criteria are related to processing and implementation, if the inoculant is a viable alternative to other inoculants. Each of these factors and their effects on design of isomorphic inoculants are outlined in the following sections.

2.3.1 ISI Criteria I: Phase and Lattice Matching

The critical phenomenalogical basis for isomorphic self inoculation is phase and lattice matching. By introducing solid particles to the melt which are the same phase as the solidifying alloy with similar lattice parameters the nucleation stage of solidification, and its requisit energy barrier, can be circumvented by direct growth of the particles. Rather than having new solid matrices form on the particles the matrix of the particle itself grow as the melt solidifies epitaxially upon it. This is shown schematically in Figure 2.13, in contrast to the traditional model schematic shown in Figure 2.9. In order for this to occur the particles must have the same structure as the solidifying melt and minimal lattice mismatching. If the lattice mismatch is too great or the structure different the particles will not inoculate isomorphically but in a more traditional manner by heterogeneous nucleation.

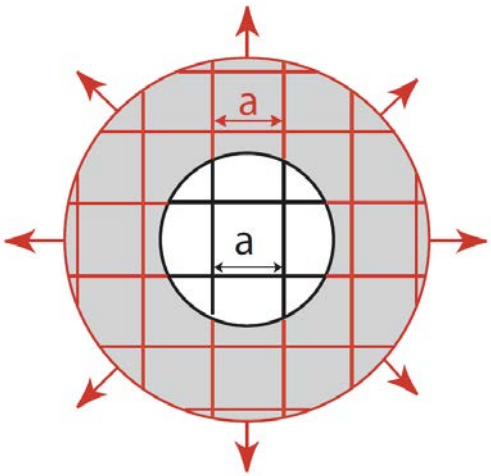

Figure 2.13: Schematic of solid growth by isomorphic self inoculation

As previously outlined, traditional inoculation relies on heterogeneous particles added to the melt which assist the nucleation of the solidfying phase by reducing the energy barrier to nucleation. Once solidification is complete the particles remain visible as inclusions/ precipitates in the room temperature microstructure as they are heterogeneous with the matrix. As such they can have positive or negative effects on the properties of the material, depending on the properties of the inoculants. In contrast the goal for isomorphic self inoculation is to develop particles which do not nucleate a new phase but simply grow, as such they should not be as visible in the room temperature microstructure, and should not have an effect on material properties beyond grain refinement. Since their matrix grows to form the bulk there should not be a significant interface left between the particle added to the melt and the matrix which grows from it. Especially in the case of TiAl alloys where solid state transformations occur after solidification, location and analysis of the particles in the room temperature microstructure may

be difficult/impossible. A schematic of the solidification behaviour of an isomorphic inoculant and its effect on the room temperature microstructure is shown in Figure 2.14, in contrast to that of a traditional inoculant, shown in Figure 2.8.

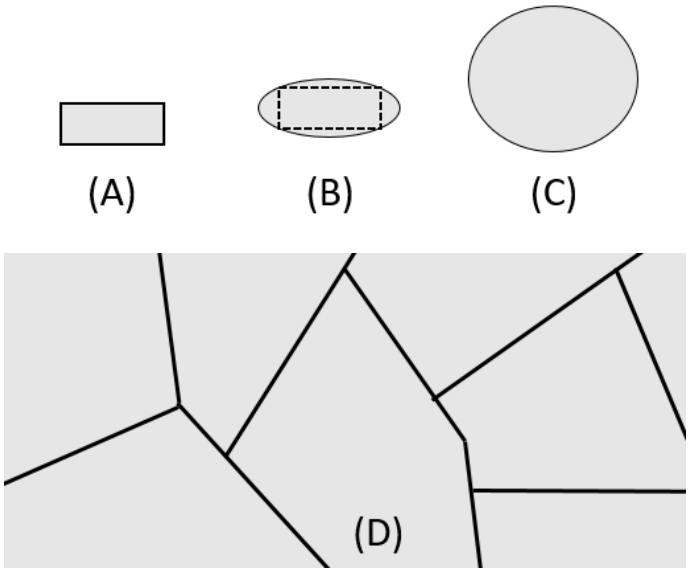

Figure 2.14: Schematic of solidification by isomorphic self inoculation showing (A) particle added to melt, (B) solid growing from particle (C) continued growth of particle and (D) final microstructure without heterogeneous remnants of inoculants.

In the case of TiAl alloys the most common solidifying phase for alloys in the peritectic region is β-Ti. As such a suitable isomorphic inoculant must consist of β-Ti at and somewhat below, to account for undercooling, the melting temperature of the target alloy. Additionally the lattice parameter of the bulk alloy must be evaluated so the inoculant alloy can be designed to match it as close as possible.

With respect to phase and lattice matching the perfect isomorphic inoculant would be particles of the same exact material as the melt. It is easy to imagine such particles acting as fully formed nuclei and growing rather than nucleating new solid as they would be identical to nuclei which formed in the melt. Such particles however would have limited application because they would not survive in the melt as they posess the same melting temperature as the melt and by virtue of the melt being liquid it is at or above that temperature. Upon addition the particles would then melt or dissolve quickly and not be able to influence solidification. They would not be able to exist in equilibrium with the melt. As such it would be difficult to separate their effect of any surviving particles on solidification from the inherent cooling effect of their addition. This leads then to the second design criteria for isomorpihc self inoculation.

2.3.2 ISI Criteria II: Stability in the Melt

The second phenomenological criteria for the design of an isomorphic inoculant is to ensure stability in the melt. Particles which match the phase and lattice of the bulk but cannot survive

long enough in the melt to affect solidification cannot be implemented as isomorphic inoculants. The stability of the particles in the melt does not have to be absolute. Some dissolution or melting is acceptable if the particles can survive past equilibrium with the melt and participate in solidification. This is shown schematically in Figure 2.15. The particle has a temperature well below that of the melt when introduced. After interacting with the melt for some time it reaches thermal equilibrium with the melt. Some dissolution or melting of the particle may occur. At this point if the particle is of identical composition to the melt it will dissolve completely. After the particles have reached equilibrium the melt is cooled and the particles grow to form grains of the bulk material.

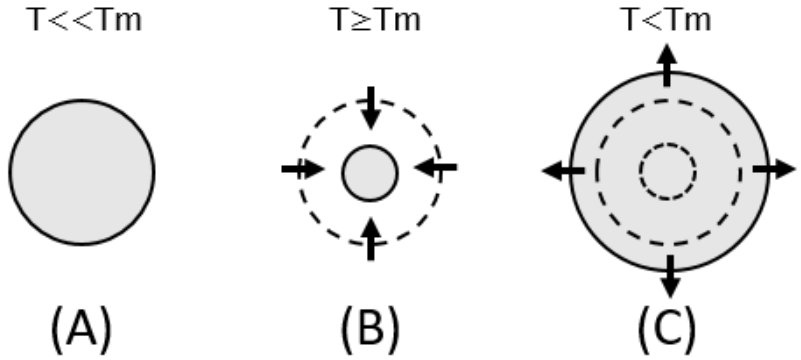

Figure 2.15: ISI particle size evolution (A) as introduced to melt (B) interaction with melt and reaching equilibrium (C) on solidification

There are two factors to account for stability of the particles in the melt, thermal stability and diffusive stability. Thermal stability is the particles ability to resist melting in the molten bulk alloy while diffusive stability is its ability to resist disolving. Of the two thermal stability is easier to achieve as all it requires is a material with a higher melting point than the melt. Diffusive stability is more difficult to acheive as the melt is at high temperature for most metallic alloys where diffusion can occur more easily than at low temperature. As well the inoculant cannot react with the melt to form other compounds as that would poison the surface needed for crystal growth. The stability of the particles must be acheived while also meeting the phase and lattice matching criteria.

In the case of TiAl alloys the melting point is already quite high. In order to produce inoculant particles which phase and lattice match while acheiving stability in the melt it is proposed to add refractory metals to the inoculant alloy. Refractory metals have high melting points and should increase the melting point of alloys they are added to providing good thermal stability. They also have quite large atoms which have a tendancy to diffuse slowly, which should help with the diffusive stability. The large atoms however will also affect the lattice parameter of the alloy. As such a balance must be met in the alloy between Ti, Al and refractory metal contents in order to produce an alloy which can meet both criteria I and II.

While particle stability in the melt is a phenomenological design criteria the degree of stability needed also depends on processing conditions. If a significant interaction time is required between the particles and melt, for example if there is a large distance the melt has to travel

from the furnace to casting mold, greater stability will be required than if less interaction time is required, for example direct casting from the furnace. This leads then to the two non-phenomenological criteria.

2.3.3 ISI Criteria III: Usability Factors

The first non-phenomenological design criterion for an isomorphic inoculant is relatively broad, usability. This refers to the ease of which the inoculant can be produced and implemented as well as its behaviour in the melt. These factors may or may not fundamentally affect whether the inoculant functions as designed but rather affect if it can realistically function as designed. An example of this would be the inoculation of a TiAl alloy with particles only slightly enriched in Ti compared to the bulk. While they may theoretically have thermal stability in the melt and good phase/lattice matching their stable interaction time in the melt would be too low to be useful in any real casting trials. Other important factors which fall into usability are the ability for the inoculant to be produced relatively easily. The elaboration process for the inoculant must be uncomplicated enough to warrent their addition to the melt they are inoculating. This also takes into account factors such as cost, since if the inoculant alloy is too expensive, either due to composition or manufacturing, it would not be implemented. Other factors such as density and magnetic behaviour must be considered. Particles which are too dense may sink to the bottom of the melt and not assist in grain refinement while those that are too light may float on the surface of the melt. Magnetic properties must be considered if induction heating is to be used as it affects their behaviour in the magnetic fields of the furnace. The propensity of the particles to fracture or agglomerate must also be considered as if they cannot be added to the melt in an efficient manner they cannot be effective inoculants.

2.3.4 ISI Criteria IV: No Negative Effects on Final Cast Product

The final criterion is that the inoculants do not negatively affect the final properties of the material. It is important to look at the elaboration process as a whole and ensure that the isomorphic inoculants do not negatively affect either the casting or final part. This is important especially for TiAl alloys which are normally used in high temperature applications where even if the as cast part may have ideal grain size with no precipitates solid state transformations may occur causing phases such as σ in the Ti-Al-Ta system, δ in the Ti-Al-Cr or ω in the Ti-Al-Nb system to form which are detrimental to mechanical properties. If any particles do remain heterogeneous in the matrix they must not be too brittle to negatively affect the ductility.

2.4 Summary

Solidification is a critical step in materials processing. Most metal products go through a solidification as part of their processing. Solidification is the process of liquid transforming to solid by first nucleation of solid then growth. In order for a stable nucleus to form a critical energy barrier must be overcome. In order to increase the nucleation in solidification heterogeneous particles are often added to the melt. This effectively grain refines the material as more nucleation results in more grains forming. How effective these particles, called

inoculants, are depends on how much they can reduce the energy barrier for nucleation. There are different theories as to how the particles reduce this energy, for smaller reductions the spherical cap model holds true while for larger reductions other models such as adsorption or wetting are more accurate. In TiAl alloys the most common inoculants are borides which are very effective at grain refining. In some cases, however, the borides which form can have detrimental morphologies which decrease ductility. A suitable ductile inoculant would then be advantageus in the TiAl system.

In order to produce such a ductile inoculant a new method of inoculation is proposed, isomorphic self inoculation. In this method particles are added to the melt which are closely related to the solid which will form. These particles do not act as centers of heterogeneous nucleation as classical inoculants but rather act as pre-formed nuclei and directly grow. This helps eliminate the energy barrier which prevents all the inoculants from participating in solidification. Four criteria are proposed to design a suitable isomorphic inoculant. I) phase and lattice matching between the particle and solidifying melt to supress inoculation and encourage direct growth of the particles. II) particle stability in the melt so the particles can exist at thermodynamic equilibrium with the melt and survive long enough to participate in solidification. III) good usability factors such as density matching with the melt for optimal mixing and alloy designs which can be easily fabricated. IV) no negative effects on the final properties of the casting, avoid forming brittle phases or other phenomena which may reduce the properties of the material.

Chapter 3 Inoculant Alloy Selection, Production, and Characterization

In order to implement the novel isomorphic self-inoculation method suitable inoculants needed to be found. Three alloy systems were considered. Once suitable compositions were found bulk ingots were produced from pure elements then cryomilled into powders which were then characterized using different methods to determine their size and microstructure.

3.1 Inoculant Alloy Selection

Before isomorphic self-inoculation trials could be conducted suitable inoculant alloys first needed to be found. A bulk base alloy of Ti-46Al was chosen and several alloy systems investigated to find suitable alloys which could be used as inoculants. Two ternary systems, Ti-Al-Nb and Ti-Al-Ta as well as the binary Ti-Ta were considered and alloy compositions within them selected.

In order to choose alloys to use for isomorphic self-inoculation the criteria outlined in Chapter 2 must be met. Potential alloys were then evaluated based on 4 criteria before potential inoculants were produced:

1) Thermodynamic Description - A thermodynamic description must exist for the system so the phase of the alloy is known at the solidification temperature of the bulk as well as what the melting temperature of the alloy is predicted to be to ensure it is greater than that of the bulk alloy.

2) Diffusivity – The diffusivity of the refractory metal addition should be relatively slow to increase the stability of the particles in the melt.

3) Lattice Parameter – The lattice parameter must be calculated for each alloy to ensure the mismatch with the β Ti-46Al phase at the solidification temperature is not too great.

4) Usability Factors – The alloy must be evaluated for factors affecting their usability such as the density of the alloy, as well as ensuring it will not cause other phases to form which may negatively affect the final properties of the alloy.

3.1.1 Selection and Description of the Bulk Base Alloy

In order to choose good candidate alloys to act as inoculants for isomorphic self-inoculation a base alloy must be chosen. In these trials a base alloy of Ti-46Al (at %) was used. For ease of fabrication a binary base alloy was chosen. The aluminum content was chosen to be 46% as it lies squarely on the peritectic plateau. It also close to the Al content of alloys used industrially to produce turbine blades such as TNB (46%) and the GE alloy (48%). In order to determine the inoculant alloys for this alloy the same 4 criteria used for the inoculant alloys must be evaluated for it as well so useful comparisons can be made.

3.1.1.1 Ti-Al Thermodynamic Description / Melting Temperature

Since Ti-46Al was chosen as the base alloy for inoculation the inoculant alloys must be selected to match its properties. It is then useful to consult a binary Ti-Al phase diagram such as shown in Figure 3.1. From the phase diagram it can be seen that the solidification phase for the bulk alloy is β. A line can be drawn from the liquidus line at the alloy composition to give a melting temperature of ~1540ºC. This means the inoculant alloys must have melting temperatures greater than 1540ºC and be in the β phase field of their systems at high temperature.

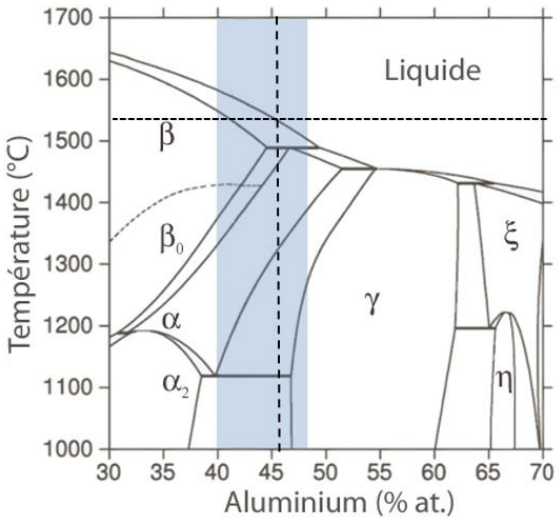

Figure 3.1: Ti-Al binary phase diagram showing bulk alloy composition [**173**]

3.1.1.2 Diffusivity

In addition to the minimum melting point the base alloy selection also affects how quickly the inoculants will dissolve in the melt. As the base alloy is β solidifying, the inoculant alloys must be β at high temperature. Figure 3.2 shows calculated diffusion rates for some refractory metals in high temperature β-Ti using A_i and Q_i values tabulated in the smithells metals reference book [**6**] and the equation:

$$D = A_1 \exp\left(-\frac{Q_1}{kT}\right) + A_2 \exp\left(-\frac{Q_2}{kT}\right) \qquad (3.1)$$

where k is the Boltzmann constant and T the temperature in K. Slower diffusion rates should correspond with slower dissolution of inoculant particles and better survivability in the melt. As it is difficult to find information for diffusivities of species in molten Ti-Al the behavior of the species in high temperature solid β-Ti is taken to be indicative of their behavior in the melt. Assuming the particles and the particle/melt interface reach thermal equilibrium with the melt their dissolution should be controlled by the slowest diffusing species out of the particles and into the melt, in order to maintain conservation of mass across the interface. Slower diffusion rates should correspond with slower diffusion of the inoculant particles and better survivability in the melt.

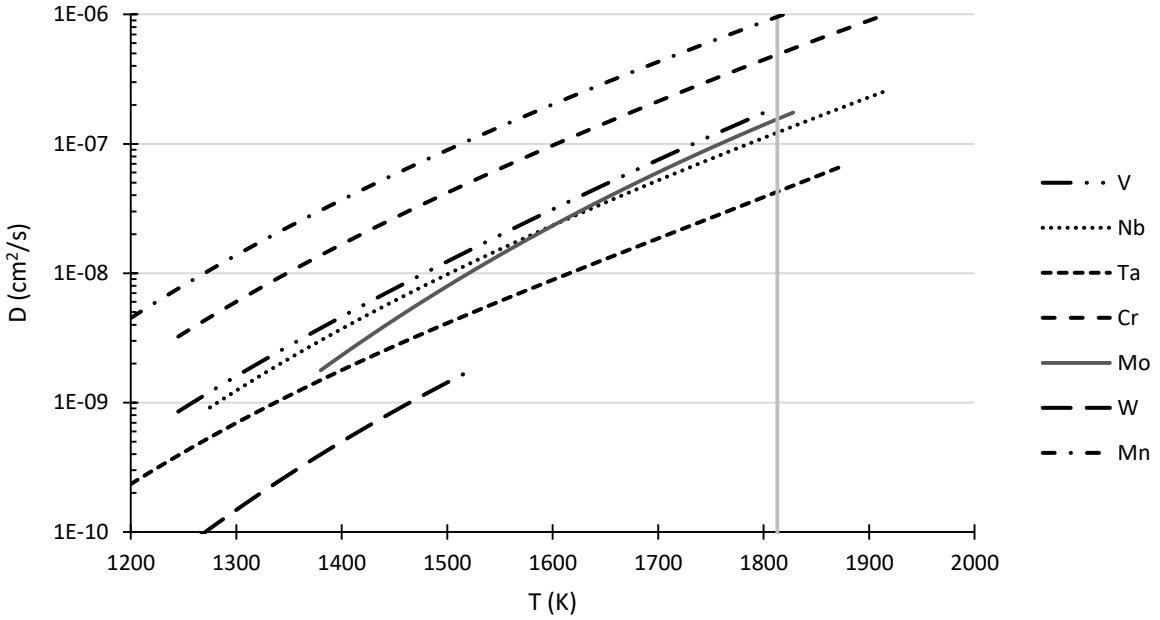

Figure 3.2: Calculated diffusion rates for some refractory metals in high temperature β-Ti [**6**].

3.1.1.3 Lattice Parameter

The lattice parameter is also important for the bulk alloy. An equation has been fit to alloys in the Ti-Al-Nb-Ta system to find their lattice parameter at high temperature [**174**]. The composition of the alloy in atomic percent (X_i) and the temperature in degrees Celsius (T) are taken as inputs and the lattice parameter is the output (α_β), as can be seen below:

$$\alpha_\beta = \alpha_\beta^{Ti(Pure)} + \sum_{j=1}^{k} e_i X_i + b \qquad (3.2)$$

where $\alpha_\beta^{Ti(Pure)}$ is the beta Ti lattice parameter at 0°C. Using reported lattice parameters for pure Ti at different temperatures first the equation could be solved for b, then each coefficient respectively using reported lattice parameters at different compositions yielding:

$$\alpha_\beta(nm) = 0.328 - 7.4 \times 10^{-5}(X_{Al}\text{in atomic percent}) + 1.23 \times 10^{-4}(X_{Nb}) + 4.6 \times 10^{-4}(X_{Ta}) + 7.4 \times 10^{-5}(Tin\ °C) \qquad (3.3)$$

This equation can be used to plot the evolution of the lattice parameter over temperature for the base alloy, giving a good range of parameters to act as a target for inoculant alloy selections. A plot of this is shown in Figure 3.3 where the lattice parameter can be seen to only vary ~1% from 750-1750°C.

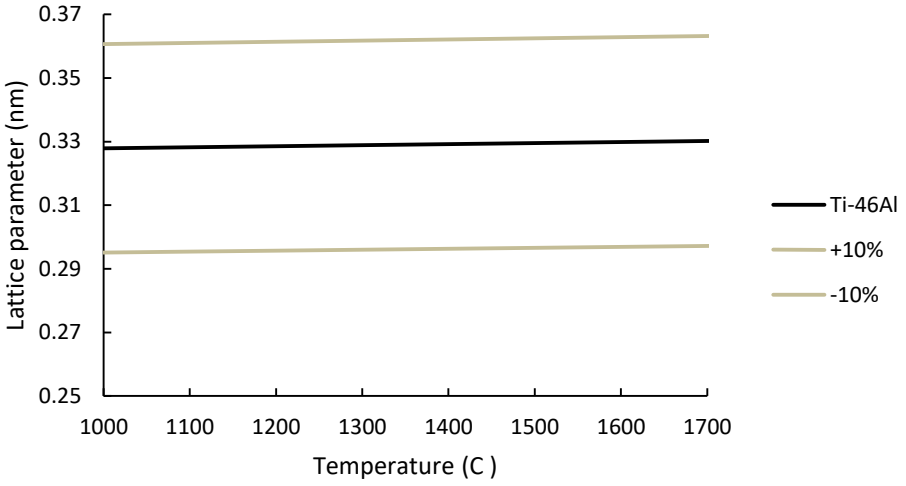

Figure 3.3: Calculated evolution of base alloy (Ti-46Al) lattice parameter with temperature.

3.1.1.4 Density

The density of Ti-Al alloys is normally in the range of 3.7-3.9 g/cm^3 at room temperature. The density of the alloys at high temperature is important as the inoculants should have densities as close as possible to the bulk alloy. If the inoculants are too dense they may sink to the bottom of the melt. If the inoculants are too light the induction stirring may be insufficient to mix them into the melt and they may remain floating on the surface. In either case the closer to the bulk alloy density the inoculants are the more similar their behavior will be to the melt which should increase their effectiveness at grain refinement. The density of the alloy at high temperature was calculated using the molar mass of the constituent elements and the calculated lattice parameter determined above. Since β-Ti is a BCC structure a unit cell contains 2 atoms. The mass of the unit cell of the alloy (m^a) can then be calculated using the molar mass of each element (Mi) and its amount in the alloy by atomic fraction (xi):

$$m^a = 2\frac{\sum M_i x_i}{N} \quad (3.4)$$

where N is Avogadro's number. Since a BCC structure is cubic the volume of a unit cell (V^a) is simply the cube of the lattice parameter at any temperature ($\alpha_\beta{}^a$), and the density of an alloy at a given temperature ($\rho_\beta{}^a$) can be calculated with:

$$\rho_\beta^a = \frac{m^a}{V^a} = \frac{2\sum M_i x_i}{N(\alpha_\beta^a)^3} \quad (3.5)$$

Applying this to the Ti-46Al alloy from room temperature to the melting temperature gives densities shown in Figure 3.4. At 1540^{o}C, the melting temperature of the alloy, the density is 3.55 g/cm^3 and at room temperature the density is 3.71 g/cm^3 (within the range of densities known for the system). The calculated room temperature density is not the true value for the alloy since it assumes the alloy is β-Ti, whereas in reality the β-Ti will transform into α and γ before cooling to room temperature.

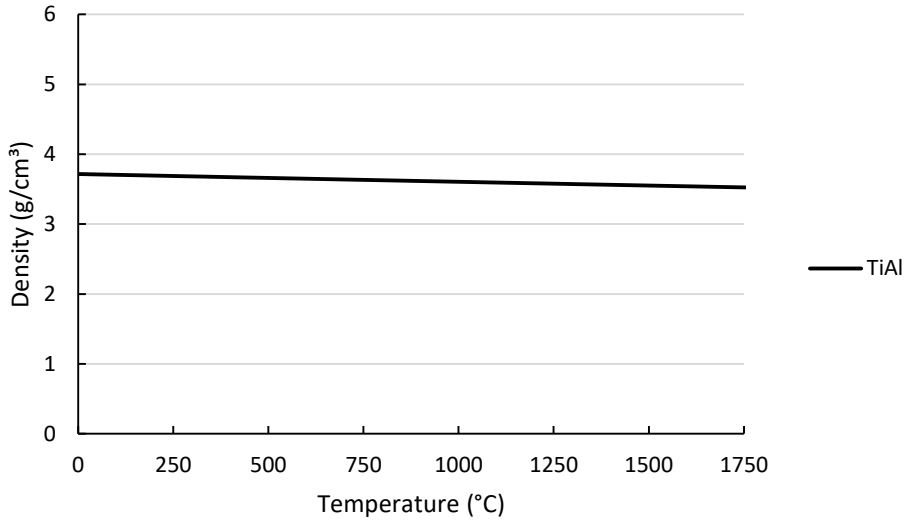

Figure 3.4: Calculated evolution of base alloy (Ti-46Al) density with temperature.

3.1.1.5 Summary

A good isomorphic self-inoculant for Ti-46Al should be β solidifying and exist as β-Ti at high temperature. The melting point of the inoculant should be above 1540°C and the refractory metal addition should not diffuse quickly in β-Ti. The lattice parameter of the inoculant should also be close to 0.329 nm at 1540°C and a density relatively close to 3.55 g/cm^3 at the same temperature.

3.1.2 Selection and Description of the Inoculant Alloys

Three inoculant alloys were chosen for isomorphic inoculation of Ti-46Al. Two ternary alloys were selected to balance the stability of the inoculants in the melt with the lattice mismatch between them and the bulk alloy, Ti-Al-Nb and Ti-Al-Ta. A third inoculant was chosen to maximize the stability of the particles in the melt while allowing a larger lattice mismatch, Ti-Ta. All three alloys are detailed below.

3.1.2.1 Ti-Al-Nb

The first system investigated for potential isomorphic self-inoculants was the ternary Ti-Al-Nb. Nb is a beta stabilizing element in the Ti system [**3**] with a relatively high melting point of 2469 °C [**175**]. In order to determine if the system is suitable and if a suitable composition exists within it for an isomorphic inoculant each of the 4 factors above were analyzed, the thermodynamic description of the system, diffusivity of the alloying elements in β-Ti, the lattice mismatch between the alloy and base metal as well as the density of the alloy. A balance between lattice mismatch, stability and density was sought to find an ideal inoculant.

3.1.2.1.1 Thermodynamic Description

Thermodynamic descriptions exist for the Ti-Al-Nb system and are quite well documented with databases available for ThermoCalc software. The Ti-Al-Nb system has a large β solidification field, as can be seen in Figure 3.5. This provides a large range of composition values where potential inoculants may exist.

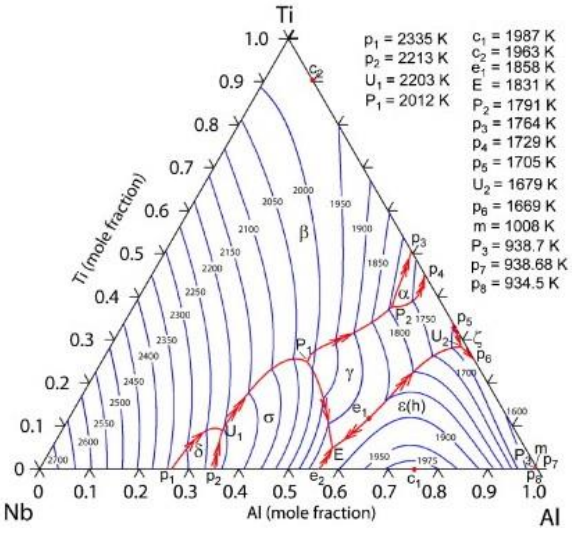

Figure 3.5: Liquidus surface map for the Ti-Al-Nb System [**118**]

Alloys of interest in the Ti-Al-Nb system often lie in the 0-30 at% range for both Al and Nb and are commonly used for biomedical applications [**176**]. Since both thermal and diffusive stability are important for the inoculant alloy an initial alloy composition of Ti-10Al-25Nb was chosen, slightly lower Al content and increased Nb content to increase stability without too much Nb to negatively affect the density. This alloy is firmly in the β solidification field and has a calculated melting temperature of ~1800ºC, obtained using ThermoCalc software. Thermocalc can also be used to calculate a phase diagram at the estimated low end of operating temperature for potential turbine blades, 900K, shown in Figure 3.6. A linear diffusion path between the inoculant and base alloys stays well away from problematic phases such as sigma. It can also be seen in Figure 3.6 (B) that above the melting point of the base alloy the proposed inoculant alloy still exists within the solid β phase field.

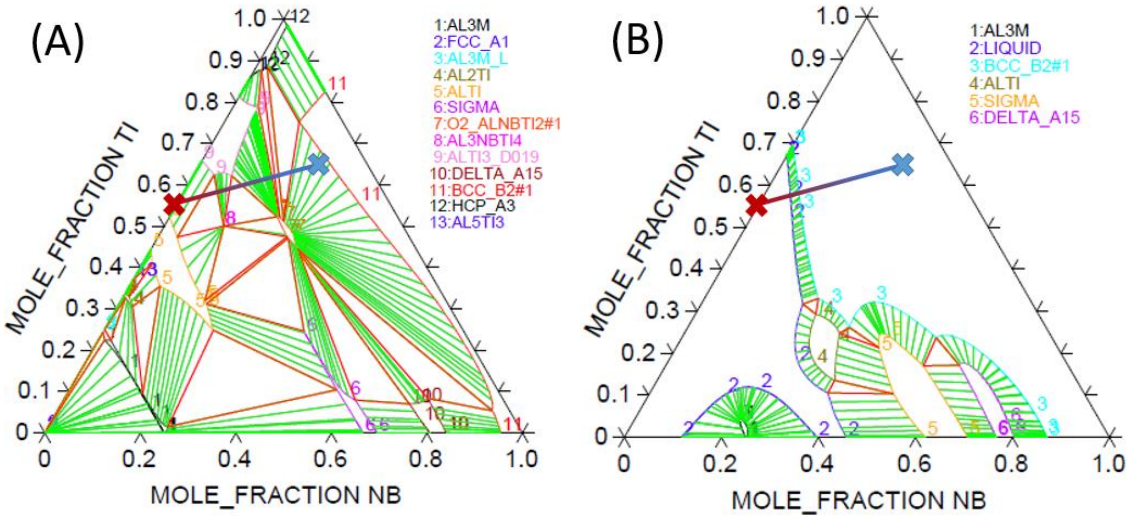

Figure 3.6: Calculated Ti-Al-Nb ternary phase diagrams using Thermocalc at (A) 900K and (B) 1900K showing the inoculant (blue X) and reference alloy (red X) compositions

3.1.2.1.2 Diffusivity

The tracer diffusivity for Nb in β-Ti can be found from Figure 3.2. At the bulk alloy melting temperature (1540ºC) the tracer diffusion coefficient for Nb is 1.4×10^{-8} cm^2/s. This however is for very low concentrations of Nb, since the alloy concentration for the inoculant is not insignificant, 25%, the interdiffusivity may be quite different. Figure 3.7 shows the evolution of diffusivity of Nb in β-Ti both with temperature and composition (at%) [7]. The indicated mark on the figure shows the Nb content of the inoculant alloy at the bulk alloy melting temperature. The interdiffusion coefficient at that temperature and composition is 1.02×10^{-8} cm^2/s. This means the real diffusion of Nb will be slightly slower in the inoculant alloy than expected from Figure 3.2, improving the survivability of the particles in the melt. This value does not however take into account the effects which the Al content has on the diffusivity since the values from literature are for binary alloys.

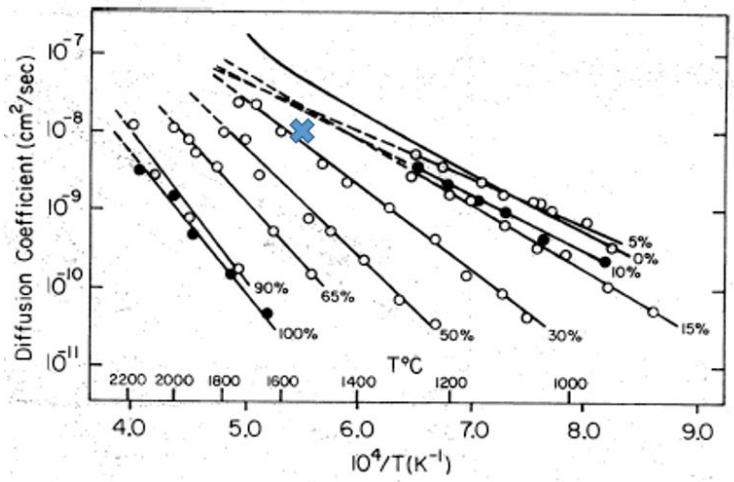

Figure 3.7: Diffusion of Nb in β-Ti [7]. Ti-Al-Nb alloy at bulk alloy melting temperature indicated.

3.1.2.1.3 Lattice Parameter

The equation presented in Section 3.1.1.3 used to determine the lattice parameter for Ti-46Al can also be applied to Ti-10Al-25Nb. At 1500ºC this gives a lattice parameter of 0.335nm, resulting in a very small lattice mismatch with Ti-46Al, less than 2%. The evolution of the lattice parameter and mismatch with temperature can be seen in Figure 3.8.

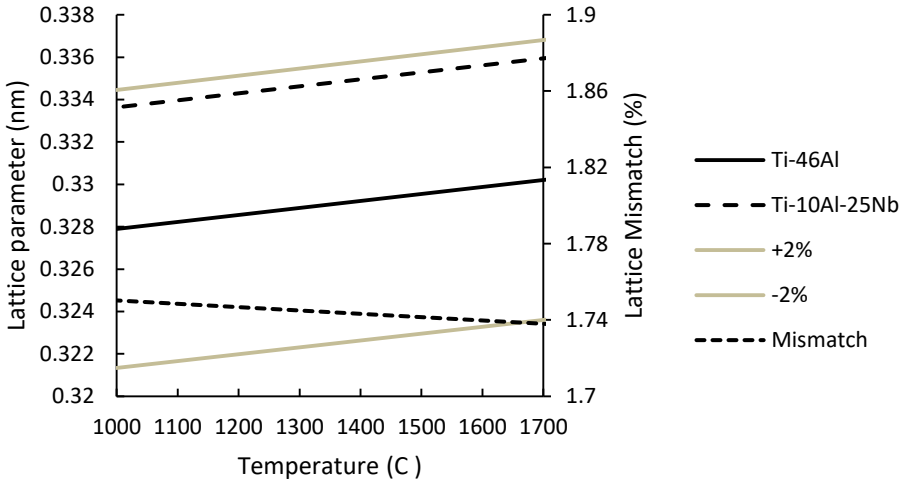

Figure 3.8: Lattice parameter evolution for Ti-10Al-25Nb from 750-1750ºC and corresponding lattice mismatch with Ti-46Al

3.1.2.1.4 Density

Similar to the lattice parameter the equation used to calculate the density of the Ti-46Al base alloy in section 3.1.1.4 can also be applied to the Ti-Al-Nb alloy. The addition of Nb to the alloy makes it much more dense with calculated densities of 5.25 g/cm^3 at room temperature and 5.02 g/cm^3 at 1540ºC, this evolution can be seen in Figure 3.9. As this alloy is stable at room temperature as β-Ti the calculated density at room temperature is more representative of the real room temperature density than that of the Ti-46Al alloy. Across the temperature range the density remains roughly 42% greater than the base alloy.

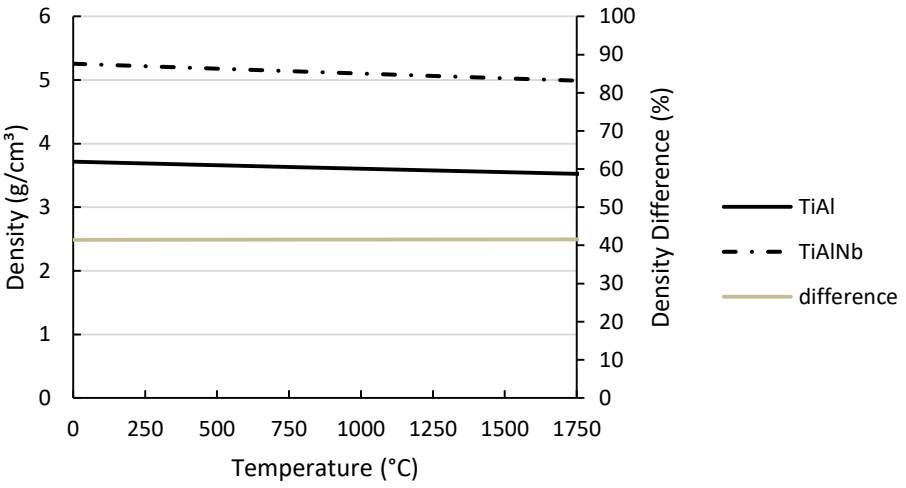

Figure 3.9: Calculated evolution of Ti-Al-Nb density with temperature and comparison with base alloy (Ti-46Al)

3.1.2.1.5 Summary

An inoculant alloy of Ti-10Al-25Nb then exists as β-phase at high temperature, has a high melting point (1800ºC), has a small lattice mismatch with the base alloy (<2%) and a interdiffusion coefficient of 1.02 $x10^{-8}$ cm^2/s. The density of the alloy is greater than that of the bulk by roughly 40%, however, the thermal and diffusive stability along with the low lattice mismatch make it a good candidate for an isomorphic inoculant.

3.1.2.2 Ti-Al-Ta

The second system proposed for an isomorphic self-inoculant was Ti-Al-Ta. Ta has a higher melting point (3017ºC [**175**]) but is more dense than Nb. The same 4 factors were considered for Ti-Al-Ta as Ti-Al-Nb. Again a compromise was sought between stability, density and lattice mismatch.

3.1.2.2.1 Thermodynamic Description

The Ti-Al-Ta system has available thermodynamic descriptions and is present in thermodynamic databases for Thermocalc. It also has a large β-phase solidification field as can be seen in Figure 3.10. A composition of Ti-25Al-10Ta was chosen to balance the thermal and diffusive properties of Ta with its high density. The refractory element content was reduced compared to the Ti-Al-Nb inoculant while the Al content increased. This composition has a lower melting point than the Nb containing inoculant (1725ºC vs 1800ºC, calculated with Thermocalc) however it is still significantly higher than the base alloy melting point (1540ºC).

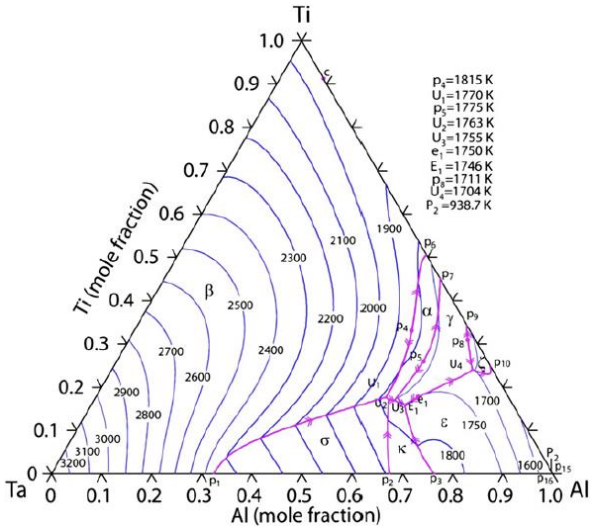

Figure 3.10: Liquidus surface map for the Ti-Al-Ta system [**119**]

Thermocalc can once again be used to calculate phase diagrams, both near the melting point of the base alloy and at an approximated working temperature, shown in Figure 3.11. As with the Nb inoculant alloy the Ta containing alloy avoids detrimental phases along the diffusion path between itself and the base alloy. The Ta containing inoculant is also β-Ti at high temperature.

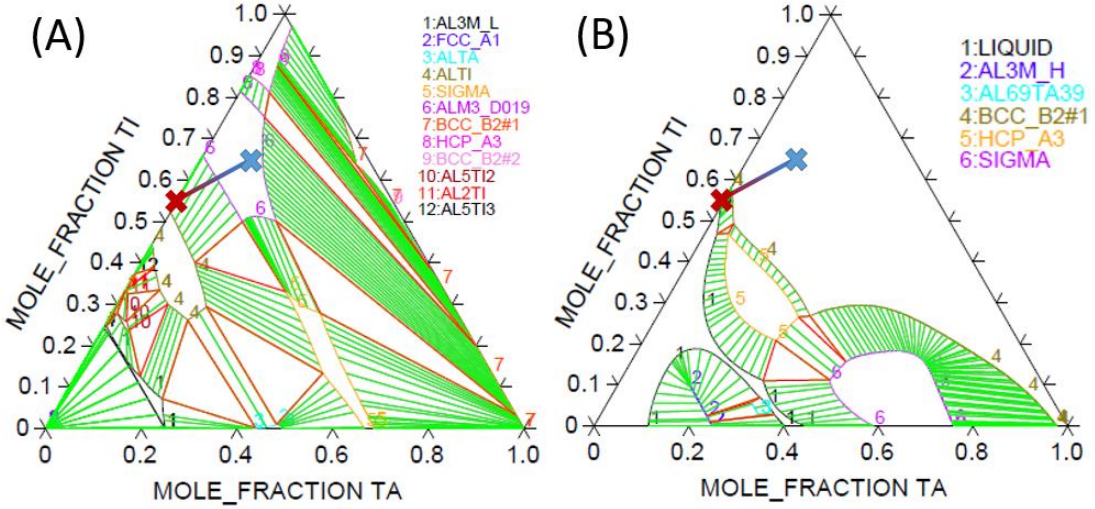

Figure 3.11: Calculated Ti-Al-Ta ternary phase diagrams using Thermocalc at (A) 900K and (B) 1800K showing the inoculant (blue X) and reference alloy (red X) compositions

3.1.2.2.2 Diffusivity

The tracer diffusion coefficient for Ta in pure β-Ti is 5.63×10^{-9} cm^2/s as obtained from Figure 3.2. The interdiffusion coefficient can be obtained for Ta at various temperatures and compositions as shown in Figure 3.12 [**8**]. From the figure, at the inoculant composition and 1540°C the interdiffusion coefficient is 1.22×10^{-8} cm^2/s. This is much faster than the tracer diffusion and is comparable to the Nb alloy interdiffusion coefficient (1.04×10^{-8} cm^2/s).

However, as with the Ti-Al-Nb alloy the effect of the Al ternary element is not captured with these diffusion coefficients so the real coefficients may be somewhat different.

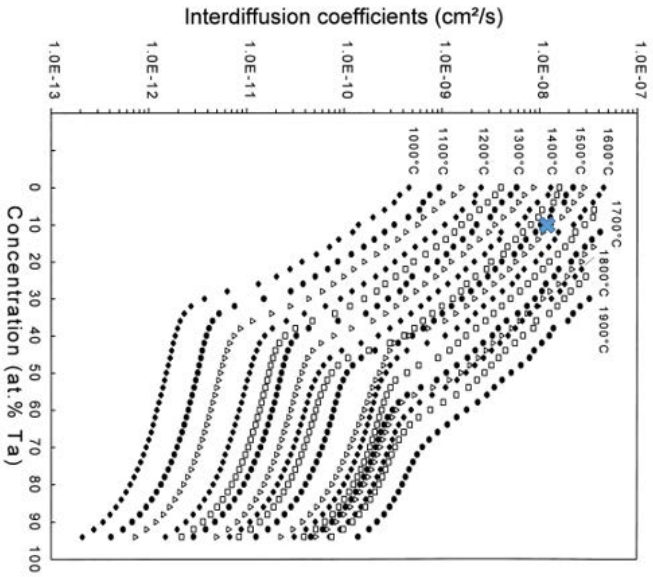

Figure 3.12: Diffusion of Ta in β-Ti [**8**]. Ti-25Al-10Ta at 1540°C indicated.

3.1.2.2.3 Lattice Parameter

The lattice parameter can be calculated for Ti-25Al-10Ta in the same manner as the Ti-46 base alloy and Ti-10Al-25Nb inoculant. At 1540°C it was found to be 0.336 nm, larger than both the base alloy and proposed Nb containing inoculant. While the mismatch with the base alloy is slightly larger for the Ta containing alloy, it is still below 2% and should provide a good lattice fit for solid growth. The calculated mismatch and lattice parameter over temperature can be seen in Figure 3.13.

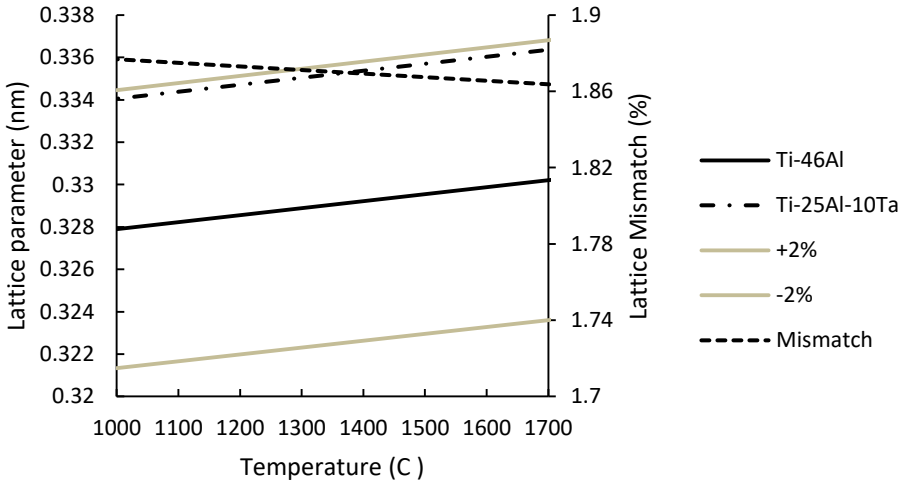

Figure 3.13: Lattice parameter evolution for Ti-25Al-10Ta from 750-1750°C and corresponding lattice mismatch with Ti-46Al

3.1.2.2.4 Density

The density was calculated for the Ti-Al-Ta alloy as shown in Figure 3.14. The density is similar to the Ti-Al-Nb alloy with 5.13 g/cm^3 at room temperature and 4.91 g/cm^3 at 1540^{o}C. Across the temperature range the density remains roughly 38% greater than the base alloy.

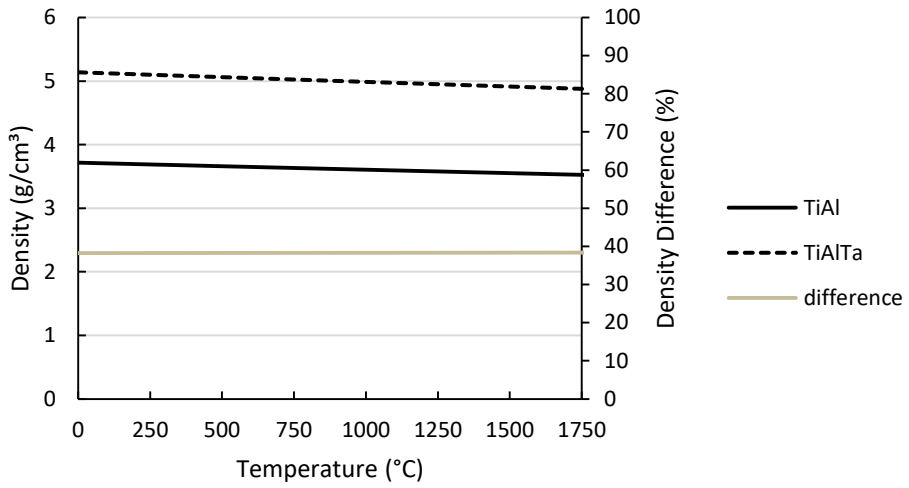

Figure 3.14: Calculated Ti-Al-Ta density with temperature and comparison with Ti-46Al

3.1.2.2.5 Summary

The proposed alloy of Ti-25Al-10Ta is then suitable as an inoculant for Ti-46Al. It has a small lattice mismatch (<2%) with the base alloy, a higher melting point (1725^{o}C) and exists as β-Ti at high temperature. The relatively slow diffusion of Ta in β-Ti (interdiffusion coefficient of 1.22 x10^{-8} cm^2/s) should provide the inoculant with good diffusive stability.

3.1.2.3 Ti-Ta

The two inoculant alloys from the ternary Ti-Al-Nb and Ti-Al-Ta systems each show good thermal stability with some diffusive stability as well as very good lattice mismatch and similar densities at high temperature as the base alloy. A third inoculant system was proposed to maximize both the thermal and diffusive stability at the expense of lattice and density mismatch. The alloy needed to maintain a lattice mismatch below 10% but as long as that was achieved maximization of stability was given greater priority than minimization of mismatch. To this end the binary Ti-Ta system was investigated.

3.1.2.3.1 Thermodynamic Description

The phase diagram for this binary system is shown in Figure 3.15 where it can be seen that alloys across the composition range from 0-100% Ta are β-Ti at high temperature and the melting point remains higher than that of the base alloy.

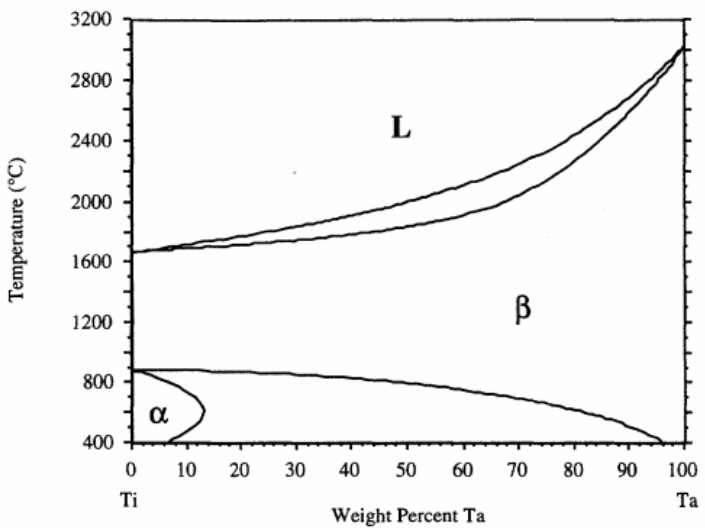

Figure 3.15: Binary Ti-Ta Phase diagram [**177**]

In order to maximize the stability of the particles in the melt a composition with as much Ta as possible was chosen. The first consideration was to avoid the possible formation of any σ phase, as such the diffusion path from the base alloy to the inoculant composition could not cross any σ forming regions on a ternary Ti-Al-Ta diagram from the solidification temperature to the approximated working temperature. These regions can be seen in Figure 3.11, where the σ forming regions are larger as the temperature decreases. To find the maximum possible Ta concentration a line can be drawn on the ternary phase diagram from the base alloy composition to the binary Ti-Ta side of the phase diagram tangential to the σ forming regions, as shown in Figure 3.16, which gives a maximum Ta concentration of 57 at%. Since the diffusion path between the Ti-Al and Ti-Ta binaries may not be linear the Ta concentration of the inoculant was reduced by 10% from this maximum to ensure no σ phase will form, resulting in a composition of Ti-47Ta. This alloy has a calculated melting temperature of 2200°C and should be relatively stable in the molten base metal.

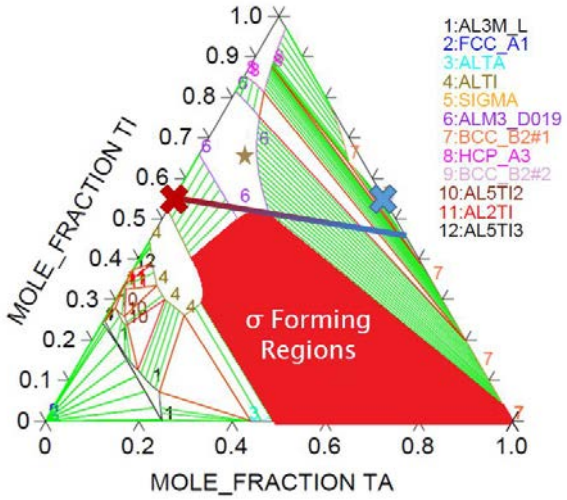

Figure 3.16: Ternary Ti-Al-Ta Phase diagram showing σ forming regions, base alloy composition (red X) and inoculant composition (blue X)

3.1.2.3.2 Diffusivity

The tracer diffusivity of Ta in a β-Ti alloy does not change from that discussed previously ($5.63x10^{-9}$ cm^2/s from Figure 3.2). However, the alloy selected increases the Ta content considerably from 10% in the previous alloy to 47% in the binary. Additionally the faster diffusing Al species is removed from the alloy. These factors together should significantly increase the diffusive stability of the inoculants in the melt. The interdiffusion for Ta at this higher concentration at 1540°C is $2.34x10^{-10}$ cm^2/s significantly slower than that of Nb in the Ti-Al-Nb alloy or Ta in the Ti-Al-Ta alloy. This value is also more representative of what can be expected in the alloy than the ternaries since in the inoculant there are no ternary effects, however since the bulk alloy contains Al there will still be ternary effects in the diffusion phenomena of the inoculants in the melt. The slow diffusion rate should make the Ti-Ta alloy the most stable of all the proposed inoculant alloys in the melt.

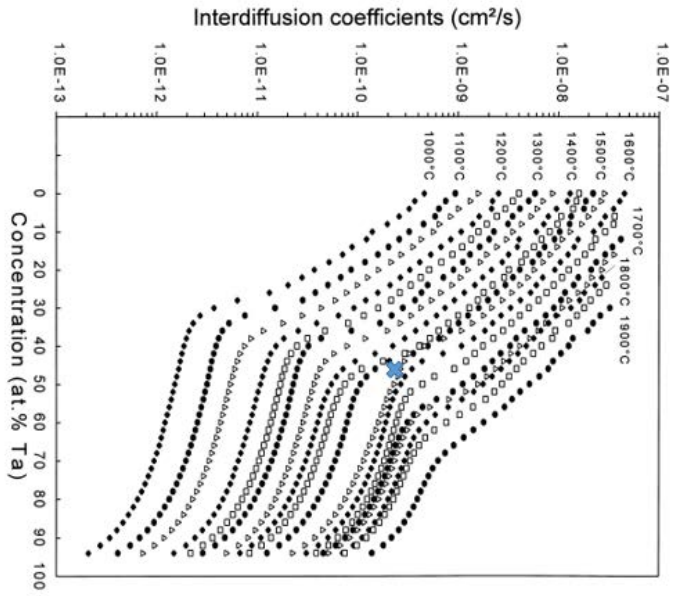

Figure 3.17: Diffusion of Ta in β-Ti [**8**]. Ti-Ta alloy at bulk alloy melting temperature indicated.

3.1.2.3.3 Lattice Parameter

Since the entire composition range is β from pure Ti to pure Ta the lattice parameter at any composition can be calculated as a weighted average, based on the alloy composition in atomic percent, of the pure Ti and Ta lattice parameters at a given temperature, which can be calculated with their coefficients of thermal expansion [**175**]. As shown for the other inoculant alloys this can be seen across a wide temperature range in Figure 3.18. The lattice parameter is much larger than the base alloy or other inoculants, however the mismatch remains below 5%.

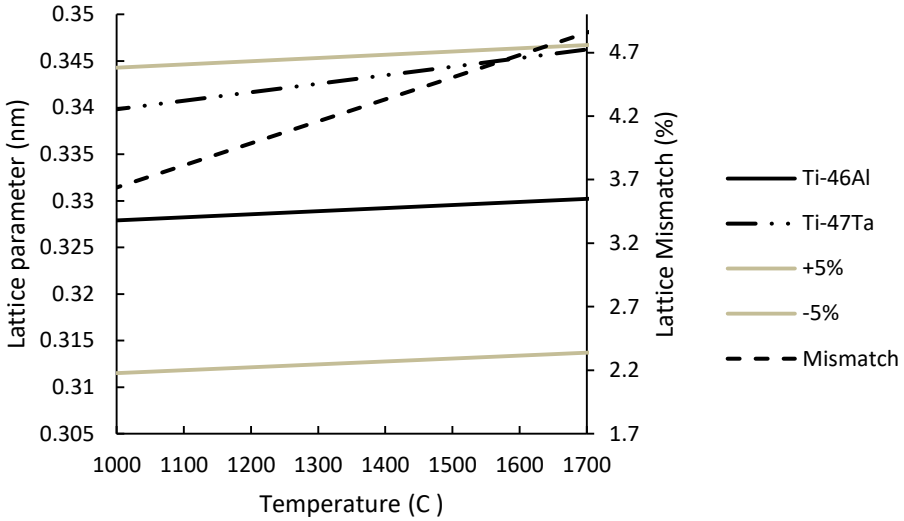

Figure 3.18: Lattice parameter evolution for Ti-47Ta from 750-1750°C and corresponding lattice mismatch with Ti-46Al

3.1.2.3.4 Density

The density was calculated for the Ti-Ta alloy as shown in Figure 3.19. The density is much higher than the others calculated, 10.14 g/cm^3 at room temperature and 8.95 g/cm^3 at 1540°C. Across the temperature range the density difference decreases from 170% at room temperature to 150% at 1540°C between the Ti-Ta alloy and base alloy. This is significantly more than the other inoculant alloys which remain below 50% different than the base alloy across the temperature range.

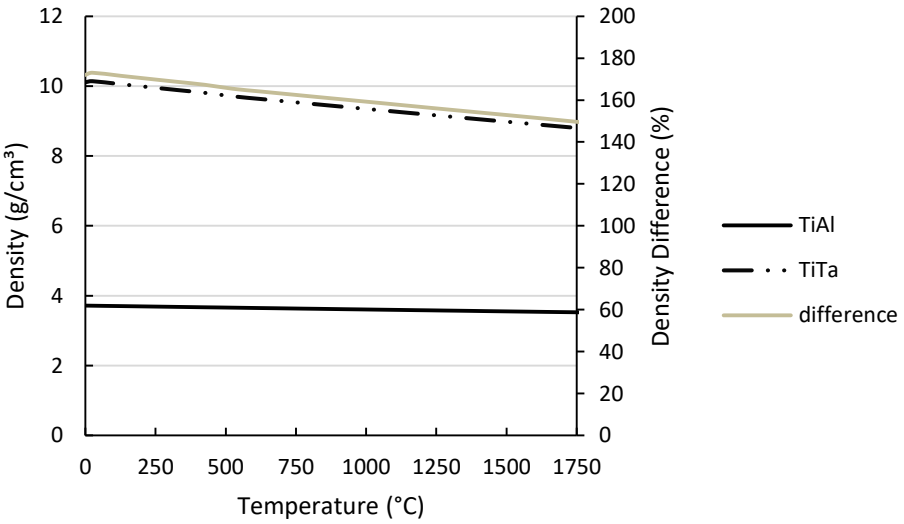

Figure 3.19: Calculated evolution of Ti-Ta density with temperature and comparison with base alloy (Ti-46Al)

3.1.2.3.5 Summary

While Ti-47Ta has a relatively high lattice mismatch (<5%) with Ti-46Al it remains low enough to be a suitable inoculant. Its high melting point (2200ºC) and the relatively slow diffusion of Ta should make it the most stable of the inoculants proposed for the base metal. The density of the alloy is much greater than the base alloy so the usability of the inoculant may be decreased and its behavior in the melt may be unideal.

3.1.3 Summary of Inoculant and Bulk Alloy Properties

Three alloys were proposed as potential isomorphic self-inoculants for a base metal of Ti-46Al, Ti-10Al-25Nb, Ti-25Al-10Ta and Ti-47Ta. All three alloys exist as the same phase as Ti-46Al at high temperature (β), have melting temperatures greater than the base alloy (1540ºC) and have lattice parameters close to the base alloy (<5% mismatch). A brief summary of these properties can be seen in Table 0.1.

Table 3.1: Selected properties of proposed inoculant alloys (at 1540ºC)

Alloy	α (nm)	T_m (ºC)	ρ (g/cm^3)		Slowest Diffusing Species	D (cm^2/s) (tracer) [**6**]	D (cm^2/s) (interdiffusion)
			25 ºC	1540 ºC			
Ti-46Al	0.330	1540	3.71	3.55			
Ti-10Al-25Nb	0.335	1800	5.25	5.02	Nb	1.40×10^{-8}	1.02×10^{-8} [**7**]
Ti-25Al-10Ta	0.336	1725	5.13	4.91	Ta	5.63×10^{-9}	1.22×10^{-8} [**8**]
Ti-47Ta	0.345	2200	10.14	8.95	Ta	5.63×10^{-9}	2.34×10^{-10} [**8**]

3.2 Powder Production

Once the inoculant alloys had been selected powders suitable for inoculation trials were produced. Bulk alloys were fabricated from pure elements then milled into powders which could be used for inoculation.

3.2.1 Bulk Alloys

The bulk inoculant alloys were fabricated from commercially pure elements. The Ti was obtained in rods (99.6% purity), the Al in pellets (99.9% purity) and the Nb in small cylinders or slugs (99.8% purity). The Ta used was taken from a bulk sample processed by electron beam remelting. Ta for the inoculant alloys were taken from the highest purity zone of the resolidified melt pool after electron beam melting. The alloys were fabricated in an induction heated cold crucible apparatus, a schematic of which can be seen in Figure 3.20. Before melting, the chamber was pumped down to a vacuum of 10^{-3} mbar then an Ar flux was applied allowing processing to occur at atmospheric pressure without risk of oxidation. The alloying element with the highest melting point was used as the base for the alloying with other elements added consecutively in order of their melting point from highest to lowest. This was done since once a material is melted it is difficult to melt another solid in the induction field. This was especially

difficult when adding Al since its low vapour pressure as a liquid meant significant superheat could not be applied.

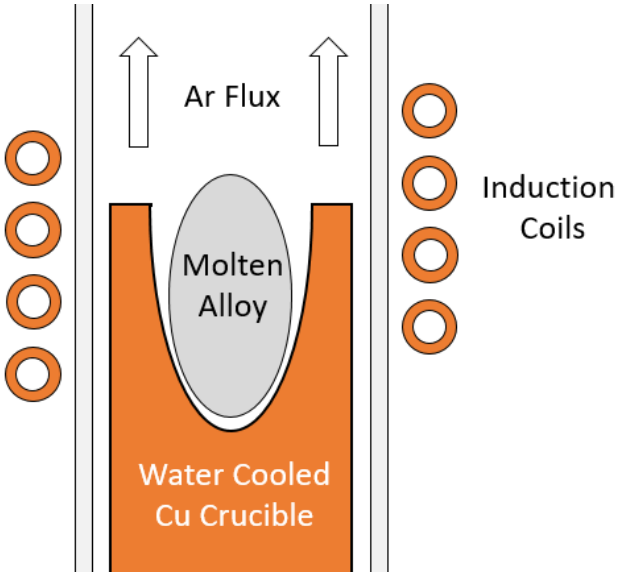

Figure 3.20: Schematic of induction heated cold crucible apparatus.

The Ti-Al-Nb and Ti-Al-Ta alloys were fabricated easily, however the Ti-Ta alloy presented some difficulties. The amount of Ta needed to make an ingot of usable size could not be melted as a bulk in the cold crucible apparatus used. The water cooling was unable to extract heat fast enough from the copper crucible as the Ta approached its melting temperature. The temperature was high enough inside the cooling channels of the crucible to vapourize the water, which decreases the rate of heat extraction. If more power were applied after this occurred the crucible would increase in temperature rapidly, the Ta could potentially alloy with the crucible and render both the apparatus and Ta charge unusable or the crucible could melt allowing water to escape the cooling channels and interact explosively with the molten Ta. As such the Ta had to be dissolved into the molten Ti as a solid. This is difficult as the Ta dissolves slowly. In order to decrease the time required to dissolve the Ta, alloying was conducted using Ta pieces smaller than 1g each, rather than a single solid mass of Ta. Solid Ti was melted with the pieces of Ta mixing into it, allowing the Ta to dissolve in the liquid Ti for 10 minute intervals before solidifying and remelting multiple times. The ingot was then cross-sectioned, polished and investigated by EDX to ensure homogeneity. Particles of Ta remained in the bulk alloy after the first round of alloying melts, however there is significant Ta in the solidified liquid as well. As the amount of Ta in the bulk increases, so too does the melting temperature of the liquid, allowing the melt to get closer to the melting temperature of the pure Ta. Since the Ta was diffusing into the liquid the same sample was again remelted using the same procedure then prepared again for analysis. After the second round of remelting there were no Ta particles seen in the cross section and the average composition was Ti-46Ta, close to the desired Ti-47Ta, as seen in Figure 3.21. The ingot was then remelted a final time to further ensure homogeneity and recombine the cross-sectioned halves.

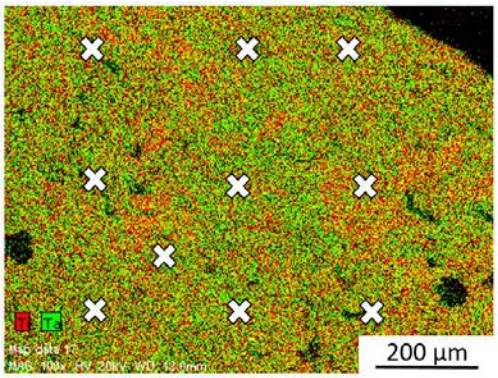

	Comp. (At%)	
Point	Ti	Ta
1	46	54
2	48	52
3	52	48
4	56	44
5	58	42
6	57	43
7	56	44
8	49	51
9	59	41
10	57	43
Mean value:	54	46

Figure 3.21: EDX map and point analysis for successfully alloyed Ti-Ta

3.2.2 Powder Milling

Once bulk alloys had been fabricated it was then necessary to turn them into powders which could be used for inoculation. This was achieved by drilling into the ingots with a 5 mm bit repeatedly to produce chips, or turnings. These turnings were then washed with water and alcohol to remove any contaminants, such as cutting lubricant or oil, which may have been introduced during drilling. SEM images of a sample of these drillings can be seen in Figure 3.22. Once as many holes had been drilled as possible in the ingots they were remelted so further holes could be drilled and the yield of drillings maximized.

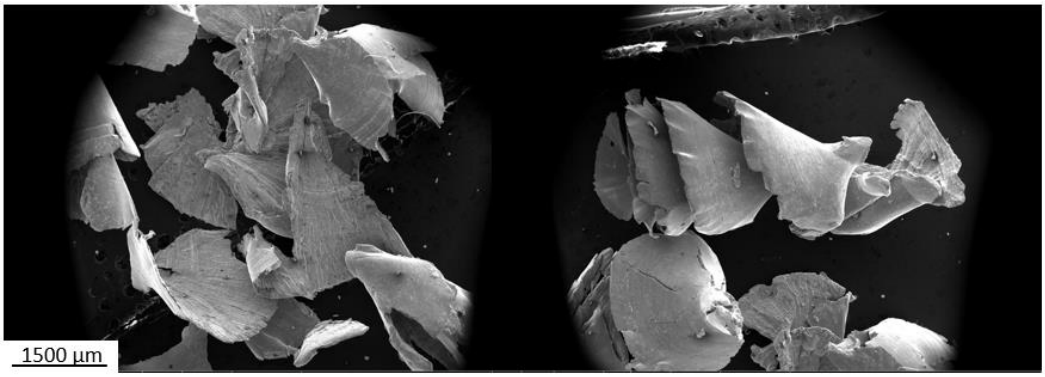

Figure 3.22: SEM SE images of Ti-Ta Drillings

The majority of the drillings obtained were fairly large, in the order of mm which were too large to be implemented in our laboratory apparatus. In order to reduce their size the powders were cryomilled in a Retsch CryoMill. Cryomilling was chosen as the low temperature would embrittle the particles as well as prevent them from sticking or agglomerating. Drillings were added to the milling container along with steel balls, approximately one steel ball was added for every gram of powder. Ten 1g balls and 10g of powder were used unless insufficient powder remained, in which case the number of balls was reduced accordingly. The apparatus automatically ran liquid nitrogen around the milling container to maintain a temperature near -196^{o}C. Milling took place in approximately 10 minute intervals of milling at 25 Hz followed by a cooling cycle where liquid nitrogen was flowed around the container and the frequency was reduced to 5 Hz. A schematic of the apparatus can be seen in Figure 3.23.

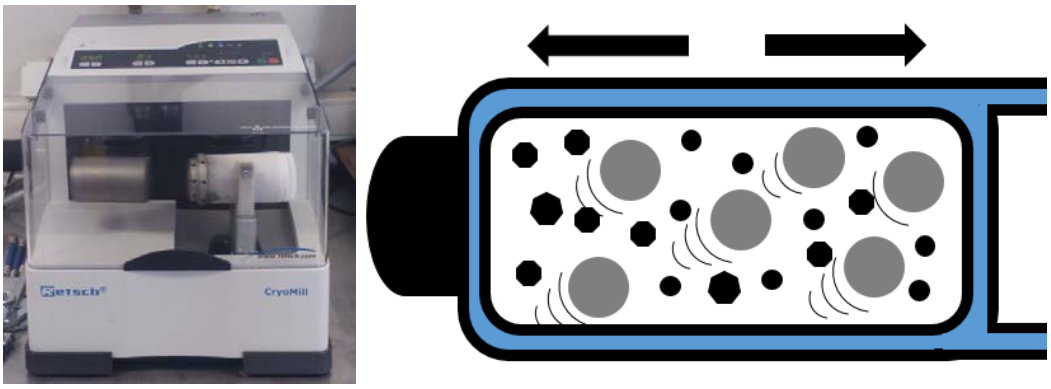

Figure 3.23: Cryomilling apparatus and schematic of milling container showing steel balls (grey), powders (black) and liquid nitrogen (blue)

To obtain particles of different sizes portions of the drillings of each alloy were milled for different lengths of time, ranging from 1.5 to 11 hours. Initially powders were milled in air, however to minimize the potential effects of oxidation the Ti-Ta powders were milled under Ar, and a further sample of Ti-Al-Nb was milled in Ar as well to compare with those milled in air. Additionally a sample of the Ti-Al-Nb powder which had been milled for 3 hours was subjected to a stress relieving heat treatment. The milled powder was heated to 650^{o}C for 2 hours under argon in an electrically heated tube furnace. This was to see the effect of the induced stress from cryomilling on the powder behavior. The heat treated powder should have much less internal stress than the initially milled powder, and may then behave differently in the Ti-Al melt. A summary of the milling conditions is shown in Table 3.2.

Table 3.2: Summary of Powder Cryomilling Conditions

Alloy	Milling Time (hrs)	Atmosphere
Ti-Al-Nb	3, 6, 9, 11	Air
Ti-Al-Ta	3, 6, 9	Air
Ti-Ta	1.5, 3, 6, 9	Ar
Ti-Al-Nb	3	Ar
Ti-Al-Nb	3	Air+HT

3.3 Powder Characterization

Once the powders had been prepared it was necessary to characterize them. The size of the powders was important to know since it is of critical importance for diffusive stability. Additionally, in order to calculate the number of particles added in an inoculation trial the size distribution must be known. In order to determine the size distribution of the powders of the alloys after each milling time two methods were used, image analysis by SEM and differential light spectroscopy (DLS). The microstructure of the particles was also characterized using transmission Kikuchi diffraction (TKD) in a SEM.

3.3.1 Size Characterization

The size of a particle with an irregular shape can be characterized using different definitions of its diameter. Normally these rely on using a characteristic of the particle, such as its surface area, perimeter, average chord length through the particle etc. and using it to find the diameter of a circle with the same characteristic [**178**] e.g. the particle size could be represented by the diameter of a circle with the same perimeter as the irregularly shaped particle. Since a group of particles are rarely of identical size it is useful to characterize the statistical distribution of sizes in the group. This is difficult to do with a single number as the distribution may not be normal and may have a complex shape. The most common way to describe a size distribution with a single number is with the median particle diameter or D50. This represents particle size when the cumulative size distribution is at 50% or 50% of the particles are smaller than it. Similarly the D99 or D15 would be the particle size when the cumulative size distribution is at 99% or 15% or when 99% or 15% of particles are smaller than them. The distributions may also be characterized by their span, which is a measure of how wide or narrow a size distribution is and is not reliant on the distribution being normal, the span of a distribution is defined as [**179**]:

$$Span = (D_{90} - D_{10})/D_{50} \qquad (3.6)$$

The D90 or D10 may be replaced by other equally dispersed values (e.g. D95/D05 or D99/D01) in certain cases depending on outliers in the distributions but D90 and D10 are the most commonly used. Span values which are small indicate a narrow distribution while large span values indicate a wide distribution. Since the span is relative to the D50 it can be easily compared between different distributions.

It is difficult to describe a particle size distribution with only one or two characteristics. The D50 and span are used in particle size analysis more commonly than the average and standard deviation used in other applications. This is because the average and standard deviation are more suited to describing normal distributions, where 99.999% of the population are within four standard deviations of the mean. If the distributions are not normal the average and standard deviation do not describe the distribution as accurately. As the distributions deviate from normal the average and median deviate from one another and the standard deviation becomes less meaningful. Using definitions such as the median (D50) and span instead allow description of distributions which are not normal as well as those which are. The median gives a better idea of the "middle" value of a non-normal distribution while the span encapsulates the relation of the almost the entire spread of the data into a single number. These values are still not perfect descriptors of a distribution but they are much better at dealing with uneven distributions than average and standard deviation.

3.3.1.1 SEM Image Analysis

The first method used to characterize the size of the particles was image analysis by SEM. A sample of powders was placed on conductive tape and inserted into the chamber of the SEM. Images were taken in both secondary electron (SE) and backscattered electron (BSE) mode.

The SE images were less sensitive to brightness/contrast changes, whereas the particles imaged with BSE could change apparent size if the imaging parameters changed, however, features unrelated to the powders, such as the texture of the tape or dust particles, appeared in the SE images but not in the BSE images. In order to mitigate these disadvantages images were captured with both SE and BSE then formed into a single composite image using ImageJ software (used throughout the size analysis). The images were combined with even 50/50 weighting. Once combined the images were cropped to remove image information (scale bars etc.) then enhance local contrast using (CLAHE) software. The image was then binarized and the binarized image was then compared to the BSE image and any regions which appeared and were not powders were erased, e.g. tape bubbles or dust. The particle analysis tool could then be used on the image to measure the areas of the particles. This tool works by finding an edge (colour change in the binarized image) then following the edge until a particle has been enveloped. This enveloped area is then measured and hidden so the next edge can be found. To remove the noise from the analysis a minimum size for the analysis was chosen such that the smallest 1% of particles detected was not the most numerous proportion. The particle areas reported by the analysis were then converted to particle diameters, assuming that the particles were spherical, and the areas reported circular. A diameter reported in this way is known as a projected area diameter (the diameter of a circle with the same 2-D projected area as the particle at a random orientation [**178**]). An example of this procedure is shown in Figure 3.24 for a single field of view of Ti-Al-Nb particles which were cryomilled for 3 hours under Ar. This procedure was repeated for multiple fields of view for each milling time of each alloy.

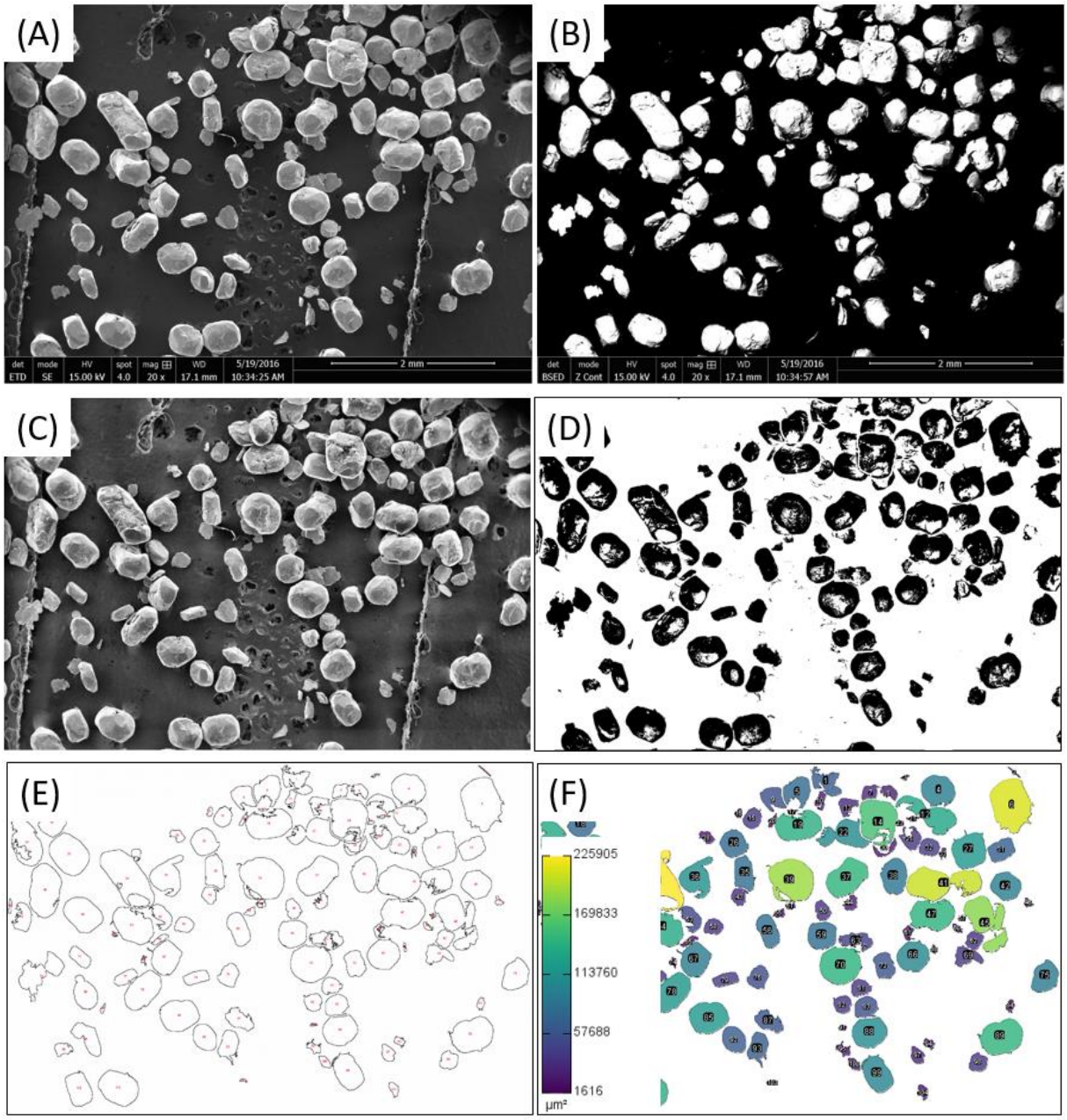

Figure 3.24: Example SEM images and procedure for powder size analysis, from Ti-Al-Nb powder milled for 3 hours under argon, showing (A) SE image (B) BSE image (C) combined and edited image (D) binarized image with erased areas (E) analyzed particles (F) colourized and measured particle areas

3.3.1.2 Diffusive Light Scattering

Size characterization was also carried out by differential laser scattering (DLS) using a Sympatec Helos BF with a He-Ne red laser. DLS works by analyzing how a distribution of particles suspended in a liquid scatter incident light [**180**]. A focused laser is shone through a suspension of particles and water. Different lenses can be used to adjust the laser to analyze particles of different sizes. As the laser travels through the suspension it is scattered by the particles. In general large particles scatter the laser less than small particles, but factors such as the shape and roughness of the particles can also play critical roles [**178**]. In order to avoid

multiple scattering events the suspension must be very dilute so the laser only encounters one particle as it travels through the suspension. A detector is then used to measure the intensity and location of the scattered light. The apparatus and a schematic of the method can be seen in Figure 3.25. The detected scatter pattern is analyzed in a proprietary software package and calculation methods which outputs the particle size distribution histogram as well as critical parameters such as the D99, D50 etc. allowing the calculation of some other parameters such as the span of the distribution. The apparatus used was capable of detecting two different size ranges, 0.25-87.5 µm for fine powders or 2.5-875 µm for coarser particles, depending on the lens used. Using the SEM characterization as a guide, the 2.5-875 µm lens was selected.

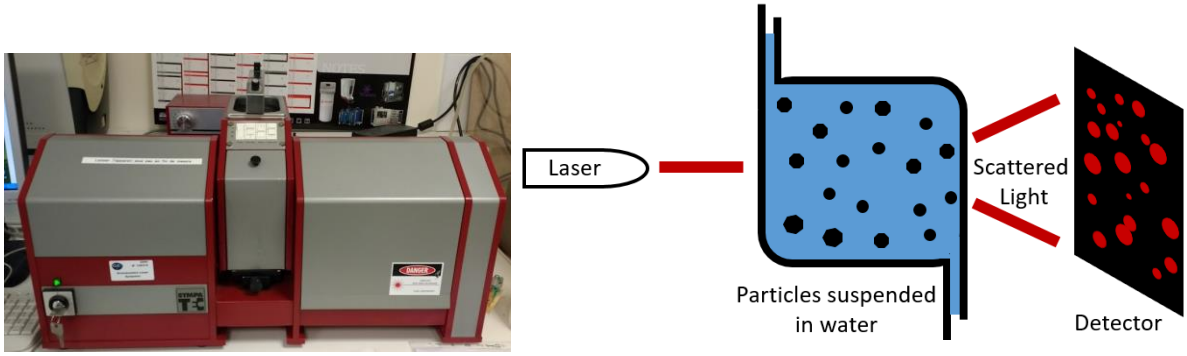

(A) (B)

Figure 3.25: Apparatus (A) and Schematic (B) of DLS setup

In order for a test to be carried out the powders were first placed into a reservoir with demineralized and purified water. The water and powder suspension was pumped into the testing chamber and two successive measurements were taken, each lasting for 10 seconds. Once the first two measurements were taken the powder suspension and water were subjected to 60 seconds of ultrasonic stirring, then two more 10 second measurements were taken. In some cases the distributions measured after ultrasonic stirring were different than those before. If ultrasonic stirring affected the measurement it normally did not change the location of the distribution mode, but decreased its intensity in favour of smaller particles, i.e. the height of the peak of the distribution decreased in favour of smaller particles. In order to best describe the size distributions an average of all four measurements was used. Once the measurements were complete the testing chamber was flushed and rinsed to remove all the particles before the next sample was tested. The drained suspensions were not recoverable, effectively making the size measurements a destructive test, therefore only one sample of each distribution was measured.

3.3.1.4 Particle Size Distribution Summaries

While the DLS and SEM measured size distributions are not directly comparable, since one measures numerical distribution and the other volumetric, it is useful to compare the trends between them to see if any measurements appear erroneous.

3.3.1.4.1 Ti-Al-Nb

A comparison between the DLS and SEM measurements of the Ti-Al-Nb distributions can be seen in Figure 3.26. The DLS volumetric measurements reported larger D50s than the numerical SEM. The increase in D50 DLS reported for the 9 hour milled sample was not correlated with a respective increase by SEM. This indicates the increase was erroneous, since the D50s otherwise follow a similar trend as grinding time increases. The slopes of the decreasing D99 are different between the DLS and SEM, with the SEM measurements decreasing much more than the DLS. After 3 and 6 hours the SEM measured larger D99s than DLS, however after 9 and 11 hours the DLS measured larger D99s. Again the 9 hour sample shows an abnormally large value compared to the other samples measured by DLS.

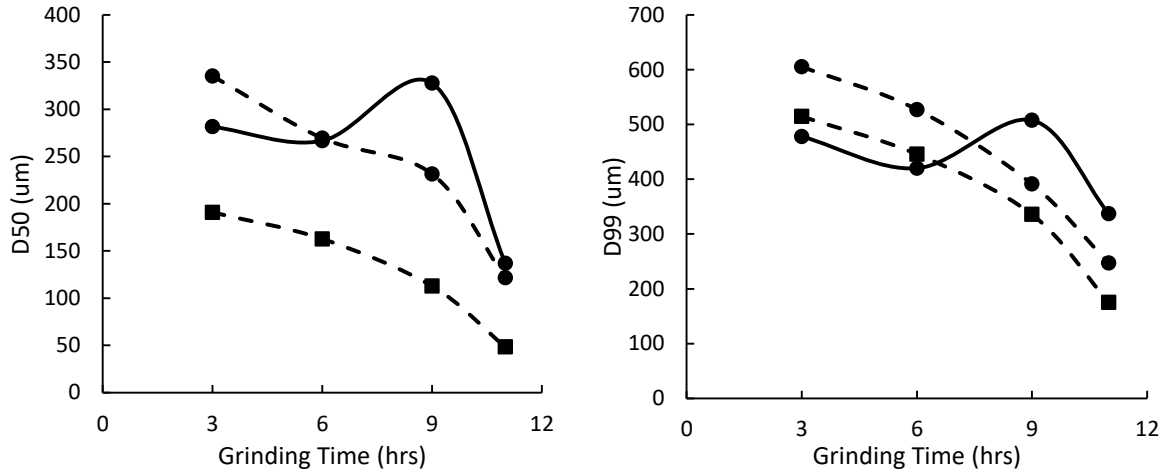

(A) (B)

Figure 3.26: Comparison of SEM (dashed line), DLS (solid line), and numerical (square points), volumetric (circle points) measured D50 (A) and D99 (B) for Ti-Al-Nb particles.

3.3.1.4.2 Ti-Al-Ta

Figure 3.27 shows a comparison of the D50 and D99 measured by SEM and DLS for the Ti-Al-Ta particles. Similar to the Ti-Al-Nb particles the DLS reports larger D50s than the SEM. The decrease in D50 measured by DLS is greater as milling time increases than that measured by SEM, where the 6 hour ground sample had the smallest D50. The difference in D50 is however not very large even when measured by DLS, only 25 μm separates the largest and smallest. Both measure decreases in D99 as milling time increases. The D99s obtained by DLS and SEM are nearly identical for the 6 and 9 hour samples but vary by more than 150 μm for the 3 hour sample. The milling of the Ti-Al-Ta powders can then be inferred to mostly reduce the size of the large particles since the D50s stay relatively constant both numerically (SEM) and volumetrically (DLS) while the D99s decrease. It is interesting that in this case the conversion from numerical to volumetric of the SEM distribution decreases the D50 and D99 moving the values further from the DLS rather than closer as with the TiAlNb particles, possibly due to the small size of the TiAlTa particles.

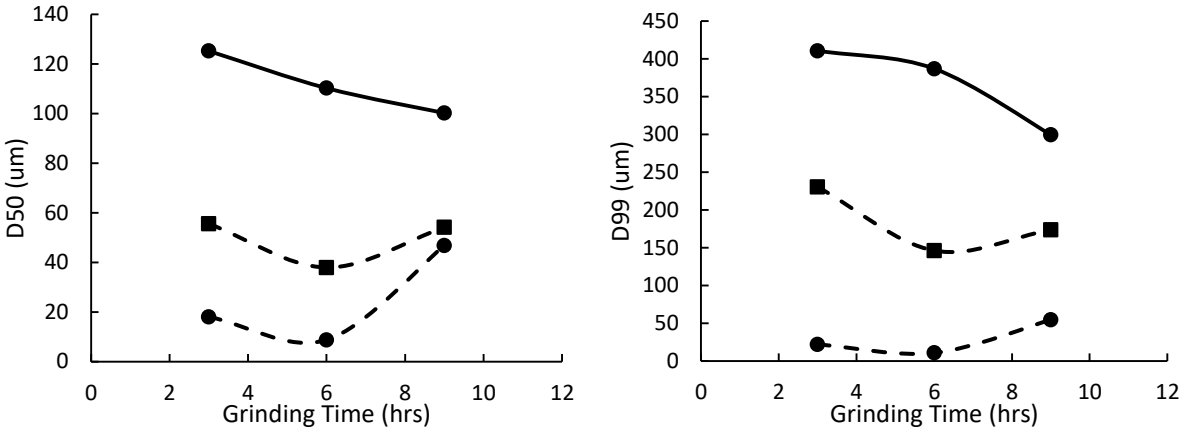

(A) (B)

Figure 3.27: Comparison of SEM (dashed line), DLS (solid line), and numerical (square points), volumetric (circle points) measured D50 (A) and D99 (B) for Ti-Al-Ta particles.

3.3.1.4.3 Ti-Ta

The measured D50 and D99 show roughly the same trends when measured by SEM or DLS for the Ti-Ta particles, as shown in Figure 3.28. The sharpest decrease is from 1.5 hours to 3 hours after which the values decrease more slowly, except in the case of the 9 hour DLS. This unexpected increase could again be due to some form of sampling error or flotation of the particles, especially since the 9 hour Ti-Ta milled particles were the smallest of any of the distributions tested.

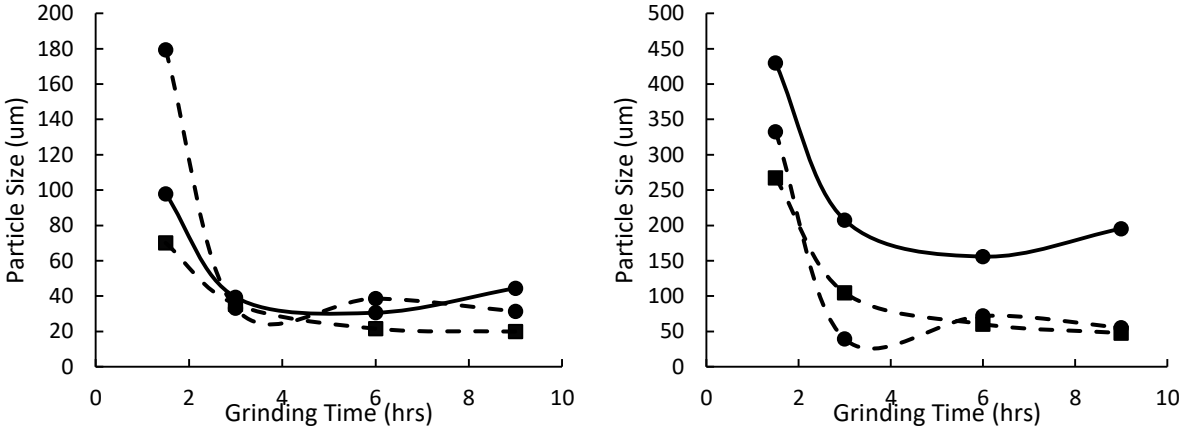

(A) (B)

Figure 3.28: Comparison of SEM (dashed line), DLS (solid line), and numerical (square points), volumetric (circle points) measured D50 (A) and D99 (B) for Ti-Ta particles.

3.3.1.5 Summary

The particles obtained by cryomilling were characterized by their size using both SEM image analysis to obtain a numerical size distribution and DLS to obtain a volumetric size distribution. For a given milling time the Ti-Al-Nb particles were the largest followed by the Ti-Al-Ta then the Ti-Ta particles. The median particle size of the distributions (D50) varied from 233-20 μm

numerically and 339-31 µm volumetrically across all the samples with maximum particles sizes (D99) varying from 775-56 µm numerically and 522-156 µm volumetrically. The DLS and SEM measurements could be used in conjunction with one another to correct any erroneous measurements possibly caused by poor sampling.

3.3.2 Microstructure Characterization

While the size of the particles is of critical importance so is their microstructure. Conventional methods of evaluating the microstructure within the particles, such as EBSD, was difficult due to the high plastic strain imparted by cryomilling. As such, on-axis transmission Kikutchi diffraction was used to obtain high resolution information about the particle microstructure.

3.3.2.1 Transmission Kikutchi Diffraction (TKD)

Transmission Kikutchi diffraction (TKD) is a relatively new method of analyzing sample microstructures by orientation mapping [**181**]. The analysis is similar to conventional EBSD methods but rather than using a bulk sample and relying on backscattered electrons for the analysis TKD uses an electron transparent sample and forward scattered electrons for the analysis. For this reason it is also known as transmission-EBSD [**182**] or transmission-EFSD. In this analysis the TKD setup was of the "on-axis" configuration, which was designed and validated at the LEM3 in Metz, where the scintillator is located in line with the electron beam, resulting in a high intensity diffraction pattern with a spot in the center [**183**]. A schematic of the TKD setup and sample Kikutchi pattern are shown in Figure 3.29. This method allows for faster pattern acquisition than an off-axis setup and is particularly well suited for characterization of plastically deformed materials [**184**]. In addition to the detector for the Kikutchi bands there are also three diodes for forward scattered electron detection (FSD). Each diode produces a single colour, when an image is formed from all three detectors it is extremely sensitive to changes in orientation but the information is qualitative, there is not a direct relation between a colour and an orientation.

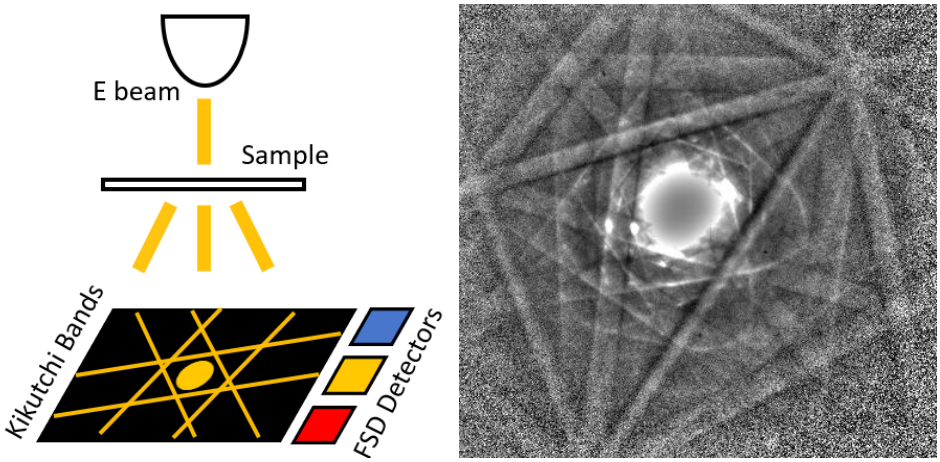

(A) (B)

Figure 3.29: Schematic of TKD setup (A) and sample Kikutchi pattern for β-Ti obtained using on-axis TKD (B)

Sample preparation for TKD is important as the sample must be electron transparent. Such samples were obtained by milling with Focused Ion Beam (FIB) using either a dual beam Zeiss Auriga 40 (at the LEM3 in Metz) or Helios Nanolab 600i (at IJL in Nancy). The procedure for this is shown in Figure 3.30, first a group of particles were placed in the FIB chamber, a suitable particle was chosen for milling then a protective mask was placed on the particle. The mask protected a portion of the particle so a thin sheet could be milled out from particle. Once the mask was in place the particle was bombarded with high energy Ga ions (30kV) which eroded away a section on either side of the mask. The sample could then be removed from the particle and further thinned by soft ion bombardment using lower accelerating voltage (2-5kV) The final samples were thinner than 60 nm. These samples could then be used for TKD analysis.

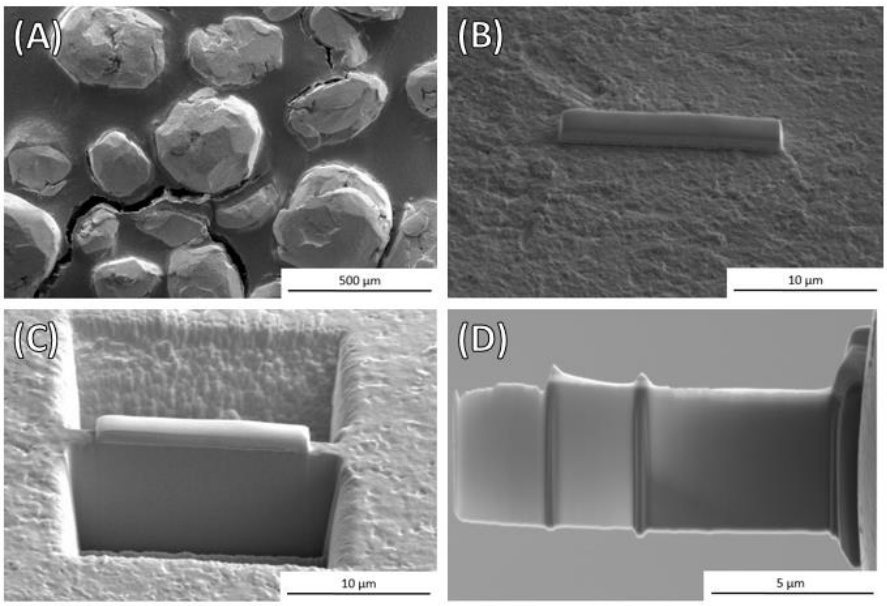

Figure 3.30: Procedure for obtaining TKD samples. (A) Selection of an appropriate particle (B) masking section of particle (C) milling of sample (D) final sample

3.3.2.2 TKD Analysis

Once the samples had be prepared TKD analysis could be conducted. TKD was performed using a Zeiss Supra 40 at 30keV, a working distance of 5-7mm, and a sample to detector distance of ~20mm. Electron detection was done using a Bruker e-flash 1000 camera or Bruker OPTIMUS detector head. Pattern acquisition and indexation was performed using Bruker espirit 2.1 software with a minimum of 5 bands for indexation. The maps obtained were 160x120 pixels. The 3 hour cryo-milled Ti-Al-Nb analysis is shown here to demonstrate the methodology. Figure 3.31 shows the orientation map and FSD image obtained for the 3 hour cryo-milled Ti-Al-Nb powder. Analysis of the orientation maps were conducted using the free software package ATOM developed at the LEM3 in Metz [**185**]. Here the chosen colour code is IPFX, this means each coloured pixel of the orientation map corresponds to a certain orientation of β-Ti where the sample direction X is parallel to some crystal direction represented by a specific colour in the standard triangle. The sample was determined to contain 100% β-Ti. Black pixels represents areas where the Kikuchi patterns could not be indexed. The

indexation rate for the map was 73%, noise reduction performed on the map improved this rate to 85%, performed by extrapolating orientations from neighboring pixels and removing single pixels with errant orientations. The unindexed regions appear mostly along grain boundaries, which makes sense because 2 patterns corresponding to each grain are often obtained in these regions making them more difficult to index. The FSD image shows similar structure to the orientation map, with what appear to be long pancaked grains. The colour changes across the grains in the FSD image indicate changes of orientation within the grain. In some cases these colour changes are more immediate indicating subgrain boundaries (low misorientation) in others they are more gradual indicating a smoother transition of the orientation of the lattice through the grain.

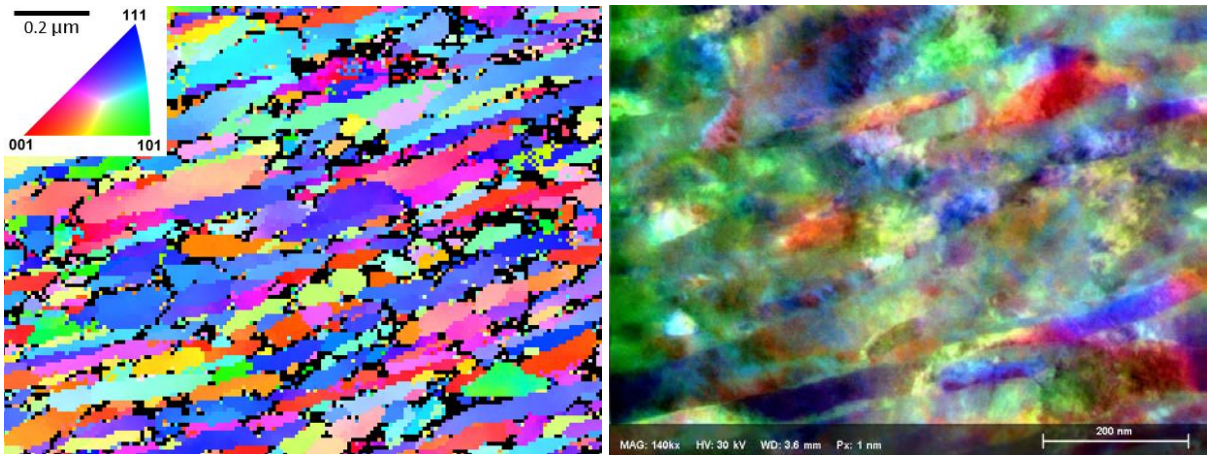

(A) (B)

Figure 3.31: 3 hour cryomilled Ti-Al-Nb (A) TKD orientation map and (B) FSD image

The orientation map can be used to map the location of boundaries between different lattice orientations, which can then be used to map the grains, as shown in Figure 3.32. The high angle grain boundaries (HAGB: misorientation angle greater than 15° in yellow) appear elongated in a direction corresponding to the pancaked shape seen by FSD. The low angle grain boundaries LAGB (2^o<green<5^o, 5^o<red<10^o, 10^o<blue<15^o) appear less dependent on this pancaked shape. There are a significant number of these LAGB and they are of a much shorter length than the HAGB and they delineate subgrains inside the elongated grains. The HAGB make up roughly 82% of the boundaries, 10% are LAGB between 5 and 15 degrees and the remaining 8% are less than 5 degrees. The LAGB appear randomly oriented while as the disorientation grows they grow longer and more likely to cut across the width of the pancaked grains and subdivide them. The pancaked grain shape becomes more obvious when the boundaries are used to map the grains as shown in Figure 3.32B where each colour represents an individual grain. There appear to be few equiaxed grains and most grains appear elongated along the same direction as previously noted.

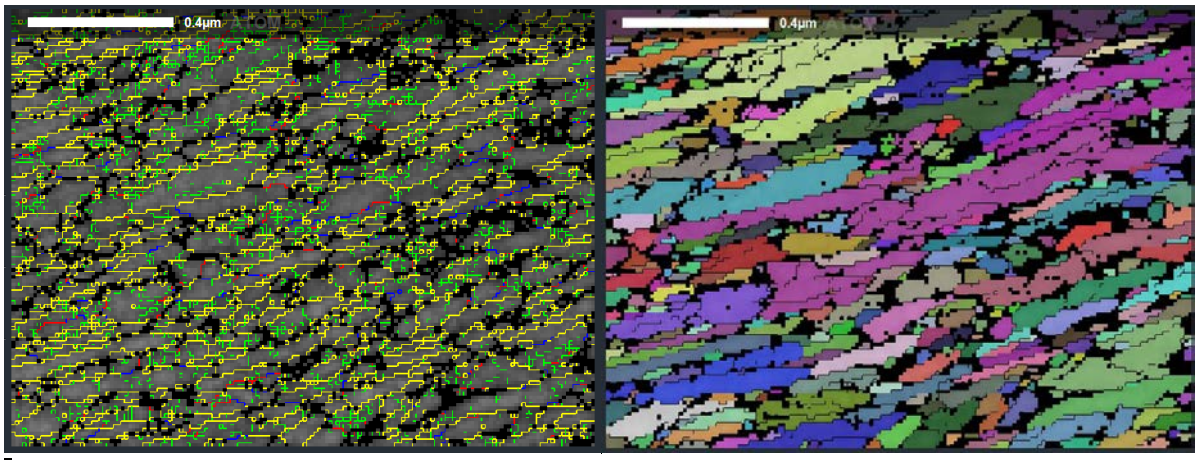

(A) (B)

Figure 3.32: 3 hour cryomilled Ti-Al-Nb (A) Boundary map showing misorientations >15º as yellow and <15º as green, red or blue and (B) Grain map

In addition to the qualitative attributes obtained from the orientation map the software can also use the map to provide detailed statistics on the grain size and shape, the distributions for both of which can be seen in Figure 3.33. This is done treating only HAGB (>15º disorientations) as grain boundaries. The average grain size was found to be 52 nm with a median size of only 38 nm. The shape of the grains can also be quantified by the ellipicty of the grains, the ratio of the difference in perpendicular radii, defined here as E=1-(b/a) where b and a are perpendicular radii [**185**]. For the 3 hour cryomilled Ti-Al-Nb the ellipicty of the grains was 0.58 and the median 0.6, a fully equiaxed structure would have average and median ellipicities near 0.

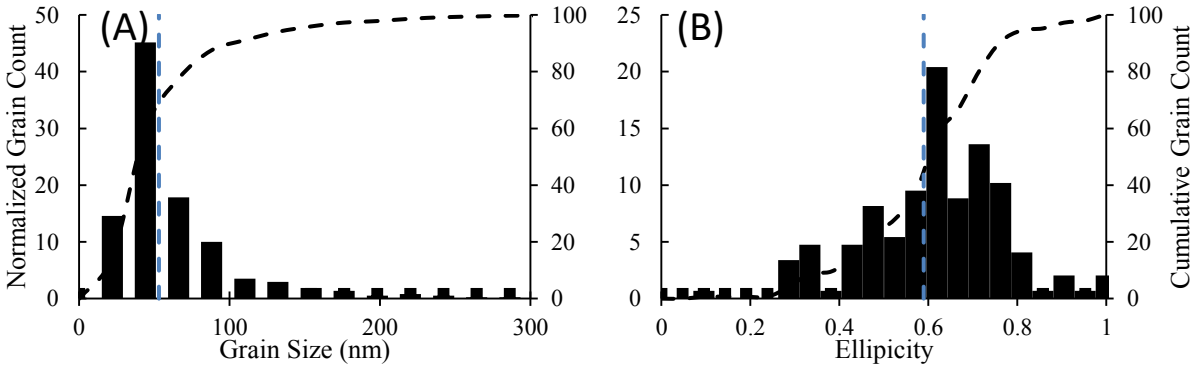

Figure 3.33: 3 hour cryomilled Ti-Al-Nb (A) grain size and (B) grain shape (averages indicated)

3.3.3 Effects on Milling

Many factors are affected by and affect the milling process. This section looks at the effects of milling on microstructure, the effect of alloy composition on as-milled particle size and the effect of heat treatment on particle microstructure.

3.3.3.1 Microstructure Effects

In order to investigate how the microstructure of the particles evolved with milling time two particles of Ti-Al-Nb were analyzed by TKD, a 3 hour cryomilled particle as shown in Section 3.3.2, and a 9 hour cryomilled particle. The orientation map and a FSD image of the 9 hour milled particle can be seen in Figure 3.34. The map had an indexation rate of 87% before noise reduction and 93% using the same noise reduction parameters as used with the 3 hour particle. Once again the particle was found to be 100% β-Ti. There are fewer long pancaked grains in either the FSD image or orientation map, however, in the orientation map the previous preferential direction of the long pancaked grains is still evident but with shorter length pancakes. There are no rainbow coloured long pancaked grains in the FSD image for the 9 hour particle and fewer grains with slight abrupt colour changes or gradual colour shifts, indicating a reduced presence of subgrains or orientation change across grains.

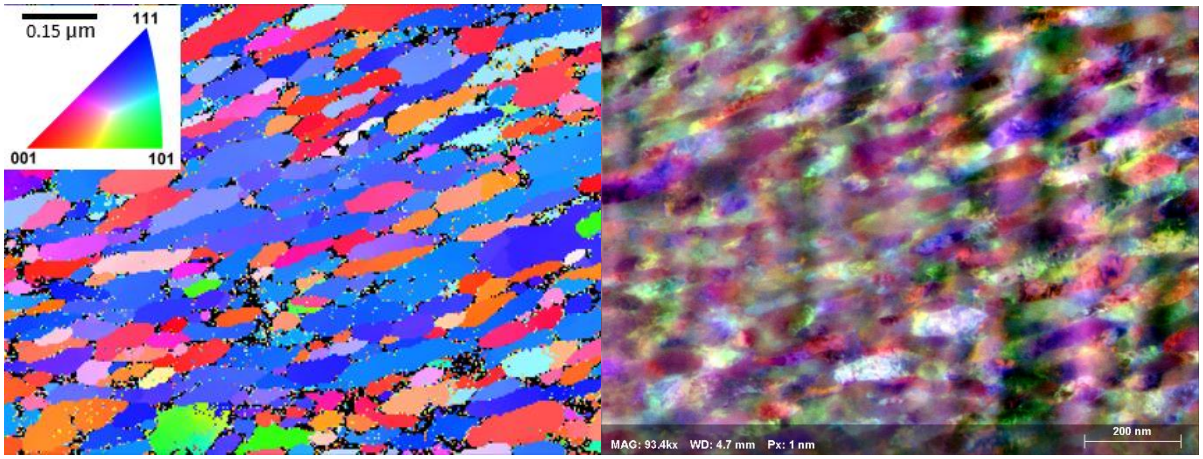

(A) (B)

Figure 3.34: 9 hour cryomilled Ti-Al-Nb (A) TKD orientation map and (B) FSD image

As with the 3 hour particle, the orientation map can be used to find the orientation boundaries and grains, shown for the 9 hour particle in Figure 3.35. There appear to be fewer boundaries found in the 9 hour particle than the 3 hour particle with the sharpest decrease being in low angle boundaries (red, blue, green). This is likely due to the extreme plastic deformation the particle has undergone, where induced stress on the particle results in sub sectioning of the original grains [**184**]. The HAGB now account for 97% of the boundaries with 2% LAGB between 5 and 15 degrees and only 1% below 5 degrees. This sub sectioning is apparent in the grain map shown in Figure 3.35B which shows many grains elongated in the same direction as the 3 hour particle but are much shorter in the elongated direction.

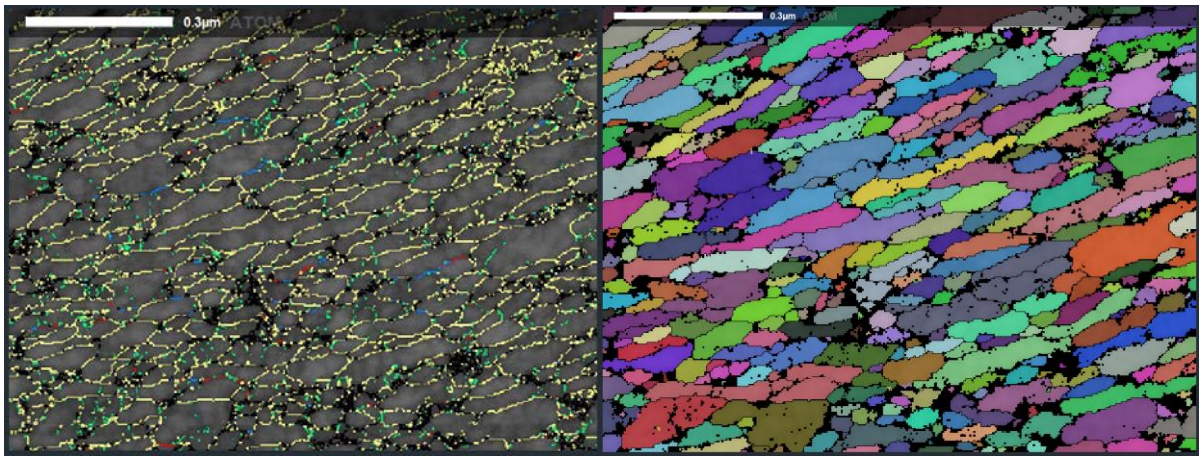

(A) (B)

Figure 3.35: 9 hour cryomilled Ti-Al-Nb (A) Boundary map showing misorientations >15º as yellow and <15º as green, red or blue and (B) Grain map

Quantitative analysis of the 9 hour milled particle grain map gives distributions as shown in Figure 3.36 and an average and median grain size of 43 and 34 nm respectively, only slightly smaller than that of the 3 hour particle (53 and 38 nm). The average and median ellipicity for the 9 hour milled grains was found to be 0.63 and 0.54 relatively close to the values found for the 3 hour milled grains ~0.6. The span of the shape distributions was 0.62 for the 3 hour particle and 0.78 for the 9 hour, meaning that the 9 hour particle had a wider distribution of grain shapes than the 3 hour. The minimum (closest to equiaxed) ellipicity was 0.08 for the 9 hour and 0.28 for the 3 hour, the maximum ellipisicies were 0.89 and 1 respectively. An ellipiscity of 1 indicates that one radii is so much longer than the other that their ratio approaches 0. The maximum and D90 grain sizes are also reduced in the 9 hour sample compared to the 3 hour, from ~300 nm to ~180nm and from 100 nm to 90 nm respectively. The presence of such large grains in the 3 hour sample may indicate that a larger map is necessary to evaluate its grain size completely.

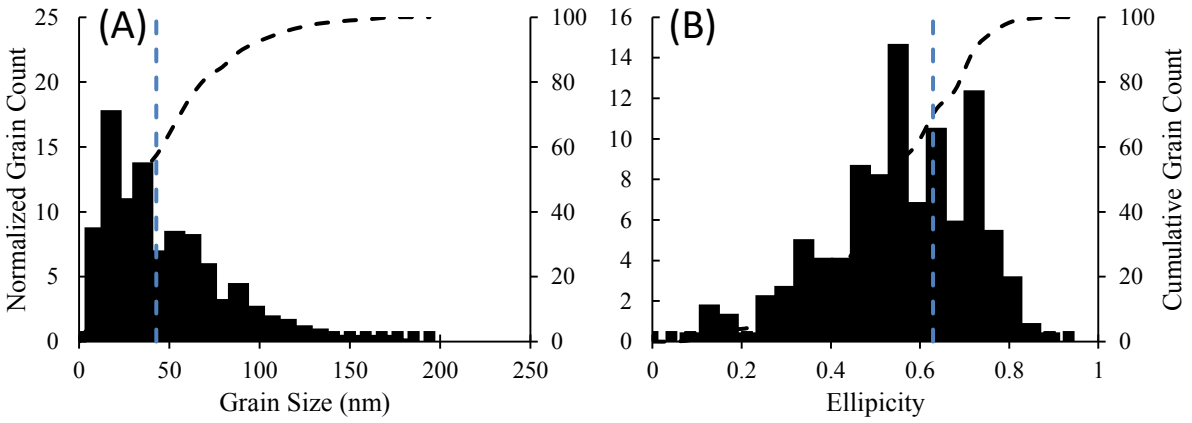

Figure 3.36: 9 hour cryomilled Ti-Al-Nb (A) grain size and (B) grain shape (averages indicated)

The particle microstructures show evidence of the onset of grain refinement due to plastic deformation [**184**]. Both particles investigated, from the 9 hour and 3 hour distributions, had

extremely small grain sizes on the nano scale. Increased milling time was seen to begin the process of sub sectioning long pancaked grains into more equiaxed structures. The median grain size remained similar (~35 nm) between 3 and 9 hours of milling. Qualitatively the number of subgrain boundaries was seen to decrease as milling time increased and the median shape changed from an ellipicity of 0.60 to 0.54, a slight tendency towards equiaxed grains

3.3.3.2 Alloy Effects

While each inoculant alloy was produced and processed in the same manner their resultant size distributions are different. Numerically, Ti-Al-Nb particles were the largest at a given grinding time, followed by Ti-Al-Ta then Ti-Ta. The spans of the distributions varied from 1.1 to 2.1. The particles were all less than 1mm in diameter and the smallest on the order of a few microns. A summary of these characteristics is presented in Figure 3.37. The spans were lowest for the Ti-Ta particles, followed by the Ti-Al-Nb then Ti-Al-Ta at a given processing time.

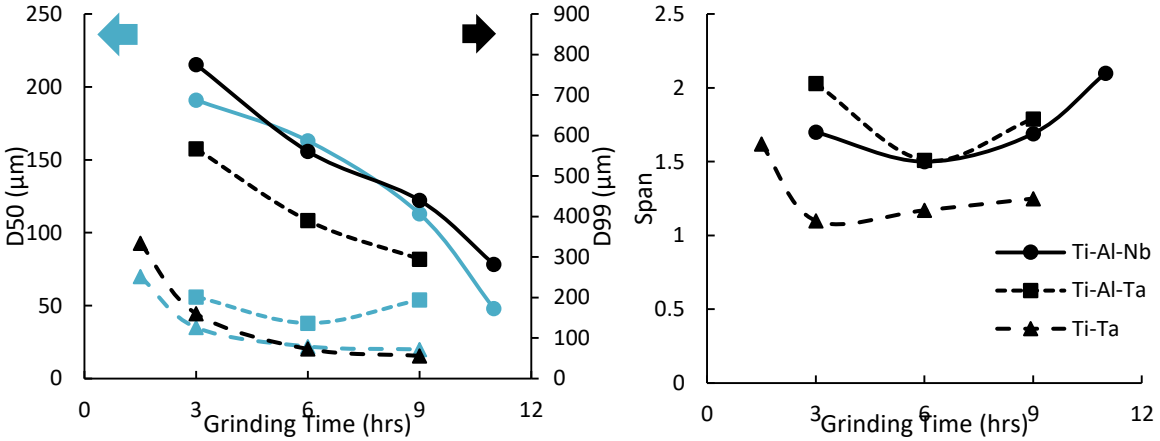

Figure 3.37: All alloy SEM particle distribution characteristics: (A) D50, D99 and (B) distribution span.

The size of each distribution of particles was evaluated volumetrically by DLS. Ti-Al-Nb particles were found to be the largest, followed by Ti-Al-Ta then Ti-Ta. The particles detected ranged from an imposed minimum of 2.5 µm, the limit of the apparatus in the configuration used, to slightly greater than 500 µm (apparatus limited to 875 µm). The results obtained showed a general trend of decreasing particle size with increasing grinding time however some distributions did not follow this trend. This was attributed to measurement issues related to the flotation of particles, evidenced by measurement differences before and after ultrasonic stirring, or a sampling problem since only a tiny fraction of the particles ground could be measured. The spans of the distributions were greatest for the smallest particles (Ti-Ta) and smallest for the largest (Ti-Al-Nb). A summary of these characteristics can be seen in Figure 3.38.

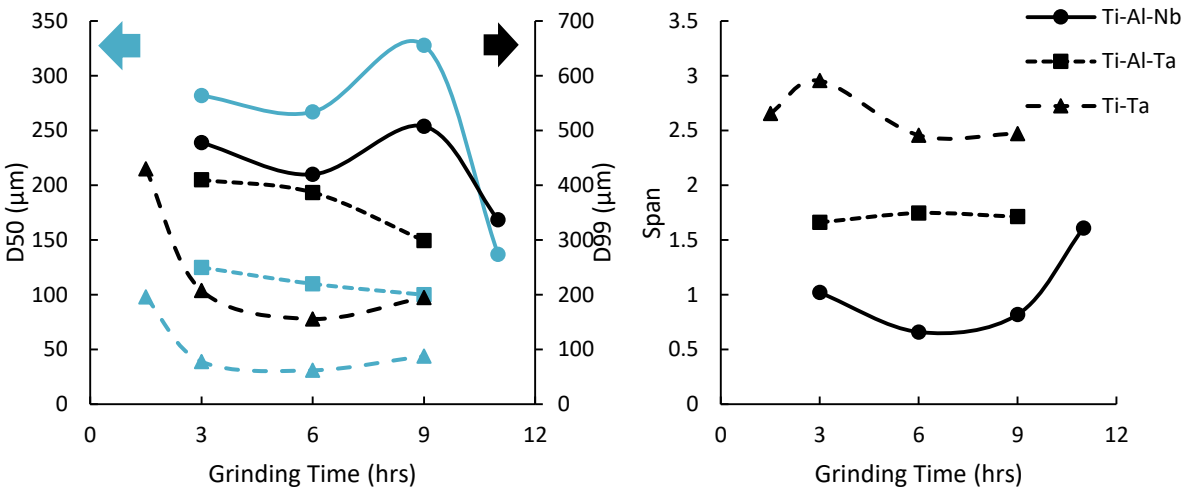

(A) (B)

Figure 3.38: All alloy DLS particle distribution characteristics: (A) D50, D99 and (B) distribution span.

3.3.3.3 Atmosphere Effects

The effect of the milling atmosphere was investigated by comparing the size distributions obtained after 3 hours of milling in air and argon. The measured SEM and DLS distributions for these cases are shown in Figure 3.39. The sample milled under Ar has a larger D50 both numerically (233 vs 191 µm) and volumetrically (339 vs 282 µm). However the D99 is larger for the Ar milled sample is larger numerically (522 vs 478 µm) but not volumetrically (607 vs 775 µm). It is possible that the presence of oxygen in the sample milled under air can embrittle the particles slightly resulting in smaller particle sizes but this effect is not definitive. Further comparisons would be required with longer milling times in order to be more sure of this effect.

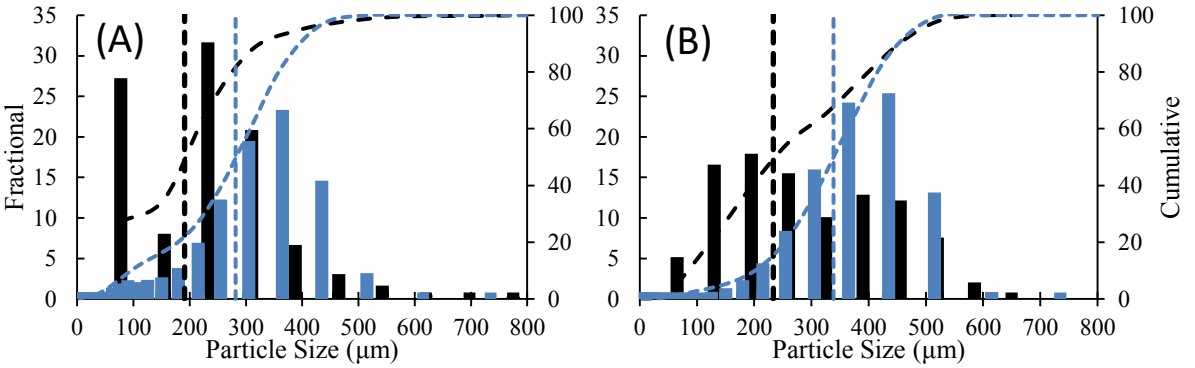

Figure 3.39: Numerical (black) and volumetric (blue) size distributions for Ti-Al-Nb alloy milled for 3 hours (A) under air and (B) under Ar.

3.3.3.4 Heat treatment Effect

The effect of the heat treatment on the sample microstructure was also evaluated by TKD. A sample of a 3 hour heat treated Ti-Al-Nb particle was produced by FIB and analyzed by TKD. The orientation map and FSD image obtained can be seen in Figure 3.40. The map was indexed

at a rate of 89%, and improved to 95% after noise reduction. The orientation map and FSD image look more similar to those obtained from the 9 hour milled particle than the 3 hour milled. There no longer appears to be a preferential elongation direction as seen in either other TKD sample. The grains in the FSD image appear to nearly homogenous in colour indicating few subgrains or orientation gradients.

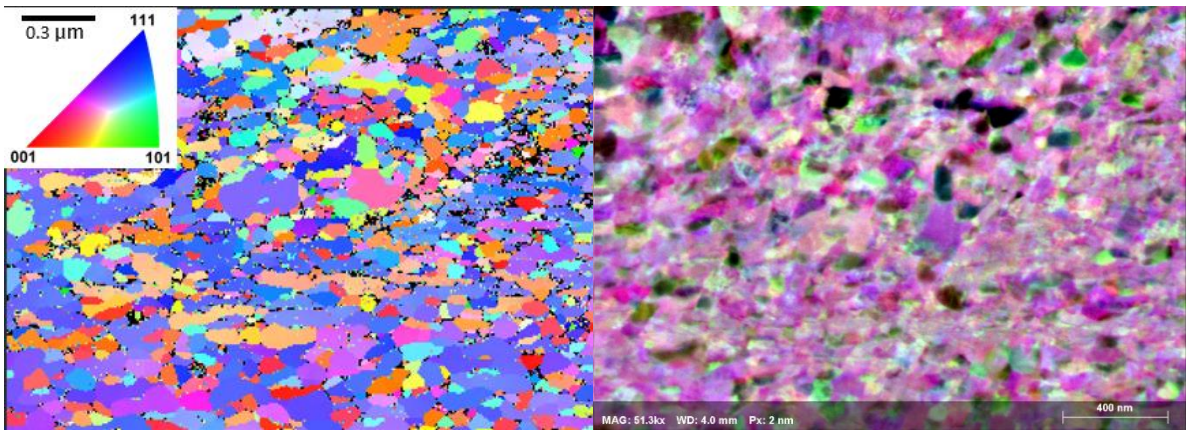

(A) (B)

Figure 3.40: 3 hour cryomilled and heat treated Ti-Al-Nb (A) TKD orientation map and (B) FSD image

In contrast to the purely milled samples the heat treated sample was not found to consist purely of β-Ti. A significant portion of the β-Ti was found to have transformed to α-Ti during the heat treatment. A phase map of the sample is shown in Figure 3.41. The α-Ti appears to be globular shaped and to have nucleated on the grain boundaries of the β-Ti grains. The phase fractions found by TKD were 27% α-Ti and 73% β-Ti. The presence of α-Ti in the particles may significantly affect their ability as isomorphic inoculants as if any α-Ti is retained at high temperature those regions will be unable to freely grow in the same manner as β-Ti.

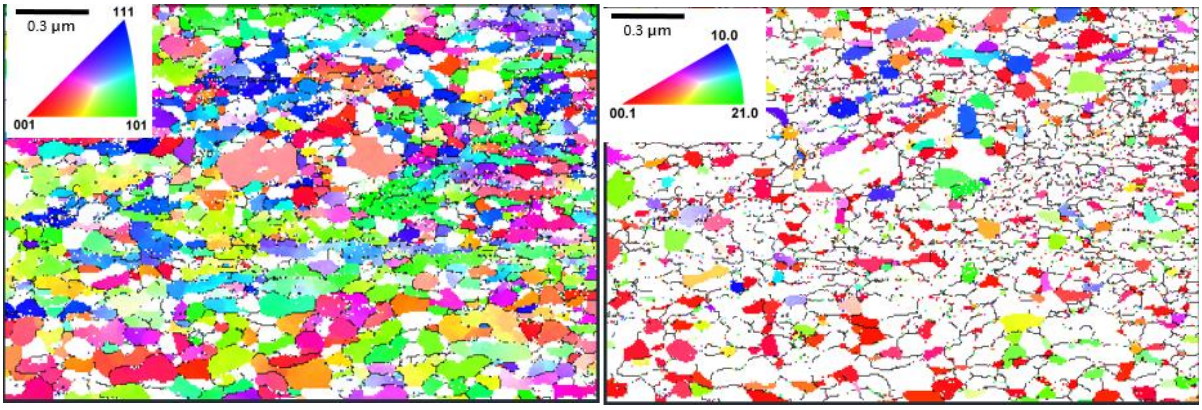

Figure 3.41: TKD orientation maps of (A) β-Ti and (B) α-Ti for 3 hour Cryomilled then heat treated powder

The boundaries and grains can be found for both phases as shown in Figure 3.42. There are a significant number of boundaries >15º, HAGB account for 90% of the boundaries, LAGB from 5 to 15 degrees 6% of the boundaries and 4% <5º. There does not appear to be any remaining

evidence of the pancaked structure found before heat treatment. There does not appear to be a discernable morphological difference between the two phases in either map and they appear indistinguishable from one another.

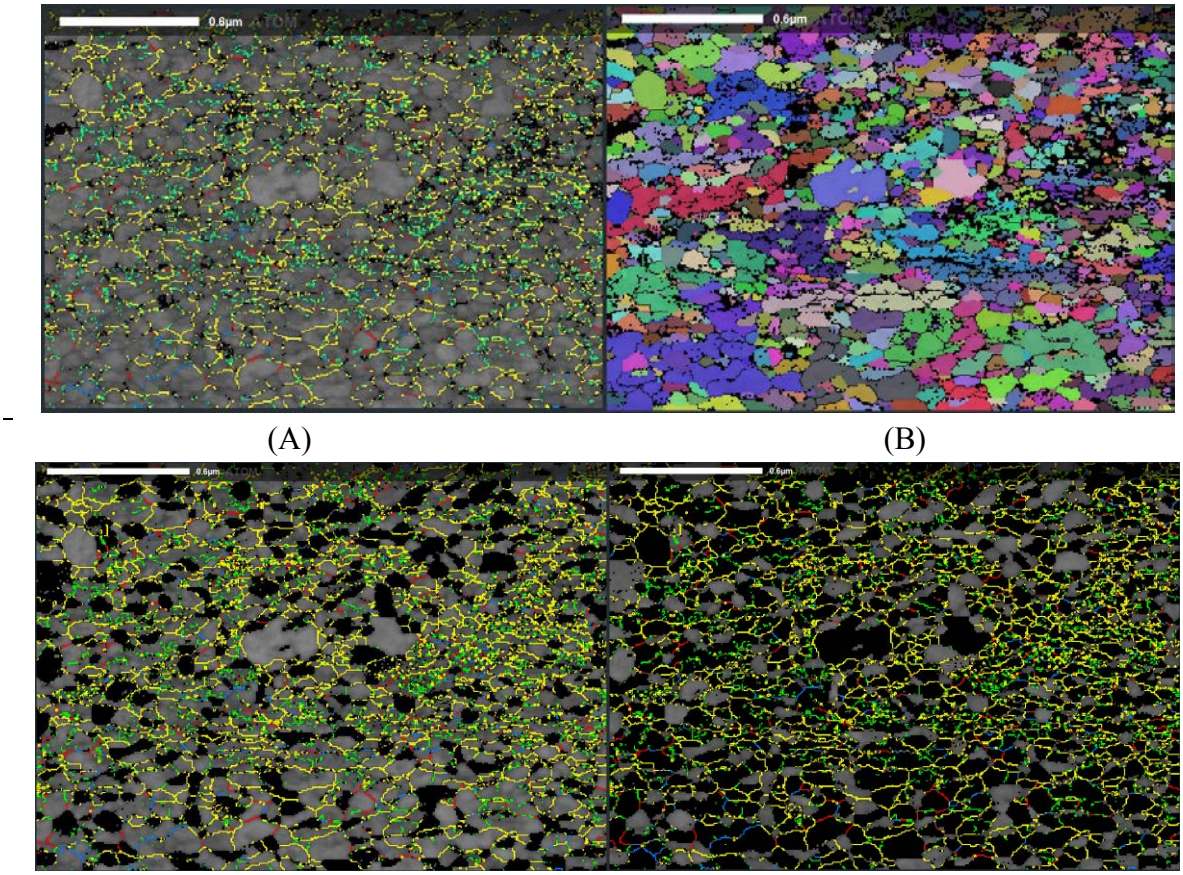

(A) (B)

(C) (D)

Figure 3.42: 3 hour cryomilled + heat treated Ti-Al-Nb (A) Boundary map showing misorientations >15° as yellow and <15° as green, red or blue and (B) Grain map (C) boundary map showing α-Ti as black and (D) boundary map showing β-Ti as black

This similarity in size continues to quantitative analysis as both phases have similar median grain sizes (35 nm for β and 31 nm for α) which are both very close to the median β grain size before heat treating (38 nm). The size and shape distributions for both phases can be seen in Figure 3.43. The median grain shape is also similar between the two phases, 0.47 for β and 0.50 for α. The shape distribution also is much more even than that of the 3 hour particle, with much more grains approaching an ellipicity of 0. Since the size and shape of the grains is similar between the two phases it is likely that both are formed by recrystallization of the highly deformed β grains concurrently.

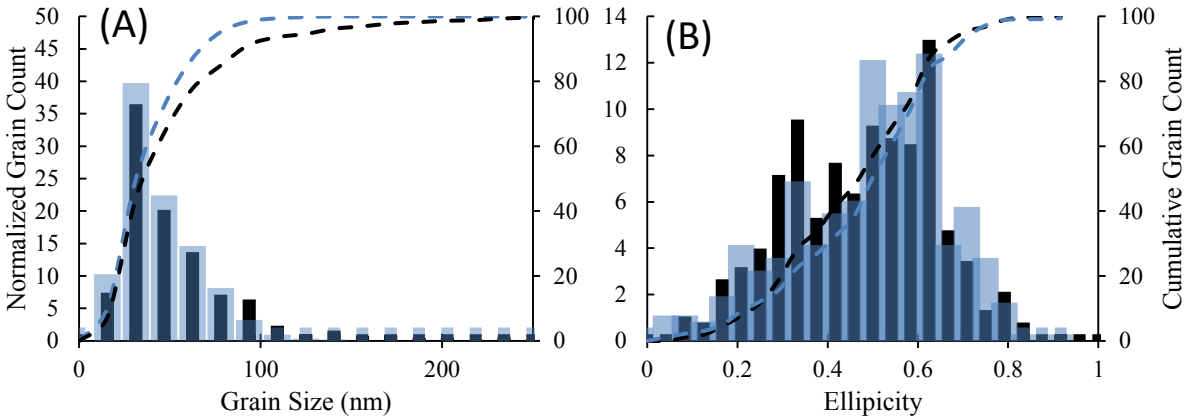

Figure 3.43: 3 hour cryomilled + heat treated Ti-Al-Nb (A) grain size and (B) grain shape for both β (black) and α (blue)

Heat treatment of the 3 hour cryomilled particles resulted in significant changes to the microstructure. While the median grain size did not change significantly, the original deformed pancake structure of β was erased and a more equiaxed two phase α/β structure formed. The size and shape distributions of the two phases were very similar with near equal median grain sizes and ellipicities, indicating their formation and growth were concurrent.

3.4 Summary

Three alloys were selected for isomorphic inoculation of a Ti-46Al base alloy. All three alloys were selected to have good lattice matching with the bulk, increased stability in the melt, and be easily produced. The first two alloys, Ti-10Al-25Nb and Ti-25Al-10Ta, were selected while prioritizing maximum lattice matching while the third, Ti-47Ta, was selected prioritizing maximum stability in the melt. Each alloy was fabricated in an induction heated cold crucible apparatus as a bulk ingot then drilled and cryomilled for different times from 1.5 to 11 hours to form particles suitable for inoculation trials.

Once suitable particles had been fabricated they were characterized by both image analysis of SEM images and DLS. Each method finds the size distribution produced, however, image analysis provides numerical distributions while DLS provides volumetric. Critical size distribution characteristics for each alloy and milling time can be seen in Table 3.3. Additionally the microstructure of three Ti-Al-Nb particles were characterized by TKD. The microstructure was found to be highly pancaked β-Ti after three hours of milling, changing to less pancaked after 9 hours as the pancaked grains subdivided. The heat treatment was found to erase the pancaked structure and replace it with a more equiaxed two phase α/β structure. In all cases the grain size was found to be incredibly small with median sizes less than 50 nm.

Table 3.3: Particle Size Summary

	Distribution D50 (μm)										
	SEM					DLS					
Alloy	1.5	3	6	9	11	1.5	3	6	9	11	Atmosphere
Ti-Al-Nb	-	191	163	113	48	-	282	267	205*	137	Air
Ti-Al-Ta	-	56	38	20*	-	-	125	110	100	-	Air
Ti-Ta	70	35	22	20	-	98	39	31	20*	-	Ar
Ti-Al-Nb	-	233	-	-	-	-	339	-	-	-	Ar
	Distribution D99 (μm)										
	SEM					DLS					
Alloy	1.5	3	6	9	11	1.5	3	6	9	11	Atmosphere
Ti-Al-Nb	-	775	561	440	282	-	478	420	370*	337	Air
Ti-Al-Ta	-	567	390	267*	-	-	410	387	299	-	Air
Ti-Ta	334	160	73	56	-	430	208	156	108*	-	Ar
Ti-Al-Nb	-	607	-	-	-	-	522	-	-	-	Ar
	Distribution Span										
	SEM					DLS					
Alloy	1.5	3	6	9	11	1.5	3	6	9	11	Atmosphere
Ti-Al-Nb	-	1.7	1.5	1.69	2.1	-	1.02	0.66	0.82	1.61	Air
Ti-Al-Ta	-	2.03	1.51	1.79	-	-	1.66	1.75	1.71	-	Air
Ti-Ta	1.62	1.1	1.17	1.25	-	2.66	2.96	2.46	2.47	-	Ar
Ti-Al-Nb	-	1.34	-	-	-	-	0.77	-	-	-	Ar

*Calculated expected values

Chapter 4 Isomorphic Self-Inoculation Casting Trials

Once suitable inoculant powders had been produced from the three alloy systems, Ti-Al-Nb, Ti-Al-Ta and Ti-Ta, they could be implemented to test the grain refinement ability of isomorphic self-inoculation. Different size distributions were tested from each alloy under the same conditions to compare their effects on grain size and morphology. The area fraction of equiaxed zone and equiaxed grain sized were measured for each trial and compared to ingots produced without inoculation.

4.1 Inoculation Procedure

The same procedure was used repeatedly to test the grain refinement ability of each size distribution of particles of the proposed alloys. Inoculation pellets were fabricated from commercially pure Al and an inoculant powder. Ingots were alloyed from commercially pure base metals in an induction heated cold crucible then the inoculation trials were conducted in the same apparatus.

4.1.1 Inoculant Preparation

In order to test the ability of the proposed alloys as isomorphic self-inoculants the particles needed a delivery system to be added to the liquid melt in a controlled manner. To facilitate this pellets were used which could be dropped into the liquid melt. Each pellet contained 1 g of inoculant powder mixed thoroughly with 1 g of fine pure (>99%) synthesis grade Al powder with a mean particle size of ~27 μm. The Al powder was added to act as a binder so the pellets would retain their shape, the Al being much more ductile than the inoculant particles. This mixture was then placed into a piston chamber as shown in Figure 4.1 and compressed at 275 MPa with a hydraulic press until a solid pellet formed.

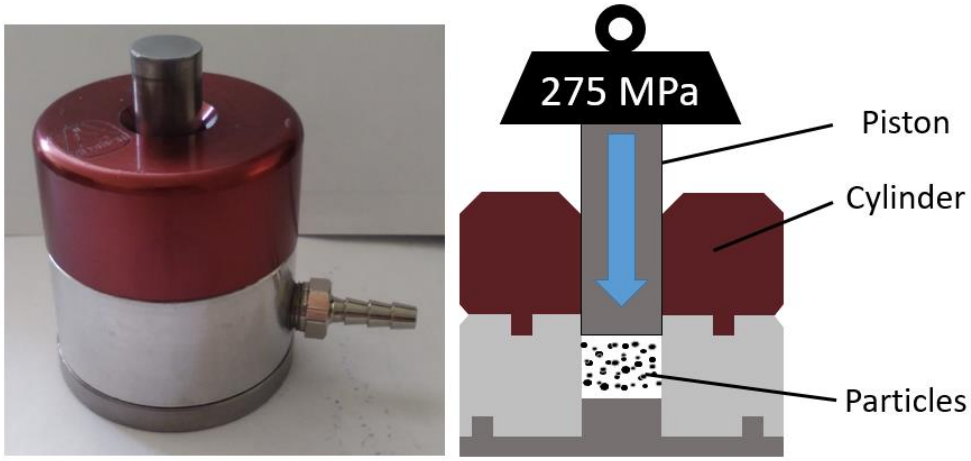

Figure 4.1: Image and schematic of pellet fabrication press

The press formed pucks which were 13mm in diameter and approximately 5mm thick. The exact thickness depended on the compaction of the pellets, which varied from trial to trial. The

compaction level could not be easily monitored with the press used, and sufficient compaction was needed such that the pellets retained their shape. In each case there was some powder loss, not all the powder added to the cylinder was compacted into the pellet, some powder was lost during processing. To account for this an excess of inoculant/Al mix was used, however these losses were not constant and resulted in slight variations in the total mass of each pellet.

4.1.2 Number of Inoculant Particles

It was also important to know the number of inoculant particles added in each inoculation trials. Since the mass of the inoculant particles added was measured, it could be used along with the size distributions obtained in Chapter 3 to calculate the number of particles added. The procedure for this is outlined below for the 3 hour milled Ti-Al-Nb particles. In order to obtain the number of particles in a defined mass it is necessary to convert the size distribution between volumetric and numerically defined or vice versa. This was done with two critical assumptions, first that the particles were spherical so their volumes could be calculated easily, and second that all the particles in each size range had a diameter exactly the average of the maximum and minimum values of the range. The conversion for both SEM and DLS obtained distributions is shown in Figure 4.2. The conversion of the DLS obtained volumetric distribution to a numerical distribution results in a distribution which does not resemble that obtained by SEM. Over 95% of particles by number are smaller than 5 μm, note the particle count in Figure 4.2B is reported in a logarithmic scale so bins besides the smallest size range are visible. In comparison it can be seen that the conversion of the numerical SEM obtained distribution results in a volumetric distribution which compares well with the volumetric distribution obtained by DLS. The volumetric D50 calculated from the SEM measurements is larger (~340 μm) than that measured by DLS (~280 μm). There is also a large peak from the SEM measurements at 800 μm not present in the DLS measurement. However, the results from converting the numerical SEM distributions to volumetric are much better than converting the DLS to numerical. As such the numerical SEM distributions were used to calculate the number of inoculant particles added in each inoculation trial.

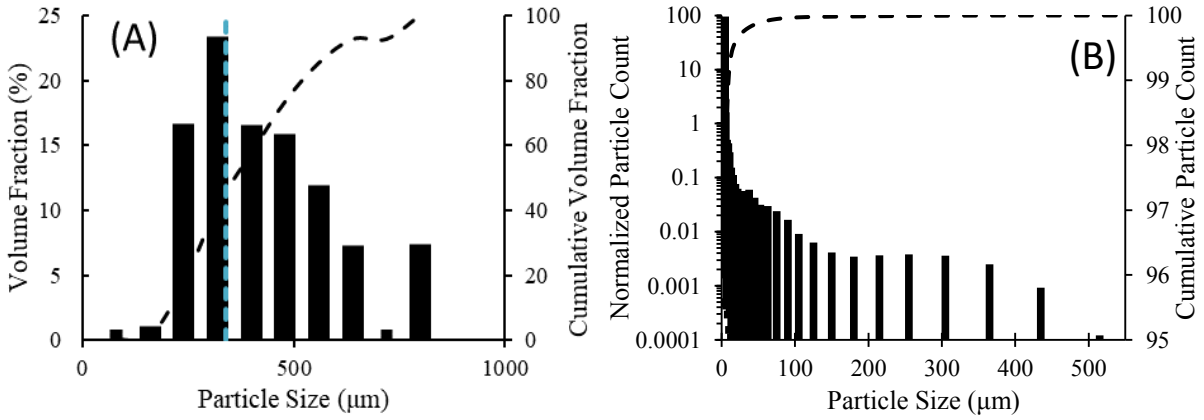

Figure 4.2: Converted 3 hr milled Ti-Al-Nb size distributions of (A) SEM numerical to volume fraction and (B) DLS volume fraction to numerical (note logarithmic scale)

The same procedure was used in each case to determine the number of inoculant particles added to the melt. Using the measured mass of inoculant (1/2 the mass of the inoculating pellet) and the calculated density of the inoculant alloy a total volume of inoculant introduced could be found. The SEM numerical size distribution was converted to a volumetric distribution and using the volume fraction of each size range the volume of inoculant added in each size range determined. This volume could then be divided by the volume of a spherical inoculant with a diameter equal to the average size of the range, the results of this for the 3 hour Ti-Al-Nb inoculation are shown in Figure 4.3. The total number of inoculants could then be found by summing the number in each size range, for the 3 hour Ti-Al-Nb inoculation the number of inoculants was calculated to be ~22000.

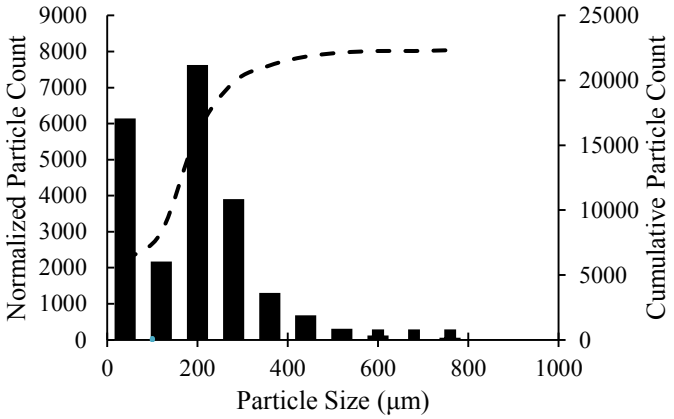

Figure 4.3: Calculated inoculant size distribution for 3 hour milled Ti-Al-Nb inoculation trial

This method can be applied to all the inoculant trials conducted. The calculated number of particles found from the introduced mass of inoculant are shown for each inoculation trial in Table 4.1 (rounded to the nearest 1000). An assumed mass of 1g of inoculant was used for all the TiTa trials except Trial B of the 1.5hr sample where a known mass of 1.11g was used. Since the unmilled Ti-Al-Nb powder could not be sized by SEM or DLS an assumed number of 10000 particles was used.

Table 4.1: Inoculant mass and estimated number of particles introduced for each trial

	Number of Particles Introduced				
Grinding time (hrs)	1.5	3	6	9	11
Ti-Al-Nb	-	23000	45000	90000	770000
Ti-Al-Ta	-	369000	-	559000	-
Ti-Ta	125000	1637000	7603000	12186000	-

	Unmilled	3hr HT	3hr Ar	Solutal
Ti-Al-Nb	10000	23000	12000	0

		Reduced Interaction Time	
	1.5 Trial B	6hr 10s	9hr 10s
Ti-Ta	139000	7603000	12186000

4.1.3 Ingot Preparation

For the Ti-Al-Nb and Ti-Al-Ta inoculation tests individual bulk ingots were prepared for each test from commercially pure base metals. The fabrication method was the same used as for the inoculant alloys described in section 3.2.1. Rods of Ti were cut to obtain pieces as close to the same mass as possible (26 g). Aluminum pellets were then melted into ingots and the surface ground off, to remove any oxide, until a solid Al ingot of the appropriate mass was obtained. For the reference ingot this was 13g, resulting in an alloy of Ti-46Al with a mass of approximately 39 g. If the same mass were used for the inoculation trials the Al included in the inoculation pellet would affect the final composition making the results incomparable. The ingots used for inoculation then had less initial Al content (Ti-44Al) and did not reach the final composition of Ti-46Al until after the inoculating pellet had been added. Before being used for inoculation the ingots were weighed, and any mass loss attributed to vaporization of Al.

As this was a tedious process requiring significant effort before each inoculation trial could be conducted another method was used to manufacture the bulk alloy for the Ti-Ta inoculations. Rather than fabricate small bulk ingots for each inoculation trial a larger apparatus was used to produce a single large ingot of Ti-46Al. For each inoculation trial a portion of the large ingot could be cut off and remelted. The apparatus functioned similarly to the small cold crucible, a vacuum was established first then Ar flux applied during melting. In contrast to the small apparatus the large cold crucible available can cast the melt from the water cooled cold crucible into a conical solid copper mold which is not water cooled. When the induction heating is turned off a nozzle (~2cm in diameter) is opened in the bottom of the crucible and the melt can fall into the mold where it solidifies, as shown in Figure 4.4.

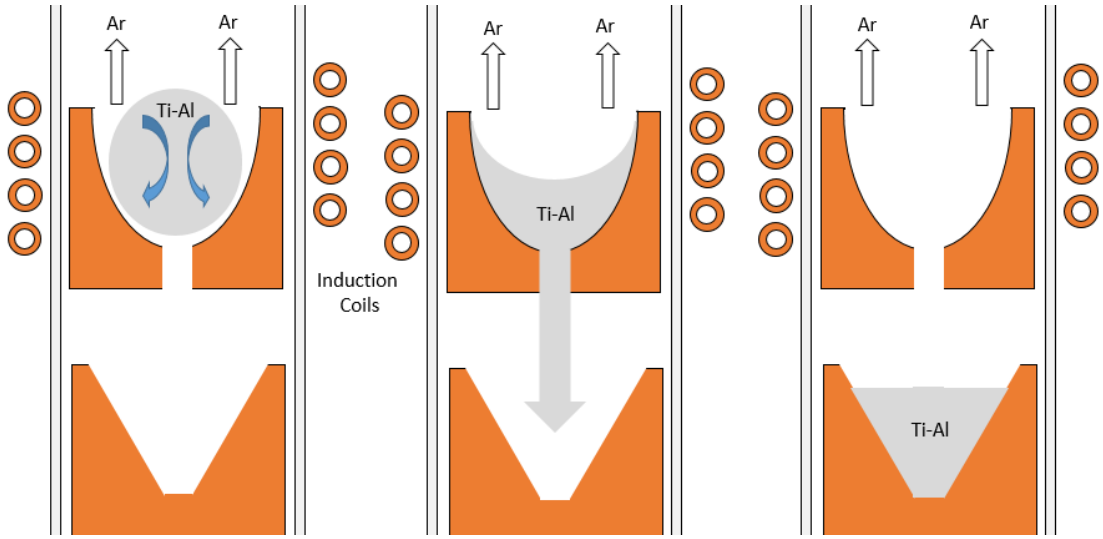

Figure 4.4: Large ingot fabrication procedure showing melting (left), casting in progress (centre) and final ingot solidification (right).

This procedure was carried out three times, as the first two castings had remnants of Ti left in the cold crucible portion of the apparatus which were too large to fit through the bottom nozzle. After three castings involving significant total (>30min) homogenization time at temperature

an ingot was obtained with no large Ti pieces remaining outside the casting. The ingot was approximately 15 cm in diameter and can be seen in Figure 4.5. As the melt must pass through a nozzle at the bottom of the crucible some alloy is invariably solidified on the crucible and in the nozzle. This portion of the melt can be seen in Figure 4.5C, where no large Ti pieces are seen to be caught above the nozzle hole. A cross section of the ingot is shown in Figure 4.5D where the solidification shrinkage is visible but no large undissolved Ti particles. The cross section is unpolished and unetched, however, in previous cases Ti particles could be distinguished by eye on the as-cut surface if they existed. This large ingot was then cut down into smaller pieces which could be combined and remelted to obtain masses similar to those of the ingots prepared individually.

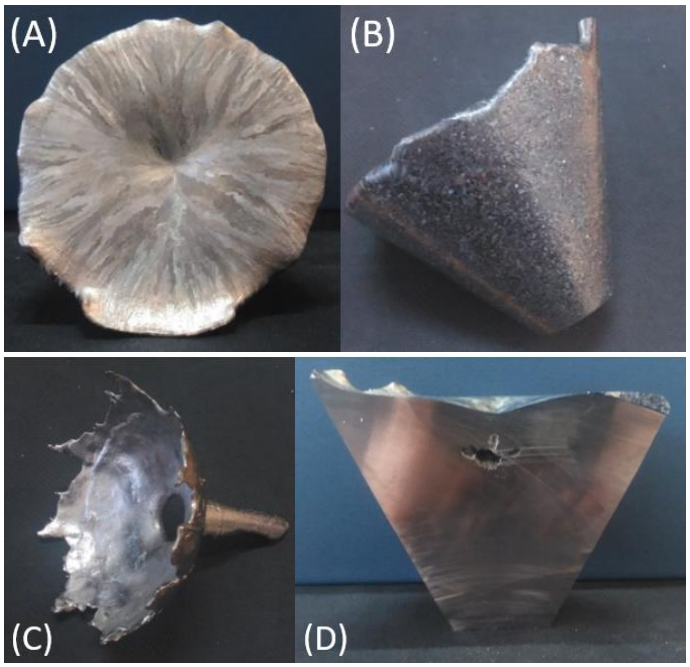

Figure 4.5: Large cast Ti-Al ingot (A) top view (B) side view (C) remaining uncast alloy solidified in the crucible and (D) cut ingot cross section

4.1.4 Inoculation

Once the inoculant pellet and bulk ingot had been fabricated the inoculants could be tested. The apparatus used was the same induction heated cold crucible as used to fabricate the alloys, and can be seen in Figure 4.6. The apparatus was designed for alloy fabrication rather than inoculation trials so there was no obvious inoculant delivery system. Since molten Ti-Al is highly reactive the melt chamber is emptied of oxygen and isolated from the atmosphere, melting takes place under a flux of Ar to further ensure the melt does not oxidize. It is non-trivial to add equipment to such an apparatus since it needs to remain sealed against the atmosphere and a limited number of ports exist to do so on the apparatus. The apparatus did have one port located at the top of the melt chamber where a pyrometer or vacuum tube could be attached, denoted with a white circle in Figure 4.6.

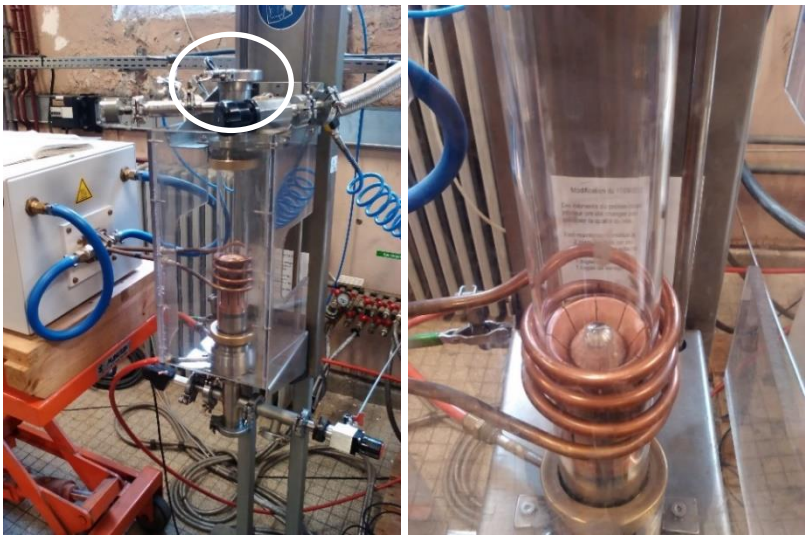

Figure 4.6: Cold crucible inoculation apparatus with top port circled in white.

While the pyrometer was not useful for the inoculation trials a method was developed to use the vacuum tube attachment to deliver the inoculant into the melt, schematized in Figure 4.7. It was for this reason that the inoculants were formed into pellets with excess Al, the vacuum tube could be used to hold a solid pellet away from the bulk alloy which would not be possible with loose powders. Sufficient vacuum is required in the tube such that the pellet does not fall prematurely, this means the melt chamber cannot be put under a vacuum to remove the atmosphere, instead a flux of Ar was imposed for at least 15 minutes at a high enough rate that the chamber had a positive pressure before melting. The pellet was stuck to the vacuum tube, the raw ingot placed in the crucible and the apparatus assembled (Figure 4.7 A). The vacuum tube was placed such that the melt chamber tube could be put in position and the pellet was as far away from the melt as possible to reduce any unwanted preheating. After the Ar flux had been imposed for at least 15 minutes, if the pellet remained retained by the vacuum tube, if the pellet fell the apparatus had to be taken apart, reassembled with the pellet again held in place and the Ar flux restarted, otherwise the power was turned on and the bulk alloy completely melted (Figure 4.7 B). Once the bulk alloy was completely melted the vacuum tube could be lowered so the pellet was closer to the melt (Figure 4.7 C). This was done so the pellet dropping into the melt disturbed it the least amount possible, a large drop could cause splashing of the liquid melt or excessive sticking to the sides of the crucible. This was done as close to the time when the pellet would be dropped into the melt to prevent significant preheating of the pellet, already just by being in the melt chamber the pellet would not be at room temperature and significant time close to the melt would likely greatly increase the temperature of the pellet. In order to simplify the experimental procedure and not have another variable affecting the inoculation the vacuum tube was not lowered until the inoculation was ready to begin. With the vacuum tube lowered the vacuum could be turned off and the pellet allowed to fall into the melt (Figure 4.7 D). Once the pellet contacted the melt a timer was started to measure the interaction time between the pellet and melt. The dissolving Al and induction stirring dispersed the inoculants throughout the melt (Figure 4.7 E). Once 20 seconds of interaction time had elapsed the power was turned off and the melt allowed to solidify (Figure 4.7 F). The Ar flux remained present until the apparatus approached room temperature and could be disassembled by hand.

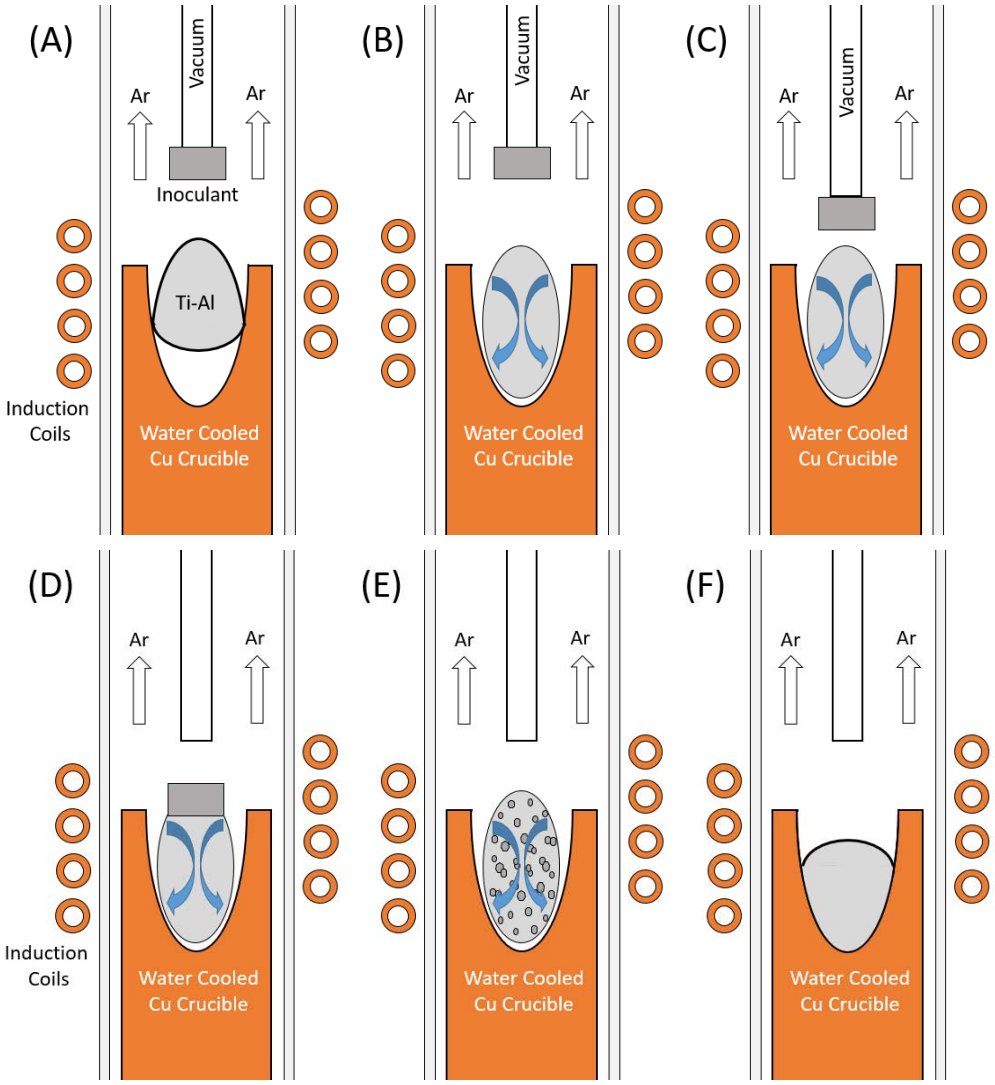

Figure 4.7: Schematic of inoculation procedure showing (A) initial setup, (B) inoculant pellet held away from molten Ti-Al, (C) lowering of pellet close to melt, (D) removal of vacuum and pellet drop into the melt, (E) interaction time between inoculant and melt and (F) final ingot solidification.

4.2 Ingot Analysis Procedure

Once the inoculation trials were complete the inoculated ingots were metallographicaly prepared then imaged with optical and electron microscopy to determine their equiaxed fraction and equiaxed grain size respectively. The procedure for this is outlined below using the reference, non-inoculated ingot as an example.

4.2.1 Sample Preparation

In order to analyze the micro and macro structure of the inoculated ingots they first needed to be metallographically prepared. The ingots had a smooth shape which could not be secured safely in a saw on their own, as seen in Figure 4.8. The ingots were then first mounted in epoxy upside-down, the epoxy could then be held by a clamp and the ingot sawn in half along its

center line. Once the ingot had been cross-sectioned each half was then again mounted in epoxy for metallographic preparation. The ingot halves were ground with SiC paper down to 4000 grit followed by polishing with a Struers OPS suspension, a colloidal silica suspension with 0.04 µm particles, for at least 15 minutes. After polishing the cross sections were etched with a modified Krolls reagent containing 67% water, 23% H_2O_2, 7% HF, and 3% HNO_3 volumetrically. This etchant improved the observation of the solidification structure over the traditional, non-modified, Krolls reagent. Etching times varied to obtain best results but averaged around 20 seconds.

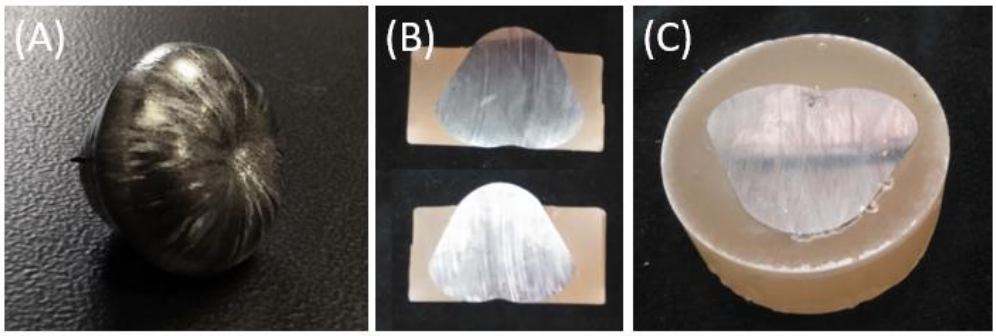

Figure 4.8: Ingot cross section preparation showing (A) the raw ingot, (B) cross sectioned ingot in first mounting and (C) ingot half mounted for polishing/etching.

4.2.2 Measurement of Ingot Equiaxed Area

Once the ingots had been polished and etched they could be imaged with optical microscopy. The entire surface of the cross section was imaged by stitching individual fields of view together using the Zeiss software MosaicX which interfaced with the microscope to automatically move the stage and track where images were taken. A complete ingot micrograph and columnar to equiaxed transition can be seen in Figure 4.9.

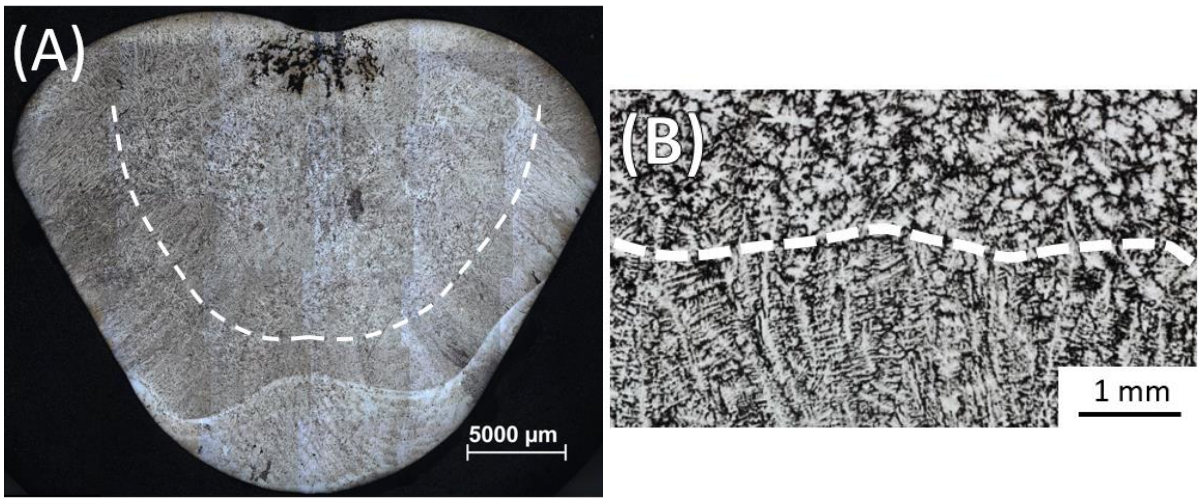

Figure 4.9: Optical images of reference ingot by (A) bright field with columnar/equiaxed transition indicated and (B) Delineation between columnar (bottom) and equiaxed (top) regions of solidified ingot

The bright field images showed interesting characteristics of the solidified ingots. Shrinkage porosity can be seen at the top center of the ingot and was present to some degree in all ingots, this indicates this was the last area to solidify. The bottom of the cross section in Figure 4.9 A shows a "cap" at the bottom of the ingot with a different structure than the bulk. This is the area which was in contact with the cold crucible during processing, the melt was then not fully levitating within the induction field. This region is likely made up of unmelted Ti-Al and possibly a first planar front solidified area before the columnar region begins. The other edges of the cross section show columnar dendritic growth almost immediately from the crucible walls after the induction field was turned off and the melt allowed to solidify. The center of the ingot is made up of equiaxed grains. This equiaxed region was of particular importance for the inoculated samples since it should be the area where the particles are acting to form new grains. It was then important to measure what fraction of the ingots were made up of equiaxed grains. This was done using ImageJ where area fractions could be measured. The equiaxed zone was delineated from the columnar along the tips of the columnar grains, as shown in Figure 4.9B. This could be done along the entire columnar front, see Figure 4.9 A, allowing the area fraction of the equiaxed zone to be measured. The total area of the cross section was measured then the areas of the shrinkage, bottom cap and columnar zones subtracted from it, with the remainder being the equiaxed fraction. This compared well with direct measurements of the area above the delineation with the shrinkage area removed.

4.2.3 Grain Size Measurement

Electron microscopy was also carried out to evaluate the equiaxed grain size of the ingots. In order to view the solidification structure images were taken in backscattered electron (BSE) mode which shows the atomic number contrast. Images were taken in the equiaxed zone of the ingots, concentrated in the region between the shrinkage porosity and bottom cap of the ingot. Images were also taken to either side of the ingot and did not deviate significantly from those taken near the center. An example BSE image of the reference ingot can be seen in Figure 4.10 where post processing in Image J to add false colours to the grains to make differentiating between them easier.

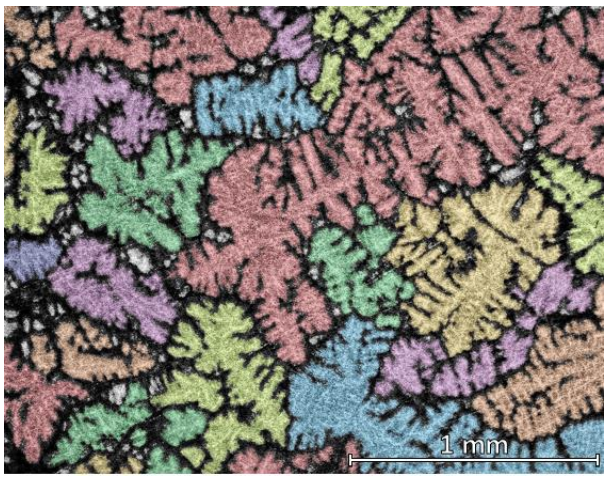

Figure 4.10: BSE image in equiaxed zone of reference ingot with post processed false coloured grains

Measuring the size of dendritic grains consistently and accurately is non-trivial. Depending on the plane of the ingot being viewed dendritic grains may appear very differently, conventional grain size measurement using the line-intercept or a similar method is not possible. In order to ensure the grain size reported reflected as close to the real grain size as possible only grains which appeared to be cut in an exact cross section were measured. One such grain in the reference ingot can be seen in Figure 4.11. Two measurements were used to characterize such grains, the linear lengths from opposing tips were measured for two pairs of tips as close to perpendicular to one another as possible, as shown in Figure 4.11. These measurements were averaged across as many grains as possible to obtain an average grain size, 696 μm in the case of the reference ingot. This method minimizes the total number of grains measured since only grains with a near complete cross section are measured but ensures each measurement relates precisely to a read dimension of a grain. Samples with larger grain sizes will have fewer grains cut in cross section and thus fewer measurements can be taken, while samples with smaller grain sizes will have more grains which can be measured, it is then more important to measure as many grains as possible in samples with large grain size as more grains can be measured easily in samples with smaller grain size. In order to have comparable results between samples the same method was used in all cases, even if there were globular shaped grains which could have their size evaluated effectively with other methods, this method was used.

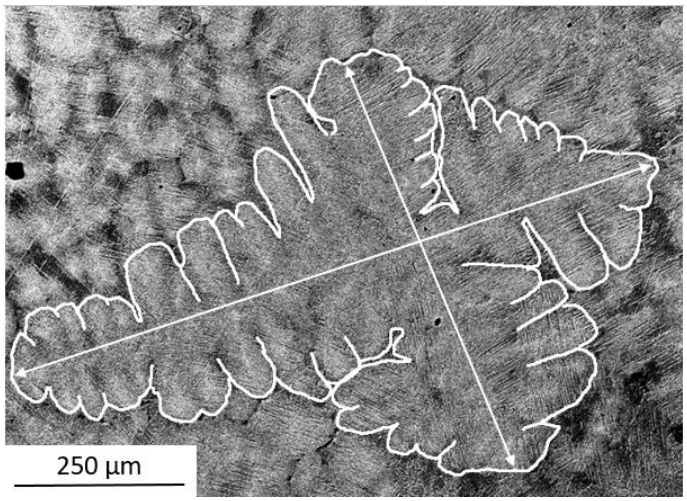

Figure 4.11: BSE image of reference equiaxed dendritic grain outlined in white with near perpendicular tip to tip measurement lines

4.3 Individual Bulk Alloy Ingot Trials

Inoculation trials were conducted on bulk alloys which were each fabricated specifically for the inoculation trial. Inoculants of both Ti-Al-Nb and Ti-Al-Ta were tested using these ingots. Eight trials of Ti-Al-Nb were conducted, two of Ti-Al-Ta as well as a reference uninoculated sample.

4.3.1 Ti-Al-Nb Trials

The first inoculation trials were conducted using particles of Ti-Al-Nb. Particles were tested which were milled for 3, 6, 9, and 11 hours resulting in different size distributions, a summary

of the experimental conditions and results of these trials is given in Table 4.2. Additionally a test were conducted to see the solutal effect of the alloying additions from the powders, as well as with unmilled powders, 3 hour milled powders which were heat treated after milling and a powders which were milled for 3 hours under Ar rather than in air, the experimental conditions and results of these trials are shown in Table 4.3.

Table 4.2: Ti-Al-Nb Experimental conditions for milling time trials

	Ti-Al-Nb			
Designation	3	6	9	11
Milling Time (hrs)	3	6	9	11
Milling Atmosphere	Air	Air	Air	Air
Distribution D50 (μm)	191	163	113	48
# Particles Introduced	23,000	45,000	90,000	770,000
Interaction Time (s)	20	20	20	20
Grain Size (μm)	336	446	337	188
Equiaxed Fraction	0.63	0.64	0.64	0.42

Table 4.3: Ti-Al-Nb Experimental conditions for further trials

	Ti-Al-Nb				
Designation	Unmilled	3Ar	3HT	Ref	Solutal
Milling Time (hrs)	0	3	3	-	-
Milling Atmosphere	-	Ar	Air	-	-
Distribution D50 (μm)	300	233	191	-	-
# Particles Introduced	10,000	23,000	12,000	0	0
Interaction Time (s)	20	20	20	-	-
Grain Size (μm)	403	397	471	696	587
Equiaxed Fraction	0.69	0.68	0.5	0.3	0.31

4.3.1.1 Milling Time Variation

The 3 hour milled particles successfully inoculated the Ti-Al ingot. The ingot cross sections look similar to those of the reference ingot, with a solid cap at the bottom, columnar zone, equiaxed zone and solidification shrinkage at the top. The size of the equiaxed zone was significantly increased to an area fraction of 63%, as can be seen in Figure 4.12. The equiaxed volume was then calculated to be over 6 cm^3, more than double that of the reference. The morphology in the equiaxed zone was changed by the inoculation. The equiaxed grains appear much more globular than those found in the reference sample and their size was reduced to an average of 336 μm. A sample micrograph showing the representative grain size and morphology can be seen in Figure 4.12. This average grain size results in a grain density of over 50000 grains/cm^3, nearly an order of magnitude higher than the reference sample, combined with the increased equiaxed area this results in over 300000 grains being present in the equiaxed zone compared to 16000 in the reference, an increase of over 18x. The density of introduced inoculant particles if they are equally dispersed throughout the ingot was 2300 /cm^3 or 3700 /cm^3 if they were constrained to the equiaxed zone.

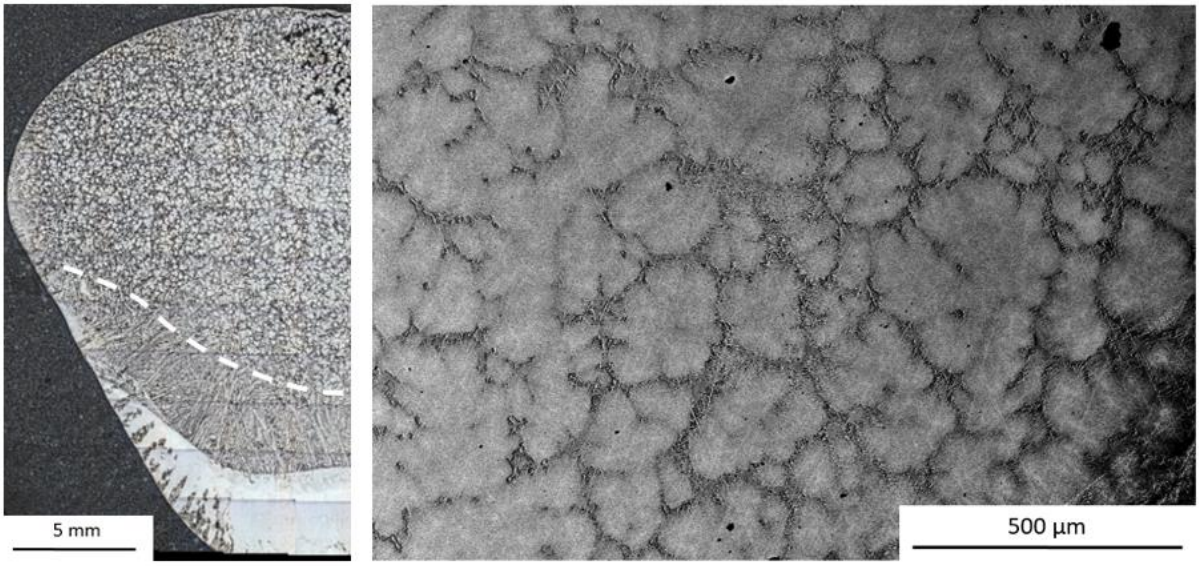

Figure 4.12: Example BF ingot cross sections and BSE micrograph of 3 hr Ti-Al-Nb inoculated microstructure

Investigating the ingot revealed no evidence of remaining Ti-Al-Nb particles. No bright spots caused by increased Nb content were found by BSE in the centre of any grains as expected or along the periphery where the columnar grains were nucleated. This seems to indicate that the inoculants all dissolved and did not participate in nucleation, however this does not explain the degree of increase of the equiaxed fraction or decrease of the grain size adequately. A small increase in equiaxed fraction and decrease in grain size could be the result of solutal growth restriction from the Nb alloying addition, however, it is unlikely that such a drastic change is due to this effect alone. It may also be incredibly difficult to locate and identify the particles as they are the same phase and structure as the solidified melt and the interface between the particles and solid should be diffuse after interacting at high temperature with both the liquid and the solid during cooling. The morphology of the equiaxed zone appeared constant from the CET to the solidification shrinkage. No significant change of grain size or shape was detected.

The same procedure was repeated for the Ti-Al-Nb particles which had been milled for 6, 9 and 11 hours. All three distributions were also successful at both reducing the grain size and increasing the equiaxed fraction. Optical images of ingot cross sections and representative BSE micrographs can be seen in Figure 4.13. The 6 and 9 hour inoculated ingots appear similar to the 3 hour ingot, bottom cap to solidification shrinkage, with equiaxed fractions of 64.3% and 63.5% respectively. The ingot inoculated with the 11 hour milled powders appears quite different. The bottom cap takes up nearly 46% of the ingot and there is an unmelted Ti particle in the equiaxed zone which takes almost 4% of the area fraction. The columnar region is however greatly reduced and the equiaxed zone is 42% of the area, still a larger fraction than that of the reference ingot. The unmelted Ti does not greatly affect the composition in the equiaxed zone, average EDX measurements gave composition of ~Ti-46Al-0.78Nb within error of measurements taken in the other ingots. It is difficult to ensure that no unmelted Ti remains in the ingots, alloying melts are done as many times as feasible, however, each set of melt cycles involves disassembling and reassembling the apparatus increasing the chance of oxidation and

ruining the ingot. The increase in the size of the bottom cap is more difficult to explain. It appears that there may be a zone in the middle of the cap which has a more equiaxed morphology, however, no clear images in that region could be obtained. It may be caused by a difference in the heating cycle causing more of the ingot to remain stuck to the crucible rather than levitating or the Ti particle may have influenced the fluid flow causing the molten droplet to have a different shape and more sticking. The heating cycle could not be measured as the port of the apparatus where a pyrometer could be mounted was being used by the vacuum tube to deliver the inoculating pellet.

The morphology of the 6 and 9 hour inoculated samples were quite similar with more globular type grains of smaller size than that of the reference sample. The 11 hour inoculated sample had the smallest average grain size, but differs from the other inoculated samples in that the grains have more developed dendrite style arms giving the microstructure a more dendritic appearance. Example micrographs from all three samples can be seen in Figure 4.13. The 6, 9 and 11 hour milled particle inoculations resulted in average equiaxed grain sizes of 446 μm, 337 μm, and 188 μm, or grain densities of over 21000, 49000, and 289000 grains/cm^3 respectively. This is contrary to traditional inoculation where larger particles are more effective at nucleating than smaller. As the grinding time increased the number of particles introduced to the melt also increased as more particles could be present within the constant 1g mass of inoculant added. Over 42000, 86000, and 733000 particles were introduced for the 6, 9, and 11 hour samples respectively, resulting in inoculant densities of over 6400, 13000, and 179000 /cm^3 if they were only in the equiaxed zone and 4100, 8800 and 76000 if they were evenly distributed. Once again however none of these particles could be seen in the solidified ingot.

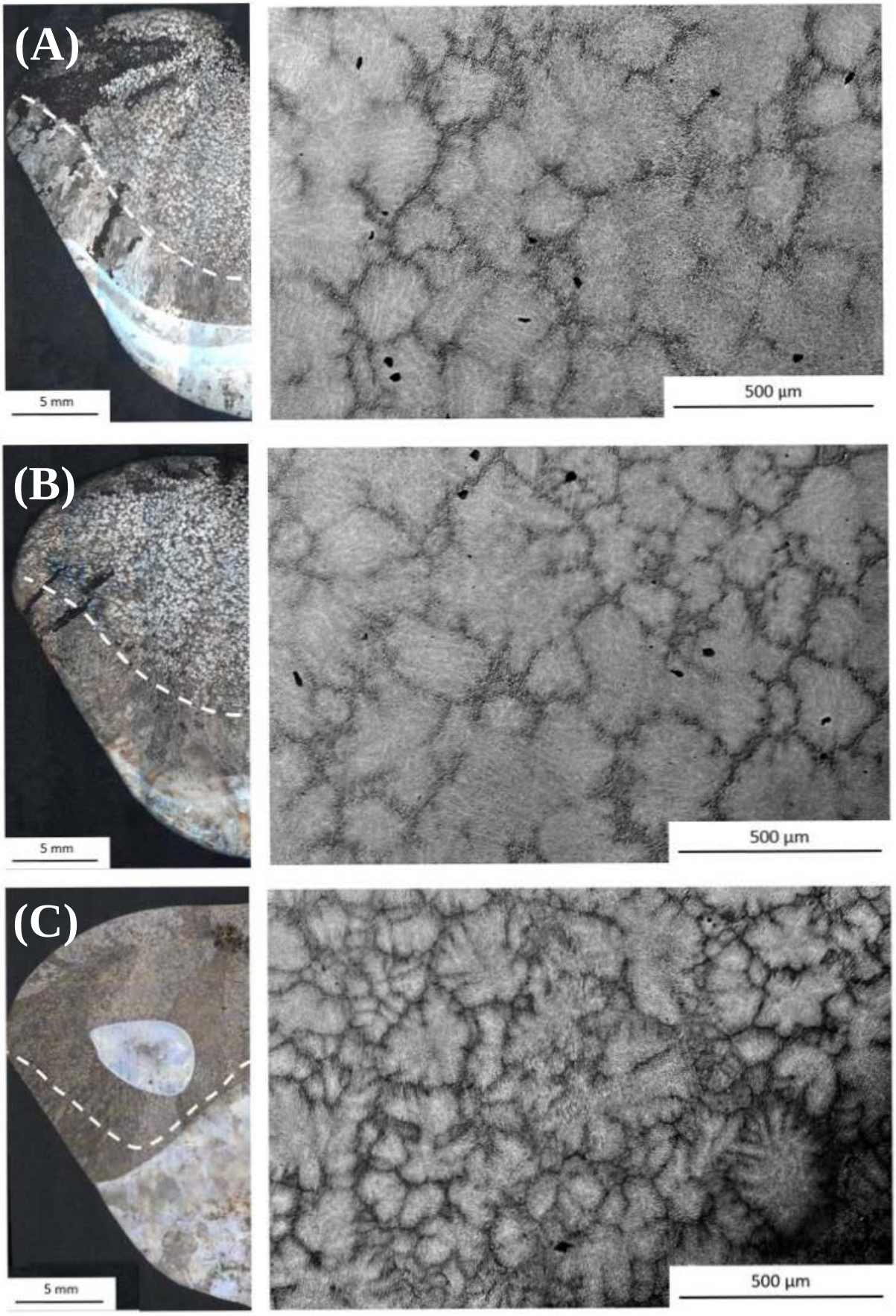

Figure 4.13: Example BF ingot cross sections and BSE micrographs with (A) 6 hr, (B) 9 hr and (C) 11 hr milled Ti-Al-Nb particles

4.3.1.2 Powder State Variation

Three further inoculant variations were tested in the Ti-Al-Nb system, particles which had not been milled, particles milled for 3 hours under argon gas rather than air and particles which were milled for 3 hours under air then subjected to a stress relieving heat treatment, however it was seen in Chapter 3 that the powders were partially transformed from pure β to a two phase α/β mixture. Cross sections and representative BSE micrographs of the resultant ingots can be seen in Figure 4.14. The equiaxed area fraction obtained was 69% with the unmilled particles 68% with the Ar milled particles and 50% with the heat treated particles. The unmilled and Ar milled ingots have similar macrostructure alignment as the other inoculated ingots, bottom cap to solidification shrinkage, however the ingot inoculated with heat treated particles is different, with a columnar region located at the top of the ingot.

The average equiaxed grain size was 403 μm with the unmilled particles, 397 μm with those milled under Ar and 471 μm with the heat treated particles, or over 29000/cm^3, 30000/cm^3 and 18000/cm^3 respectively, example micrographs for each ingot are shown in Figure 4.14. Again the microstructure of the unmilled and Ar inoculated ingots appear similar to the other inoculated structures, being of a more globular morphology while the particles which were heat treated resulted in more dendritic type equiaxed grains.

The heat treatment greatly reduced the effectiveness of the 3 hour milled particles. Without heat treatment the particles reduced the average equiaxed grain size to 336 μm while after heat treatment the equiaxed grains were reduced to only 471 μm, the least effective of any of the inoculants. Even particles which had larger sizes, and thus fewer added the melt, were more effective. It is possible that the induced compressive stress from milling contracts the lattice giving a slightly better fit between the particles and solidifying melt, since the particles without stress had a slightly larger lattice parameter than the bulk alloy. Additionally since the heat treated particles contained some α-Ti the heat treatment was not a true stress relieving treatment. Since no comparative analysis of the lattice parameters between the heat treated and cryo-milled particles was undertaken a change in lattice parameter between the states cannot be confirmed as the reason for the reduced effectiveness of the heat treated particles. The presence of regions of α-Ti within the particles may reduce their effectiveness. The solidification phase of the bulk alloy is β-Ti so there is no direct lattice matching between it and the regions of α in the particles. These portions of the particles are then ineffective as isomorphic inoculants. They may still be able to heterogeneously nucleate solidifying β, however as discussed in Chapter 2 that would be significantly less efficient than the isomorphic inoculants.

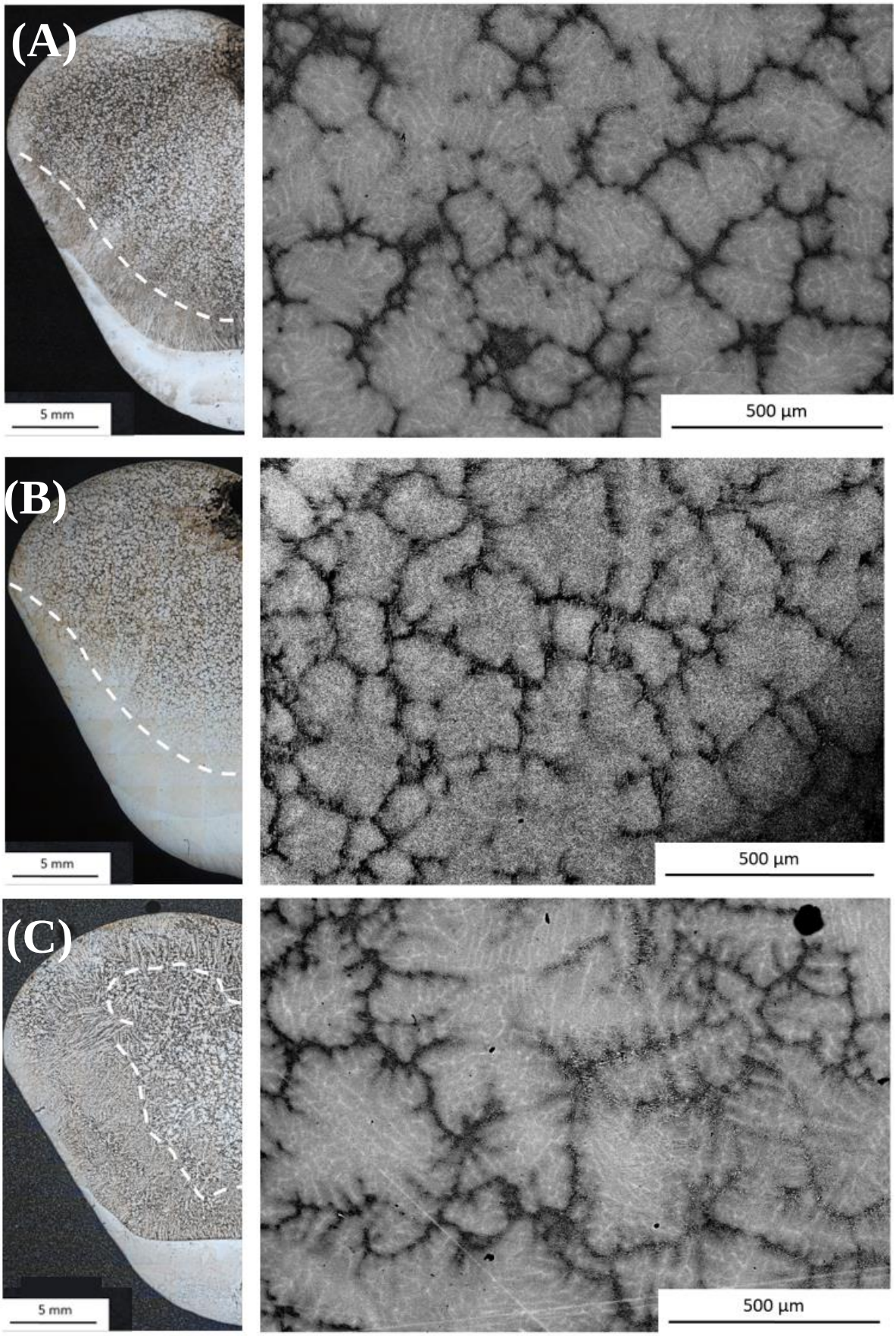

Figure 4.14: Example BF ingot cross sections and BSE micrographs with (A) unmilled, (B) 3 hr Ar and (C) 3 hr HT Ti-Al-Nb particles

4.3.1.3 Nb Solutal Effect

A reference ingot was prepared without any inoculant but following the same procedure as outlined above. Optical and SEM images of the ingot can be seen in Figure 4.9 and Figure 4.10 respectively. The results of image analysis gave an equiaxed grain size of 696 μm with an equiaxed area fraction of 30%. Assuming the grains to be spherical this gives a grain density of 5600 grains/cm^3, thus there are approximately 17000 grains present in the ~3 cm^3 equiaxed zone. For comparison, a sample image which was used for grain size characterization can be seen in Figure 4.15.

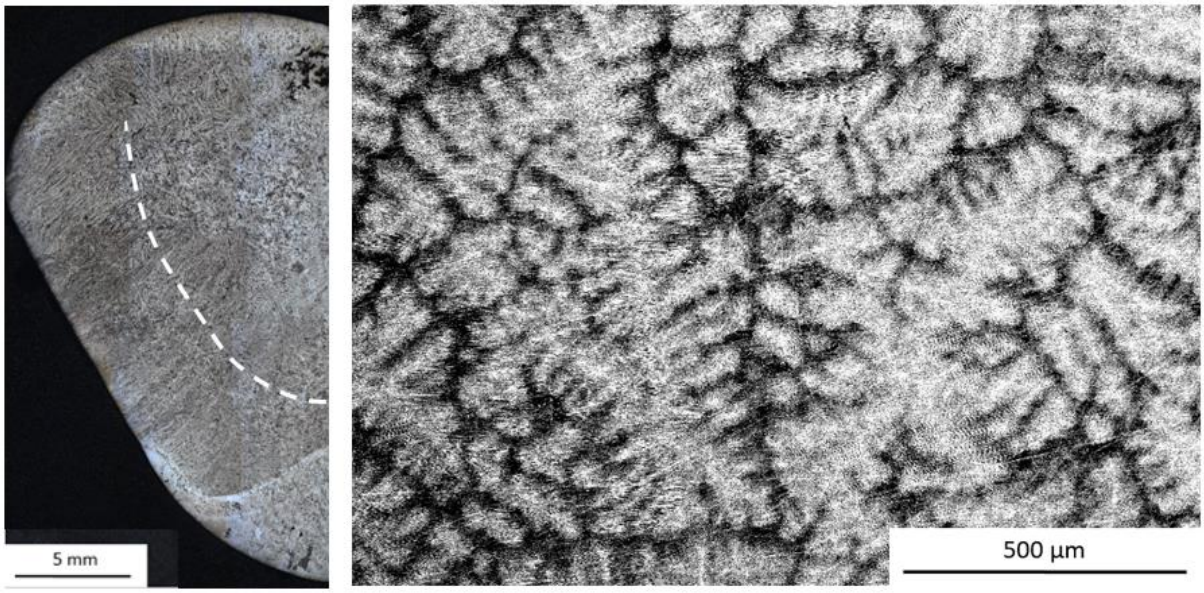

Figure 4.15: Example BF ingot cross sections and BSE micrograph of reference ingot

A further ingot was prepared to investigate the solutal effect of the alloying addition from the inoculant particles, i.e. the effect if the particles did not survive the melt and were completely dissolved. The ingot was produced in the same manner as the inoculated ingots but the inoculating pellet was treated in the same manner as alloying additions, with longer times spent interacting with the melt and multiple remelting cycles. The resultant ingot cross section can be seen in Figure 4.16. The area fraction of equiaxed grains was found to be 31%, nearly identical to the reference sample (30%). The presence of Nb in the melt should slow the growth of the solidifying grains, giving more time for equiaxed grains to nucleate. It can be seen from the ingot cross section that more columnar grains were nucleated from the top of the ingot when compared to the reference or inoculated samples.

The average equiaxed grain size was affected by the presence of Nb in the melt and decreased over 100 μm compared to the reference sample to 587 μm, a grain density of 9400/cm^3. The microstructure remains dendritic like the reference and the grains did not have the more globular shape found in the inoculated samples. An example micrograph of the equiaxed structure can be seen in Figure 4.16. Since this ingot differs from the inoculated ingots in both micro and macro structure it can be assumed that the inoculant powders did not completely dissolve into

the melt even though they could not be located in the inoculated ingots. The reduction in grain size due to the solutal effect also means that even particles which did dissolve into the melt and cannot reduce the grain size by growing new grains assist with grain refinement by their Nb content being added to the melt.

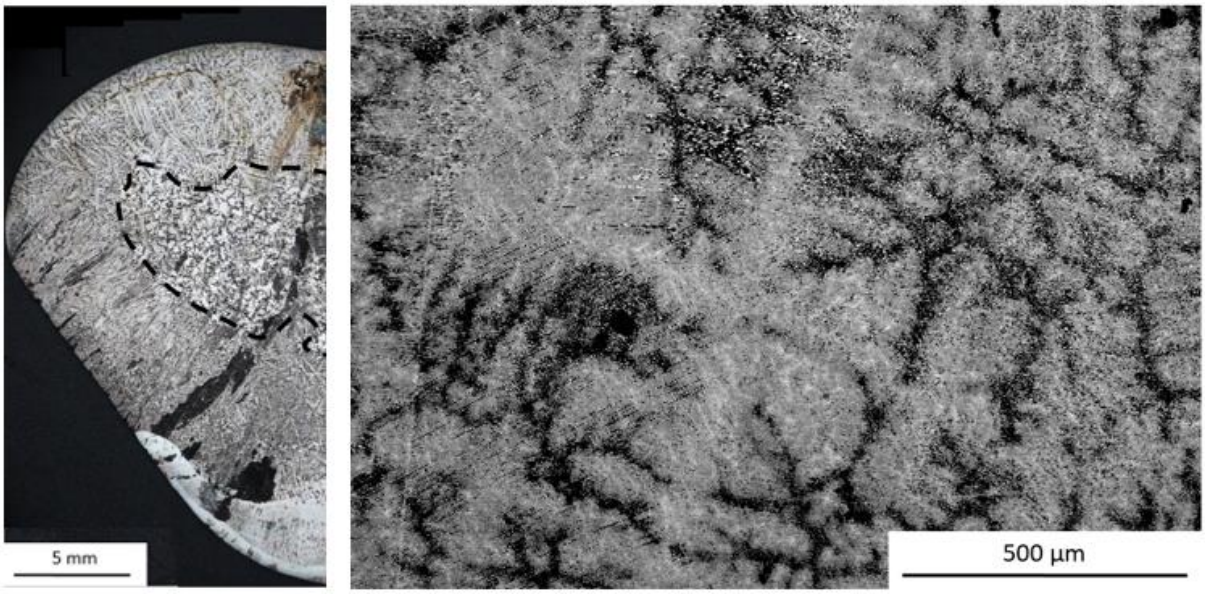

Figure 4.16: Example BF ingot cross sections and BSE micrograph showing solutal effect of Nb addition

4.3.2 Ti-Al-Ta Trials

Further trials were conducted using the Ti-Al-Ta particles. Once again individual bulk alloy ingots were prepared for each inoculation trial. Two trials were conducted using the Ti-Al-Ta particles, one using particles milled for 3 hours and the other using particles milled for 9 hours. A summary of the inoculation trial conditions and results are shown in Table 4.4.

Table 4.4: Ti-Al-Ta Experimental conditions for milling time trials

	Ti-Al-Ta	
Designation	3	9
Milling Time (hrs)	3	9
Milling Atmosphere	Air	Air
Distribution D50 (µm)	56	53
# Particles Introduced	369000	559000
Interaction Time (s)	20	20
Grain Size (µm)	335	308
Equiaxed Fraction	0.52	0.64

4.3.2.1 Milling Time Variation

Both 3 hour and 9 hour particle distributions were successful at reducing the as-cast grain size and increasing the equiaxed fraction in the ingots. Optical cross sections of the ingots produced

can be seen in Figure 4.17 where the columnar to equiaxed transitions are shown. The equiaxed fraction was seen to be 52 % when inoculated with 3 hour milled particles and 64% with 9 hour milled particles.

The average equiaxed grain size was similar between the ingots, 335 μm with 3 hour milled particles and 308 μm with 9 hour milled particles. It can be seen in Figure 4.17 that while the grain sizes are similar the morphology is much more dendritic with the 3 hour particles than the 9 hour particles. The similarity in grain size does make sense as both distributions had similar D50s, 56 μm and 54 μm numerically and 125 μm and 100 μm volumetrically for the 3 hour and 9 hour milled particles respectively.

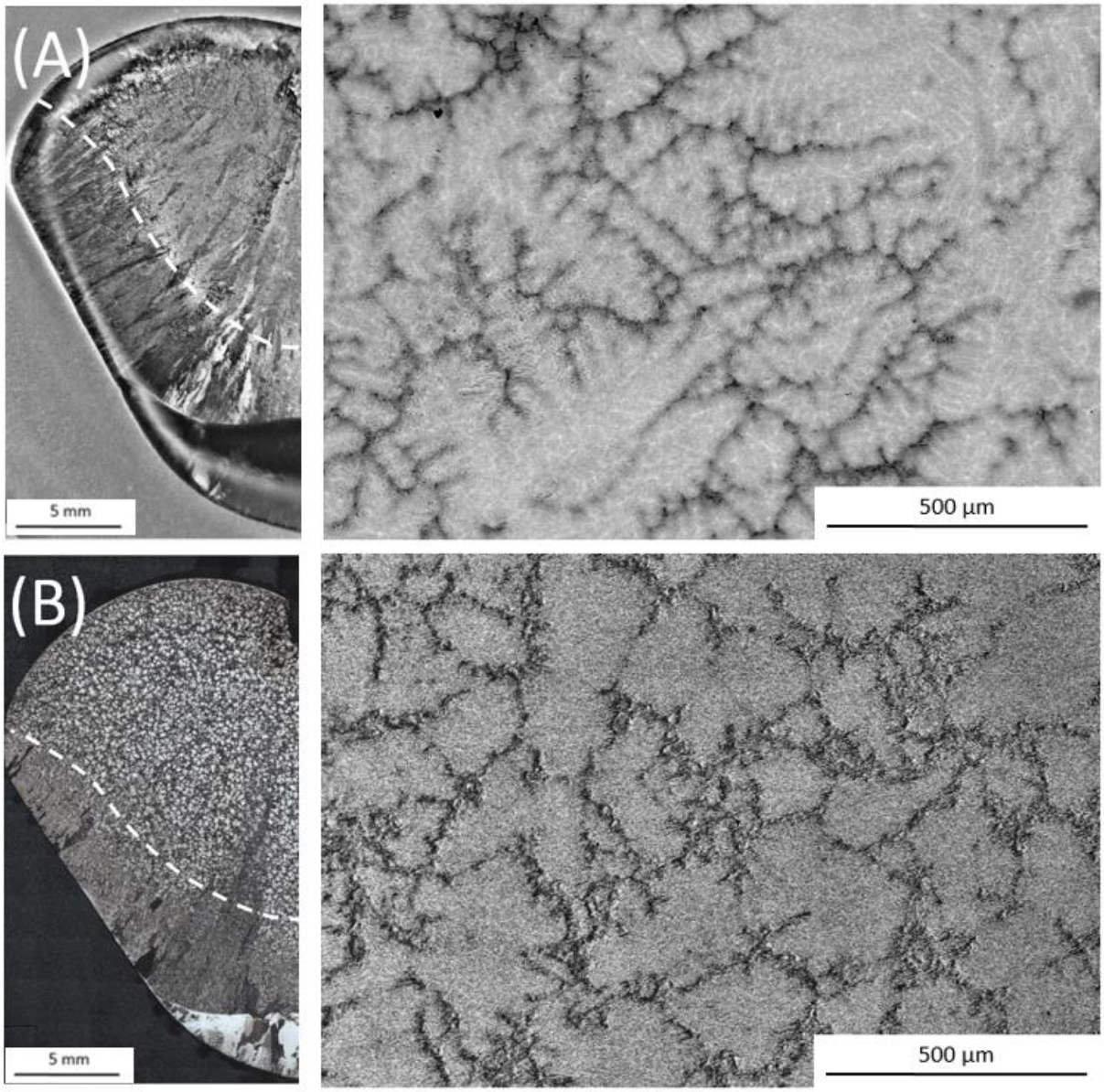

Figure 4.17: Example BSE micrographs with (A) 3 hr and (B) 9 hr milled Ti-Al-Ta particles

4.3.3 Summary of Individual Ingot Trials

Seven different particle preparation methods were tested to produce powders of Ti-Al-Nb, and two of Ti-Al-Ta, to inoculate a Ti-Al melt. In each case the particles were successful at reducing the as cast grain size and increasing the equiaxed fraction of the ingot. No appreciable difference in results was found between using particles ground in air or Ar. Stress relieving the particles after milling resulted in larger grain sizes and a smaller equiaxed fraction than using the as milled particles. No evidence of the particles remained in the as cast ingots, however, testing the effects of the alloying elements of the powders if complete dissolution occurred resulted in larger grains and smaller equiaxed fraction than found during any of the inoculation trials. The particles are likely then too well incorporated into the bulk solid to be detected, supporting the theory that they act as centers of grain growth rather than nucleation.

4.4 Ti-Ta Trials

The inoculant alloy designed for maximum stability in the melt, Ti-47Ta, was also tested. Inoculation trials were conducted using particles milled for 1.5, 3, 6 and 9 hours. Rather than producing individual ingots from base metals for these trials a single large bulk alloy ingot was produced and cut into sections which were remelted for the inoculation trials. With the exception of the manner of the bulk ingot fabrication the inoculant trials were carried out identically to those of the Ti-Al-Nb and Ti-Al-Ta inoculants. In contrast to the ternary alloys none of the trials with the large ingot sections and binary Ti-Ta alloy showed any grain refinement. The structures of the ingots were complex and not enough obvious equiaxed grains were found in the ingots to facilitate statistically relevant measurements, the conditions and results of these trials are given in Table 4.5. Two further trials were attempted using the remelted large ingot sections but with reduced interaction time to increase the number of inoculants present on solidification, however these two were unsuccessful. A final trial was attempted once again fabricating the bulk alloy individually for the inoculation trial and using 1.5 hour milled Ti-Ta particles. This trial was successful and grain refined the ingot compared to the bulk individual ingot as well as increased the equiaxed fraction. The conditions and results of these three trials are given in Table 4.6.

Table 4.5: Ti-Ta Experimental conditions for milling time trials

	Ti-Ta				
Designation	1.5	3	6	9	Ref
Milling Time (hrs)	1.5	3	6	9	-
Milling Atmosphere	Ar	Ar	Ar	Ar	-
Distribution D50 (μm)	70	35	22	20	-
# Particles Introduced	125,000	1,637,000	7,603,000	12,186,000	0
Interaction Time (s)	20	20	20	20	-
Grain Size (μm)	-	-	-	-	-
Equiaxed Fraction	0	~0.5	0	0	0

Table 4.6: Ti-Ta Experimental conditions for further trials

	Ti-Ta		
	Large Ingot		Small ingot
Designation	6	9	1.5B
Milling Time (hrs)	6	9	1.5
Milling Atmosphere	Ar	Ar	Ar
Distribution D50 (μm)	22	20	70
# Particles Introduced	7,603,000	12,186,000	139,000
Interaction Time (s)	10	10	20
Grain Size (μm)	-	-	359
Equiaxed Fraction	<0.1	<0.1	0.69

4.4.1 Ti-Ta Collective Bulk Alloy Trials

Inoculation trials were conducted with Ti-Ta particles using remelted portions of the large TiAl ingot produced as the bulk alloy. Particles were initially tested which had been milled for 3, 6 and 9 hours. Further trials were also conducted with particles which were only milled for 1.5 hours as well as 6 and 9 hour samples but with the interaction time with the melt reduced by half to 10 seconds.

4.4.1.1 Milling Time Variation

Initial inoculation trials in the Ti-Ta system used particles milled for 3, 6 and 9 hours. Ingots produced with these inoculants were much more difficult to characterize than the other inoculant systems. The columnar to equiaxed transition was difficult to identify from the ingot cross sections, shown in Figure 4.19, making accurate determination of the equiaxed fraction impossible. It was possible to make a rough approximation of the equiaxed fraction of the ingot inoculated with particles milled for 3 hours, determined to be approximately 50%. This is more than present in the reference sample but less than found with the other inoculant systems. The other ingots did not show a columnar to equiaxed transition which could be determined well enough to measure any sort of equiaxed fraction.

The morphology of the ingots required higher magnification in order to be evaluated. Example micrographs showing representative microstructure of the ingots in the region below the solidification shrinkage which was representative of the equiaxed zone in the other systems can be seen in Figure 4.19. The microstructure appears equiaxed in the ingot treated with particles milled for 3 hours however the dendrite morphology is different than found in the reference ingot or when using inoculants from the other systems. In the previously analyzed ingots the dendrites appear congruous, allowing them to be measured relatively easily. In this case the dendrites are not congruous making an estimation of the limits of the grain envelops very difficult. The bright regions of the micrographs appear to be segments of primary or secondary dendrite arms, determining to which dendrite each region belongs is nigh impossible. It can be seen in the centre of Figure 4.19A that there appears to be an equiaxed dendrite cut in cross section which would be perfect to measure, however it is difficult to determine where each of

the primary arms ends. Additionally, opposed to the dendrites found when inoculating with the other alloy systems it has six narrow arms rather than four thicker arms. The change from four to six arms may indicate that the solidification phase has changed from cubic, BCC, β-Ti to hexagonal, HCP, α-Ti. In all three micrographs of Figure 4.19 it can be seen that the secondary dendrite arms are not entirely perpendicular to the primary arms, which also indicates a change from solidifying as β-Ti.

The dendrites imaged in the center of the ingots inoculated with 6 hour and 9 hour milled are also not equiaxed but columnar. In Figure 4.18 it can be seen that there is no equiaxed region between the bottom cap and solidification shrinkage but that the whole ingot is columnar. It is then unlikely that particles forming new grains were present in the center of the ingot during solidification. The ingots inoculated with six and nine hour milled particles do appear similar, and were the smallest sized particles tested, it is possible that the inoculant particles dissolved completely in the 20 second interaction time before solidification began. It's also possible that the addition of the particles encouraged columnar growth as the equiaxed region of the reference ingot was greater than that found in the ingots inoculated with these particles.

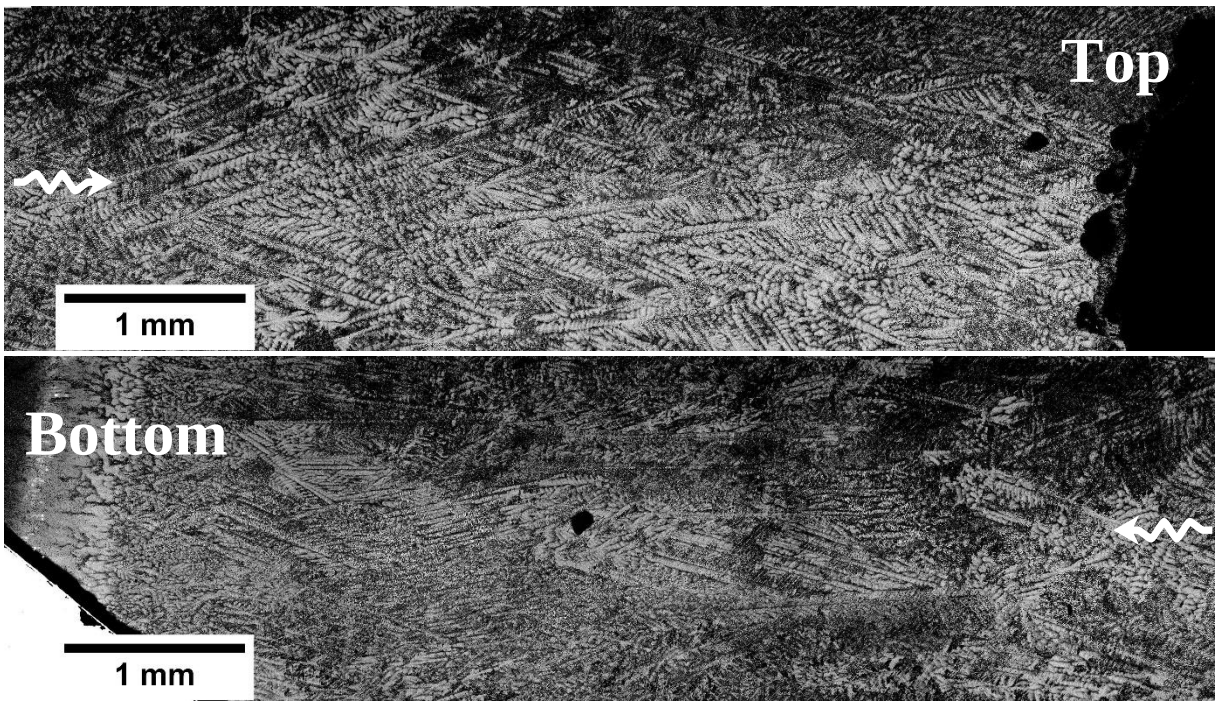

Figure 4.18: Continuous SEM BSE image of ingot inoculated with 9 hour milled Ti-Ta particles showing columnar grains present from bottom cap to top solidification shrinkage

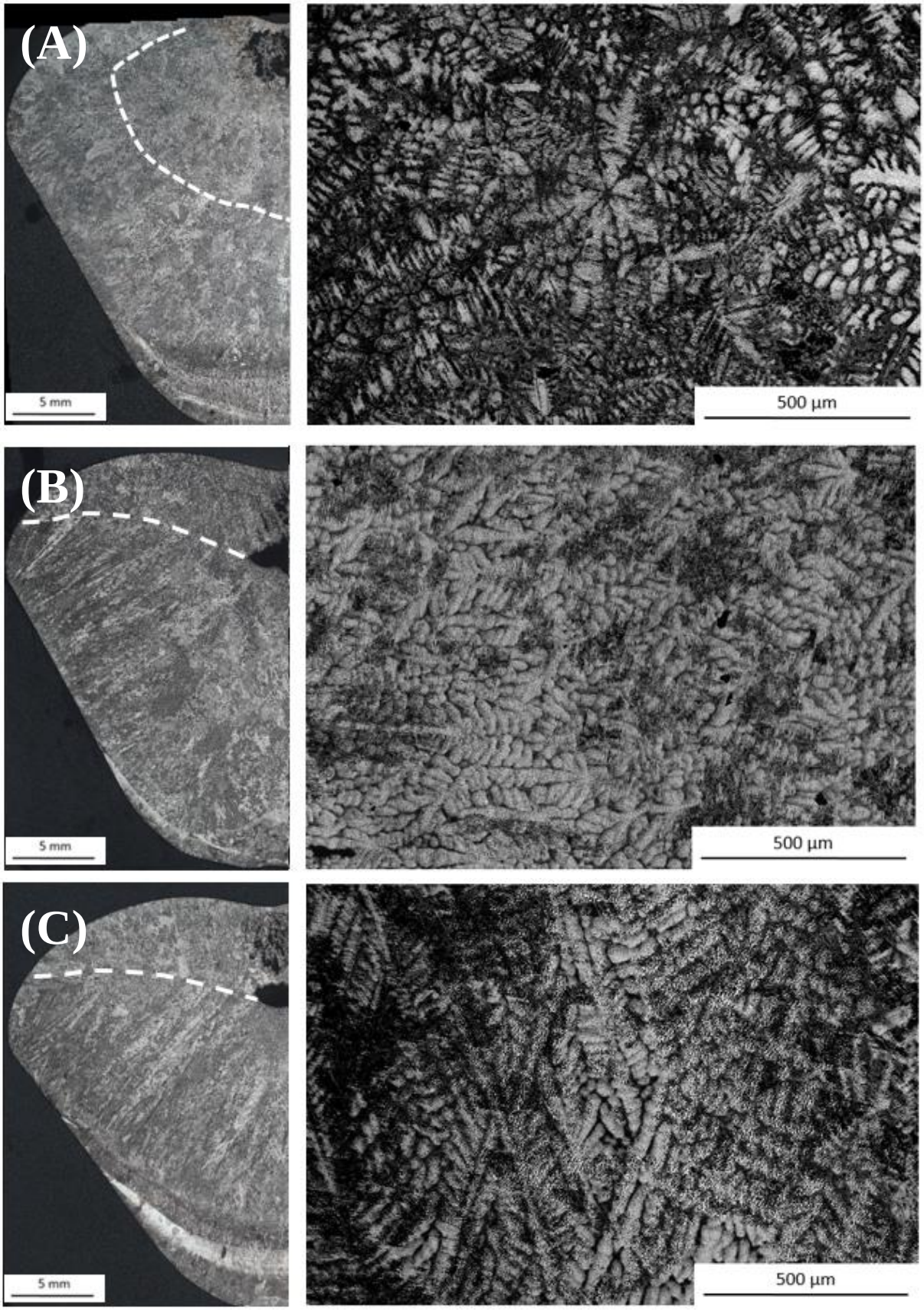

Figure 4.19: Example BF ingot cross sections and BSE micrographs with (A) 3 hr, (B) 6 hr and (C) 9 hr milled Ti-Ta particles

An attempt was also made at inoculating using Ti-Ta particles which had been milled for 1.5 hours. Particles of a larger size were tested to reduce the possibility that the particles could dissolve completely in the melt before solidification occurred. A cross section of the ingot prepared with these particles, returning to an interaction time of 20 seconds, can be seen in Figure 4.20. It appears similar to the other Ti-Ta inoculation trials with an indeterminate equiaxed fraction. The grains in the region expect to be equiaxed also appear similar to those of the 6 hour and 9 hour samples, as show in Figure 4.20. The grains appear much more columnar and again have shapes which make accurate measurement difficult.

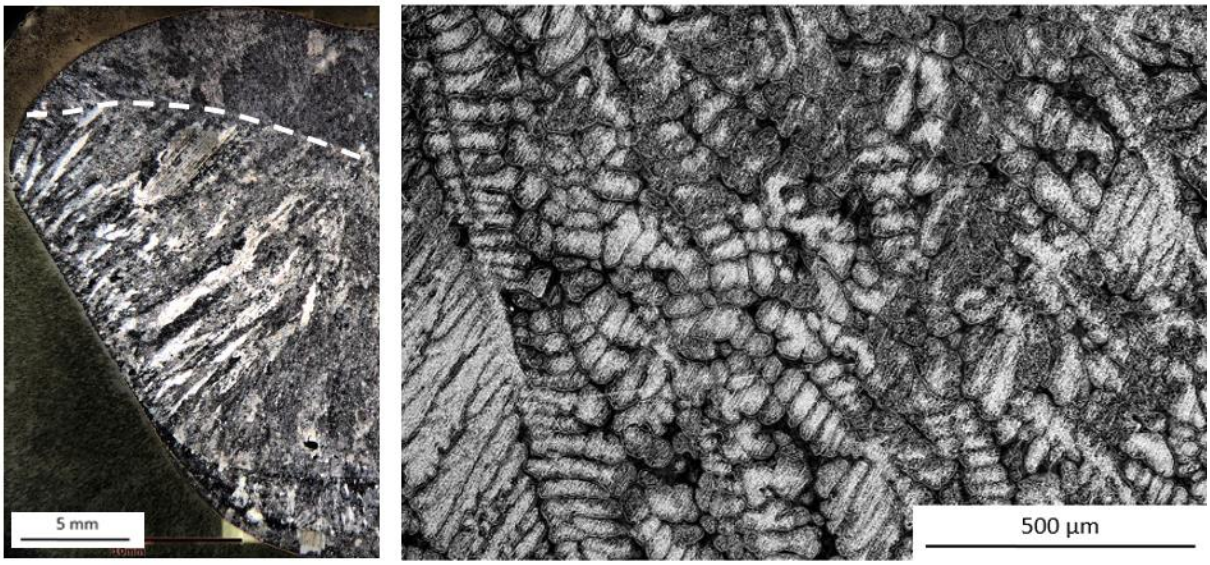

Figure 4.20: Example BF ingot cross sections and BSE micrograph for 1.5 hr milled Ti-Ta particles

4.4.1.2 Interaction Time Variation

In order to investigate the possibility that the particles milled for 6 and 9 hours dissolved completely in the 20 seconds of interaction time with the molten Ti-Al the inoculation trials with them were repeated but with a reduction of the interaction time by half, to 10 seconds. It can be seen in Figure 4.21 that there is once again an equiaxed zone present in the ingots, however, it is still quite small, less than 20% in either ingot. The measurements are only approximations as again the delineation between columnar and equiaxed zones was quite difficult, especially due to equipment malfunctions which prevented the use of the optical microscope for mosaic images. The cross sections were instead imaged by stereo microscope as single macrographs and the images processed to enhance the contrast and visualization of grains.

Higher magnification images were obtained by SEM in the equiaxed zone, as shown in Figure 4.21. The equiaxed dendrites appear closer in morphology to those found when using inoculants of the Ti-Al-Nb or Ti-Al-Ta systems than the previous Ti-Ta inoculations, however, they still maintain the incongruous nature as before making their measurement difficult. There appear to be some dendrites which appear as parallel stacked incongruous ovals, which may be BCC β-

Ti grains, however there remains dendrites in both ingots with angled secondary arms indicative of α-Ti HCP structure. The shape of the equiaxed grains also varies significantly with some grains having a primary arm significantly longer than the others resulting in a more columnar shape, an example of which is shown in Figure 4.21B where the equiaxed grain in the center of the grain has a long arm which extends out the right of the image, while others had a traditional equiaxed shape. Once again no inoculant particles were found in the equiaxed zone of the ingots.

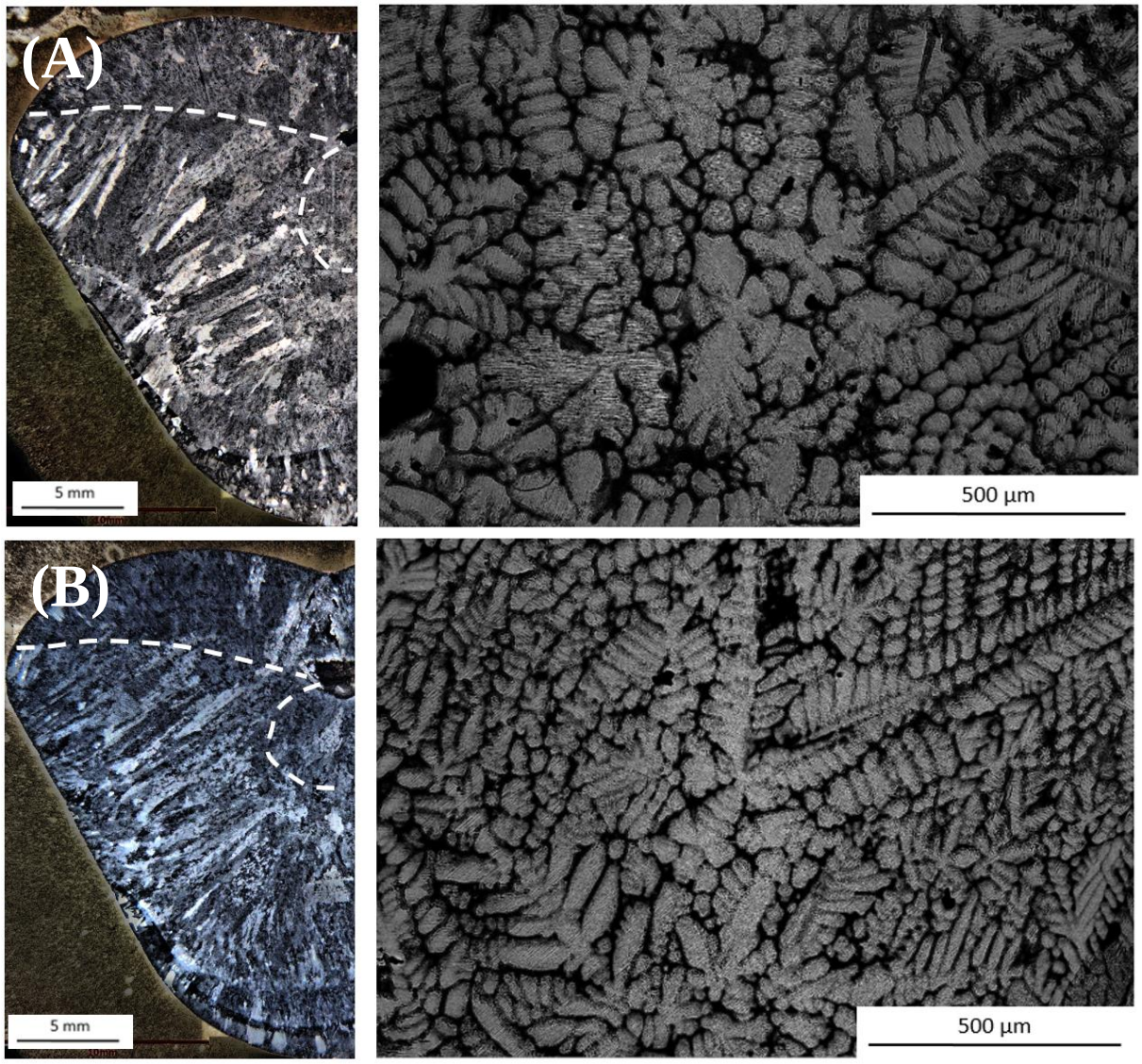

Figure 4.21: Example BSE micrographs with (A) 6 hr, (B) 9 hr milled Ti-Ta particles and reduced interaction time to 10 seconds

4.4.1.3 Remelted Bulk Alloy Reference Ingot

In order to evaluate the inoculation trials using portions of the large ingot as the bulk alloy a reference ingot was prepared. Cut portions of the large ingot totalling ~40g were remelted in the small cold crucible apparatus to replicate the procedure of the inoculation trials. The microstructure of the ingot was hard to distinguish. SEM investigations of the ingot cross

section did not reveal any dendrites cut in cross section well enough to determine their size. A representative micrograph and optical ingot cross section are shown in Figure 4.22. Some columnar grains were found growing from the top surface of the ingot as well as some columnar shaped grains just below the shrinkage porosity. These two factors combined leads to the conclusion that no equiaxed zone exists in the reference alloy. Additionally the columnar grains found had secondary arms growing at 60^{o} from the trunks rather than perpendicular as found with the individual ingots. This indicates that the solidification phase has changed from β (cubic) to α (hexagonal).

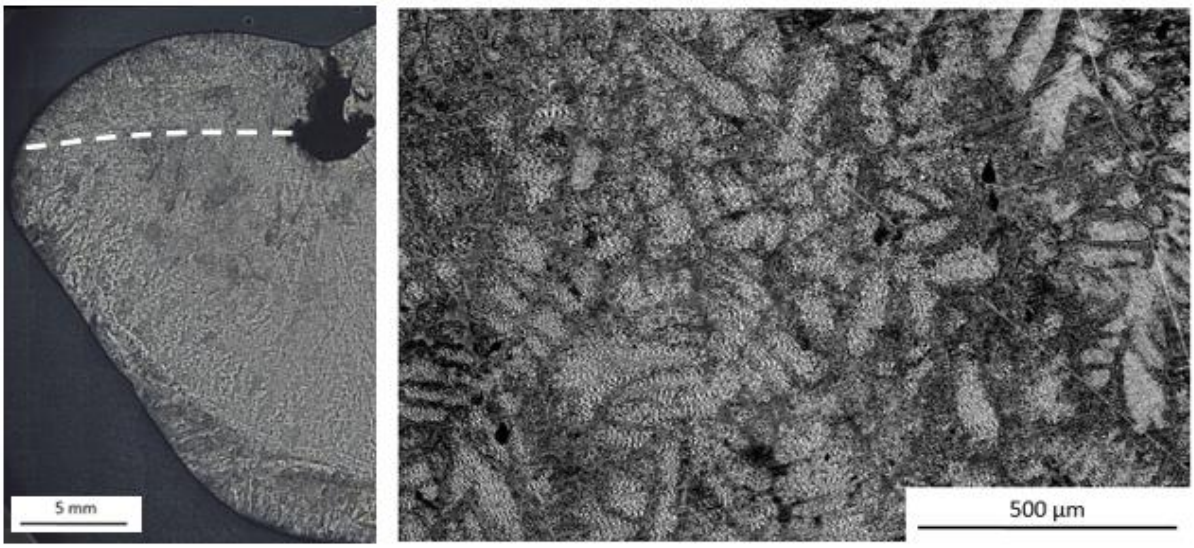

Figure 4.22: Example BF ingot cross sections and BSE micrograph of remelted large ingot

4.4.2 Individual Bulk Alloy Ingot Trial

A final inoculation trial was attempted with the Ti-Al particles using a bulk alloy which was fabricated individually rather than from the remelted large ingot. The same procedure was used as for the Ti-Al-Nb and Ti-Al-Ta trials, but using 1.5 hour milled Ti-Ta particles. The resultant ingot cross section and representative BSE micrograph can be seen in Figure 4.23. In contrast to the trial using the same particles and the remelted portion of the large ingot the inoculation trial was successful and the equiaxed fraction was increased along with a decrease in the equiaxed grain size. The equiaxed fraction was comparable to the other individual ingot trials, 69%. This is in contrast to when the same particles were tested with the bulk alloy from the large ingot and no equiaxed grains were found. The average equiaxed grain size was 359 µm. The grain morphology was similar to the ingot inoculated with 3 hour milled Ti-Al-Ta particles, dendritic but with branches which were not too fine.

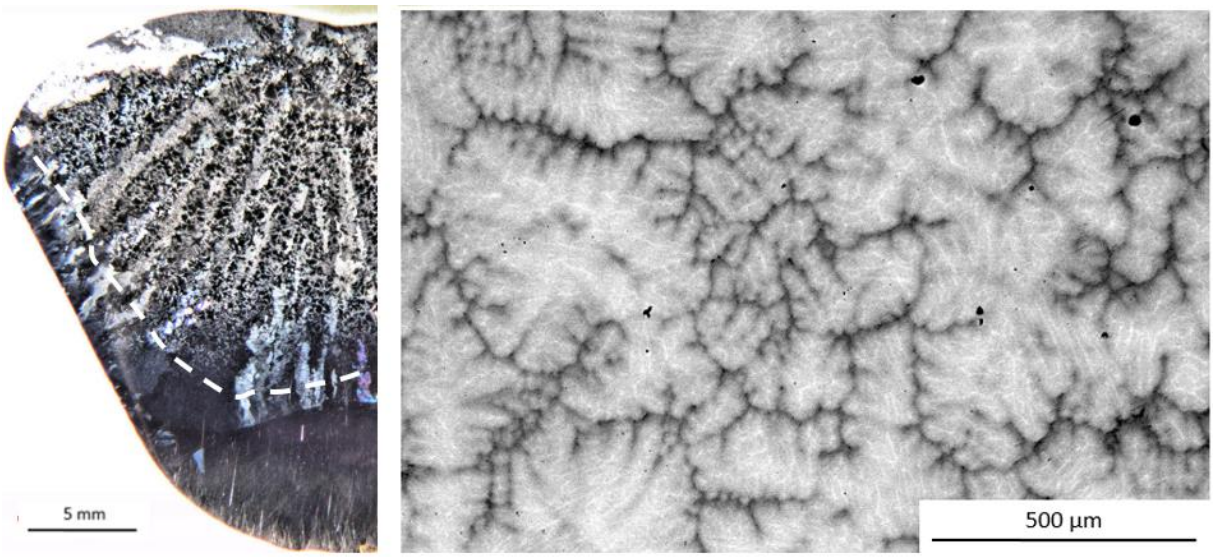

Figure 4.23: Example BF ingot cross sections and BSE micrograph for individually fabricated bulk alloy ingot inoculated with 1.5 hr milled Ti-Ta particles

The region of the ingot between the solidification shrinkage and bottom cap was almost completely equiaxed, as can be seen in Figure 4.24. A large Ti-Ta particle was present just above the bottom cap, just as in the other Ti-Ta trials.

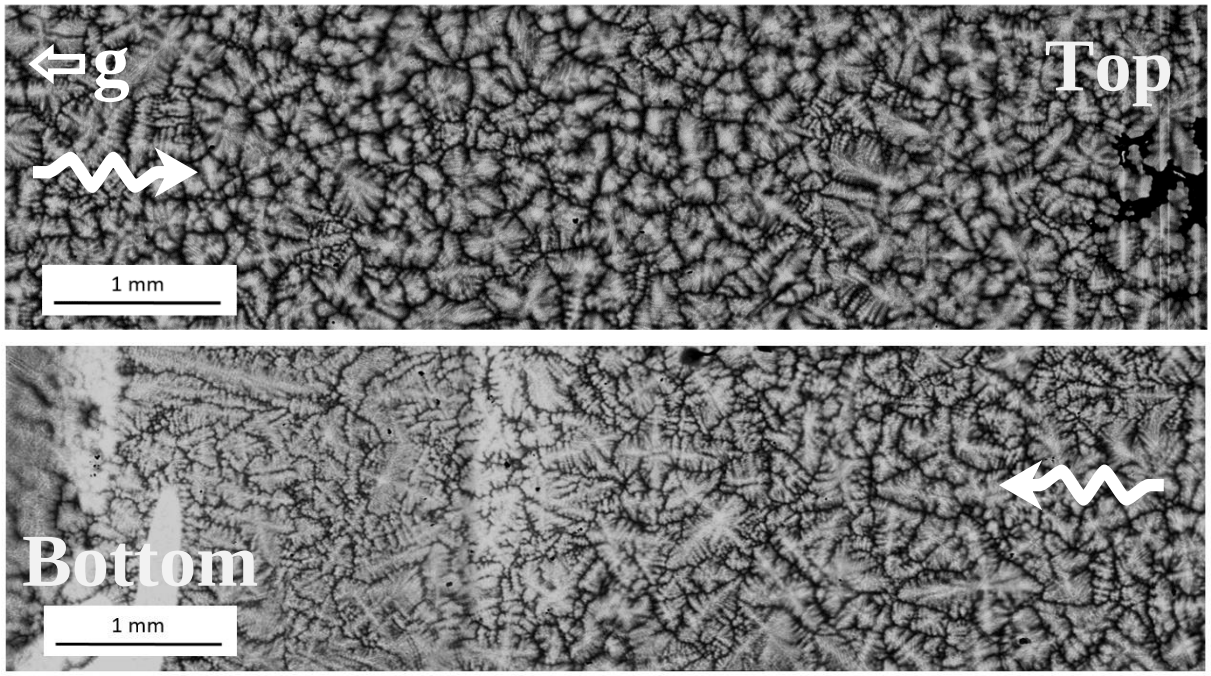

Figure 4.24: Continuous SEM BSE image of individual ingot inoculated with 1.5 hour milled Ti-Ta particles showing nearly total equiaxed structure

4.4.3 Summary

Four different particle size distributions of Ti-Ta were tested as isomorphic inoculants for TiAl. A large ingot was produced of the base Ti-46 alloy and used as the bulk alloy for six inoculation

trials. Each inoculant particle distribution was tested in the same manner as the other inoculants as well as the 6 hour and 9 hour distributions being tested with a reduced interaction time of ten seconds. None of these trials were successful at grain refinement. The ingots had a much more complex appearance to evaluate than the other trials. The solidification phase appeared to change from β-Ti in the previous trials to α-Ti in the trials where portions of the large ingot were used. None of the ingots produced had enough equiaxed grains present in their cross sections to adequately evaluate their grain size. The remaining 1.5 hour milled Ti-Ta inoculant powder was used in an inoculation trial with an individually fabricated bulk ingot. This trial was successful at grain refining and increasing the equiaxed fraction. Both the grain refinement and increase in equiaxed fraction were to the same degree as found with the ternary alloys and individually fabricated ingots. In all the Ti-Ta inoculation trials particles of Ti-Ta were observed settled to the bottom of the ingots, including "superlarge" particles which were greater than the measured D99s of their distributions.

4.5 Conclusions

Inoculants were tested from three alloy systems, Ti-Al-Nb, Ti-Al-Ta and Ti-Ta. Particles from the distributions shown in chapter 3 were mixed with aluminium powder and compressed into pellets which were dropped into the molten base metal and allowed to interact with the melt for 20 seconds before cooling to room temperature. The inoculants from the ternary systems were successful at both grain refining the base alloy and increasing the fraction of the ingots which were composed of equiaxed grains. To test the ternary alloys individual bulk alloys were fabricated for each inoculation trial. Ti-Al-Nb particles were tested which were drilled directly from the bulk alloy, cryomilled for 3, 6, 9 or 11 hours in air, cryomilled for 3 hour under Ar or cryomilled for 3 hours under air then heat treated. All of these particles both grain refined and increased the equiaxed fraction. A further trial where the particles were allowed to fully dissolve was also conducted and resulted in less grain refinement than the inoculation trials. Ti-Al-Ta particles were also tested which had been cryomilled for 3 or 9 hours and also grain refined the ingots. To test the binary Ti-Ta alloy a large ingot was fabricated of Ti-Ta which was then portioned and remelted to provide the base alloy for the inoculation trials. Ti-Ta particles which were cryomilled for 3, 6 and 9 hours were tested and did not grain refine or increase the equiaxed fraction in a discernable manner, however and increase in the columnar region was found. The 6 and 9 hour milled particles were tested with a reduced interaction time to 10s but these were also unsuccessful at refining the structure, larger particles which were only milled for 1.5 hours were tested but had similar effects on the ingot as the other Ti-Ta trials. A final trial was attempted with 1.5 hour milled Ti-Ta particles and an individually fabricated ingot which was successful comparably to the ternary alloys.

Chapter 5 Influence of Inoculant Alloys and Their Processing Parameters

While many of the particle distributions tested were shown to function as grain refiners in Chapter 4 the degree of their refinement was not uniform. This section looks at how the properties of the particle distributions effected their ability to grain refine. The effect of the size distributions is investigated as well as the alloy density and the interaction time between the particles and the melt before solidification.

5.1 Anomalous Ti-Ta Results

While the Ti-Ta particles were designed to have the greatest stability in the melt none of the inoculation trials which used them were successful at reducing the as-cast equiaxed grain size. Both the Ti-Al-Ta and Ti-Al-Nb particles were however successful and reduced the grain size. While no particles were found in the equiaxed region of any of the inoculated ingots some Ti-Ta particles were found to have survived processing. These particles were found in the bottom of the ingot, either in the columnar zone or in the semi-solid cap at the bottom of the ingot. Figure 5.1 shows SEM BSE images from this semi-solid bottom cap/ columnar zone for representative ingots inoculated with each alloy. Particles were only seen in the ingots inoculated with Ti-Ta.

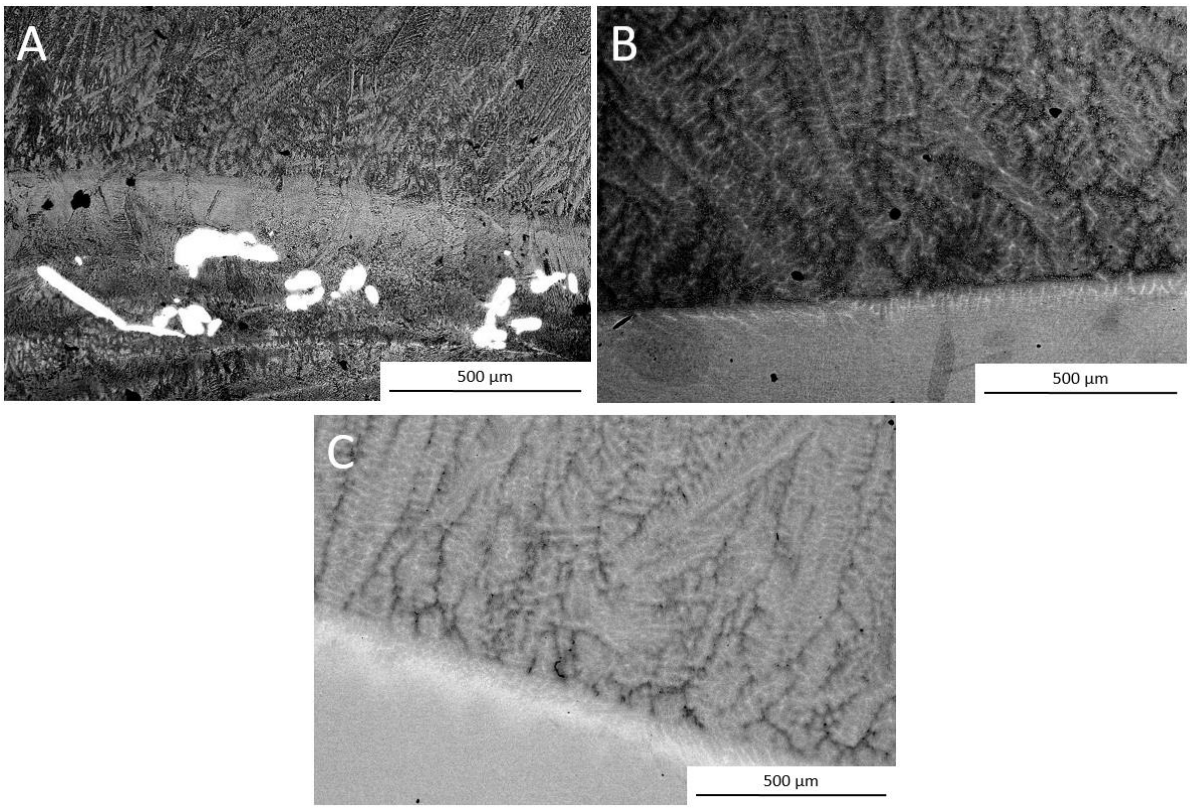

Figure 5.1: BSE images of bottom region of ingots inoculated with (A) Ti-Ta, (B) Ti-Al-Nb and (C) Ti-Al-Ta particles

EDX analysis was performed on the particles found in the ingots inoculated with Ti-Ta, an EDX map of a representative particle from the 1.5 hour inoculation trial is shown in Figure 5.2. The particles were confirmed to contain both Ti and Ta with compositions near the expected (Ti-47Ta).

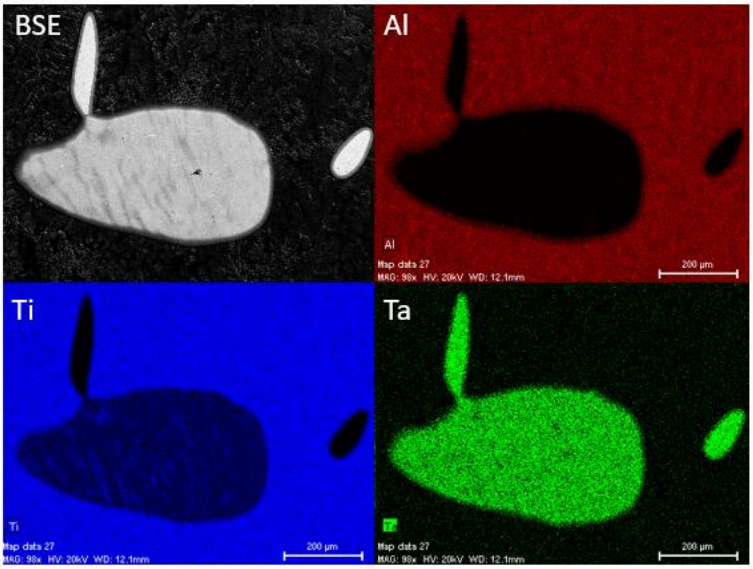

Figure 5.2: EDX analysis of particle located at the bottom of inoculated ingot showing composition to be Ti-Ta

5.1.1 Density Effects

Particles of Ti-Ta were found only in the columnar and bottom caps of their ingots, not in the equiaxed zone. Particles in these regions did not help form equiaxed grains as the region they are in has no equiaxed grains. The question is then how the Ti-Ta particles were deposited in this region when there are no Ti-Al-Ta or Ti-Al-Nb particles detected in the same regions of their respective ingots. The fluid flow of the molten Ti-Al alloy should be the same in each inoculation trial as the processing conditions remain constant, however, the particles may behave differently from one another in the melt as they have different sizes and densities. It is difficult to calculate how the particles move in the melt as the induction field induces complex 3-dimensional fluid flow into the molten drop which cannot be easily approximated. The solid bottom cap is humped in the center of the ingot and has a shape matching that of the fluid rolls. Many of the TiTa particles are found in this central humped region indicating that, rather than being carried by the fluid flow and dispersed throughout the ingot, they have been ejected from the flow and settled in this region where they are not useful for grain refinement of the equiaxed zone.

5.1.2 Oxygen Content

The ingots inoculated with TiTa also showed dendrite morphologies which matched the α phase (hexagonal) rather than β (cubic). This could be the result of oxygen pickup during the high temperature processing required to produce the inoculant alloy. β-TiTa has a large oxygen

solubility so this transition to α was not seen in the bulk inoculant alloy, however, the oxygen solubility is much less in β-TiAl [**34**]. EDX analysis of the Ti-Ta powders reported an oxygen content of 14.5 at% which is significant. EDX analysis of an inoculated ingot reported an average oxygen content of 5.8 at%, however EDX is not a reliable method to measure low concentrations of lightweight elements so these values are useful as guidelines but cannot be considered quantitative. An increase in oxygen content of the alloy may then also be poisoning its effectiveness at grain refinement as if the solidification phase has changed from β to α the lattice and phase matching for which the inoculant was designed no longer exist.

It should be noted that even if the alloy solidifies as α rather than β the TiTa inoculants should still be able to grain refine the casting. This is due to the Burgers orientation relationships present between the two phases, $(110)_\beta$ // $(0001)_\alpha$. This means that while the TiTa will not function as an isomorphic inoculant as phase matching is not present, it should function as an effective traditional inoculant. The low misfit between the cubic and hexagonal lattices, along the prescribed directions, should be effective at reducing interfacial energy between the inoculant particle and nucleating melt increasing the nucleation rate and decreasing the as cast grain size. Since such grain refinement was not observed the lack of grain refinement with the TiTa inoculants cannot be solely attributed to the change in solidification phase. Additionally an equiaxed region was only observed in the ingot inoculated with the largest (1.5 hr milled) particles. Since traditional inoculation is a particle size dependent process it could be that the equiaxed zone was caused by heterogeneous nucleation of the α phase from the larger TiTa particles. However, no TiTa particles were found in this region so its presence may be due to other effects.

5.1.3 Superlarge Particles

It can be noted that the mapped particle has a length over 600 μm and a width of 300 μm, this is significantly larger than the both the D50 (70 μm) or D99 (334 μm) for the distribution. The BSE image of the particle shows a somewhat banded structure which can also be seen particularly well in Ti composition map. This indicates that it exists as a single particle rather than an agglomeration of smaller particles. This is interesting as such large particles were not detected by SEM image analysis nor by DLS. The small number of these particles do not lend well to their detection by imaging methods, however, they should have been detected by DLS as their large volume makes up a significant portion of the distribution. It is possible that the superlarge particles were too large to be detected by the DLS apparatus used (2.5-875 μm detectable range used), the mapped particle was 600 μm long after dissolution and larger particles were also found in the as-cast ingots. A single particle of such size has a mass equal to 0.06 wt% of the distribution, compared to 0.02% for a particle identical to the D99 or 0.0002% for the D50. It then does not take very many large particles existing in the distribution to severely decrease the number of particles available for inoculation This could help explain why the Ti-Al trials did not show any grain refinement, as super large particles unaccounted for in the distributions reduced the number of active particles added to the melt.

5.1.4 Individual Bulk Alloy Trial

The individual bulk alloy trial with Ti-Ta inoculants was the only trial which resulted in grain refinement using the Ti-Ta inoculants, it was also the only Ti-Ta inoculated ingot which appeared to solidify as β-Ti. It is possible that the fabrication process for the large Ti-Al bulk ingot resulted in more oxygen pickup in the alloy than the process for the small individual ingots. The oxygen content within the inoculants was insufficient to change the solidification phase when an individually prepared ingot was used. As with the other Ti-Ta trials no remaining inoculant particles were found in the equiaxed zone but particles were found in the bottom of the ingot including at least one superlarge particle. It is interesting to note that the superlarge particle appears to be blocking the growth of columnar grains, shown in Figure 5.3, as the region around it is entirely equiaxed grains and the only columnar grain appears nearly half a millimetre away from the tip of the particle. This may explain why no large columnar zone is present between the shrinkage and bottom cap. Such a columnar blocking mechanism could also help explain the equiaxed zone of the 1.5hr collective bulk alloy trial.

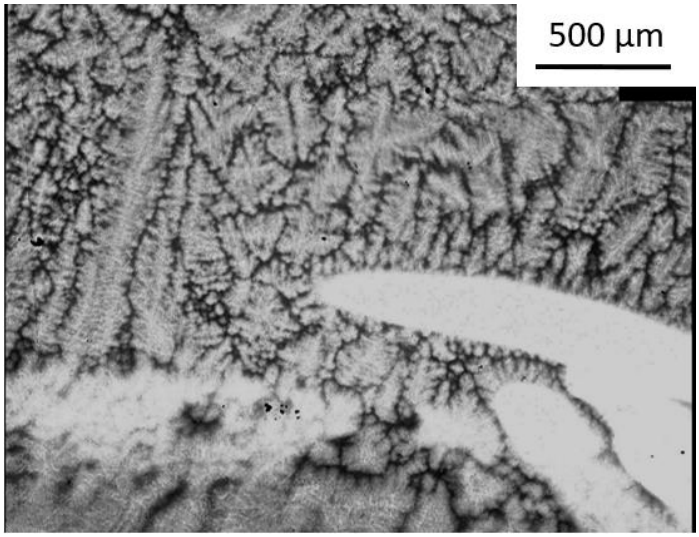

Figure 5.3: Superlarge Ti-Ta particle blocking growth of columnar grains

In contrast to the other individually fabricated bulk alloy inoculation trials the equiaxed grains do not appear homogeneous in size across the equiaxed zone. The grain size evolution across the ingot can be seen in Figure 5.4. Quantitatively the average grain size cannot be said to change significantly from the bottom of the ingot to the top. The minimum grain sizes measured remains constant across the ingot, approximately 250 µm, but the maximum size seems to decrease as the grains approach the shrinkage. This could also be the result of the settled particles hindering columnar growth. The hindrance of the columnar growth could lead to different solidification conditions such as an increase in undercooling which would lead to a different grain size. It is then difficult to attribute the grain refinement found in this trial to isomorphic inoculation by Ti-Ta. Small particles of Ti-Ta were found in other ingots indicating that they could survive processing and be located after solidification, however none were found in the equiaxed zone in this case even though grain refinement was observed. Additionally the

presence of a superlarge particle which blocked the growth of columnar grains changes the solidification conditions which could result in the change of grain size observed.

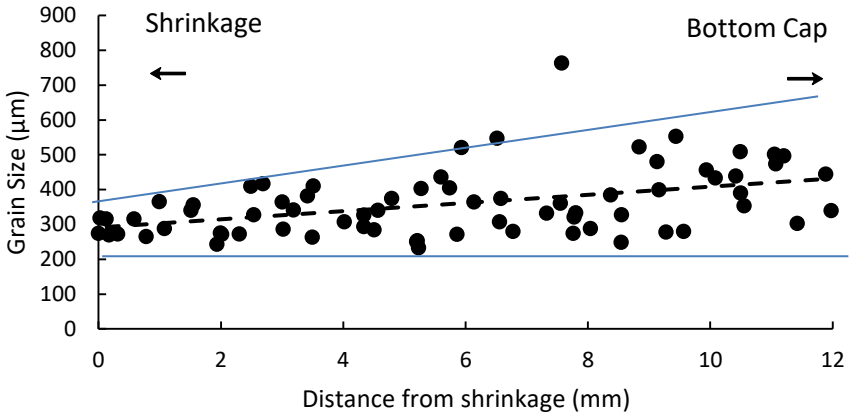

Figure 5.4: Grain size evolution across individually fabricated ingot inoculated with 1.5hr milled Ti-Ta particles

5.1.5 Summary

It is then likely that a combination of these factors lead to the TiTa particles being ineffective. The high density of the particles results in the particles settling to the bottom of the ingot removing the particles from the equiaxed zone where they are useful for decreasing the equiaxed grain size, ensuring the inoculants are ineffective. The presence of superlarge particles which account for a large portion of the inoculant mass added to the melt reduces the number of inoculants added to the melt. The inoculants which were added to the melt may be poisoning it against them by added oxygen and inducing a change of the solidification phase from β to α and the grain refinement mechanism from isomorphic to traditional inoculation. The critical factor is most likely the high density difference between the particles and the melt since the other factors would limit the grain refinement ability of the particles but not eliminate it.

5.2 Ti-Al-Nb and Ti-Al-Ta Grain Refinement

The two ternary alloys tested as isomorphic inoculants both were successful grain refiners. The degree of grain refinement observed was not constant between alloys and distributions implemented. The effect of the inoculant alloy and distribution are discussed along with a potential explanation for their anomalously high refinement efficiency.

5.2.1 Distribution Effects

All the inoculation trials with Ti-Al-Nb and Ti-Al-Ta particles were successful in both decreasing the equiaxed grain size and also increasing the fraction of the equiaxed zone in the ingots. The magnitude of the grain refinement and enlargement of the equiaxed zone depended on the alloy and particle size distribution used. It can be seen that the equiaxed grain size tended to decrease as the milling time increased except in the case of the 6 hour milled sample which

has a larger grain size than expected, however the grain size is still reduced compared to the reference or solutal samples. The increase of its grain size relative to the other inoculated samples is likely due to the increased Al content of the bulk alloy, further explanation can be found in Appendix A. Milling in Ar resulted in larger equiaxed grains than particles equivalently milled in air. The same was true for the resultant equiaxed fractions, milling in Ar was less effective at increasing the equiaxed zone compared to air. The equiaxed fraction stayed relatively constant between the air milled particles with the exception of the 11 hour milled sample which had a large unmelted Ti particle inherited from primary ingot elaboration and larger bottom cap present in the cross section. The Ti-Al-Ta particles reduced the grain size roughly the same amount as equivalently milled Ti-Al-Nb particles, however the three hour Ta containing particles did not increase the equiaxed fraction as much as the others.

It was also important to know the number of inoculant particles added in each inoculation trial. Since the mass of the inoculant particles added was measured, it could be used along with the size distributions obtained and calculated densities to determine the number of particles added. This was done assuming the particles were spherical and that all the particles in each size range had a diameter exactly the average of the maximum and minimum values of the range. Using the measured mass of inoculant (≈1g) and the calculated density of the inoculant alloy a total volume of inoculant introduced could be found. The particles were also assumed to be spherical when calculating their size from projected 2D areas, however, if an ellipsoid diverges from a spherical shape (with a constant average radius) its volume will decrease. The calculated number of particles then may be underrepresented if the particles vary significantly from spheres.

The size range of the two Ti-Al-Ta distributions tested are between the 9 and 11 hour milled Ti-Al-Nb particles. The two particle sizes both reduce the grain size somewhat less than that of the Ti-Al-Nb 11 hour milled distribution which has the closest D50 to the Ti-Al-Ta distributions used. However, when the number of particles introduced is considered the grain sizes are much closer to the trend of the Ti-Al-Nb particles. The Ti-Al-Ta trials introduced more particles than when the 9 hour milled Ti-Al-Nb particles were used but less than with11 hour Ti-Al-Nb particles. As the same mass of inoculant is introduced in each trial, particle size and number of particles introduced are directly correlated. If we compare Ti-Al-Nb (11h) and Ti-Al-Ta (9h) with roughly the same median particle size, we can see that the refining power of the Ti-Al-Nb is greater because the number of particles is higher, indicating that the critical parameter is not the size of the particles but rather the number of particles introduced. This is in direct contrast to traditional inoculation where the size of the particles introduced is the most critical as larger particles can nucleate new grains at smaller undercoolings [**142**].

The resultant grain size as powder size and number of particles introduced to the melt increase can be seen in Figure 5.5(a) and (b), respectively, for the Ti-Al-Nb and Ti-Al-Ta inoculation trials. The reported error is the standard deviation of the grain size measurements. Since only equiaxed dendrites with nearly complete cross sections are measured the number of grains measured is limited. Ingots with larger grain sizes will have fewer grains cut in cross section that may be measured and thus the standard deviation of their measurements will be larger, this

is also true of structures which are more dendritic compared to globular. This may obscure some of the trends observed but ensures that the reported grain sizes are representative of real structures within the ingots. When evaluated based on the size of the particles introduced the Ar milled sample does not appear to behave significantly differently from those milled under air. While milling under Ar for 3 hours resulted in larger particles than the same time under air the resultant grain size and equiaxed fraction are roughly what would be expected for particles milled under air with the same size. The Ar milled powders also behaved as the particles milled in air with respect to the resultant equiaxed fraction. The six hour milled sample (D50 = 160 μm) resulted in a larger grain size than expected. Since each bulk alloy was produced individually some variation in the composition is to be expected. This variation may account for the six hour inoculations apparent deviation as it has the leanest Al composition of all the inoculated ingots. This is important since the grain size has been shown to increase in ingots produced with similar processing as Al content decreases due to changes in the dendrite fragmentation mechanism [**186**]. This means that while the grain size may be larger than expected in the ingot inoculated with the six hour milled particles the reduction in grain size due to the inoculation may be greater than shown, since the bulk alloy would have had a larger grain size than the measured reference sample due to its decreased Al content. Further analysis is presented in Appendix B showing the effect of Al content on the grain size.

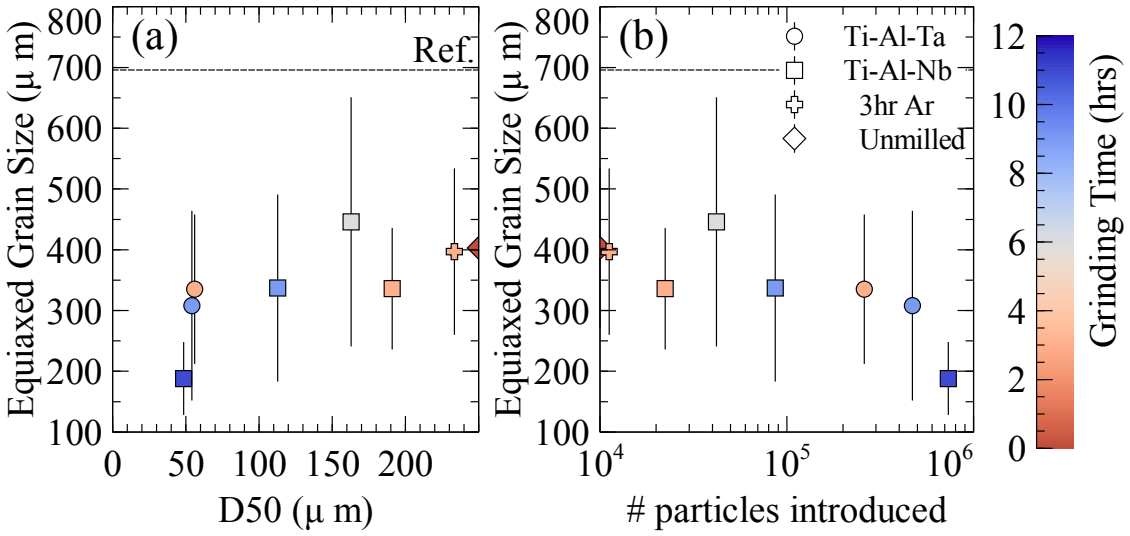

Figure 5.5: Influence of (a) particle size and (b) number of particles introduced on equiaxed grain size. The error bars correspond to the standard deviation of grain size measurements.

Using the average equiaxed grain size the grain density in the equiaxed zone (#/cm^3) can be compared to the density of particles added to the melt (#/cm^3), as shown in Figure 5.6(a). This assumes that all the particles added were evenly distributed in the equiaxed zone. This gives the most pessimistic results of inoculant efficiency as this is the maximum density the particles could have during solidification, if they were evenly dispersed throughout the ingot their density in the equiaxed zone would be reduced. It is also assumed that no particles completely dissolve, meaning that the same number of particles is present during solidification as was added to the melt. In Figure 5(a) the dashed line indicated a 1:1 ratio, where each particle would add a single grain to the solidified ingot. In every case except the 9 hour Ti-Al-Ta (which still close to this

1:1 ratio) the grain density is larger than the introduced particle density, this means more grains were formed than particles added to the melt. Moreover, it can be seen that when the number of particles introduced exceeds $5x10^4$ particles/cm^3 the efficiency tends towards 1. When fewer particles are added the grain size does not change drastically, rather the efficiency of the particles for isomorphic inoculation increases. This is in strong contradiction to traditional inoculation where the number of grains formed is significantly less than the number of particles added to the melt [**9**,**10**]. The authors previously proposed that this drastic increase in efficiency was due to the suppression of the nucleation step allowing direct particle growth [**187**] and the increase above a 1:1 ratio of particles to grains due to a process of particle breakup. The effect of particle size on particle break-up is estimated in Figure 5(b), where the evolution of the number of equiaxed grains formed by single particle is compared with the number of introduced particles, the distribution D50s are indicated. There is a sharp increase in number of grains formed per particle with large particles compared to small particles. The smaller particles (~50 μm) result in 1 or 2 grains formed per particle with both Ti-Al-Nb and Ti-Al-Ta while the Ti-Al-Nb particles of intermediate size (100-170 μm) have 2-5 grains formed per particle and the Ti-Al-Nb particles larger than 170 μm result in more than 10 grains formed per particle. It is then possible that the close diffusivity and processing method results in particles which break up in roughly equivalent manners between the two alloys. The difference in effectiveness may then be attributed to the mechanical properties of the particles which behave differently under milling resulting in different distributions, and a greater difference in particle number for roughly equivalent particle D50s. The general efficiency of the inoculation then depends on the number of particles introduced, however, the particle size distribution must also be taken into account since if the particle size is large significant particle breakup may occur while when the particle size is low the breakup factor tends towards one. This means when the introduced particle size is low the correlation between number of particles introduced and number of grains formed is stronger than with large particles where the distribution may be more affected by interaction with the melt.

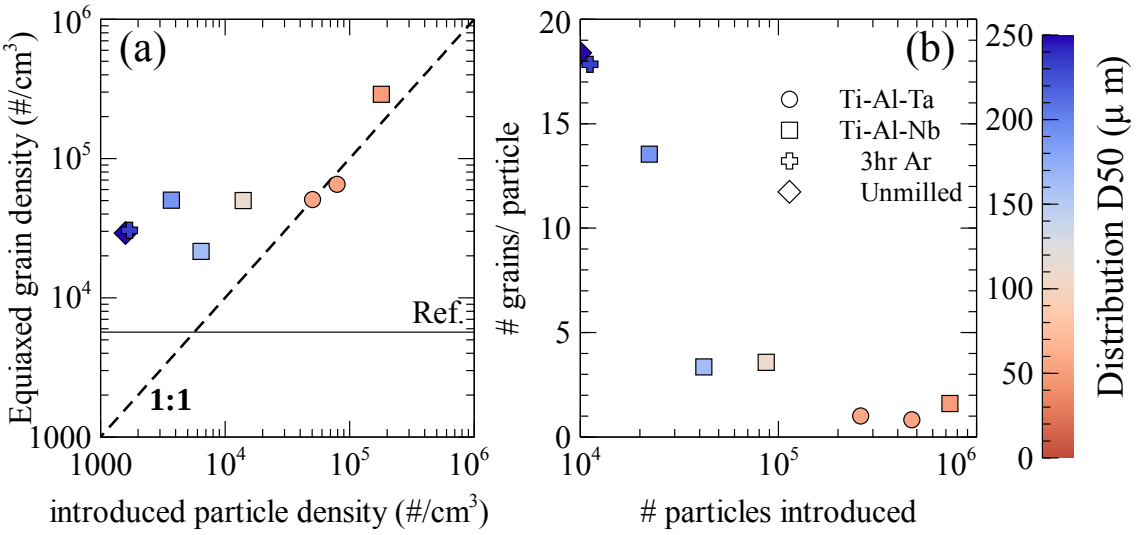

Figure 5.6: (a) Influence inoculant particle density and (b) Relationship between # of grains formed by each inoculant and number of particles introduced (only in the equiaxed zone).

5.2.2 Particle Break Up

A particle of 9 hour milled TiTa was also evaluated, in this case after an interaction time of 10s. The general location of the particle is shown in Figure 5.7. It is located within a grain and not attached to a grain boundary. The particle appears to be approximately 35 μm in diameter.

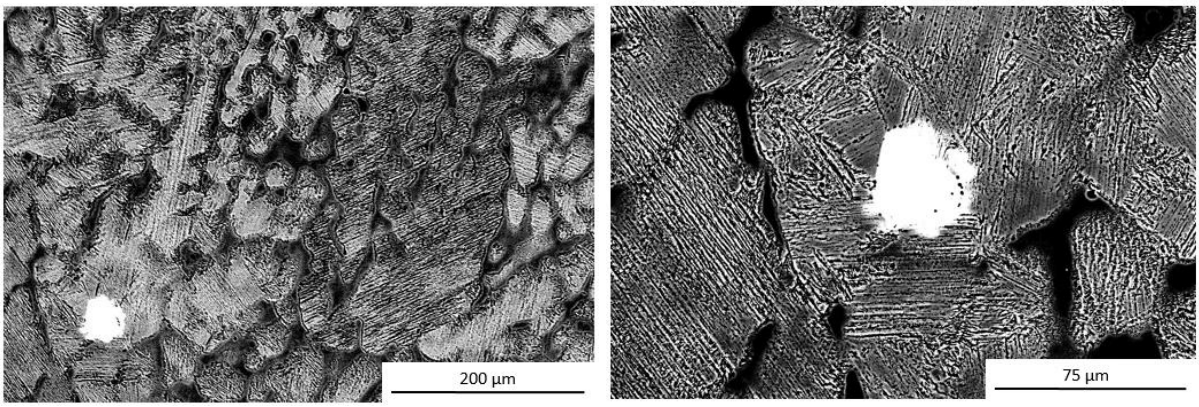

Figure 5.7: SEM BSE images showing region of columnar zone where the particle of interest was located

The process of particle breakup was observed in this particle. In Figure 5.8, the bright Ta rich regions are portions of a particle which are in the process of breaking up while the dark regions are the bulk alloy. By adjusting the brightness and contrast when obtaining the images the particle shape can be seen to vary from a monolithic single particle to a collection of smaller particles separated by regions of lower Ta concentration. This may occur by preferential dissolution [**11**] and/or impingement of the liquid along the grain boundaries of the particle [**188**]. Such impingement or wetting of a liquid like phase along grain boundaries has been observed in-situ along Al grain boundaries by liquid Ga [**189**]. Such wetting may occur if the grain boundary energy is higher than that of two solid liquid interface [**190**] i.e. $\sigma_{\beta/\beta} > 2(\sigma_{\beta/\ell})$. In this case the liquid will fully wet along the grain boundary which would permit separation of the particles in the melt along the grain boundaries. The dark liquid can be seen to ingress along preferential paths resulting in the breakup of the particle. As the size of the particles increases so does the number of grains formed by each particle. This could be due to an increased number of cracks or grains present in each large particle when compared to the smaller ones, as they have been milled for less time. These cracks which on further milling result in particle breakup during milling may act as preferential dissolution paths in the melt resulting in a larger breakup effect during inoculation. This would also explain the decrease in the number of grains formed by each particle as the number of particles introduced increases. The smaller particles which were introduced in more plentiful numbers were also more likely to dissolve completely and less likely to break up into more particles. Again the breakup and dissolution of particles likely reduces the global maximum and increases the global minimum number of particles present on solidification, the number and size of particles introduced to the melt are indicative of, but not entirely representative of, the distribution present on solidification.

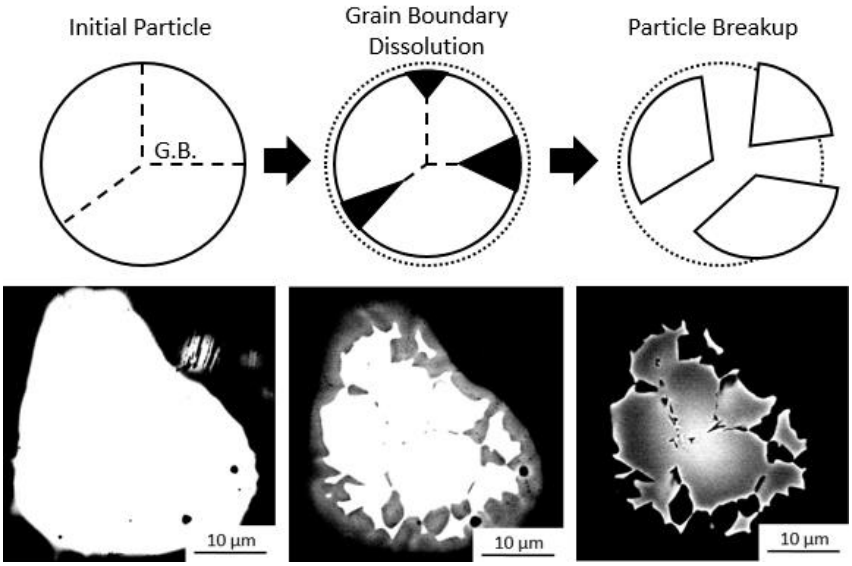

Figure 5.8: Schematic of particle breakup process: whole polycrystalline particle, preferential grain boundary dissolution, particle breakup and BSE micrographs of Ti-Ta particle in solidified ingot demonstrating particle breakup by adjusting imaging contrast

5.3 Particle-Melt Interactions

It is then important to consider the interaction between the inoculant particles and the molten bulk alloy. This includes both the movement of the particles within the melt, as the Ti-Ta particles primarily settled to the bottom of the ingots, and the diffusive behaviour between the particles and the melt.

5.3.1 Effect of Particle Size and Density on Velocity in the Melt

When considering the movement of the particles in the fluid flow both the relative density of the particles and their size are important. The deposition of TiTa super large particles in the bottom of the ingots make sense as they are both large and much denser than the liquid. The measured TiTa distributions however had smaller D50s and D99s than the Ti-Al-Ta or Ti-Al-Nb particles. It is then necessary to quantify how the particles move in the melt depending on the alloy (density) and milling time (size). In order to do any calculations related to the flow of the molten melt the viscosity (η) and density (ρ) of the liquid need to be determined. Measurements of the physical properties of molten metals are non-trivial, as such values must be found which most closely relate to the Ti-46Al alloy of interest. The viscosity of different Ti-Al-Nb alloys was investigated by Zhou et al. and given for a Ti-45Al alloy, suitably close to the Ti-46Al alloy of interest, by [**191**]:

$$\eta_{Ti45Al} = 0.921 \exp(1.114 \times 10^4 / RT) \quad mPa\ s$$

where R is the ideal gas constant and T the temperature in kelvin. The density of a liquid (ρ_L) Ti-45.5Al-8Nb alloy, close to the alloy of interest however higher Nb content may result in

calculated densities higher than reality, was determined as part of the European IMPRESS project and is given by [**192**]:

$$\rho_L = 3.85 - 4.57 \times 10^{-4}(T - T_L) \quad g/cm^3$$

where T is the temperature of the melt and T_L the liquidus temperature of the alloy. This equation gives a higher density at the liquidus temperature than calculated for solid β Ti-46Al (3.85 vs 3.55 g/cm^3) due to the higher Nb content, however, no more suitable data could be found.

As the problem of determining how the particles move within the 3-D liquid flow loops, along with the effects of the magnetic field of the induction coils, would require a complex mathematical model to evaluate effectively a simplification of the problem is desired to roughly estimate how the particles will move relative to on another. One such simple calculation is the terminal settling velocity of the particles in molten TiAl which is no longer flowing. This is representative of the maximum velocity the particles can settle at during the cooling of the melt and its solidification. A force balance on the particle in a static fluid yields a terminal velocity equation of [**193**]:

$$V = \sqrt{\left(\frac{4}{3}\right)\frac{gD}{C_d}\left(\frac{\rho_s - \rho_L}{\rho_L}\right)}$$

where g is the acceleration due to gravity, D the diameter of the particle, C_d the drag coefficient and ρ_s and ρ_L the solid and liquid densities respectively. If the particle is assumed to be spherical the drag coefficient can be assumed to be 0.47 if it is in laminar flow [**193**]. Applying this to the different alloys and particle sizes gives velocities as can be seen in Figure 5.9 along with the D50s of each distribution. The terminal velocities of the distribution D50s remain below 6 cm/s. The maximum D50 velocities for each alloy were 4.45, 2.08 and 5.09 cm/s for the Ti-Al-Nb, Ti-Al-Ta and Ti-Ta distributions respectively, in each case the largest D50 had the largest velocity. The superlarge particle shown in Figure 5.2 is also shown as a blue X and has a velocity of over 13 cm/s, more than double that of the D50s, which helps explain how the super large particles are so easily found at the bottom of the ingots. For equivalent particle sizes and grinding times the TiTa particles will then settle out of the equiaxed zone much faster than the Ti-Al-Nb or Ti-Al-Ta particles. However, the smaller TiTa distributions have velocities within the range of the larger sized particles of the other alloys when they were introduced to the melt. It is however possible that the increased survivability of the TiTa particles is a detriment to their effectiveness as inoculants as dissolution will decrease the size of the Ti-Al-Nb and Ti-Al-Ta particles once they have been added to the melt to a greater extent than the Ti-Ta particles. This means that the effective settling velocities may still be greater for Ti-Ta particles on solidification or after a set period of time in the melt than the particles of the other alloys.

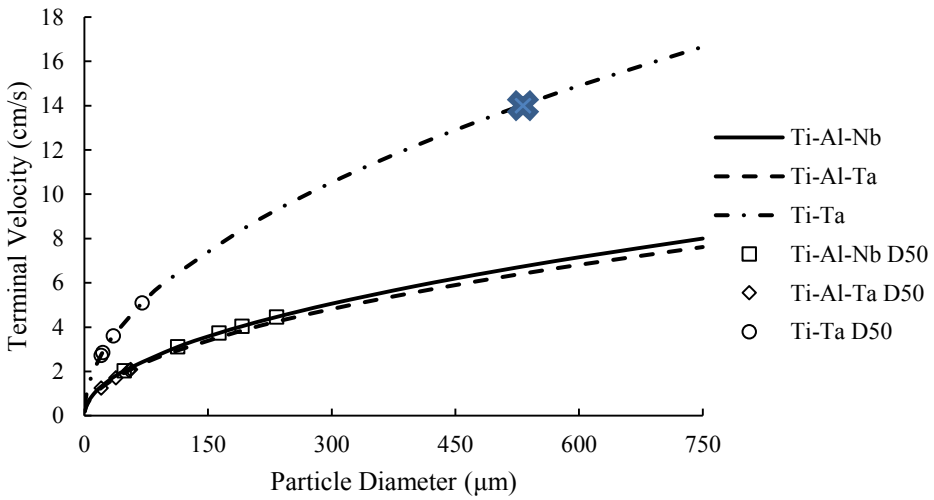

Figure 5.9: Terminal settling velocities of particles in unstirred melt.

5.3.2 Diffusion between Particles and Molten Alloy

In order to evaluate the diffusivity between the inoculant particles and the melt EDX line scans were conducted across Ti-Ta particles which were found in the as-cast ingots. Ti-Ta particles were evaluated since they were the only particles found in the ingots after casting. For illustrative purposes a 9 hour milled Ti-Ta powder with only a 10s interaction time is shown here, 9 hour and 6 hour particles after 20s of interaction time analysis are presented in Appendix C . The particles selected had similar sizes on solidification (~65 μm) this means that the 20s particle was likely a larger particle when it was introduced to the melt as it had longer time to dissolve in the melt. The general location of the particle, the particle itself and the particle investigated after 20s interaction time can be seen in Figure 5.10. A particle was chosen as far from the solid cap at the bottom of the ingot as possible. The particle had a smooth two phase solid/liquid envelope and jagged solid envelope. The depth of the ingresses into the solid and their distance from one another were similar regardless of interaction time, ~5 μm and ~11 μm respectively. The average width of the two phase region for the 10s particle is smaller however (2.9 μm) than that of the 20s particle (4.1 μm). It is then likely that the distance between the ingresses and their depth are intrinsic to the particles, possibly due to preferential grain boundary dissolution, while the width of the two phase region is more related to the interaction time.

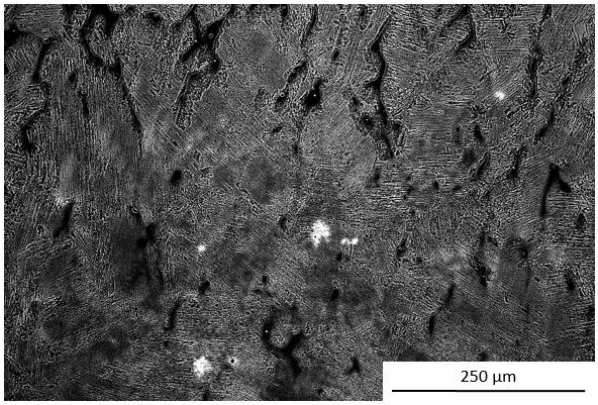

(A)

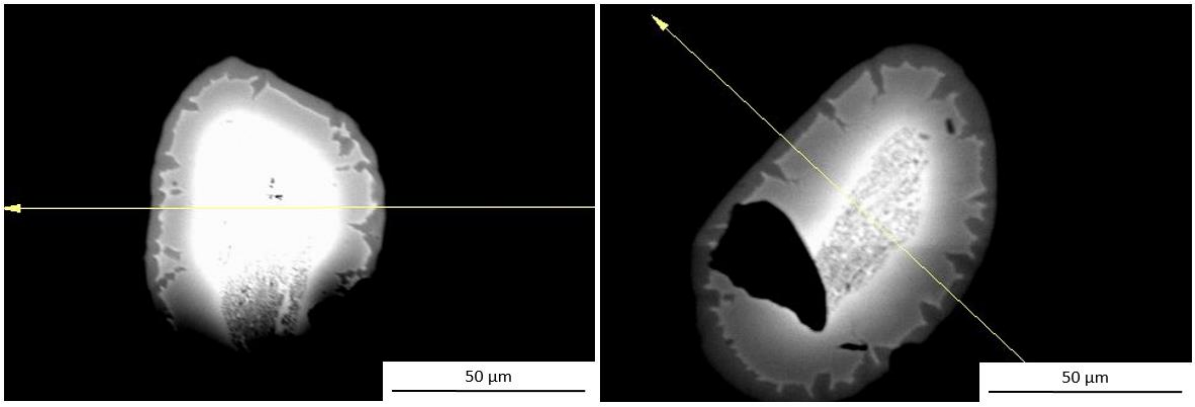

(B) (C)

Figure 5.10: SEM BSE images showing (A) region of columnar zone where the particle of interest was located and 9 hr milled TiTa particle after (B) 10s and (C) 20s interaction time

An EDX line scan was performed across the particle to find the composition gradients, as shown in Figure 5.11. The bulk and center of the particle roughly show compositions as expected, Ti-46Al and Ti-47Ta respectively. The Al diffusion length is further into the particle than the Ta diffusion out. The Al diffusion into the particle is less symmetric in this case, diffusing nearly 20 µm from the solid/ two phase interface on one side and less than 15 µm on the other. In both cases the diffusion is over a shorter distance than found in the 20s particle, which makes sense due to the reduced time for diffusion. It is interesting to note that on the side with a further Al diffusion distance the Ta concentration drops almost immediately to 0 outside of the two phase region while on the side with a shorter Al diffusion distance the Ta diffuses nearly 5 µm into the bulk from the two phase region.

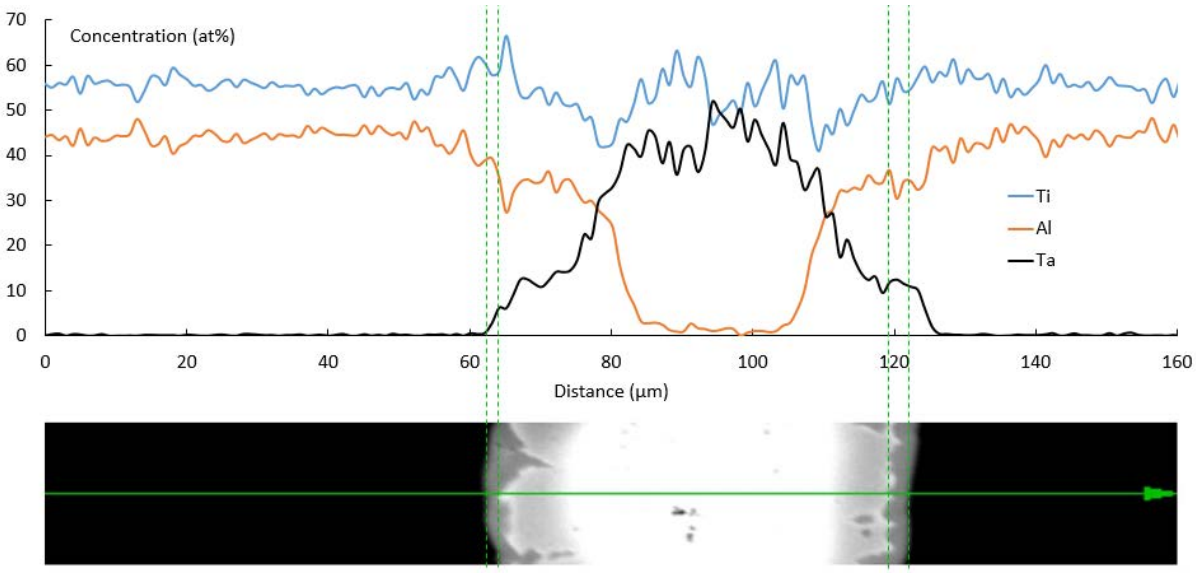

Figure 5.11: EDX line scan across 9 hr cryomilled TiTa particle after 10s interaction time

The interface compositions can be compared to the phase diagram to find the temperature of the interface, for the 10s particle this is shown in Figure 5.12. This method gave an interface Temperature of 1950 K. Since the interface temperature is the same for particles evaluated after 20s interaction time it can be assumed that the particles have reached thermal equilibrium with the melt and the interface temperature can then be taken as the temperature of the melt. This means that in these trials the melt was at 1950K, or a superheat of 137°. This also means that the particles in the 20s interaction trial spent at least 10s at 1950K.

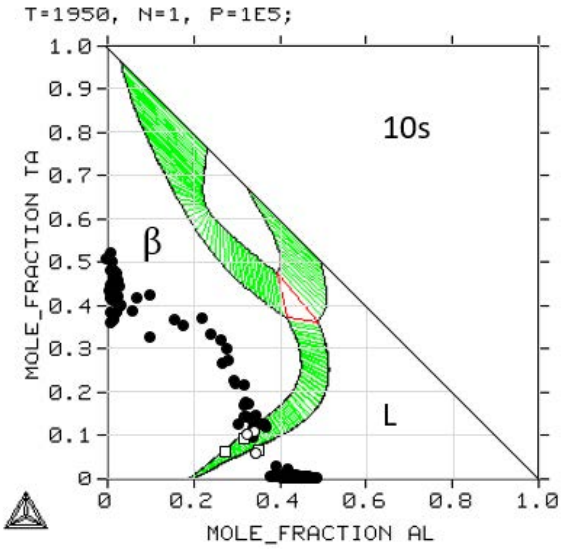

Figure 5.12: EDX profile showing interface compositions (hollow points) of particle after 10s interaction time compared to isothermal section of the Ti-Al-Ta phase diagram at 1950 K

After only 10s Al has already diffused quite far into the Ti-Ta particle and the Ta concentration within the particle has also been reduced. Additionally the slope of the concentration change on the isothermal section of the phase diagram shown in Figure 5.12 is quite steep below 35% Ta or above 20% Al. Both these factors indicate that diffusion is quite fast between the particles

and molten alloy. If this is the case for the Ti-Ta particles which were designed to be the most stable the ternary inoculants would experience even greater interdiffusion between themselves and the melt. This also explains why none of the ternary particles were found in the as-cast ingots as there would be very little atomic contrast between the particles and the bulk since significant diffusion between them has occurred.

5.4 Conclusions

It was found that the grain refinement due to the inoculants was dependent on the number of particles added to the melt as well as their size. In each successful inoculation trial more new grains were formed than particles added to the melt. This is in direct contrast to traditional inoculation where many particles are required to form a single new grain. This is attributed to a change in mechanism from traditional inoculants acting as nucleation sites while the isomorphic inoculants act as formed nuclei and direct centers of growth. The particles were seen to exist in two size ranges for inoculation. Particles whose distribution had a D50 below 200 μm were seen to be responsible for forming less than 10 new grains each, while particles with a distribution D50 greater than 200 μm were found to form more than 10 new grains each.

While the TiTa particles were not successful at reducing the grain size of the ingots they provide insight into the mechanisms occurring between the melt and the particles. The high density and presence of superlarge particles within the distributions were the likely cause of the failure of the TiTa particles to grain refine. The superlarge particles reduce the number of particles added to the melt as they make up a significant portion of the mass percent inoculants added to the melt, the high density of the particles cause them to settle quickly in the melt and become trapped in the columnar and semi-solid cap regions of the ingot, rather than being spread into the equiaxed zone to grain refine. Additionally the increased stability of the TiTa particles allowed them to fully survive the melt and be analyzed after solidification. From the interface temperatures after 10s and 20s interaction times the melt was found to be at 1950 K, a superheat of 137^{o}. The interface between the particles and melt was seen to be rough and consist of many large ingresses toward the center of the particles attributed to preferential grain boundary dissolution. The steep composition gradients and fast diffusion between the particles and the melt also explain why no ternary particles were found in their ingots.

Chapter 6 Inoculant-Melt Interactions

It was shown in Chapter 5 that the grain refinement effect of isomorphic inoculants is dependent on the number of inoculants present in the melt. Two competing effects on the number of particles which remained in the melt were postulated, total dissolution of the particles and breakup of particles by preferential grain boundary dissolution. This chapter aims to make strides in quantifying these effects to better estimate the real number of particles in the melt during solidification.

6.1 Inoculant Alloy Interaction with Melt

As no particles were found in the ingots which were successfully grain refined another method had to be developed in order to see the interface between the inoculants and melt. A sample of an inoculant alloy which could survive the melt was necessary. In order to do this a rod of Ti-10Al-25Nb was fabricated which could then be inserted into molten Ti-46Al in order to approximate the behaviour of the two alloys in the inoculation trials.

6.1.1 Rod Dipping Procedure

In order to see the interface between Ti-Al-Nb and Ti-Al after the two have interacted in similar conditions to the inoculation trials a sample of Ti-Al-Nb of sufficient size was needed to place in the melt. A rod was chosen since it could be fabricated easily in our apparatus and introduced to the melt in a controllable manner. The rod was formed by vacuum pulling as detailed in Appendix D. Once the rod assembly was prepared it could be used for a dipping experiment. A bulk Ti-46Al alloy was prepared in the same manner as for the inoculation experiments. The same procedure was used as in the inoculation trials but with the Ti-Al-Nb rod in place of the inoculating pellet. The rod was held away from the bulk alloy until it was fully molten, the rod was then inserted directly into the melt and held at temperature for 20 seconds before the furnace power was turned off and the melt allowed to solidify. The assembly of the rod and ingot was cut along four planes as shown in Figure 6.1. Each of these planes were metallographically prepared in the same manners as outlined previously. Planes A, C and D were circular cross sections of the rods diameter while plane B was a rectangular cross section along the length of the rod. Planes A and B were used for investigations of the melt/rod interface which follow, while planes C and D were useful for the rod grain size analysis presented in Appendix D.

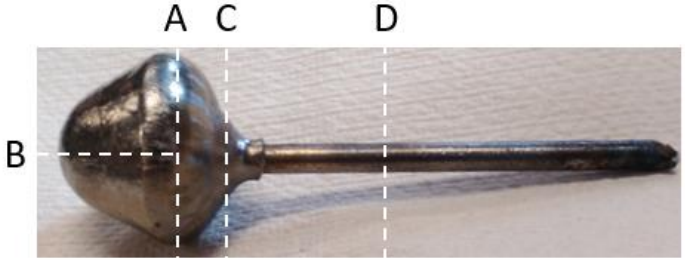

Figure 6.1: Ti-Al-Nb Rod in Ti-Al ingot and cutting planes for metallographical preparation

6.1.2 Dissolution of Rod in Melt

The first investigations of the rod were conducted by optical microscopy. Optical micrographs of both section A and D are shown in Figure 6.2. The optical micrograph of the rod after interaction with the melt shows radial columnar growth in the bulk originating from the rod giving the micrograph the appearance of a sun or star. The rod appears less uniform in its circularity after interaction with the melt than before. Using ImageJ software both cross sections were matched to a circular area. The rod had a measured area of 16.7 mm^2 before interacting with the melt and 15.0 mm^2 after. This corresponds to equivalent diameters of 4.6 mm and 4.4 mm, a radial dissolution of 125 μm.

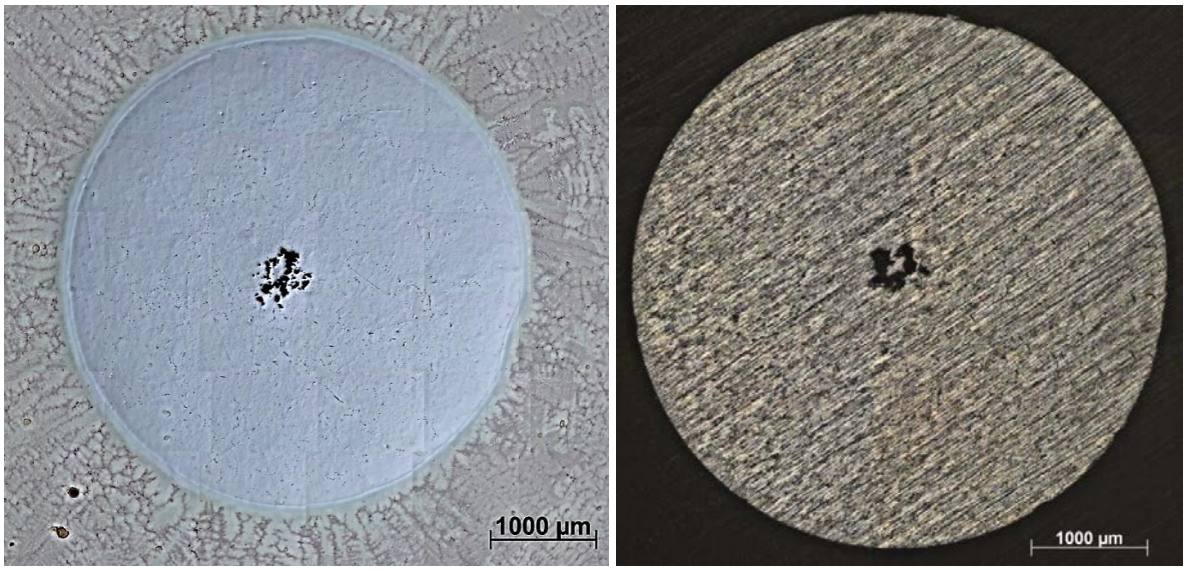

(A) (B)

Figure 6.2: Optical image of circular rod cross section (A) section A after dipping and (B) section D which did not contact the melt.

The two rectangular cross sections of the rod obtained by cutting section B were also investigated by optical microscopy, both micrographs are shown in Figure 6.3. The top cross section had a significant pore within it, however it did not reach the walls of the rod so should not have had a significant influence on the interface. It also had some porosity at the bottom of the rod (the left of the micrographs). I significant increase in dissolution is seen where the porosity reaches the melt. An entrained gas pore is also seen to have been trapped below the rod near the porosity. The average width of the top cross section with the pore was 4.3 mm while the bottom cross section without pores was 2.9 mm. It is then certain that the cut along section B was not directly down the center of the rod since the two halves have very different widths. This makes it difficult to compare the widths of the cross sections to the undissolved radius of the rod.

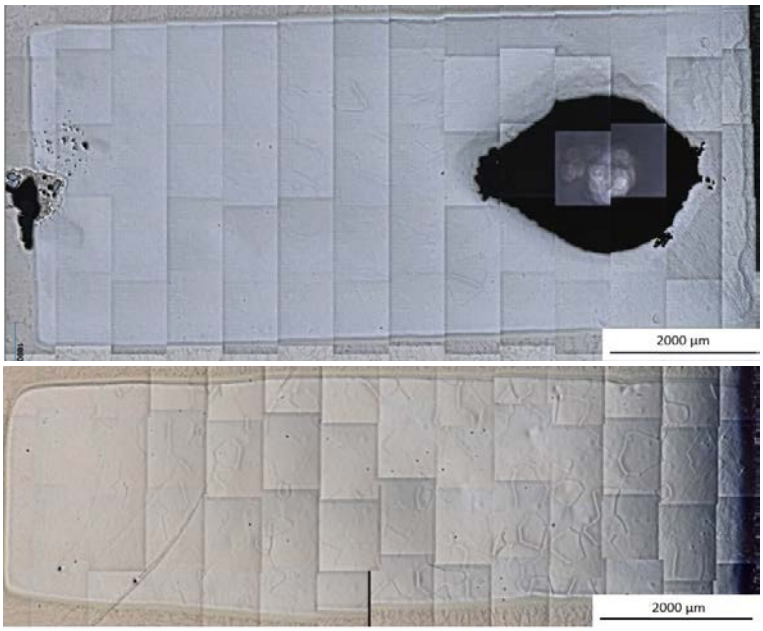

Figure 6.3: Rectangular rod cross sections along section B after interaction with the melt

In order to account for this difference in width between the cross sections a normalization process was conducted. The diameter obtained from the dissolved circular cross section was compared to the measured widths at the top of the rectangular sections (the right of Figure 6.3). These should be very similar regions of the rod, only separated by the width of the cut along section A and amount of material removed when polishing the circular cross section. The difference was found to be a factor of 1.03 for the cross section with a pore and 1.58 for without. This factor was applied to the width measurements for both sections and the corrected disolved radii are shown along the length in Figure 6.4. The corrected average width from the cross section with pore was 4.40 mm and 4.45 mm without. The average diameter of the rod was decreased by 188 µm during the rod/melt interaction. This gives a linear radial dissolution length of 94 µm.

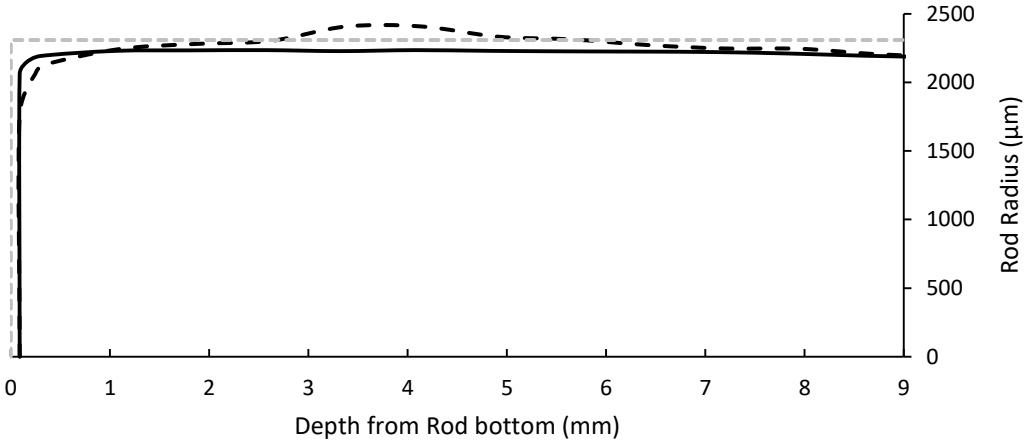

Figure 6.4: Variation of radius along the length of the rod after interaction with the melt from cross section with pore (solid line) and without (dashed line) undissolved dimensions in grey.

6.2 Influence of Thermal Effects on Particle Grain Size

As the predicted mechanism for the anomalous efficiencies observed with isomorphic inoculation is particle breakup by preferential grain boundary dissolution the size of the grains within the particles is of critical importance. This section investigates how the grain size in the particles evolves during the heating and holding stage of inoculation trials.

6.2.1 Particle annealing

The thermal treatment the particles will undergo on interaction with the melt is similar to the process of annealing where the size and shape of grains change. As the cryomilled particles are strongly deformed, this process is split into three steps, recovery, recrystallization and grain growth [**194**]. Recovery is the movement of dislocations to minimize their energy, recrystallization the formation of new dislocation free grains, and grain growth is these new grains increasing in size. These processes can be significantly affected by the structure of the material, such as the presence of multiple phases, precipitates and dislocation structure [**195**]. In the following, the recovery and recrystallisation stages will be neglected, since the holding temperature of 1600°C is high enough to make grain growth the dominant parameter. A simple model to predict grain size after annealing is given by [**196**]:

$$D^2 - D_o^2 = Kt \qquad (6.1)$$

where D is the final grain size, Do the initial grain size, t the time at an isothermal temperature and K a rate constant.

6.2.2 As-Milled Particle Microstructure

It was seen in section 3.3.2 that the grain size did not change significantly between Ti-Al-Nb particles milled for 3 or 9 hours. This indicates that extended milling times primarily reduced the particle size rather than both the particle size and grain size. While the grain size within the particles did not change significantly the fraction of subgrain (<15°) boundaries decreased as milling time increased. This can be seen in the internal grain disorientation maps shown in Figure 6.5 where the 3 hour milled particle shows higher disorientations within the grains when compared to the 9 hour particle.

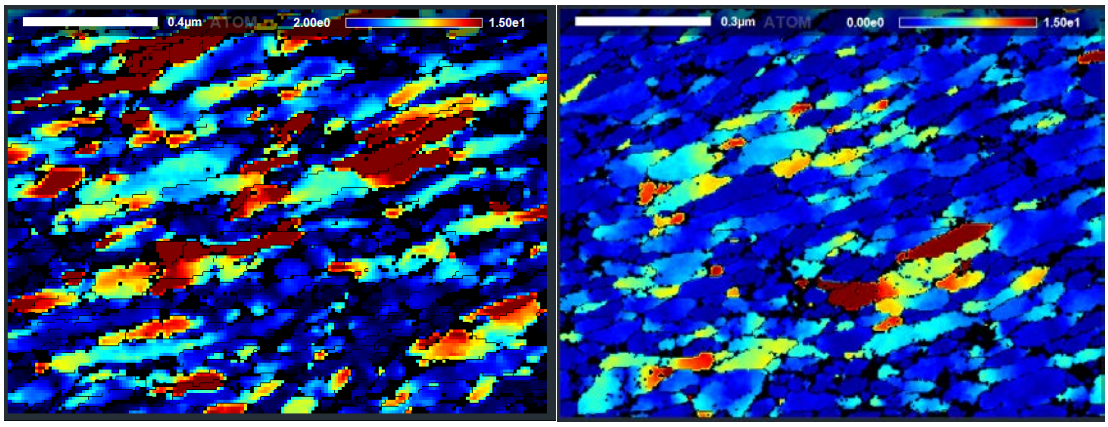

(A) (B)

Figure 6.5: Internal grain disorientation maps from TKD analysis of (A) 3hr and (B) 9 hr milled Ti-Al-Nb powder (0° misorientation dark blue, 15° dark red)

This can also be visualized by looking at the calculated geometrically necessary dislocations, as shown in Figure 6.6. Geometrically necessary dislocations are the calculated dislocations in the structure to accommodate the strain gradients. For the 9 hour milled structure the geometrically necessary dislocations are mostly located on the grain boundaries while for the 3 hour milled structure there are still significant concentrations of dislocations within the grain interiors.

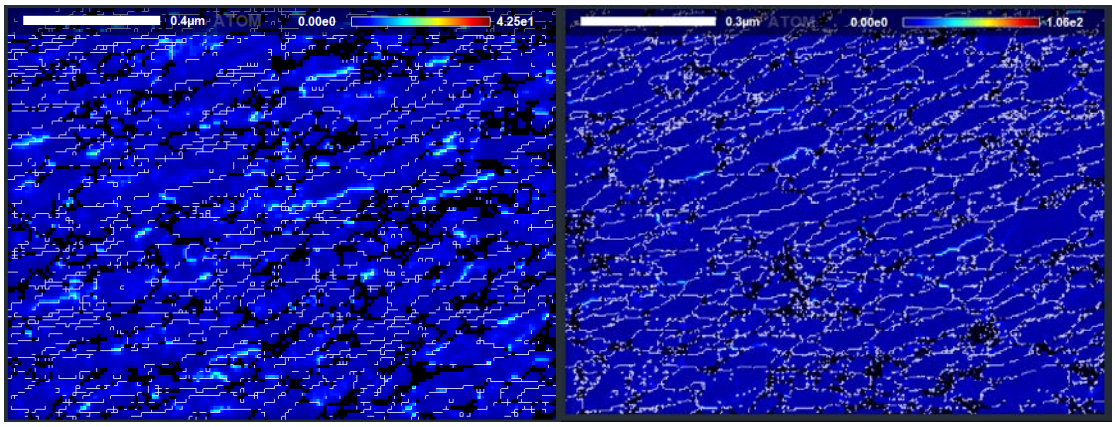

(A) (B)

Figure 6.6: Geometrically necessary dislocations for (A) 3 hr and (B) 9 hr milled powder

While the grain size is the same regardless of milling time the internal structure within the grains differs. This means that the starting point for grain growth is not the same in all the particles since the recovery and recrystallization steps may proceed at different rates due to the differing dislocation/misorientation conditions. There may then be a difference between the structures of the particles after thermal treatment if they were highly plastically deformed or not, as the highly plastically deformed particles may progress through the recovery and recrystallization processes at different rates and have differing times for grain growth. In contrast, the similar size of the grains and their small size regardless of milling time may result in similar structures after thermal treatment since as mentioned above the characteristics of the initial structure may be disregarded when the final grain size is significantly larger than the

initial, and as observed with the rod (see Appendix D), the grain size was seen to increase drastically after interaction with the melt.

6.2.3 Recreating Particle Thermal Treatment

In order to better understand the grain growth occurring in the Ti-Al-Nb particles during their interaction time with the melt experiments were conducted to find the grain size within the particles after long and short times at high temperature. In order to prevent oxidation and provide faster heating rates than possible in gaseous environments the particles were heat treated in CaF_2 salt which melts at ~1400°C. The molten salts were heated to 1600°C to recreate the thermal environment of the molten Ti-Al used in the casting trials. In the case of the long interaction time, 5 minutes, the particles and salt were heated in a quenching directional solidification furnace, while the shorter interaction time experiments, 20 s, were conducted by simply adding the powders to preheated liquid CaF_2. The experimental setups and procedures are outlined in Appendix E. A sample of three hour milled Ti-Al-Nb powder and nine hour milled Ti-Al-Nb powder were both investigated. Once the samples had fully cooled the particles in the solidified CaF_2 matrix were metallographically ground and polished, then imaged by BSE in in an SEM. Representative micrographs of both the 3 and 9 hour milled samples after 5 minutes and 20s are shown in Figure 6.7.

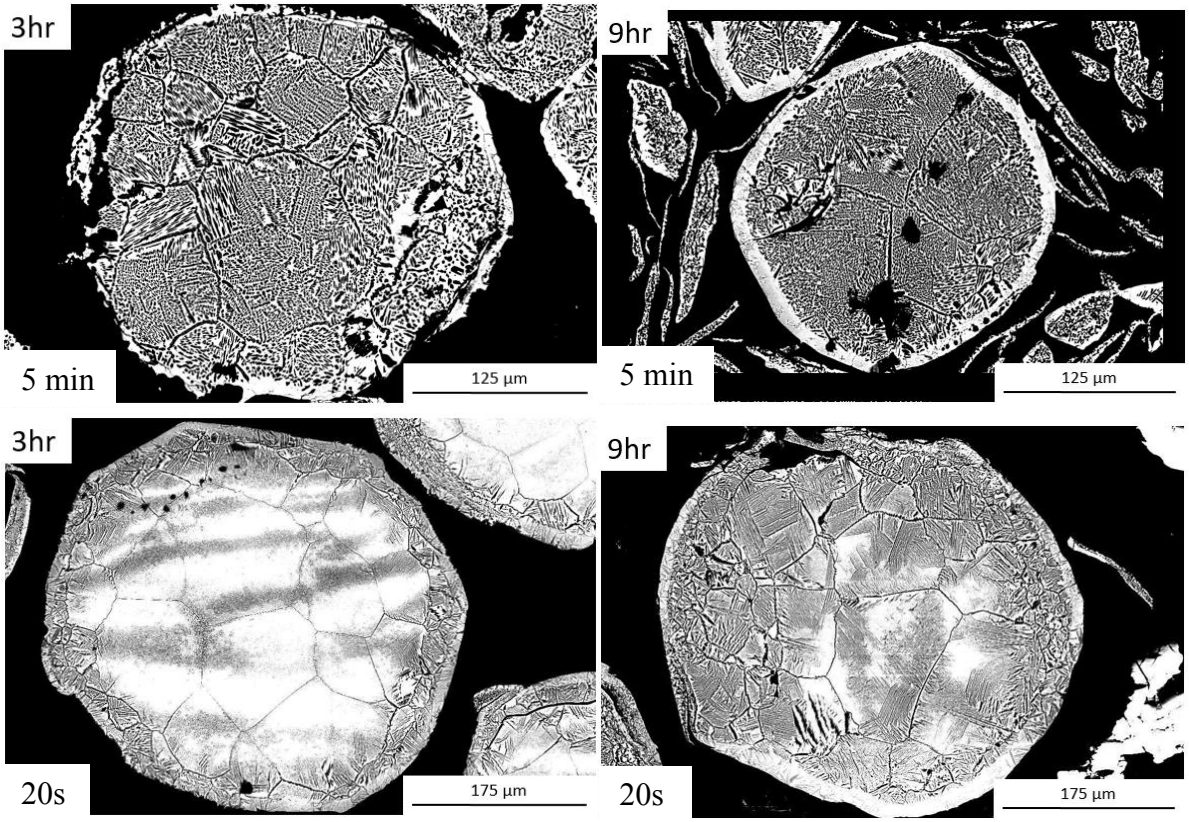

Figure 6.7: BSE micrographs of 3 hour milled and 9 hour milled Ti-Al-Nb powders after 5 min and 20s holds at 1600°C

In the samples heat treated for 5 minutes the high temperature β grains have transformed into an α/γ lamellar structure on cooling. The prior β grain boundaries can be seen as the boundaries

between the lamellar colonies, defined by similar directions of laths within the colony. In the case of the 20s heat treatment some particles were composed of totally transformed α/γ lamellar colonies while others retained untransformed β grains in the center of the particles. In all cases there were some lamellar colonies around the periphery of the particles. Additionally the grain size appeared to be largest in the center of the particles, even if the center was lamellar, with smaller grains closer to the edge. These demarcations were identified by eye and their areas measured using imageJ software. The grain size of the prior β grains was taken to be the equivalent circular area of the α/γ colonies. In the case of the 9 hour milled particles after 5 min heat treatment the particles also had a layer of α martensite on their periphery. This indicates that the powders were cooled more quickly than the 3 hour particles which did not have such a martensite layer. To size the prior β grains these particles the colony boundaries were extrapolated to the particle edge rather than the martensite layer where they stopped. The size of the prior β grains was evaluated for the powder samples along with the size of the parent particle they were measured within, the results of which are shown in Figure 6.8. The particle size is taken to be the equivalent circular diameter of the particle cross section evaluated. The error bars are the standard deviation of the grain size measurements taken in each particle.

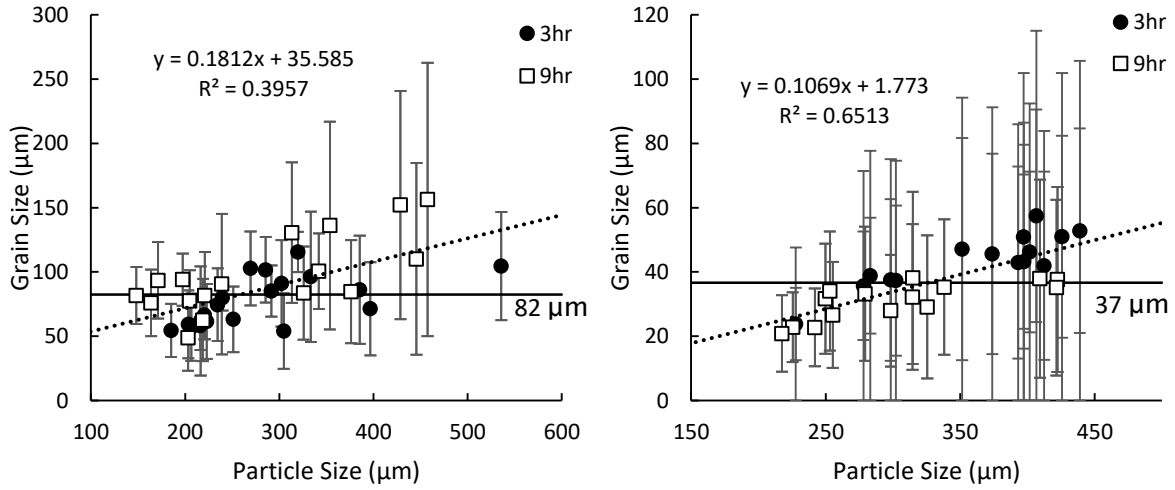

Figure 6.8: Particle grain size of heat treated 3hr and 9hr milled Ti-Al-Nb particles after (A) 5 minutes and (B) 20s at 1600°C

For the five minute heat treatment 20 particles of 3hr milled Ti-Al-Nb and 17 particles of 9hr milled were found with cross sections that had α/γ colonies which had clear boundaries. The average prior β grain size found was 82 µm across both samples, 76 µm for the 3 hr milled particles and 94 µm for the 9 hr. The average particle size was ~282 µm for both milling times. The global average grain size was within error, taken as one standard deviation, for all the particles measured except the smallest 3hr particle. There does appear to be a slight trend of increasing β grain size as the particle size increases but it is not strong enough across the particles measured to be conclusive, especially since the spread of the grain sizes increases as well with particle size. The size of the particles seems to have a greater effect on the grain size than the particle milling time. Since all the particles have grain sizes which agree with the average the grain size can be taken to be the same between the 3hr and 9hr particles after

extended high temperature exposure. This means that the change in the subgrain structure seen in the as-milled particles does not have a large effect on the grain size after this treatment, once again indicating that the main effect of extended milling times is a reduction of particle size and does not have a strong effect on the microstructural properties of import for the process.

For the 20s heat treatment fifteen particles from each milling time were measured, their size and grain size evaluated in the same manner as the longer duration heat treatment. The average grain size of the three hour milled samples was 44 μm while it was only 31 μm for the nine hour milled particles. The overlap in the size of the particles measured is smaller than in the extended time experiment, the three hour particles measured had an average size of 360 μm while the nine hour particles averaged 305 μm. The global average grain size of 37 μm does not appear to agree as well with all the particles as the global average did for the extended time experiments, however all the sizes agree well with a linear trend of increasing grain size with increasing particle size. This could be the result a surface effect leading to the aforementioned smaller grain sizes along the surface of the particles compared to their centers. Again this indicates that the size of the particles has a larger effect on the grain size after thermal treatment than the differences in the initial microstructure.

It was determined that the grain size of the particles after thermal treatment did not very significantly as milling time of the particles increased. The size of the particles was seen to have a greater effect on the grain size than the milling time. The average grain sizes were found to be 37μm after 20s and 82μm after 300s. The average measured grain sizes do not match well with the simple grain growth model described by equation (6.1) but fit reasonably well to power law trend, as shown in Figure 6.9. The power law trend can then be used to predict the average grain size in the particles after a given time at 1600^{o}C. The grain size/particle size relation found after 20s of interaction time at 1600^{o}C can be used to more accurately predict the grain size within the particle size distributions and number of grains introduced in each of the inoculation trials.

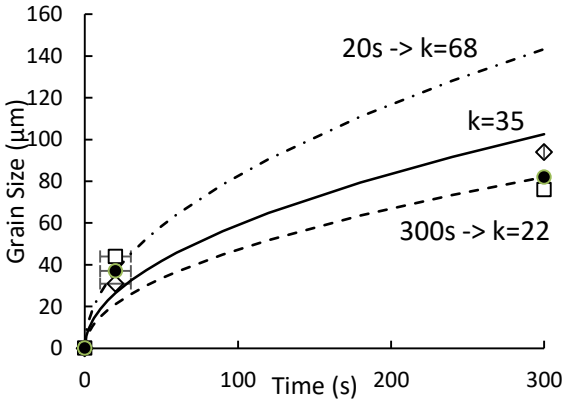

Figure 6.9: Average grain size with thermal treatment at 1600oC (A) fitting equation (6.1) to the experimental data for 20s (k=68), 300s (k=22) and the best fit (k=35) and (B) fitting a power law trend.

6.3 Particle Dissolution in Liquid Melt

In addition to the size of the grains inside the particles increasing, the interaction between the particles and the melt will also result in some dissolution of the particles. The size of the large particles will be decreased, both by standard dissolution as well as particle breakup, while some smaller particles will be dissolved completely. This is important for the inoculation trials as the particles which dissolve completely cannot participate in solidification and assist in grain refinement.

6.3.1 Influence of Fluid Flow

In order to give a better idea of particle dissolution fluid flow must be considered. To that end this section discusses dissolution of Ti-Al-Nb in Ti-Al fluid flow. Since the fluid flow in the liquid is 3D and complex a mathematical model outside the scope of this thesis is required to accurately describe the motion and dissolution of the particles. A simplified first calculation is then presented to begin to understand how dissolution affects the population of particles present on solidification of the melt.

The dissolution of a particle can be described as the mass transport of solute atoms away from the solid/liquid interface resulting in a decrease in the size of the solid [**197**]. Either the transport of the solute across the interface or the transport of the solute into the bulk liquid may be considered to be the rate limiting step. In this case the rate limiting step is considered to be the transport of the solute away from the interface, as is the case in film theory [**198**]. Normally when using this theory the liquid is assumed to have infinite volume and thus there is no solute buildup effect. Hsu and Lin developed a model, which is implemented below, where the volume of the liquid interacting with the solid is also considered [**197**]. The basis of the model is three assumptions, that the particles dissolving are spherical, that there is a layer between the solid and bulk liquid, and that the movement of solute through the layer controls the dissolution rate. The schematic of the interface and parameters considered is shown in Figure 6.10. The hydrodynamic boundary layer is shown as δ_b, the mass transfer boundary layer as δ, The bulk solute concentrations in the solid and liquid as C_s and C_L respectively, and C_L* being the interface concentration in the liquid, C_s* the interface concentration in the solid and V_L the velocity of the liquid and V_i the interface velocity.

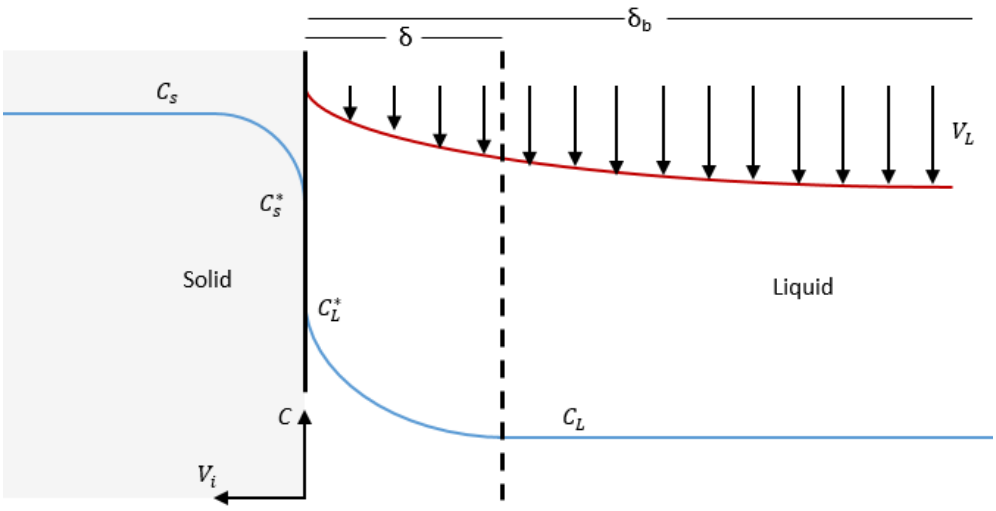

Figure 6.10: Schematic of Interface with Fluid Flow

As discussed previously, particle size and density affect their velocity in the melt. Since the particles are not stationary in the melt their relative velocity compared to the melt must be known in order find the width of the displacement layer. Since the fluid flow in the ingot is complex some simplifications were required, the velocity of the particles was considered to be the maximum relative velocity possible for the particles in the flow (V_{rel}). This occurs when gravity is acting against the fluid flow, and the maximum relative particle velocity can be calculated from a simple force balance in a moving reference frame as shown in Figure 6.11.

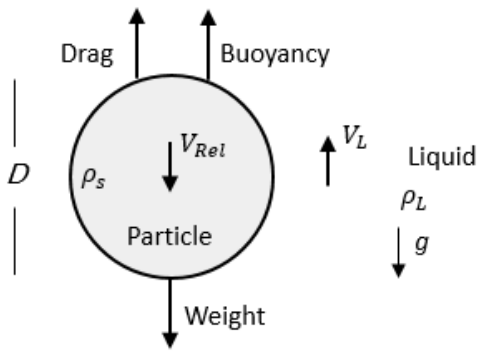

Figure 6.11: Force balance on particle in moving reference frame

where g is acceleration due to gravity, D is the particle diameter, ρ_s and ρ_L the particle and liquid density respectively and C_D the drag coefficient. The maximum relative velocity (V_{rel}) occurs when these forces are balanced, and can be found with:

$$V_{rel} = \sqrt{{4gD(\rho_s - \rho_L)}/{3C_D\rho_L}} \qquad (6.2)$$

The drag coefficient depends on the Reynolds number of the particle as shown in Figure 6.12.

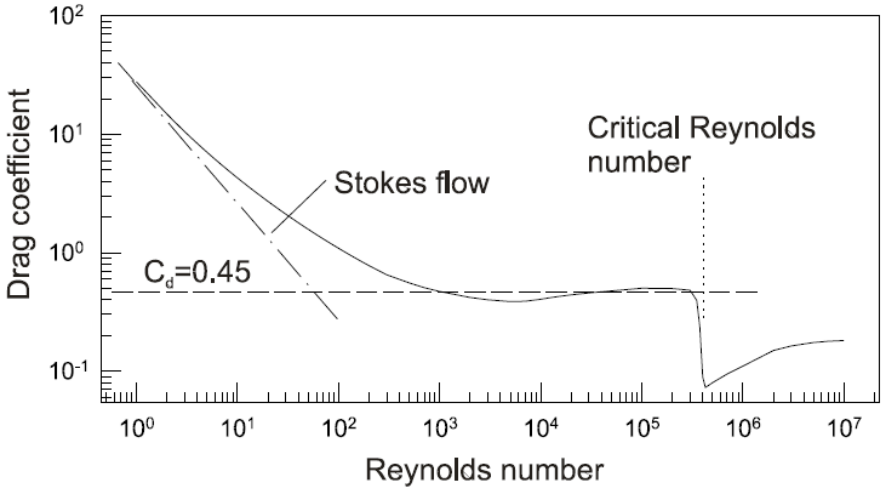

Figure 6.12: Variation of drag coefficient with Reynolds number, from [**193**]

In this case none of the particles investigated had Reynolds numbers above the critical number so the flow can be assumed to be laminar and the drag coefficient taken to be [**193**]:

$$\begin{matrix} C_D = 24/Re & Re < 53 \\ C_D = 0.45 & 53 < Re \end{matrix} \qquad (6.3)$$

Since the drag coefficient and Reynolds number rely on one another, finding the velocity is an iterative process. The initial velocity to find a starting Reynolds number was taken to be the fluid velocity, i.e. assuming stationary particles. The calculations were iterated to find the velocity, Reynolds number and drag coefficient. The smallest particles were found to take the most iterations to achieve stability in the velocity results but after ten iterations the variation was less than 1% from the previous iteration. Once the particle relative velocities were found the size of the layer could be determined. Since in the case considered there is fluid flow the layer is assumed to be dependent on the boundary layer. The boundary layer thickness is the distance from the particle where the fluid flow has returned to 99% of its free flowing velocity. This distance, δ, assuming laminar flow, is given by [**199**]:

$$\delta_b = 5x/\sqrt{Re} \qquad (6.4)$$

where x is the distance along a flat plate, here taken to be the radius of the particle r. This is the hydrodynamic boundary layer, the mass transfer boundary layer (δ) which is important for these calculations can be found by dividing the hydrodynamic boundary layer by the Schmidt number (the ratio of viscous and mass diffusion rates):

$$Sc = v/D_L \qquad (6.5)$$

where is the kinematic viscosity of the liquid and D_L the solute diffusion coefficient in the liquid. For the sake of boundary layer calculations the particles are assumed to be flat plates so

simplify calculations. A schematic of these layers and flat plate assumption is shown in Figure 6.13.

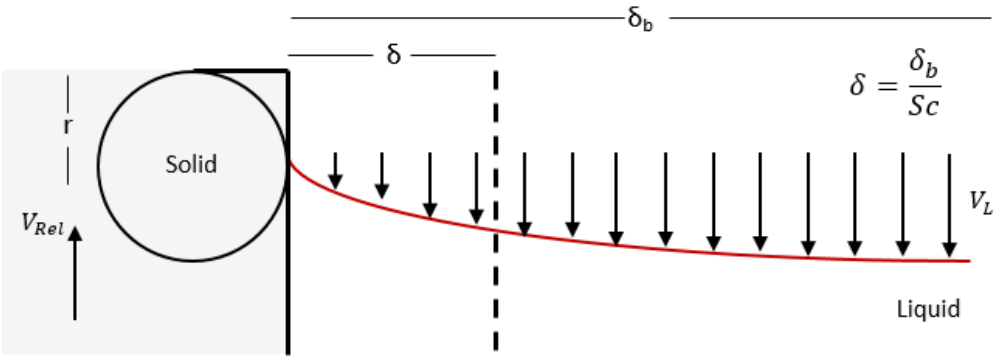

Figure 6.13: Particle boundary and displacement layers at point r, the radius of the particle.

Once these values were known the model of Hsu and Lin could be implemented. They define the following dimensionless variables in their model, radius, layer, time and concentration [**197**]:

$$r^* = r/r_o \quad (6.6)$$
$$\delta^* = \delta/r_o \quad (6.7)$$
$$t^* = 4\pi t D_L N r_o/3V \quad (6.8)$$
$$C^* = (C_i - C_l)/[4\pi\rho r_o^3 N/3VM] \quad (6.9)$$

where r is the radius after dissolution, r_o the initial radius, δ the layer thickness, t the time for dissolution, D_L the diffusion coefficient of the solute in the liquid, N the number of particles, V the volume of the liquid which the particles can interact with, C_i the interface concentration of solute, C_l the bulk liquid concentration of solute, ρ the liquid density and M the molar mass of the solute. Beginning with a mass balance across the layer and assuming pseudo-steady state conditions and a relatively thin layer the change in the radius with time assuming a finite liquid can be found with [**197**]:

$$t^* = -\delta^*\{a_1 \ln((r^* + \delta^*)/(1 + \delta^*)) + a_2 \ln((r^* + \alpha)/(1 + \alpha)) + \left(\frac{1}{2}\right) b_2 \ln\left(\frac{((r^* - \alpha/2)^2 + \frac{3\alpha^2}{4})}{((1 - \alpha/2)^2 + \frac{3\alpha^2}{4})}\right) + (b_2\alpha + 2c_2)(\tan^{-1}\left(\frac{2r^* - \alpha}{\sqrt{3}\alpha}\right) - \tan^{-1}(\frac{2-\alpha}{\sqrt{3}\alpha}))/\sqrt{3}\alpha\} \quad (6.10)$$

$$\alpha^3 = C^* - 1$$
$$a_1 = -\delta^*/(\alpha^3 - \delta^{*3})$$
$$b_1 = \delta^*/(\alpha^3 - \delta^{*3})$$
$$c_1 = -\delta^{*2}/(\alpha^3 - \delta^{*3})$$
$$d_1 = \alpha^3/(\alpha^3 - \delta^{*3})$$
$$a_2 = (b_1\alpha^2 - c_1\alpha + d_1)/3\alpha^2$$
$$b_2 = (2b_1\alpha^2 + c_1\alpha - d_1)/3\alpha^2$$
$$c_2 = (-b_1\alpha^2 + c_1\alpha + 2d_1)/3\alpha$$

The solute species is assumed to be Nb since it should be the slowest diffuser. The diffusion coefficient of Nb in the liquid was estimated using the Stokes-Einstien relation:

$$D = \frac{k_B T}{6\pi\eta r} \qquad (6.11)$$

where k_B is the boltzman constant, η the dynamic viscosity and r the atomic radius of a Nb atom. The requisit variables to apply the model to the rod dissolution are shown in Table 7.

Table 7: Variables for rod dissolution in fluid flow assuming solute is Nb

Variable	Symbol	Units	Value	Ref
Boundary Layer	δ	m	3.35×10^{-5}	PW
Initial Radius	r_o	m	2.50×10^{-3}	PW
Number of Particles	N	-	1	PW
Solute Liquid Diffusion	D_L	m^2/s	2.14×10^{-9}	PW (see discussion)
Ingot Liquid Mass		g	38	PW
Volume of Liquid	V	m^3	9.84×10^{-6}	PW
Particle Density	ρ_s	g/ m^3	5.01×10^6	PW (see ch.3)
Liquid Density	ρ_L	g/ m^3	3.82×10^6	[**200**]
Solute Molecular Weight	M	g/mol	93	[**175**]
Solute Liquid Concentration	C_L	mol/ m^3	0	PW
Solute Interface Concentration	C_i	mol/ m^3	8164	[**120**]
Kinematic Viscosity	*v*	m^2/s	4.93×10^{-7}	[**201**]
Dynamic Viscosity	η	Pa s	1.88×10^{-3}	[**201**]
Temperature	T	°C	1600	PW

Applying this to the case of the rod dissolution can be seen in Figure 6.14. Assuming the liquid interaction volume was equal to that of the whole molten bulk alloy used in the experiment (~40g or 9.8×10^{-6} m^3) at 1600°C the measured dissolution length was achieved after ~13s and 10s of interaction resulted in ~75 μm of dissolution. Considering the assumptions and uncertainties of the calculation this is relatively good agreement between the calculation and measured values for the rod dipping experiment.

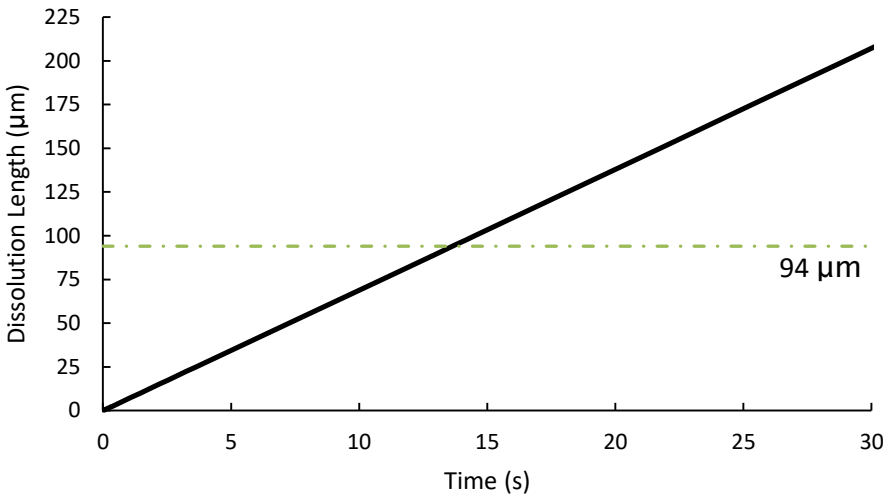

Figure 6.14: Dissolution of Rod Considering Fluid flow and Finite or Infinite liquid

6.3.2 Application of the Model to Different Particle Sizes

Since the model agreed fairly well with the experimental dissolution rate observed it could then be applied to the inoculation trials. It is interesting to see how the model reacts to changes in particle sizes and volume of liquid which the particles interact with. It can be seen in Figure 6.15 that at a Reynolds number of 53 where the change from stokes flow to the laminar approximation occurs for the drag coefficient the particle velocity changes to linear growth and the boundary layer switches from decreasing exponentially to increasing linearly with particle size.

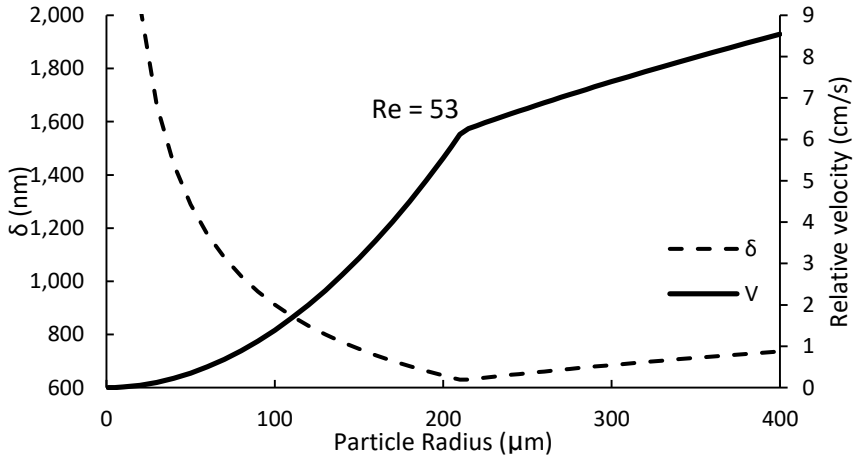

Figure 6.15: Effect of particle size on relative velocity and width of boundary layer

This behaviour caries on when using the model to approximate the dissolution length. When the particles have a radius of ~200 µm the behaviour of the dissolution length changes. It can be seen in Figure 6.16 that this holds true both when the volume of the liquid the particles can interact with is held constant, i.e. the volume fraction of liquid the particles interacts with changes, and if the volume fraction of liquid is held constant, i.e. the total volume of liquid changes but the volume fraction of particles remains constant. In both cases when the particles

are moving in stokes flow (Re<53, r<200 μm) the dissolution length evolves similarly increasing rapidly as the radius increases at small radii then slows as it approaches the limit of stokes flow. If the volume of liquid the particles interact with is held constant the dissolution length drops rapidly outside of stokes flow, as the volume fraction of particles also increases. If the volume fraction of introduced particles is held constant the drop after stokes flow is much less dramatic. This decrease is due to boundary layer increasing in size after stokes flow is surpassed.

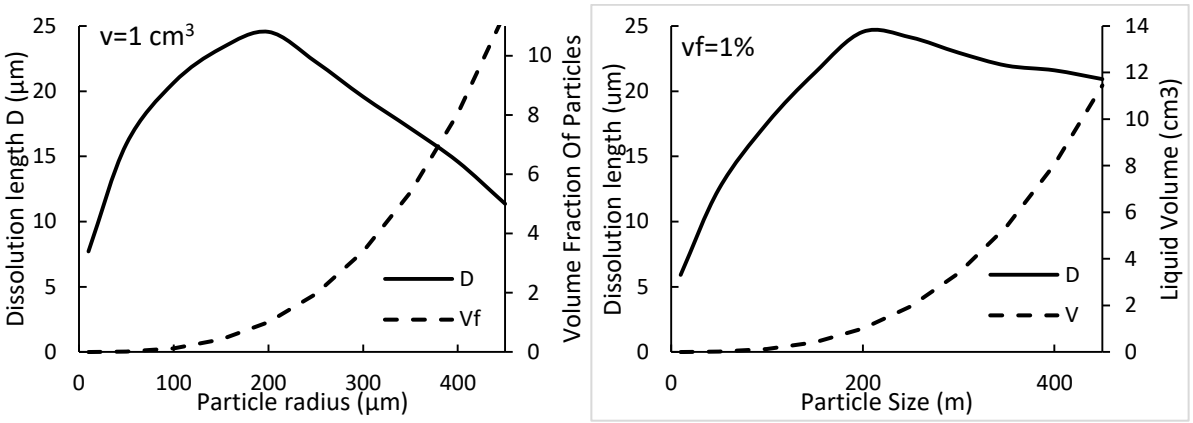

(A) (B)

Figure 6.16: Effect of particle size on dissolution length (A) with a constant volume of liquid and (B) with a constant volume fraction of introduced particles

The sharp decrease in dissolution length after stokes flow when the volume of liquid the particles interact with is held constant can be explained by the increase in volume fraction of the particles. As shown in Figure 6.17 as the volume fraction of particles increases the dissolution length decreases rapidly between 0.0001% and 0.01%. At volume fractions below this the dissolution length does not change very much, indicating that the solute rejection into the liquid has little effect on the dissolution rate. At particle volume fractions above 0.01% the dissolution length approaches 0 since the solute from the particles has significant buildup in the liquid and dissolution is then slowed considerably.

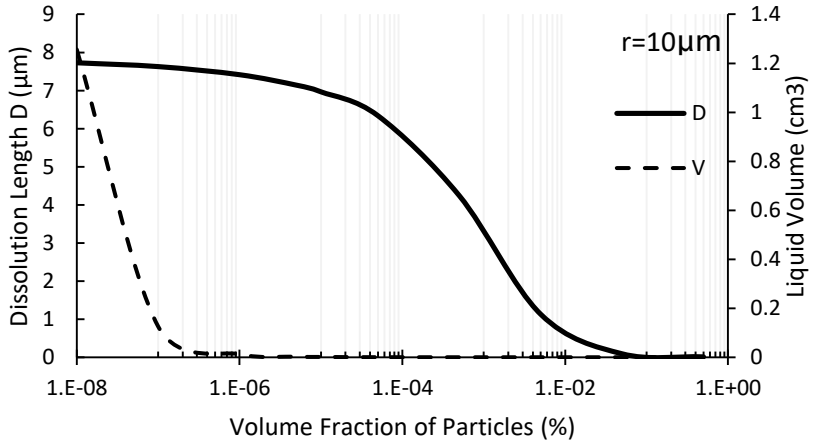

Figure 6.17: Effect of liquid interaction volume (volume fraction of particles) on dissolution length

6.4 Repercussions on Isomorphic Inoculation Trials

The effects of grain growth and particle dissolution are both important to better understand the grain refinement found in the inoculation trials. The mechanisms of dissolution and particle breakup counteract one another to change the number of growth sites for solidification present in the melt.

6.4.1 Number of Grains Present During Solidification

Combining the information gained in the previous sections on grain growth and particle dissolution the number of particles present during solidification can be estimated. The method for this is schematized in Figure 6.18 for particles of a given size. The size distribution of the introduced particles is taken as the starting point of the calculation, from which the number of particles introduced of a given size can be found. Using the method for particles in a fluid low described in Section 6.3.2 the effect of dissolution on the population of particles and their volume can be determined. Similarly the initial particle size can be used to determine the grain size according to the grain size/particle size trend found in Section 6.2.3 for particles after 20s at 1600ºC. The initial particle size is used for this as the particles were assumed not to dissolve at all in the grain growth experiments. The number and volume of particles after dissolution can be combined with the grain size to find the number of grains in each particle which, assuming 100% particle breakup along grain boundaries, is the number of remaining particles after dissolution and breakup which are present during solidification. In effect this method implements the dissolution and grain growth in an independent and sequential manner while in reality both phenomena occur concurrently and would influence one another, however, modeling such concurrent behaviour is outside the scope of the preliminary nature of these calculations.

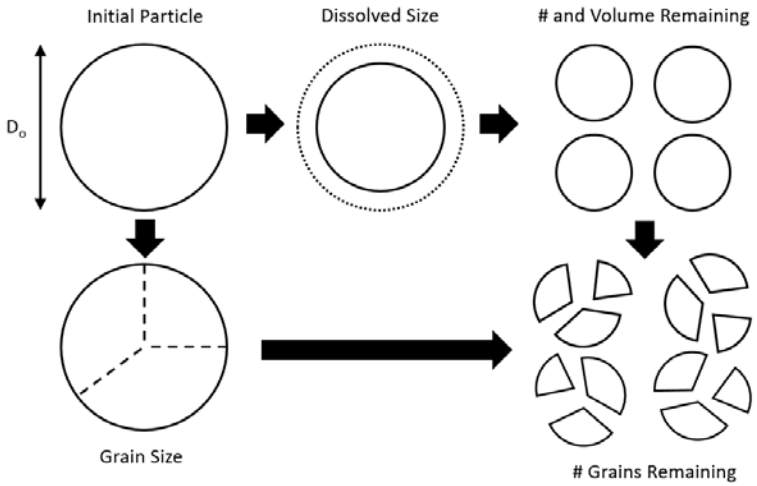

Figure 6.18: Method to determine number of particles present during solidification

The procedure for particle dissolution in fluid flow can be repeated for each particle size of each distribution in order to obtain a dissolution length for each, assuming the liquid interaction volume fraction of the melt for particles of a given size is equal to their volume fraction of the

particle size distribution. For a given size the number of particles will not change unless the dissolution length is equal to or longer than the particle radius, in which case the number drops to zero. The volume of the particles does change for every size of particle, as shown in Figure 6.19 along with the size distributions of the 3hr milled Ti-Al-Nb particles before and after dissolution. It can be seen that some particle sizes have increased their volume fraction while others have decreased, this is because the dissolution rate is not constant between particle sizes and depends on the particle velocity in the fluid, which varies with the size of the particles.

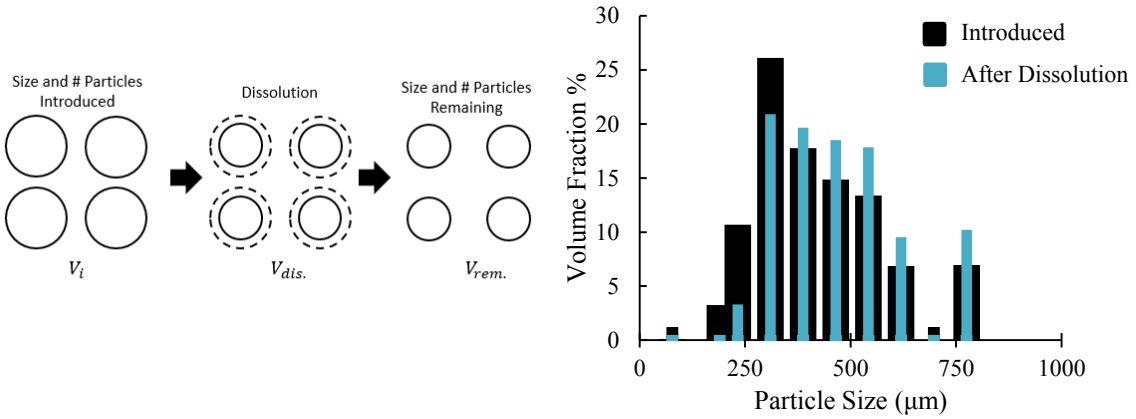

Figure 6.19: Evolution of volume of the particles of a given size and 3hr milled particle size distribution of particles by volume before and after dissolution

If only dissolution is considered and the particles themselves are considered to be the grain refining inoculants then the difference between the inoculant behaviour before and after dissolution can be seen in Figure 6.20 A and B. In Figure 6.20 A it can be seen that considering dissolution increases the particle efficiency as the points move further from the 1:1 ratio. Similarly, in Figure 6.20 B it can be seen that the number of grains formed by each particle increases if dissolution is considered. The particle size after dissolution is decreased due to the interaction with the melt dissolving some of the particles. This makes sense as the effect dissolution has on the particle distribution is to reduce the number of particles present. Since the grain refinement obtained with each distribution is known, considering dissolution results in an increase in the apparent efficiency of each particle. The 11 hour milled powders have the largest change in efficiency since less than 2% (by number) of the particles introduced survived until melting. This is likely an overestimation of the dissolution as only the initial particle conditions are considered in the dissolution calculations. A more robust model would consider the change in velocity and boundary layer as dissolution occurs which would likely decrease the complete dissolution of particles.

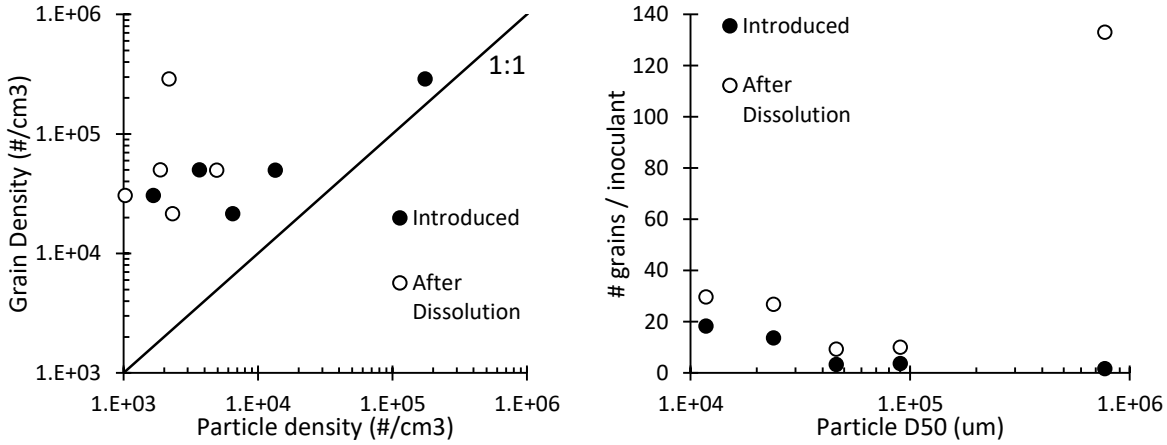

(A) (B)

Figure 6.20: Effect of particle dissolution on inoculation efficiency (A) grain and particle number density comparison, (B) # grains formed by each particle

The next step is to include the breakup of particles into individual grains which then act as grain refiners. This is done on the assumption that the particle breakup occurs independently of and after particle dissolution. This means that the initial particle size is used to calculate the grain size within the particle, not the dissolved size. It also means that no dissolution calculations are performed on the broken up grains. This is schematized in Figure 6.21 where V_{grain} is the volume of an average single particle grain from a certain particle size and V_{rem} is the remaining volume of particles of the same size after dissolution. The smallest grains measured in the grain growth experiments were ~4 μm (particles >100μm) while the smallest calculated grain size, for the smallest particles of the 11 hr milled powder (22μm), was >3 μm. These can then be taken as reasonable values of grain size since they are not significantly smaller than the smallest grains found in much larger particles.

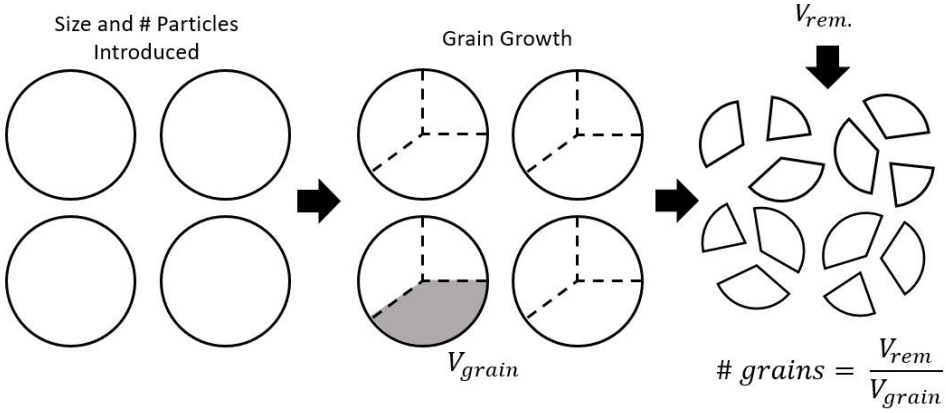

Figure 6.21: Schematic of calculation method for # of particle grains remaining for solidification

If all these grains are considered to be the grain refiners as postulated then their efficiency can be seen in Figure 6.22. The number of introduced grains is determined is the same manner as the remaining grains but using the introduced volume of the particles rather than after dissolution. In contrast to when the particles are considered the grains do not produce more than

one new grain each which makes sense since the mechanism for the particles doing so was postulated as the breakup into grains. When the introduced grains are considered as the grain refiners they have efficiencies lower than AlTiB traditional inoculation of Al, still significantly higher than AlTiB inoculation of Ti. After dissolution the efficiencies for all but the 11 hour milled powders appear clustered around one new grain formed by each grain which has split from the particles remaining in the melt. The anomalously high efficiency of the 11 hour milled powders is due to the large fraction of particles which dissolved, as was seen when only the particle dissolution were considered as is likely due to similar reasons.

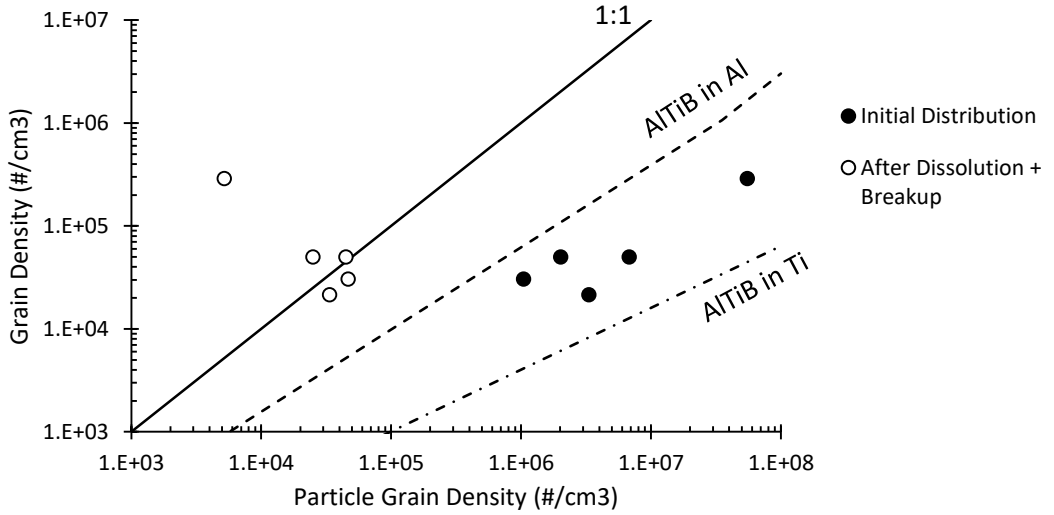

Figure 6.22: Particle grain density and equiaxed grain density for particle grains and comparison to traditional AlTiB inoculation of Al [**202**] and Ti [**203**].

It is also interesting to compare the number of grains formed by each inoculant particle as shown in Figure 6.23. The experimental breakup factor is the number of equiaxed grains formed by each particle introduced to the melt, the error bars being the uncertainty based off the standard deviation of the grain size and measurements. The introduced and post dissolution and breakup efficiency factors are the average number of internal grains per particle introduced to or remaining in the melt. It can be seen that once dissolution and grain growth are considered there is good agreement between the experimental and calculated efficiency factors. This means that particle breakup along grain boundaries is very likely the mechanism responsible for the anomalously high efficiencies seen with isomorphic inoculation as the average number of grains per particle is close to the number of equiaxed grains formed by each particle introduced to the melt.

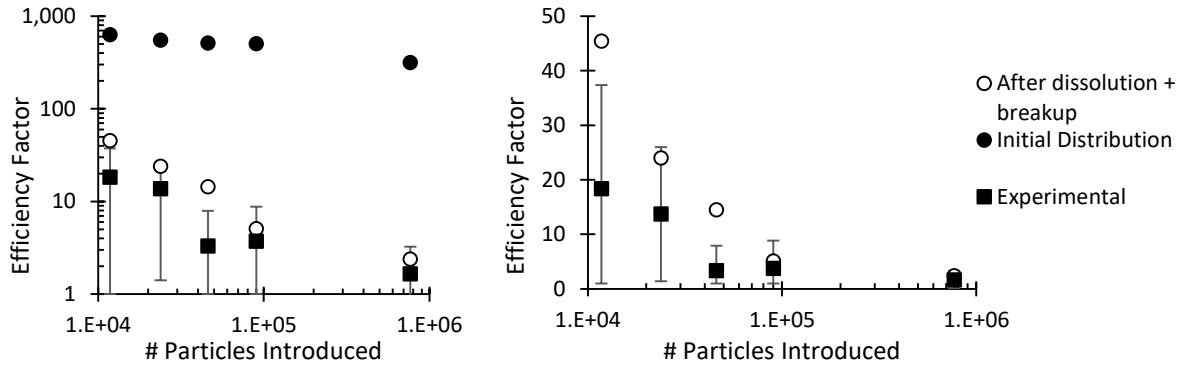

Figure 6.23: Relationship between # particles introduced and Efficiency factor considering the experimental results and calculations

6.5 Conclusions

The interaction between Ti-Al-Nb particles and the Ti-Al melt were investigated. A solid rod of Ti-Al-Nb was submerged into molten Ti-Al and allowed to interact for the same time as the inoculation trials. The grains inside the rod were seen to increase by a factor of three between a cross section of the rod far from the melt and a cross section which was submerged in the melt. An EBSD investigation of the interface between the rod and melt showed orientation relationships between the rod and bulk indicating epitaxial growth. Heat treatment experiments were carried out at the interaction temperature of the melt and inoculant particles using molten CaF_2 and holding times of ~20s and 5 minutes to see the change in grain size in the particles. The grain size was seen to depend on the size of the particles more strongly than the initial milling conditions of the particles. Smaller particles had smaller grains, it was also observed that grains closer to the surfaces of the particles were smaller than those in the center "bulk" regions. A linear trend was found between the particle size and grain size after 20s of interaction at 1600^{o}C which could be used to approximate the grain size of the Ti-Al-Nb particles in the inoculation trials. The rod was also seen to have dissolved approximately 94 μm in the melt. Calculations were carried out based on film theory to calculate the dissolution of the particles in the fluid based on the diffusion of Nb through the displacement boundary layer being the rate limiting step. This method also took into account the finite volume of liquid Ti-Al the rod interacted with and resulted in a dissolution time of ~13s for a 94 μm dissolution length, which is not too far from the experimentally determined time of 10s. The grain growth and dissolution calculations were applied to the Ti-Al-Nb particle distributions used in the inoculation trials to determine the number of particle grains which could be present in the melt on solidification. The efficiencies of the particle grains were close to one except in the case of the 11 hour milled samples which may have had their dissolution overestimated. It should also be noted that the ingot which was inoculated with the 11 hour milled particles had a remaining Ti chunk and odd stuck region which could be affecting these results. The average number of grains calculated within each particle after considering both grain growth and dissolution approached the experimental values of number of equiaxed grains formed by each inoculant particle. This indicates that the mechanism of breakup along grain boundaries within the particles and particle dissolution are responsible for the anomalous inoculation efficiencies observed in the isomorphic inoculation trials.

Chapter 7 Conclusions and Recommendations

This section summarizes the major conclusions which can be taken from the work and presents recommendations and potential future work

7.1 Conclusions

A new method of inoculation was developed for Ti-Al alloys which does not leave heterogeneous particles in as-cast ingots. This method uses particles which are of the same phase as the solidifying melt with similar lattice parameters, rather than acting as centers of nucleation the particles act as direct centers of growth bypassing the nucleation step of solidification. The particles are not indefinitely stable in the melt, they have thermal stability but their diffusive stability is not complete. Since the particles are polycrystalline, during interaction with the liquid bulk alloy a mechanism of grain boundary dissolution results in breakup of the particles into multiple smaller particles. This allows each particle which is introduced to the melt to form more than one grain in the solidified ingot.

In order to implement isomorphic inoculation trials alloys of Ti-10Al-25Nb, Ti-25Al-10Ta and Ti-47Ta were selected as isomorphic inoculants for a Ti-46Al base alloy. The ternary alloys were selected to balance lattice mismatch with stability in the melt while the binary Ti-47Ta alloy was selected prioritizing stability in the melt over lattice mismatch. Powders of each inoculant alloy were produced from drillings of alloyed ingots which were cryomilled for durations ranging from 1.5 to 11 hours to produced different size distributions of particles. The particles were sized using both SEM image analysis and DLS. The median particle size varied from 233 μm for Ti-Al-Nb particles milled for 3 hours under argon to 20 μm for Ti-Ta particles milled for 9 hours. The grain size of the 3 and 9 hour milled Ti-Al-Nb particles were evaluated with TKD and found to be less than 50nm in both cases, however the pancaked structure found in the 3 hour milled particle was found to subdivide into a more equiaxed type structure in the 9 hour milled particles. To introduce the particles to the melt a pellet was prepared from each size distribution containing equal mass inoculant and aluminum powder, to act as a binder. Each pellet was dropped into the molten Ti-46Al alloy, solidification occurring 20s after the pellet contacted the melt. Trials with both ternary alloys, Ti-Al-Nb and Ti-Al-Ta were successful at reducing the as-cast equiaxed grain size as well as increasing the equiaxed fraction in the ingots. A large Ti-46Al ingot was prepared and sectioned for testing the Ti-Ta inoculants however they were unsuccessful with both 20 and 10s interaction times. A successful Ti-Ta refined ingot was produced using the same ingot procedure as the ternary ingots.

The lack of grain refinement in the Ti-Ta trials was attributed mainly to their high density compared to the bulk liquid alloy. Even the mixing present in the melt due to the induction heating was insufficient to prevent the particles from settling to the bottom of the melt. Particles of Ti-Ta were found at the bottom of each ingot where they were tested. Additionally the size distributions were found to contain superlarge particles not detected when the particles were sized. The trials using sections of a large Ti-46Al ingot also were seen to solidify as α-Ti rather than β-Ti. While this would prevent the particles from acting as isomorphic inoculants the

orientation relationships between the phases should allow them to act as traditional inoculants, however no grain refinement was observed. The ingot which was grain refined by Ti-Ta addition could not have its grain refinement conclusively attributed to the isomorphic mechanism since Ti-Ta particles were found in the bottom of the ingot but not the equiaxed zone and the growth of columnar grains from the bottom of the ingot was blocked by the presence of a superlarge particle which may have significantly changed the solidification process making it incomparable with the other ingots.

The grain refinement produced by the ternary isomorphic inoculants was found to depend not only on the size of the particles, as with traditional inoculation, but also on the number of particles added. Traditional inoculation is size dependent since only particles greater than a certain size can nucleate new grains at a given undercooling. This was not found to be the case with isomorphic inoculants as more than one new equiaxed grain was found to be formed by each particle added to the melt. Large particles (D50>200μm) were found to form more than 10 grains each while smaller particles (D50<200μm) were found to form fewer than 10 grains each. While none of the ternary inoculants were found in the as-cast ingots insight into their behaviour was found from the surviving TiTa particles. Al was found to diffuse quickly into the binary inoculants and Ta out as well, this makes locating the particles difficult especially if the refractory addition is Nb as it has weaker atomic contrast than Ta. A surviving particle of TiTa was also seen to be in the process of breaking up into multiple smaller particles by ingress of liquid (or egress of Ta) along preferential paths. These paths are postulated to be grain boundaries and the process of particle breakup to be by preferential grain boundary dissolution or grain boundary wetting. This would explain the anomalous efficiency (>1) of the isomorphic inoculants as each particle introduced to the melt is breaking into multiple grains which can then grow and form equiaxed grains in the as-cast ingot.

Investigations were carried out to evaluate the interactions between the particles and melt. It was found that Ti-Al-Nb can epitaxially grow on Ti-Al during solidification, confirming that nucleation is not necessary with properly designed isomorphic inoculants. The grain size within the particles was found to increase drastically after thermal treatment similar to that imposed by interaction with the melt. These were corroborated by calculations using a simple model of grain growth. The dissolution of the particles was also found to be important to calculate the number of particles present during solidification. The particle dissolution rate is also affected by the size of the particles as the relative velocity between the particles and melt changes as the particle size increases or decreases. The relative velocity of the particles changes the size of the characteristic boundary layer around them and thus the diffusion/dissolution rate.

A new method of grain refinement was developed called isomorphic inoculation. This process functions by the addition of particles to liquid metal which assist in solidification by direct growth rather than nucleation of new solid as in tradition inoculation. This method was successfully implemented in the Ti-Al system to grain refine as-cast ingots without the presence of precipitates in the bulk. Grain refinement was found to be anomalously high, each particle added to the melt was responsible for more than one new grain forming in the as-cast ingot. This was explained by the phenomena of particle breakup where the particles added to the melt

were split along grain boundaries into multiple particles which could participate in solidification. Grain growth within the particles and particle dissolution are both critical factors to determining how the number of particles present in the melt evolves between their introduction and solidification. This process, while currently in its infancy, may have significant industrial applications both for Ti-Al alloys and other systems where traditional inoculants are unideal.

7.2 Recommendations

Further research in this area could be broken into two main research paths, the furthering of the isomorphic inoculants towards industrial applications for Ti-Al as well as the increase of understanding into the mechanism of isomorphic inoculation.

7.2.1 Ti-Al Applications

In order to apply these isomorphic inoculants to industrial fabrication of TiAl parts further work is required. Both the Ti-10Al-25Nb and Ti-25Al-10Ta isomorphic inoculants were successfully implemented in small scale laboratory tests, a next step would be to test these alloys for larger scale castings with processing conditions more similar to industrial cases. Work could also be done on optimizing the size distribution of particles to maximize grain refinement. The size distributions could be refined by sieving to narrow the range of particles introduced and the most efficient sizes determined. Only these most efficient sized particles could then be used to maximize grain refinement. Optimization of the interaction time should also be conducted by testing multiple times from introduction to complete dissolution to find the interaction time which provides the greatest grain refinement for a given alloy and size of particles. Since the anomalous efficiency of the isomorphic inoculants was found to be due to the phenomena of particle breakup along grain boundaries an optimal time should exist which permits maximum breakup balanced with dissolution of small particles to have the highest possible number of possible particles present on solidification. For a given industrial application the microstructure and particle size of the isomorphic inoculants could be manipulated to provide a maximum possible grain refinement for an existing industrial process. Mechanical testing could also be carried out on samples to ensure no unintended phenomena are resulting in a decrease in properties.

7.2.2 Mechanism of Isomorphic Inoculation

Work could also be done to improve the understanding of the mechanism at work in isomorphic inoculation. An isomorphic inoculant could be found for a system which is less reactive than Ti-Al and does not have solid state phase transformations after solidification to make analysis less complicated. Very small scale experiments could be conducted quenching small samples with few particles added after increasing interaction times to better observe the process of particle breakup, dissolution and solidification. Particles used would have to be of similar size and microstructure, on solidification, to one another to ensure comparison is possible. Ideally a system could be found with a suitable isomorphic inoculant that could be used with radiography

to observe the process of isomorphic inoculation in-situ. The process of particle breakup and growth could then be observed as they occurred and the effects of factors such as stirring could be evaluated. It would also be beneficial even in the Ti-Al system to conduct casting trials at reducing interaction times until remaining inoculant particles were observable in the as-cast ingot. Investigations could be carried out on the surviving particles by EBSD to see the orientation relationship between the particle and solidifying melt or by TEM to definitively conclude if the growth of the particles is epitaxial and no new solid is nucleating.

References

1 Dimiduk, D.M. Gamma titanium aluminide alloys—an assessment within the competition of aerospace structural materials. *Materials Science and Engineering A*, 263 (1999), 281-288.

2 Z.M. Sun, H. Hashimoto. Fabrication of TiAl alloys by MA-PDS process and the mechanical properties. *Intermetallics*, 11 (2003), 825-834.

3 Huang, S.C. Alloying considerations in gamma-based alloys. In *Structural Intermetallics* (Warrendale, PA 1993), TMS, 299.

4 Shaffer, P.T.B. *Plenum press handbooks of high temperature materials: No. 1 Materials Index*. Springer, 1964.

5 Andersson J.O., Helander T., Höglund L., Shi P.F., and Sundman B.. Thermo-Calc and DICTRA, Computational tools for materials science. *Calphad*, 26 (2002), 273-312.

6 W.F. Gale, T.C. Totemeier. *Smithells metal reference book (8th edition)*. Elsevier, 2004.

7 G.B. Gibbs, D. Graham, D.H. Tomlin. Diffusion in titanium and titanium-niobium alloys. *Phil. Mag. Letters*, 8, 92 (1963), 1269-1282.

8 D. Ansel, I. Thibon, M. Boliveau, J. Debuigne. Interdiffusion in the body centered cubic beta-phase of Ta-Ti alloys. *Acta. Mater.*, 46, 2 (1998), 423-430.

9 D. Gosslar, R. Gunther, C. Hartig, R. Bormann, J. Zollinger, I. Steinbach. Grain Refinement of Gamma-TiAl Alloys by Inoculation. *Materials Research Society Symposium Proceedings*, 1128 (2009), 91-96.

10 Quested, T.E. *Phd Thesis: "Solidification of Inoculated Aluminium Alloys"*. University of Cambridge, 2004.

11 T.E Hsieh, R.W. Balluffi. Experimental study of grain boundary melting in aluminium. *Acta Metallurgica*, 37, 6 (1989), 1637-1644.

12 Kim, Y.W. Ordered intermetallic alloys, part III: Gamma Titanium aluminides. *JOM*, 43, 7 (1991), 30-39.

13 *Light Weight Alloys - Titanium Aluminides Website: https://amg-nv.com/innovation/titanium-aluminides/ Accessed: February 2018*.

14 GENERAL ELECTRIC AVIATION. *The GEnx commercial Aircraft engine Website: https://www.geaviation.com/commercial/engines/genx-engine Accessed: February 2018*.

15 S. Kim, J. Hong, Y. Na, J. Yeom, S. Kim. Development of TiAl alloys with excellent mechanical properties and oxidation resistance. *Materials and Design*, 54 (2014), 814-819.

16 Wu, X. Review of alloy and process development of TiAl Alloys. *Intermetallics*, 14 (2006), 1114-1122.

17 N. Barbi, F. Diologent, R. Goodall, A. Mortensen. Fracture of convoluted and lamellar a2 þ g TiAl alloys. *Intermetallics*, 22 (2012), 176-188.

18 M.T. Jovanovic, B. Dimcic, I. Bobic, S. Zec, V. Maksimovic. Microstructure and mechanical properties of precision cast TiAl turbocharger wheel. *Materials processing technology*, 167 (2005), 14-21.

19 Jaffee, H. R. OgdenD. J. MaykuthW. L. FinlayR. I. Constitution of Titanium-Aluminum Alloys. *JOM*, 3, 12 (1951), 1150-1155.

20 D.J. McPherson, M. Hansen. Der Aufbau binärer Legierungssysteme des Titans. *Z. Fur Met*, 45 (1954), 76-81.

21 Murray, J.L. Calculation of the Titanium-aluminium phase diagram. *Metallurgical Transactions A*, 19 (1988), 243-247.

22 J.C. Shuster, M. Palm. Reassessment of the binary Aluminium-Titanium phase diagram. *Journal of phase equilibria and diffusion*, 27, 3 (2006), 255-277.

23 V.T. Witusiewicz, A.A. Bondar, U. Hecht, S. Rex, T.Y. Velikanova. The Al–B–Nb–Ti system IV: Thermodynamic re-evaluation of the constituent binary system Al-Ti. *Journal of alloys and compounds*, 465 (2008), 64-77.

24 H. Wang, R.C. Reed, J.-C. Gebelin, N. Warnken. On the modelling of the point defects in the ordered B2 phase of the Ti–Al system: Combining CALPHAD with first-principles calculations. *CALPHAD*, 39 (2012), 21-26.

25 Y-K. Kim, H-K. Kim, W-S. Jung, B-J. Lee. Atomistic modelling of the Ti-Al binary system. *Computational materials science*, 119 (2016), 1-8.

26 V.T. Witusiewicz, A.A. Bondar, U. Hecht, S. Rex, T.Y. Velikanova. The Al-B-Nb-Ti System III. Thermodynamic re-evaluation of the constituent binary system Al-Ti. *J. Alloys Compd.*, 465, 1-2 (2008), 64-77.

27 Burgers, W.G. On the process of transition of the BCC modification into the HCP modification of Zirconium. *Physica*, 1 (1934), 561-586.

28 Blackburn, M.J. Some aspects of phase transformations in Ti alloys. In *The Science Technology and Applications of Titanium* (London 1968), 633-643.

29 Guide, S. *Thesis: Evolution microstructurale d'un alliage a base TiAl. Sollicitation mécanique par compression dynamique et stabilité thermique*. Ecole De Mines, Nancy, 2006.

30 Amelio, S. *Thesis: Evolution Microstructurale d'un alliage a base TiAl. Sollicitation mechanique par compression dynamique et stabilite thermique*. Nancy, 2005.

31 S. Zhang, Y. Zhao, C. Zhang, J. Han, M. Sun, M. Xu. The microstructure, mechanical properties, and oxidation behaviour of beta-gamma TiAl alloy with excellent hot workability. *MSEA*, 700 (2017), 366-373.

32 Paris, A. *Thesis: Etude des transformations de phase dans des alliages base TiAl faiblement allies en Silicium*. Nancy, 2015.

33 Denquin, A. *Thesis: Etude des transformations de phase et approche du comportement mechanique des alliages biphases a base de TiAl: Une contribution au developpement de nouveaux alliages intermetalliques*. Lille, 1994.

34 Zollinger, J. *"Influence de l'oxygene sur le comportement a la solidification d'aluminiures de titane binares et allies au niobium bases sur le compose intermetallique g-TiAl"*. L'institut national polytechnique de lorraine, Nance, 2008.

35 I.V. Okulov, M.F. Sarmanova, A.S. Volegov, A. Okulov, U Kuhn, W. Skrotzki, J. Eckert. Effect of boron on microstructure and mechanical properties of multicomponent titanium alloys. *Materials Letters*, 158 (2015), 111-114.

36 R. Cao, J.H. Chen, J. Zhang, H. Zhu. Effects of repeated loading on the fracture behaviour of notched TiAl specimens. *Engineering fracture mechanics*, 75 (2008), 4019-4035.

37 M.F Stroosnijder, V.A.C. Haanappel, H. Clemens. Oxidation behaviour of TiAl-based intermetallics—influence of heat treatment. *Materials Science and Engineering A*, A239-240 (1997), 842-846.

38 L. Song, J. Lin, J. Li. Effects of trace alloy elements on the phase transformation behaviours of ordered w phases in high Nb-TiAl alloys. *Materials and Design*, 113 (2017), 47-53.

39 Y. Wu, S.K. Hwang. Microstructural refinement and improvement of mechanical properties and oxidation resistance in EPM TiAl-based intermetallics with yttrium additions. *Acta Materiallia* , 50 (2002), 1479-1493.

40 M. Naveed, A. F. Renteria, S. WeiS. Role of alloying elements during thermocyclic oxidation of b/g-TiAl alloys at high temperature. *Journal of Alloys and compounds*, 691 (2017), 489-497.

41 W. Ahmed, A. Elhissi, M.J. JacksonE. Ahmed. 2.1.2 Basic aspec of titanium metallurgy. In *The Design and Manufacture of Medical Devices*. Woodhead Publishing, 2012.

42 J. Yang, J.N. Wang, Q. Xia, Y. Wang. Effect of cooling rate on the grain refinement of TiAl-based alloys by rapid heat treatment. *Materials letters*, 46 (2000), 193-197.

43 P. Erdely, R. Werner, E. Schwaighofer, H. Clemens, S. Mayer. In-situ study of the timeetemperature-transformation behaviour of a multi-phase intermetallic b-stabilised TiAl alloy. *Intermetallics*, 57 (2015), 17-24.

44 S-W. Kim, J.K. Hong, Y-S. Na, J-T. Yeom, S.E. Kim. Development of TiAl alloys with excellent mechanical properties and oxidation resistance. *Materials and Design*, 54 (2014), 814-819.

45 L. Aihui, L. Bangsheng, N. Hai, S. Yanwei, G. Jinggie, F. Hengzhi. Study of interfacial reactions between TiAl alloys and four ceramic molds. *Rare metal materials and engineering* , 37 (2008), 956-959.

46 F. Gomes, J. Barbosa, C.S. Ribeiro. induction melting of g-TiAl in CaO crucibles. *Intermetallics*, 16 (2008), 1292-1297.

47 T. Tetsui, T. Kobayashi, A. Kishimoto, H. Harada. Structural optimization of an yttria crucible for melting TiAl alloy. *Intermetallics*, 20 (2012), 16-23.

48 Suryanarayana, C. Electron microscopic characterization of g-TiAl alloy. *Materials Letters*, 29 (1996), 281-284.

49 O. Yeheskel, M.P. Dariel. The effect of processing on the elastic moduli of porus g-TiAl. *Materials Science and Engineering A*, 354 (2003), 344-350.

50 W. Shouren, G. Peiquan, Y. liying. Centrifical precicion cast TiAl turbocharger wheel using ceramic mold. *Journal of materials processing technology*, 204 (2008), 492-497.

51 S. Bolz, M. Oehring, J. Lindemann, F. Pyczak, J. Paul, A. Stark, T. Lippmann, S. Schrüfer, D. Roth-Fagaraseanu, A. Schreyer, S. Weiß. Microstructure and mechanical properties of a forged b-solidifying g TiAl alloy in different heat treatment conditions. *Intermetallics*, 58 (2015), 71-83.

52 H.Z. Niu, Y.Y. Chen, Y.S. Zhang, J.W. Lu, W. Zhang, P.X. Zhang. Producing fully-lamellar microstructure for wrought beta-gamma TiAl alloys without single a-phase field. *Intermetallics*, 59 (2015), 87-94.

53 H.Z. Niu, Y.Y. Chen, S.L. Xiao, L.J. Xu. Microstructure evolution and mechanical properties of a novel beta g-TiAl alloy. *Intermetallics*, 31 (2012), 225-231.

54 F. Appel, J. D.H. Paul, P. Staron, M. Oehring, O. Kolednik, J. Predan, F.D. Fischer. The effect of residual stresses and strain reversal on the fracture toughness of TiAl Alloys. *Materials science and engineering A*, 709 (2018), 17-29.

55 F. Yang, F. Kong, Y. Chen, S. Xiao. Hot workability of as-cast Ti–45Al–5.4V–3.6Nb–0.3Y alloy. *Journal of alloys and compounds*, 589 (2014), 609-614.

56 P. Erdely, P. Staron, E. Maawad, N. Schell, J. Klose, H. Clemens, S. Mayer. Design and control of microstructure and texture by thermomechanical processing of a multi-phase TiAl alloy. *Materials and Design*, 131 (2017), 286-296.

57 R.K. Gupta, V. Anil Kumar, R. Ramesh Babu, A. Gourav Rao. Development of ductile γ+α2 titanium aluminide through ingot metallurgy route, thermomechanical processing and characterization. *Materials Science and Engineering A*, 703 (2017), 124-136.

58 M.A. Morris, M. Leboeuf. Grain-size refinement of gamma-Ti-Al Alloys: effect on mechanical properties. *Materials science and engineering A*, A224 (1997), 1-11.

59 S. Zeng, A. Zhao, L. Luo, H. Jiang, L. Zhang. Development of B-Solidifying, G-Ti-Al alloys Sheet. *Materials Letters*, 198 (2017), 31-33.

60 G. Cao, L. Fu, J. Lin, Y. Zhang, C. Chen. The relationship of microstructure and properties of a fully lamellar TiAl Alloy. *Intermetallics*, 8 (2000), 647-653.

61 A.V. Kartavykh, E.A. Asnis, N.V. Piskun et. al. A promissing microstructure/deformability adjustment of B-stabilized g-TiAl intermetallics. *Materials Letters*, 162 (2016), 180-184.

62 J. Fan, J. Liu, S. Tian, et. al. Effect of solidification parameters on microstructural characteristics and mechanical properties of directionally solidified binary TiAl Alloy. *Journal of alloys and compounds*, 650 (2015), 8-14.

63 A. Rusinko, K. Rusinko. *Plasticity and Creep of Metals*. Springer, Berlin, 2011.

64 W. Harrison, Z. Abdallah, M. Whittaker. A Model for Creep and Creep Damage in the γ-Titanium Aluminide Ti-45Al-2Mn-2Nb. *Materials*, 7 (2014), 2194-2209.

65 R. Hetnarski, M. Reza Eslami. *Thermal Stresses- Advanced Theories and Applications*. Springer, 2009.

66 W.J. Zhang, S.C. Deevi. Analysis of the minimum creep rates of TiAl Alloys. *MSEA*, 362 (2003), 280-291.

67 Messerschmidt, U. *Dislocation dynamics during plastic deformation*. Springer, 2010.

68 D.J. Bacon, Yu. N. Osetsky, Z. Rong, K. Tapasa. Dislocation glide in the presence of solute atoms or glissile loops. In *IUTAM Symposium on Mesoscopic Dynamics of Fracture Process and Materials Strength. Solid Mechanics and its Applications* (dordrecht 2004), 173-182.

69 Z. Abdallah, R. Ding, N. Martin, M. Dixon, M. Bache. Creep deformation in a G titanium aluminide. *MSEA*, 673 (July 2016), 616-623.

70 H. Zhu, D.Y. Seo, K. Maruyama, P. Au. Effect of microstructure on creep deformation of 45XD TiAl alloy at low and high stress. *MSEA*, 483-484 (2008), 533-536.

71 D. Sturm, M. Heilmaier, H. Saage, et. al. Creep strength of centrifugally cast Al-rich TiAl alloys. *MSEA*, 510-511 (2009), 373-376.

72 Y.L. Pei, M. Song, Y. Ma, S.K. Gong. Effects of heat shock at 800 °C on mechanical properties of γ-TiAl alloys. *Intermetallics*, 19 (2011), 202-205.

73 D. Daloz, U. Hecht, J. Zollinger, H. Combeau, A. Hazotte, M. Zaloznik. Microsegregation, macrosegregation and related phase transformations in TiAl alloys. *Intermetallics*, 19 (2011), 749-756.

74 Z. Min, S. Xi-ping, Y. Long, et. al. In situ observation of fatigue crack initiation and propagation behaviour of a high-Nb TiAl Aloy at 750C. *MSEA*, 622 (2015), 30-36.

75 A. Dlouhy, K. Kucharova, A. Orlova. Long-term creep and creep rupture characteristics of TiAl based intermetallics. *MSEA*, 510-511 (2009), 350-355.

76 T. Kruml, K. Obrtlik. Microstructure degredation in high temperature fatigue of TiAl alloy. *International Journal of Fatiuge*, 65 (2014), 28-32.

77 J. Ding, Y. Liang, X Xu, H. Yu, C. Dong, J. Lin. Cyclic deformation and microstructure evolution of high Nb containing TiAl alloy during high temperature low cycle fatigue. *international journal of fatigue*, 99 (2017), 68-77.

78 Y-f. Chen, S-q. Zheng, J-p. Tu, S-l. Xiao, J. Tian, L-j. Xu, Y-y. Chen. Fracture characteristics of notched investment cast TiAl alloy through in situ SEM observation. *transactions of nonferrous metals society of china*, 22 (2012), 2389-2394.

79 R. Gnanamoorthy, Y. Mutoh, N. Masahashi, Y. Mizuhara. fracture properties of g-base TiAl alloys with lamellar microstructure at room temperature. *Materials science and engineering A*, 184 (1994), 37-44.

80 Y.S. Park, S.W. Nam, S.K. Hwang, N.J. Kim. The effect of the applied strain range on fatigue cracking in lamellar TiAl alloy. *Journal of Alloys and compounds*, 335 (2002), 216-223.

81 C.C. Engler-Pinto Jr., C. Noseda, M.Y. Nazmy, F. Rezai-Aria. Interaction between creep and thermo-mechanical fatigue of CM247LC-DS. In *Superalloys 1996*. TMS, 1996.

82 I. Salam, A. Tauqir, A.Q. Khan. Creep-fatigue failure of an aero engine turbine blades. *Engineering failure analysis*, 9 (2002), 335-347.

83 B. Dambrine, J-P. Mascarell. Designing turbine blades for fatigue and creep. *Def. Sci. J.*, 38, 4 (1988), 413-430.

84 M.H. Sabour, R.B. Bhat. lifetime prediction in creep-fatigue environment. *materials science poland*, 26, 3 (2008), 563-584.

85 A. Semenov, S. Semenov, A. Nazarenko, L. Getsov. computer simulation of fatigue creep and thermal-fatigue cracks propagation in gas turbine blades. *Materials and Technology*, 3 (2012), 197-203.

86 A. Nitta, T. Ogata. Creep-Fatigue damage evaluation of high temperature components and materials for boiler and steam turbines. *materials aging and component life extension* (1995), 37-48.

87 N. Ejaz, I.N. Qureshi, S.A. Rizvi. Creep failure of low pressure turbine blade of an aircraft engine. *Engineering Failure Analysis*, 18 (2011), 1407-1414.

88 S. Kumari, D.V.V. Satyanarayana, M. Srinivas. Failure analysis of gase turbine rotor blade. *Engineering failure analysis*, 45 (2014), 234-244.

89 H. Tang, D. Cao, H. Yao, M. Xie, R. Duan. Fretting fatigue failure of an aero engine turbine blade. *Engineering failure analysis*, 16 (2009), 2004-2008.

90 D.A. Porter, K.E. Easterling. Ch. 4 Solidification. In *Phase transformations in metals and alloys*. CRC Press, 2004.

91 Chalmers, B. Principles of solidification. In *Applied solid state physics*. Springer, 1970.

92 J.A. Dantzig, M. Rappaz. *Solidification*. CRC press, Lausanne, 2009.

93 Flemmings, M.C. Solidification Processing. *Metallurgical Transactions*, 5 (1974), 2121-2134.

94 W. Kurz, D.J. Fisher. *Fundamentals of solidification Reprinted Third Edition*. Trans Tech Publications, Aedermannsdorf, Switzerland, 1992.

95 Quin, Ma. Heterogeneous nucleation on potent spherical substrates during solidification. *Acta Materialia*, 55 (2007), 943-953.

96 Qian, M. Heterogeneous nucleation on potent spherical substrates during solidification. *Acta materialia*, 55 (2007), 943-953.

97 Fletcher, N.H. Size effect in heterogeneous nucleation. *The Journal of Chemical Physics*, 29 (1958), 572-576.

98 Turnbull, D. Kinetics of hetorgeneous nucleation. *Journal of Chemical Physics*, 18 (1950), 198-203.

99 Cantor, B. Heterogeneous nucleation and adsorption. *Phil. Trans. Royal Society of London A*, 361 (2003), 409-417.

100 B.E. Sundquist, R.A. Oriani. Homogeneous Nucleation in a Miscibility Gap System. A Critical Test of nucleation theory. *The journal of chemical physics*, 36 (1962), 2604-2615.

101 Sundquist, B.E. On "nucleation catalysis in supercooled liquid tin". *Acta Metallurgica*, 11 (1963), 630-632.

102 F.M. Kuni, A.K. Shchekin, A.I. Rusanov, B. Widom. Role of surface forces in heterogeneous nucleation on wettable nuclei. *Advances in colloid and interface science*, 65 (1996), 71-124.

103 Z. Wang, W. Zhao. Mg-Based Quasicrystals. In *New Features on Magnesium Alloys*. INTECH, 2012.

104 D. Holland-Moritz, D.M. Herlach, K. Urban. Observation of the Undercoolability of Quasicrystal-Forming Alloys by Electromagnetic Levitation. *Physical review letters*, 71, 8 (1993), 1196-1199.

105 K.F. Kelton, G.W. Lee, A.K. Gangopadhyay, R.W. Hyers, T.J. Rathz, J.R. Rogers, M.B. Robinson, D.S. Robinson. First X-Ray Scattering Studies on Electrostatically Levitated Metallic Liquids: Demonstrated Influence of Local Icosahedral Order on the Nucleation Barrier. *Physical Review letters*, 90 (2003), 1-4.

106 H. Nguyen Thi, J. Gastaldi, T. Schenk, G. Reinhart, N. Mangelinck-Noel, V. Cristiglio, B. Billia, B. Grushko, J. Hartwig, H. Klein, J. Baruchel. In situ and real-time probing of quasicrystal solidification dynamics by synchrotron imaging. *Physical Review E*, 74 (2006), 1-6.

107 R. Tanaka, S. Ohhashi, N. Fujita, M. Demura, A. Yamamato, A. Kato, A.P. Tsai. Application of electron back scattered diffraction (EBSD) to quasicrystal-containing microstructures in the Md-Cd-Yb system. *Acta Materialia*, 119 (2016), 193-202.

108 G. Kurtuldu, A. Sicco, M. Rappaz. Icosahedral quasicrystal-enhanced nucleation of the fcc phase in liquid gold alloys. *Acta Materialia*, 70 (2014), 240-248.

109 G. Kurtuldu, P. Jarry, M. Rappaz. Influence of Cr on the nucleation of primary Al and formation of twinned dendrites in Al–Zn–Cr alloys: Can icosahedral solid clusters play a role? *Acta Materialia*, 61 (2013), 7098-7108.

110 H. Men, Z. Fan. Effect of lattice misfit on prenucleation by molecular dynamics simulation. In *Proceedings of the 6th decenniel international conference on solidification processing* (Old Windsor, UK 2017).

111 G. Kurtuldu, A. Sicco, M. Rappaz. Icosahedral quasicrystal-enhanced nucleation of the fcc phase in liquid gold alloys. *Acta Materialia*, 70 (2014), 240-248.

112 I. Maxwell, A. Hellawell. A simple model for grain refinement during solidification. *Acta Metallurgica*, 23 (1975), 229-237.

113 M. Rappaz, P. Thevoz. Solute diffusion model for equiaxed dendritic growth. *Acta Metallurgica*, 23 (1987), 229-237.

114 M.A. Easton, D.H. StJohn. A model of grain refinement incoroporating alloy constitution and potency of heterogeneous nucleant particles. *Acta Materialia*, 49 (2001), 1867-1878.

115 Lesoult, G. *Thermodynamique des Materiaux*. PPUr, Lausanne, 2010.

116 R. Schmidt-Fetzer, A. Kozlov. Thermodynamic aspects of grain growth restriction in multicomponent alloy solidification. *Acta Materialia*, 50 (2011), 6133-6144.

117 F. Wang, Z. Liu, D. Qiu, J.A. Taylor, M. A. Easton, M-X. Zhang. Revisiting the role of peritectics in grain refinement of Al alloys. *Acta materialia*, 61 (2013), 360-370.

118 V.T. Witusiewicz, A.A. Bondar, U. Hecht, T.Ya. Velikanova. The Al-B-Nb-Ti System: IV. Experimental study and thermodynamic re-evaluation of the binary Al–Nb and ternary Al–Nb–Ti systems. *Journal of alloys and compounds*, 472, 1-2 (2009), 133-161.

119 V.T. Witusiewicz, A.A. Bondar, U. Hecht, et. al. Experimental study and thermodynamic modelling of the ternary Al-Ta-Ti system. *Intermetallics*, 19, 3 (2011), 234-259.

120 V.T. Witusiewicz, A.A. Bondar, U. Hecht, Ya. T. Velikanova. The Al–B–Nb–Ti system: IV. Experimental study and thermodynamic re-evaluation of the binary Al–Nb and ternary Al–Nb–Ti systems. *Journal of alloys and compounds*, 472 (2008), 133-161.

121 Greer, A.L. Grain refinement of alloys by inoculation of melts. *Phil. Trans. R. Soc. Lond. A*, 361 (2003), 479-495.

122 Y. Ali, D. Qiu, B. Jiang, F. Pan, M-X. Zhang. The influence of CaO on grain refinement of cast magnesium alloys. *Scripta Materialia*, 114 (2016), 103-107.

123 F. Wang, D. Qiu, Z-L. Liu, J.A. Taylor, M.A. Easton, M-X. Zhang. The grain refinement mechanism of cast aluminium by zirconium. *Acta materialia*, 61 (2013), 5636-5645.

124 H. Men, Z. Fan. Effect of solute content on grain refinement in an isothermal melt. *Acta Materialia*, 59 (2011), 2704-2712.

125 D.H. StJohn, M. Qian, M.A. Easton, P. Cao. The interdependence theory: the relationship between grain formation and nucleant selection. *Acta materialia*, 59 (2011), 4907-4921.

126 M. Easton, D. StJohn. An analysis of the relationship between grain size, solute content, and the potency and number density of nucleant particles. *Metallurgical and Materials transactions A*, 36A (2005), 1911-1920.

127 M.A. Easton, M. Qian, A. Prasad, D.H. StJohn. Recent advances in grain refinemnet of light metals. *current opinion in solid state and materials science*, 20 (2016), 13-24.

128 Z. Liu, D. Qiu, F. Wang, J.A. Taylor, M. Zhang. Grain refinemnet of cast zinc through magnesium inoculation: characterisation and mechanism. *Materials characterization*, 106 (2015), 1-10.

129 Z. Liu, D. Qiu, F. Wang, J.A. Taylor. The grain refinement mechanism of cast zinc through silver inoculation. *Acta Materialia*, 79 (2014), 315-326.

130 L. Lu, A.K. Dahle, D.H. StJohn. Heterogeneous nucleation of Mg-Al Alloys. *Scripta Materialia*, 54 (2006), 2197-2201.

131 H-T. Li, Y. Wang, Z. Fan. Mechanisms of enhanced heterogeneous nucleation during solidification in binary Al-Mg alloys. *Acta Materialia*, 60 (2012), 1528-1537.

132 T. Wang, Z. Chen, H. Fu, L. Gao, T. Li. Grain refinement mechanism of pure aluminium by inoculation with Al-B master alloys. *MSE A*, 549 (2012), 136-143.

133 Z. Chen, T. Wang, L. Gao, H. Fu, T. Li. Grain refinement and tensile properties improvement of aluminium foundry alloys by inoculation with Al-B master alloy. *MSE A*, 553 (2012), 32-36.

134 Birol, Y. AlB3 master alloy to grain refine AlSi10Mg and AlSi12Cu aluminium foundry alloys. *Journal of alloys and compounds*, 513 (2012), 150-153.

135 Q. Jin, J-P. Eom, S-G. Lim, W-W. Park, B-S. You. Grain refining mechanism of a carbon addition method in a Mg-Al magnesium alloy. *Scripta materialia*, 49 (2003), 1129-1132.

136 Ma Qian, P. Cao. Discussions on grain refinement of magnesium alloys by carbon inoculation. *Scripta materialia*, 52 (2005), 415-419.

137 G.I. Toth, G. Tegez, T. Pusztai, L. Granasy. Heterogeneous Crystal Nucleation: the effect of lattice mismatch. *Physical Review Letters*, 108 (2012), 1-4.

138 M-X. Zhang, P.M. Kelly, Ma Qian, J.A. Taylor. Crystallography of grain refinemnet in Mg-Al based alloys. *Acta Materialia*, 53 (2005), 3261-3270.

139 C. Sheng, J. Sun, D.P. Wang, Y.H. Zhang, L.J. Li, X.R. Chen, H.G. Zhong, Q.J. Zhai. Heterogenous nucleation of pure gold on highly smooth ceramic substrates and the influence of lattice mismatch and cooling rate. *Journal of Materials Science*, 53 (2018), 4612-4622.

140 L. Yang, M. Xia, J.G Lin. Epitaxial growth in heterogeneous nucleation of pure aluminium. *Materials Letters*, 132 (2014), 52-54.

141 Fan, Z. An epitaxial model for heterogeneous nucleation on potent substrates. *Metallurgical and Materials Transactions A*, 44 (2013), 1409-1418.

142 T.E. Quested, A.L. Greer. The effect of size distribution of inoculant particles on as cast grain size in aluminium alloys. *Acta Materialia*, 52 (2004), 3859-3868.

143 A.L. Greer, A.M. Bunn, A. Tronche, P.V. Evans, D.J. Bristow. Modelling of nucleation of metallic melts: Application to grain refinement of aluminium by Al-Ti-B. *Acta Materialia*, 48 (2000), 2823-2835.

144 A. Tronche, A.L. Greer. Electron back-scatter diffraction study of inoculation of Al. *Philosophical magazine letters*, 81 (2001), 321-328.

145 T.E. Quested, A.L. Greer. Grain refinement of Al Alloys: Mechanisms determining as-cast grain size in directional solidification. *Acta Materialia*, 53 (2005), 4643-4653.

146 Da Shu, B. Sun, J. Mi, P.S. Grant. A quantitative study of solute diffusion field effects on heterogeneous nucleation and the grain size of alloys. *Acta Materialia*, 59 (2011), 2135-2144.

147 D. Qiu, M.-X. Zhang. Effect of active heterogeneous nucleation particles on the grain refining efficiency in an Mg-10 wt% Y cast alloy. *Journal of alloys and compounds*, 488 (2009), 260-264.

148 T. Wang, H. Fu, Z. Chen, J. Xu, J. Zhu, F. Cao, T. Li. A novel fading resistant Al-3Ti-3B grain refiner for Al-Si alloys. *Journal of alloys and compounds*, 511 (2012), 45-39.

149 P. Li, S. Liu, L. Zhang, X. Liu. Grain refinement of A356 alloy by Al-Ti-B-C master alloy and its effect on mechanical properties. *Materials and Design*, 47 (2013), 522-528.

150 Y. Ali, D. Qiu, B. Jiang, F. Pan, M-X. Zhang. Current research progress in grain refinement of cast magnesium alloys: A review article. *Journal of alloys and compounds*, 619 (2015), 639-651.

151 D. Qiu, M-X. Zhang, J.A. Taylor, P.M. Kelly. A new approach to designing a grain refiner for Mg casting alloys and its use in Mg-Y-based alloys. *Acta materialia*, 57 (2009), 3052-3059.

152 M.E. Hyman, C. McCullough, C.G. Levi, R. Mehrabian. Evolution of Boride Morphologies in Ti-Al-B Alloys. *Metallurgical Transactions A*, 22A (1991), 1647-1662.

153 E. Schwaighofer, B. Rashkova, H. Clemens, A. Stark, S. Mayer. Effect of carbon addition on solidification behaviour, phase evolution and creep properties of an intermetallic beta-stabilized gamma-TiAl based alloy. *Intermetallics*, 46 (2014), 173-184.

154 M. DeGraef, J.P.A. Loflander, C. McCullough, C.G. Levi. The evolution of metastable Bf borides in a Ti-Al-B alloy. *Acta Metallurgica Materialia*, 12 (1992), 3395-3406.

155 J. Han, S. Xiao, J. Tian, Y. Chen, L. Xu, X. Wang, Y. Jia, H.K.S. Rahoma, Z. Du, S. Cao. Microstructure characterization, mechanical properties and toughening mechanism of

TiB2-containing conventional cast TiAl-based alloy. *Materials Science and Engineering A*, 645 (2015), 8-19.

156 U. Hecht, V. Witusiewicz, A. Drevermann, J. Zollinger. Grain refinement by low boron addition in niobium rich TiAl-based alloys. *Intermetallics*, 16 (2008), 969-978.

157 D. Gosslar, R. Gunther, U. Hecht, C. Hartig, R. Bormann. Grain refinement of TiAl-based alloys: the role of TiB2 crystallography and growth. *Acta Materialia*, 58 (2010), 6744-6751.

158 A.V. Kartavykh, M.V. Gorhenkov. Grain refinement mechanism in advanced gamma-TiAl boron-alloyed structural intermetallics: the direct observation. *Materials Letters*, 142 (2015), 294-298.

159 J. Zollinger, U. Hecht. *Presented at the DFG summer school within the SPP No. 1296*. Herzogenrath, 2008. (Unpublished).

160 B.G. Liu, L.H. Liu, W.D. Xing, R.C. Liu. Structural stability and the alloying effect of TiB polymorphs in TiAl alloys. *Intermetallics*, 90 (2017), 97-102.

161 C. Yang, D. Hu, A. Huang, M. Dixon. Solidification and grain refinement in Ti45Al2Mn2Nb1B subjected to fast cooling. *Intermetallics*, 32 (2013), 64-71.

162 D. Hu, C. Yang, A. Huang, M. Dixon, U. Hecht. Grain refinement in beta-solidifying Ti44Al8Nb1B. *Intermetallics*, 23 (2012), 49-56.

163 J. Han, S. Xiao, J. Tian, Y. Chen, L. Xu, X. Wang, Yi Jia, Z. Du, S. Cao. Grain refinement by trace TiB2 addition in conventional cast TiAl-based alloy. *Materials Characterization*, 106 (2015), 112-122.

164 M. Apel, J. Eiken, U. Hecht. Phase field model for heterogeneous nucleation: Application to inoculation in alpha solidifying Ti-Al-B. *European Physical Journal: Special Topics*, 223 (2014), 545-558.

165 C.J. Cowen, C.J. Boehlert. Comparison of the Microstructure, Tensile, and Creep Behavior for Ti-22Al-26Nb (At. Pct) and Ti-22Al-26Nb-5B (At. Pct). *Metallurgical and Materials transactions A*, 38A (2007), 26-34.

166 Hu, D. Effect of boron addition on tensile ductility in lamellar TiAl alloys. *Intermetallics*, 10 (2002), 851-858.

167 D. Hu, H. Jiang, X. Wu. Microstructure and tensile properties of cast Ti-44Al-4Nb-4Hf-0.1Si-0.1B alloy with refined lamellar microstructures. *Intermetallics*, 17 (2009), 744-748.

168 A. Sankaran, E. Bouzy, J.J. Fundenberger, A. Hazotte. Texture and microstructure evolution during tempering of gamma massive phase in a Ti-Al based alloy. *intermetallics*, 17 (2009), 1007-1016.

169 X. Wu, D. Hu. Microstructural refinement of cast TiAl alloys by solid state transformations. *Scripta Materialia*, 52 (2005), 731-734.

170 C. Ruirun, Z. Deshuang, G. Jingjie et. al. A novel method for grain refinement and microstructure modification in TiAl alloy by ultrasonic vibration. *MSE A* , 653 (2016), 23-26.

171 A. Ramirez, Ma Qian, B. Davis, T. Wilks, D.H. StJohn. Potency of high intensity ultrasonic treatment for grain refinement of magnesium alloys. *Scripta Materialia*, 59 (2008), 19-22.

172 M.J. Bermingham, S.D. McDonald, D.H. St John, M.S. Dargusch. Titanium as an endogenous grain-refining nucleus. *philosophical magazine*, 90, 6 (2010), 699-715.

173 V.T. Witusiewicz, A.A. Bondar, U. Hecht, S. Rex, T.Y. Velikanova. The Al–B–Nb–Ti system IV: Thermodynamic re-evaluation of the constituent binary system Al-Ti. *Journal of alloys and compounds*, 465 (2008), 64-77.

174 S. Khallouk. *Developpement d'une nouvelle generation d'inoculants pour les aluminures de titane*. Nancy, 2015.

175 Shaffer, P. *No.1 Materials Index: Plenum Press Handbooks of High-Temperature Materials*. Springer, 1964.

176 C.J. Boehlert, C. J. Cowen, J.P. Quast, T. Akahori, M. Niinomi. Fatigue and wear evaluation of Ti-Al-Nb alloys for biomedical applcations. *materials science and engineering C*, 28 (2008), 323-330.

177 J.D. Cotton, J.F. Bingert, P.S. Dunn, D.P. Butt, R.W. Margevicius. Titanium-tantalum alloy development. In *TMS annual meeting* (Anaheim CA 1996).

178 A. jillavenkatesa, S. J. Dapkunas, L-S. H. Lum. *NIST Reccomended Practice guide: Particle Size Characterization*. NIST, 2001.

179 HORIBA SCIENTIFIC. *A guidebook to particle size analysis*. Irvine. Ca, 2017.

180 M.E. Fayed, L. Otten. *Handbook of powder science and technology*. Springer, 1997.

181 G. C. Sneddon, P.W. Trimby, J.M. Cairney. Transmission Kikuchi diffraction in a scanning electron microscope: A review. *Materials Science and Engineering R*, 1, 10 (2016), 1-12.

182 R.R. Keller, R.H. Geiss. Transmission EBSD from 10 nm domains in a scanning electron microscope. *Journal of Microscopy*, 245, 3 (2012), 245-251.

183 E. Brodu, E. Bouzy, J-J. Fundenberger, J. Guyon, A. Guitton, Y. Zhang. On-axis TKD for orientation mapping of nanocrystalline materials in SEM. *Materials Characterization*, 130 (2017), 92-96.

184 H. Yuan, E. Broudu, C. Chen, E. Bouzy, J-J. Fundenberger, L.S. Toth. On-axis versus off-axis Transmission Kikuchi Diffraction technique: application to the characterisation of severe plastic deformation-induced ultrafine-grained microstructures. *Journal of Microscopy*, 0, 0 (2017), 1-11.

185 B. Beausir, J.-J. Fundenberger. *ATOM-Analysis Tools for Orientation Maps, http://atom-software.eu/*. Metz, 2015.

186 N.T. Reilly, B. Rouat, G. Martin, D. Daloz, J. Zollinger. Enhanced dendrite fragmentation through the peritectic reaction in TiAl-based alloys. *intermetallics*, 86 (2017), 126-133.

187 J.R. Kennedy, D. Daloz, B. Rouat, E. Bouzy, J. Zollinger. Grain refinement of TiAl alloys by isomorphic self inoculation. *Intermetallics*, 95 (2018), 89-93.

188 B.B. Straumal, A.S. Gornakova, O.A. Kogtenkova, S.G. Protasova, V.G. Sursaeva, B. Baretzky. Continuous and discontinuous grain-boundary wetting in ZnxAl1−x. *Physical Review B*, 78 (2008), 054202.

189 E. Pereiro-Lopez, W. Ludwig, D. Bellet, J. Baruchel. Grain boundary liquid metal wetting: A synchrotron micro-radiographic investigation. *Nuclear Instruments and Methods in Physics Research B*, 200 (2003), 333-338.

190 B. B. Straumal, A. A. Mazilkin , O. A. Kogtenkova , S. G. Protasova, B. Baretzky. Grain boundary phase observed in Al–5 at.% Zn alloy by using HREM. *Philosophical Magazine Letters*, 87, 6 (2007), 423-430.

191 K. Zhou, H.P. Wang, J. Chang, B. Wei. Surface tension measurement of metastable liquid Ti-Al-Nb alloys. *Applied Physics A*, 105 (2011), 211-214.

192 I. Egry, R. Brooks, D. Holland-Moritz, R. Novakovic, T. Matsushita, E. Ricci, S. Seetharaman, R. Wunderlich, D. Jarvis. Thermophysical properties of gamma-Titanium aluminide: The European IMPRESS Project. *International Journal of Thermophysics*, 28 (2007), 1026-1036.

193 C.T. Crowe, J.D. Schwarzkopf, M. Sommerfeld, Y. Tsuji. *Multiphase Flows with Droplets and Particles*. CRC Press, 2012.

194 F.J. Humphreys, M. Hatherly. *Recrystalization and related annealing phenomena*. Elsevier, 1995.

195 A. Dhal, S.K. Panigrahi, M.S. Shunmugam. Insight into the microstructural evolution during cryo-severe plastic deformation and post-deformation annealing of aluminium and its alloys. *Journal of Alloys and Compounds*, 726 (2017), 1205-1219.

196 J.E. Burke, D. Turnbull. Recrystallization and Grain Growth. *Progress in Metal Physics*, 3 (1952), 220.

197 J.P. Hsu, M.J. Lin. Dissolution of Solid Particles in Liquids. *Journal of Colloid and Interfacial Science*, 141 (1991), 60-66.

198 T.K. Sherwood, R.L. Pigford, C.R. Wilke. *Mass transfer*. McGraw-Hill, 1975.

199 H. Schlichting, K. Gersten. *Boundary-Layer Theory*. Springer, 2016.

200 I. Egry, D. Holland-Moritz, R. Novakovic, E. Ricci, R. Wunderlich, N. Sobczak. Thermophysical Properties of Liquid AlTi-Based alloys. *international journal of thermophysics* (2010).

201 K. Zhou, H.P. Wang, J. Chang, B. Wei. Surface tension measurements in metastable liquid Ti-Al-Nb alloys. *Appl. Phys. A*, 105 (2011), 211-214.

202 Quested, T.E. *Solidification of Inoculated Aluminum Alloys*. University of Cambridge, 2004.

203 D.-H. Gosslar, R. Guenther, C. Hartig, R. Bormann, J. Zollinger, I. Steinbach. Grain Refinement of G-TiAl Based Alloys by Inoculation. In *Mater. Res. Soc. Symp. Proc. Volume 1128* (2009), 91.

Appendix A –Particle Size Distributions

This appendix presents the particle size distributions obtained using both SEM image analysis to determine number fractions and DLS for volume fraction.

A.1 SEM Image Characterization

The size distributions obtained using the procedure outlined in Ch. 3 are presented.

A.1.1 Ti-Al-Nb SEM Particle Size Analysis

Using the procedure outlined above the size distributions for the milled Ti-Al-Nb powders were obtained, and can be seen in Figure A0.1. The D50, or median particle size, for the distributions ranged from almost 200 µm after 3 hours to less than 50 µm after 11 hours.

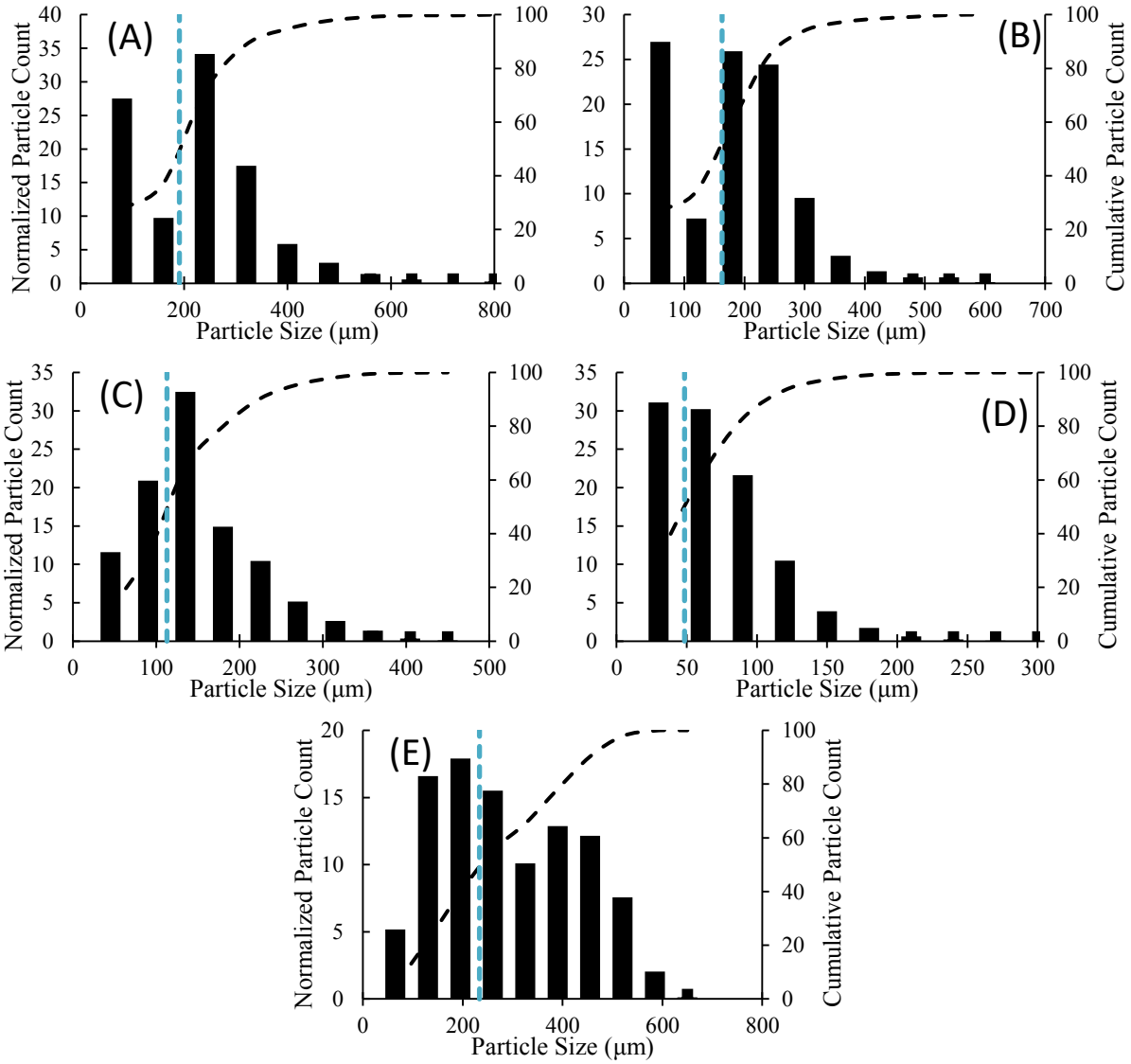

Figure A0.1: SEM obtained Ti-Al-Nb Ground Particle Distributions after (A) 3 hrs, (B) 6 hrs, (C) 9 hrs, (D) 11 hrs and (E) 3 hrs under Ar. The cumulative distributions are shown as dashed lines and the vertical dashed lines are the distribution D50

Both the D50 and maximum particle sizes (D99) detected decreased as grinding time increased for the Ti-Al-Nb powders. The span, D50 and D99 for each distribution are given in Table A0.1.

Table A0.1: SEM obtained Ti-Al-Nb particle size distribution characteristics

	Ti-Al-Nb				
Grinding Time (hrs)	3 Ar	3	6	9	11
D50 (µm)	233	191	163	113	48
D99 (µm)	607	775	561	440	282
Span	1.34	1.70	1.50	1.69	2.10

The particles milled under argon have a larger D50 than those milled under air for the same time period but have a smaller maximum particle size and narrower distribution. The distribution is narrowest for the Ar milled sample but does not seem to depend significantly on the milling time.

A.1.2 Ti-Al-Ta SEM Particle Size Analysis

Similarly, the particle distributions were obtained for the milled Ti-Al-Ta powders. These obtained distributions can be seen in Figure A0.2. The particles obtained were smaller than the Ti-Al-Nb at equivalent milling times. The distributions also appeared more significantly one tailed than those of the Ti-Al-Nb particles.

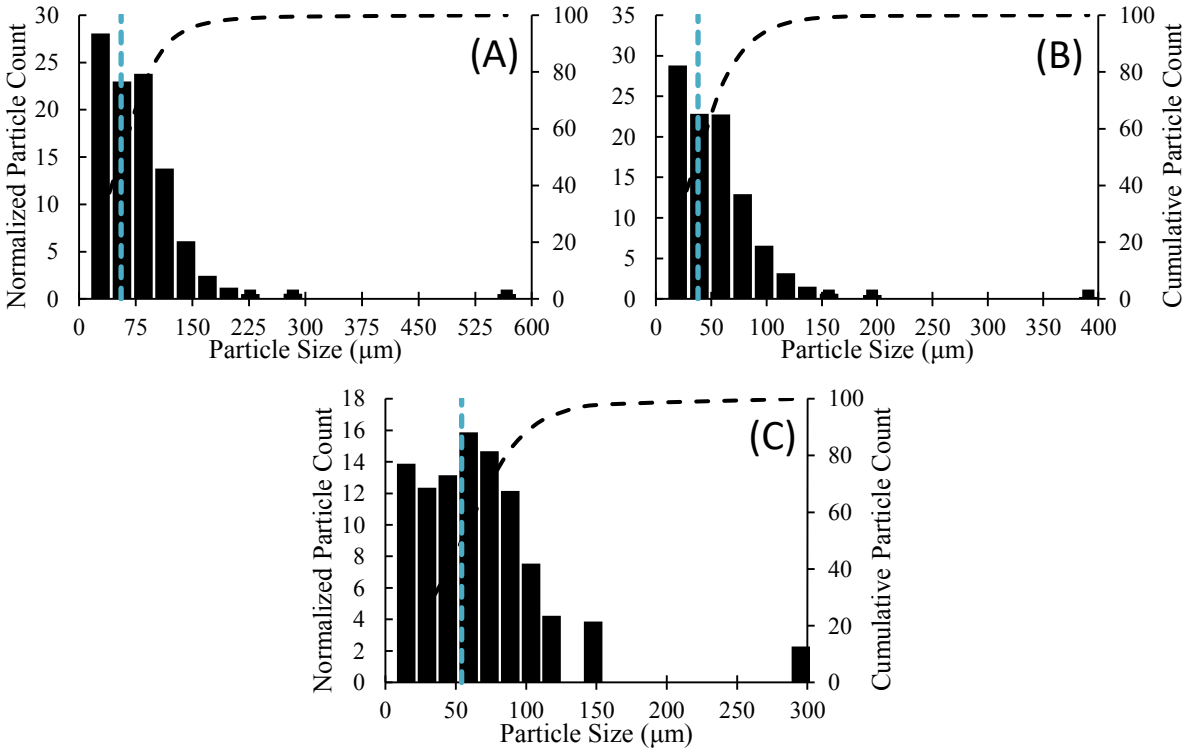

Figure A0.2: SEM obtained Ti-Al-Ta Ground Particle Distributions after (A) 3 hrs, (B) 6 hrs and (C) 9 hrs. The cumulative distributions are shown as dashed lines and the vertical dashed lines are the distribution D50

In contrast to the Ti-Al-Nb powders the D50 did not decrease significantly as the milling time increased, varying less than 20 μm between milling times. The 6 hour milled particles showed the smallest D50 (38 μm) while the 3 and 9 hour samples had nearly the same D50 (56 and 54 μm respectively). However, the maximum particle size did decrease significantly in each distribution as the milling time increased. This is shown along with the span of each distribution in Table A0.2.

Table A0.2: SEM obtained Ti-Al-Ta particle size distribution characteristics

	Ti-Al-Ta		
Grinding Time (hrs)	3	6	9
D50 (μm)	56	38	54
D99 (μm)	567	390	295
Span	2.03	1.51	1.79

The span of the distributions for the Ti-Al-Ta particles is larger than that of the Ti-Al-Nb particles at a given grinding time. This appears to make sense as in the Ti-Al-Nb distributions the D99 and D50 both decrease as milling time increases, whereas in the Ti-Al-Ta samples only the D99 significantly changes. The shape of the size distribution appears to not change significantly between 3 and 6 hours, however the distribution moves closer to normal for the 9 hour milled sample.

A.1.3 Ti-Ta SEM Particle Size Analysis

The same procedure was used to characterize the Ti-Ta powders. As with the Ti-Al-Nb samples, both the D50 and maximum particle size decrease as grinding time increases, as shown in Figure A0.3.

The D50 is significantly smaller at each milling time than the Ti-Al-Nb or Ti-Al-Ta powders. The maximum particle sizes are also much smaller as well. As the milling time increases the distributions appear to move towards a more normal shape (less one tailed). The spans of the distributions range between 1 and 2, as can be seen in Table A0.3.

Table A0.3: SEM obtained Ti-Ta particle size distribution characteristics

	Ti-Ta			
Grinding Time (hrs)	1.5	3	6	9
D50 (μm)	70	35	22	20
D99 (μm)	334	160	73	56
Span	1.62	1.1	1.17	1.25

After only 3 hours of grinding the Ti-Al particles are smaller (both by D50 and D99) than any of the Ti-Al-Nb or Ti-Al-Ta powders, even after their maximum grinding times. The D50 only varied by 50 μm across the distributions while the maximum particle size decreased from over 300 μm to less than 60 μm.

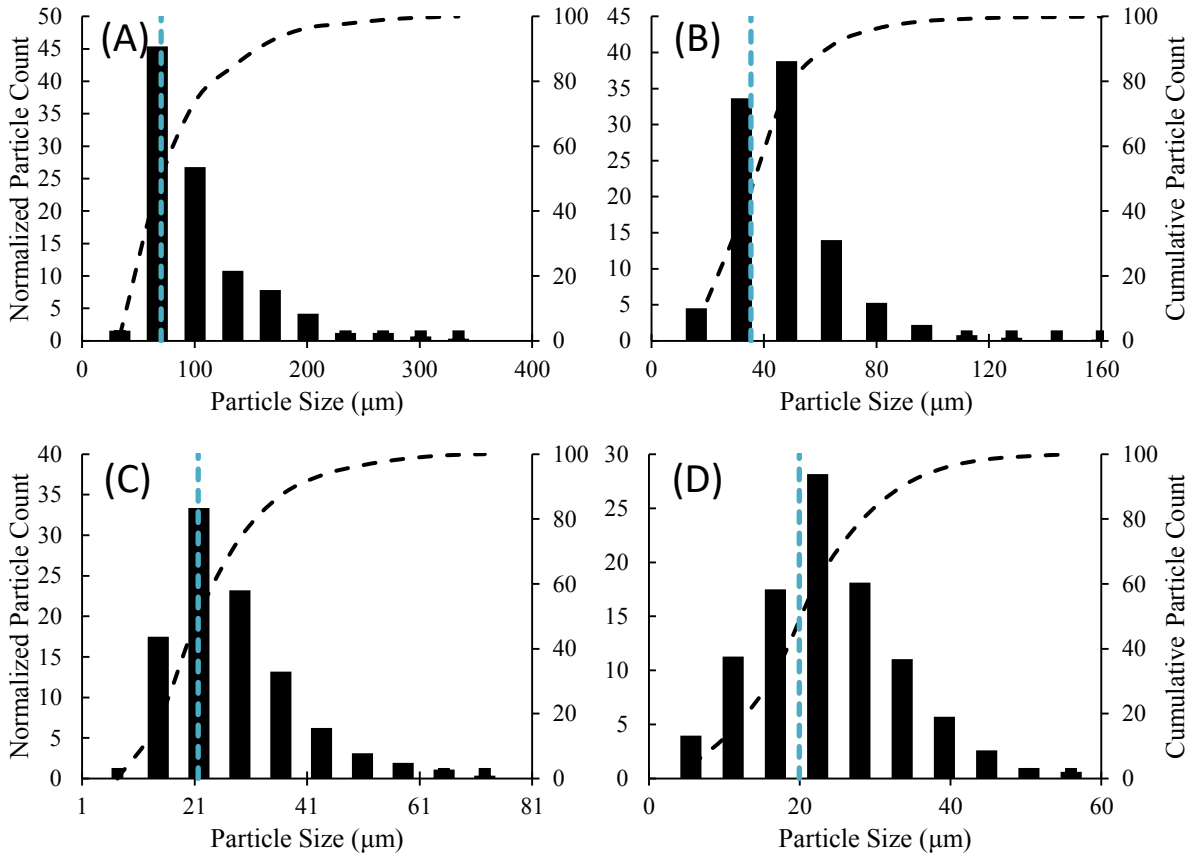

Figure A0.3: SEM obtained Ti-Ta Ground Particle Distributions after (A) 1.5 hrs, (B) 3 hrs, (C) 6 hrs and (D) 9 hrs. The cumulative distributions are shown as dashed lines and the vertical dashed lines are the distribution D50

This type of analysis gives a numerical size distribution. The number of particles of each size are counted and the number within a size range is directly correlated to the height of the bar for the size range. If more particles are counted within one size range than another its bar will be higher. This is shown schematically in Figure A0.4.

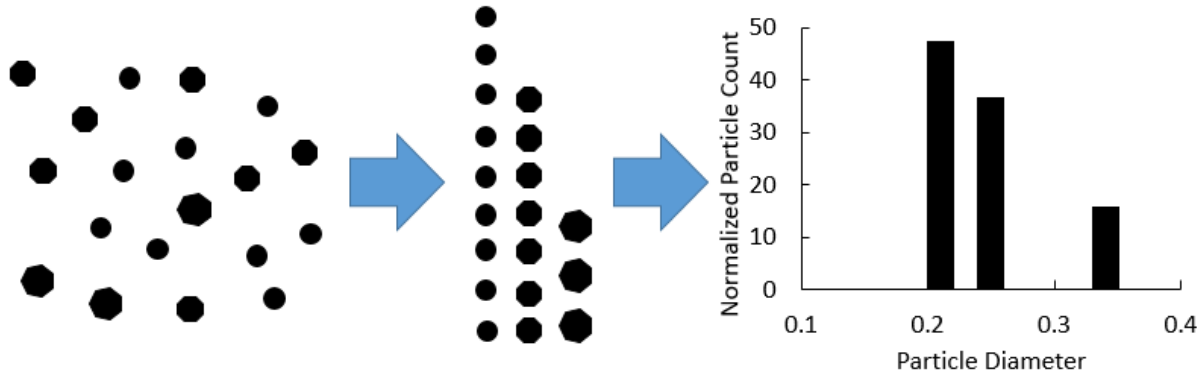

Figure A0.4: Schematic of numerical size distribution determination

A.2 Differential Laser Scattering Characterization

The size distributions obtained using the procedure outlined in Ch. 3 are presented.

A.2.1 Ti-Al-Nb DLS Particle Size Analysis

Using the procedure outlined above the volumetric size distributions were obtained for all the milled Ti-Al-Nb particles and can be seen in Figure A0.5. The 11 hour milled particles show a multimodal type distribution with a major peak near 200 μm and a minor peak closer to 60 μm. This multimodal behavior was more prominent in the measurements after ultrasonic stirring than those before. Similar multimodal behavior was also seen in both 3hr milled samples, under air and Ar, after ultrasonic stirring but to a much lesser extent than seen in the 11 hour sample. A proposed reason for these differences is the possibility that some particles, especially the smaller ones, may not be fully dispersed into the suspension before ultrasonic stirring and may be floating on top of the water. The ultrasonic stirring may break the surface tension and allow the particles to disperse more freely.

The 9 hour milled sample shows a volumetric D50 and D99 greater than that of the 6 hour or 3 hour milled samples, only the sample milled under Ar for 3 hours showed larger particle sizes, as shown in Table A0.4. It did not show significant differences between the measurements with or without ultrasonic stirring. The span of its distribution was larger than the 6 hour milled, but smaller than the 11 hour milled samples. It would be expected that at the very least the D99 decreases as milling time increases since the particles should be reduced in size by the action of milling. This is why it is useful to have measured particle sizes with two methods, as is the SEM characterization the 9 hour milled samples were bigger than the 11 hour but smaller than the 6 hour milled samples as expected. The abnormality is then likely some form of sampling error, as the DLS analysis is carried out on a very small mass of particles.

Table A0.4: DLS obtained Ti-Al-Nb particle size distribution characteristics.

	Ti-Al-Nb				
Grinding Time (hrs)	3 Ar	3	6	9	11
D50 (μm)	339	282	267	328	137
D99 (μm)	522	478	420	508	337
Span	0.77	1.02	0.66	0.82	1.61

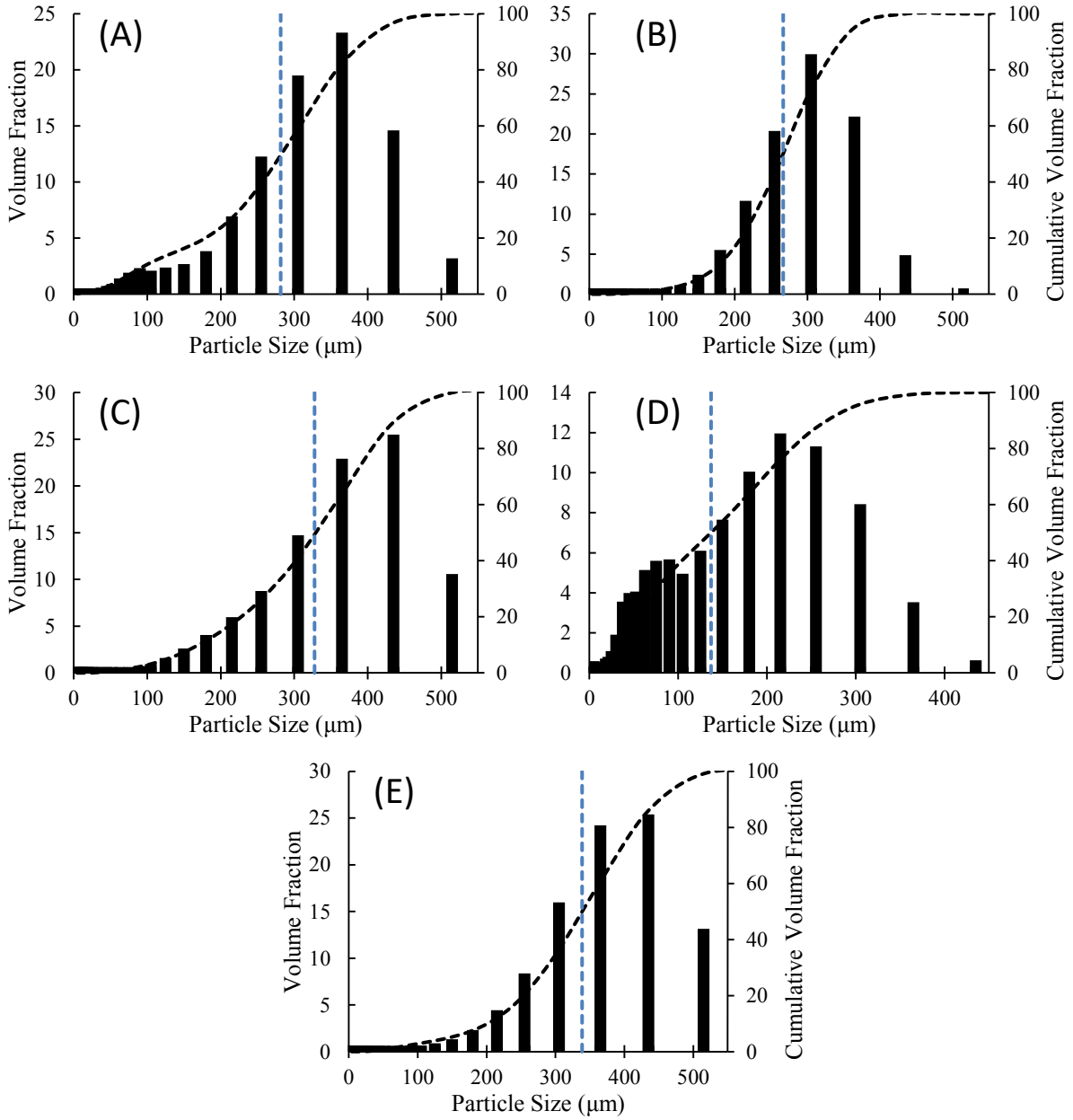

Figure A0.5: DLS obtained Ti-Al-Nb Ground Particle Distributions after (A) 3 hrs, (B) 6 hrs, (C) 9 hrs, (D) 11 hrs and (E) 3 hrs under Ar. The cumulative distributions are shown as dashed lines and the vertical dashed lines are the distribution D50

A.2.2 Ti-Al-Ta DLS Particle Size Analysis

The size distributions were obtained in the same manner for the Ti-Al-Ta milled particles as shown in Figure A0.6. Unlike the Ti-Al-Nb samples who showed little variation between measurements the Ti-Al-Ta samples showed variations both before and after ultrasonic stirring as well as between the measurements taken under the same conditions. This became more pronounced as the particle sizes decreased with the D50 of the 9 hour milled sample varying from 75-130 μm depending on the measurement.

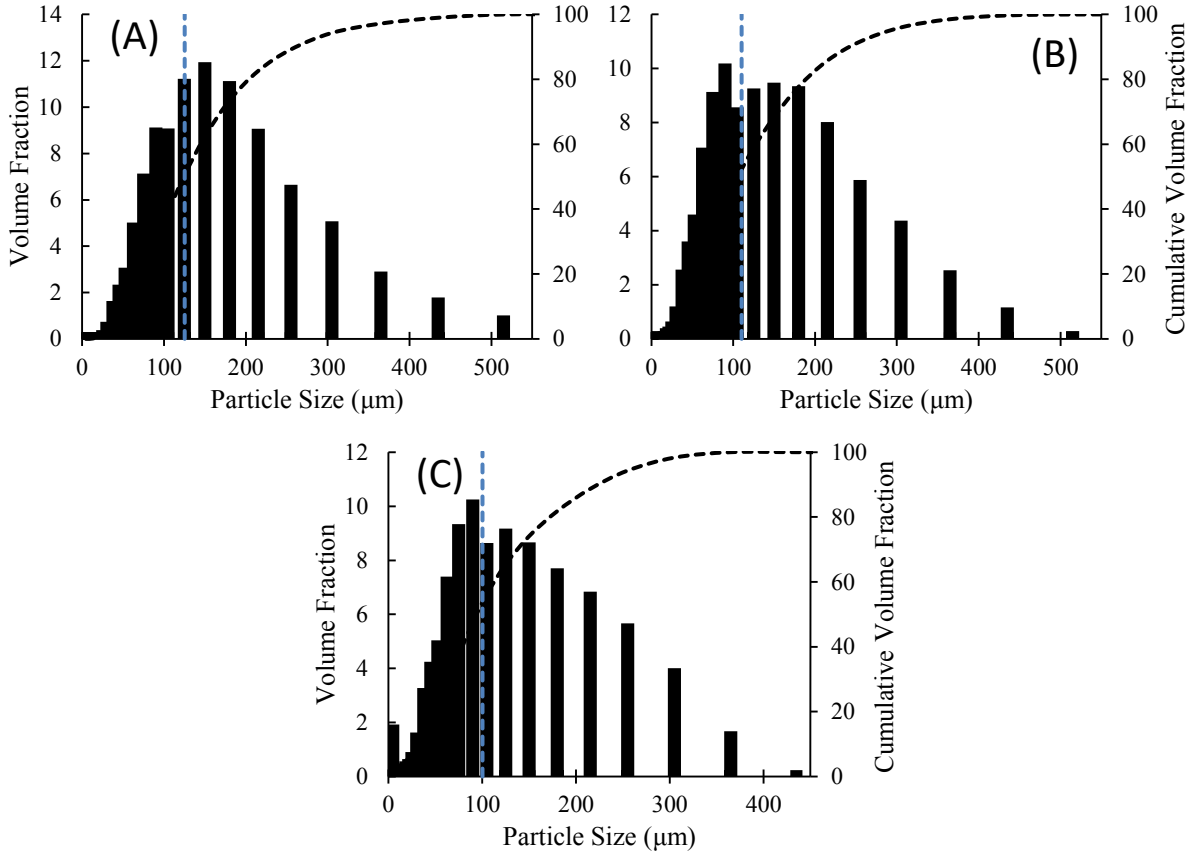

Figure A0.6: DLS obtained Ti-Al-Ta Ground Particle Distributions after (A) 3 hrs, (B) 6 hrs and (C) 9 hrs. The cumulative distributions are shown as dashed lines and the vertical dashed lines are the distribution D50

The distributions appear one-tailed towards larger particles unlike the Ti-Al-Nb particles which were one tailed towards smaller particles when analyzed by DLS. The average D50 and maximum particle size both decreased as milling time increased as expected, shown in Table A0.5. The spans of the distributions found with DLS were quite large, greater than 1.5 for each distribution. The D50 only decreased by 25 μm across the distributions which the D99 only decreased by approximately 100 μm.

Table A0.5: DLS obtained Ti-Al-Ta particle size distribution characteristics

	Ti-Al-Ta		
Grinding Time (hrs)	3	6	9
D50 (μm)	125	110	100
D99 (μm)	410	387	299
Span	1.66	1.75	1.71

A.2.3 Ti-Ta DLS Particle Size Analysis

The obtained size distributions for the Ti-Ta particles found with DLS are shown in Figure A0.7. The measurements showed less variation than found for Ti-Al-Ta but some multimodality was also seen after ultrasonic stirring.

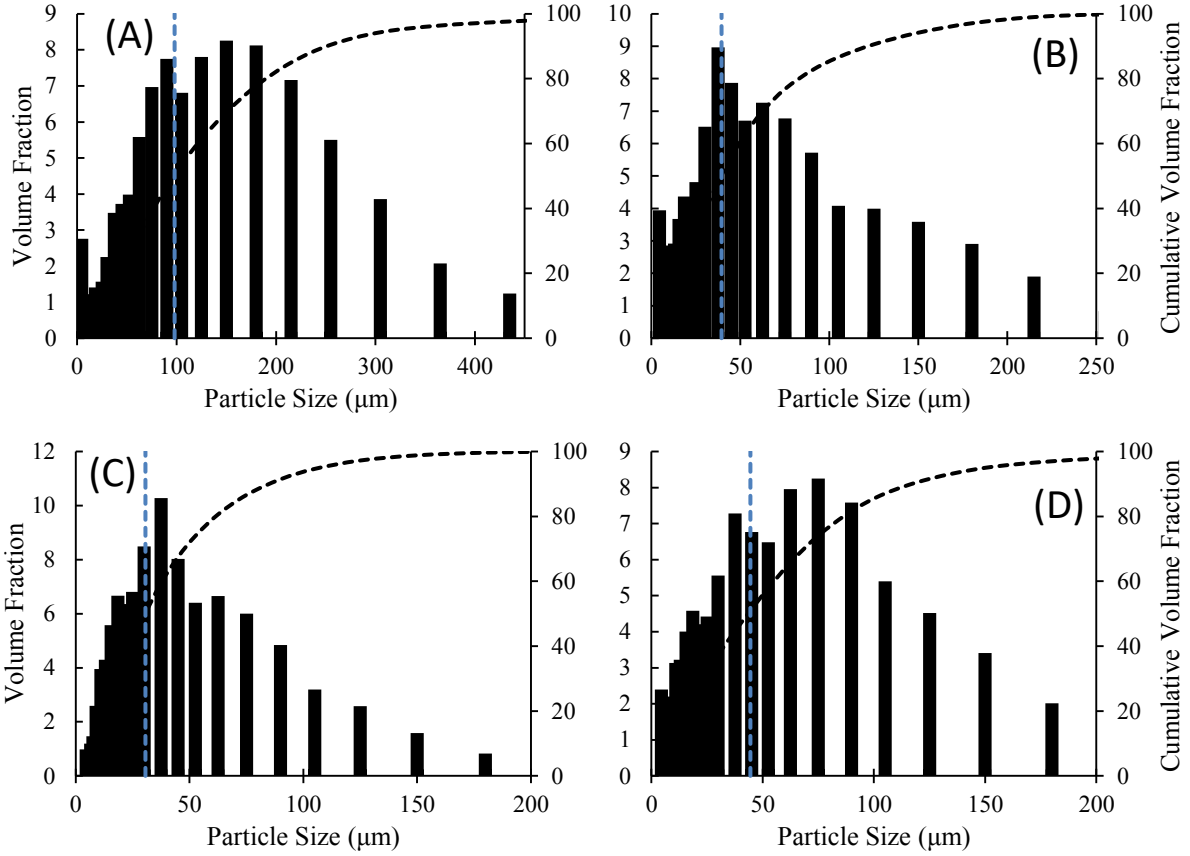

Figure A0.7: DLS obtained Ti-Ta Ground Particle Distributions after (A) 1.5 hrs, (B) 3 hrs, (C) 6 hrs and (D) 9 hrs. The cumulative distributions are shown as dashed lines and the vertical dashed lines are the distribution D50

The Ti-Ta particles remain the smallest measured, with the D50s of all the distributions less than 100 μm. The Ti-Ta distributions had mainly particles which could have been more accurately analyzed using the lens of the apparatus for particles 0.25-87.5 μm however the presence of larger particles existing outside that size range (see D99 values in Table A0.6) precluded its use. The 9 hour milled sample does not follow the trend of longer milling times resulting in smaller particles based on its D50, D99 or span. This is again likely due to an issue from flotation or sampling. The spans for the Ti-Ta particles were the largest measured, all of the distributions had spans greater than two.

Table A0.6: DLS obtained Ti-Ta particle size distribution characteristics

	Ti-Ta			
Grinding Time (hrs)	1.5	3	6	9
D50 (μm)	98	39	31	44
D99 (μm)	430	208	156	195
Span	2.66	2.96	2.46	2.47

In contrast to the SEM characterization the size distribution reported by DLS is not numerical but volumetric i.e. the fraction of the distribution in each bin is the volume fraction. In the SEM

characterization the fraction in each bin is numerical since it is based on the number of particles counted. In contrast DLS does not count individual particles but rather determines relative volumes of particles within a certain size class based on intensities of detected diffracted light. In Figure A0.8 the same sample distribution as shown in Figure A0.4 is shown but with its volumetric size distribution rather than numerical. It can be seen that while the largest particles are not the most numerous their size results in their having the largest volume fraction of the size classes. In contrast the smallest particles are the most numerous, they have the smallest volume fraction. While the distributions found with SEM and DLS then are not directly comparable they each give insight into the characteristics of the particle distributions.

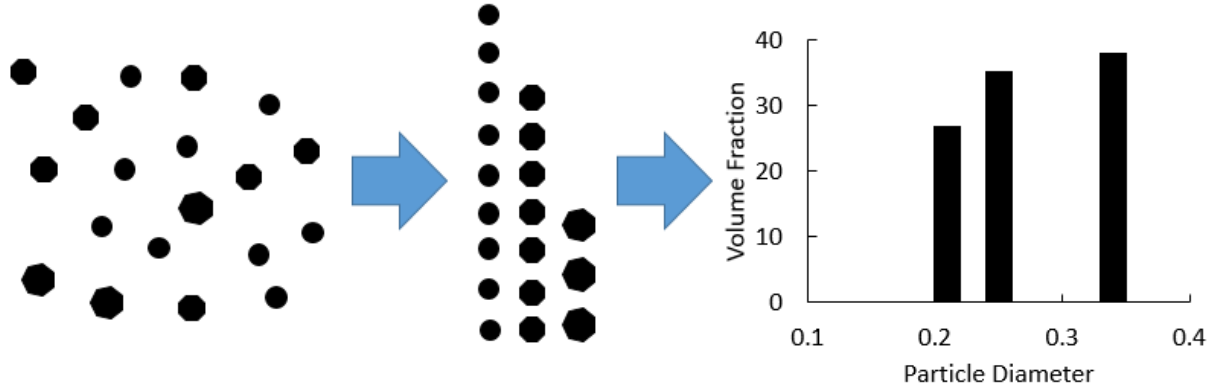

Figure A0.8: Schematic of volumetric size distribution determination

A.3 Trends in Particle Distributions with Grinding Time

The trends found as grinding time increases for the distribution D50s and D99s are evaluated here.

A.3.1 Ti-Al-Nb

If the 9 hour DLS measurements are disregarded the D50s measured by both DLS and SEM can be seen in Figure A0.9 to decrease quadratically as grinding time increases while the D99s decrease linearly. The fit for these trends is quite good and can be used to calculate expected values for the D99 and D50 of the 9 hour milled sample. This results in a volumetric D50 of 205 µm rather than 328 µm and a difference from the numerical D50 of ~100 µm, in line with the other distributions. The expected D99 value was calculated to be 370 µm rather than 508 µm. Since the fit of the trends are very good and have the same behavior regardless of the measurement technique for both D50 (quadratic) and D99 (quadratic) these calculated expected values for the 9 hour sample can be used rather than the measured values which show a drastic increase in particle size after milling for more time than the 3 or 6 hour samples. Ideally further DLS measurements would be taken to verify if the initial measurement was erroneous or if there was another phenomenon influencing particle size, e.g. agglomeration, however not enough of the particles remained after the measurements (SEM and DLS) and inoculation trials for further measurements to be possible.

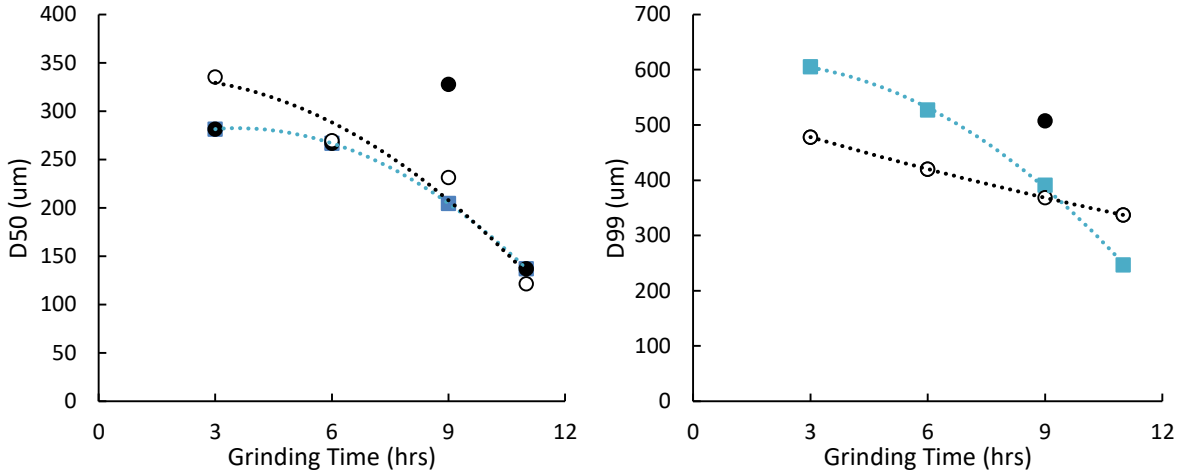

(A) (B)

Figure A0.9: Ti-Al-Nb (A) D50 and (B) D99 evolution trends when measured by SEM (blue) and DLS (Black).

A.3.2 Ti-Al-Ta

As with the Ti-Al-Nb samples the trends from one measurement method can be applied to the other in order to correct erroneous measurements. In the case of the Ti-Al-Ta samples the 9 hour milled sample appears to have a larger D50 and D99 than expected when measured by SEM. Using the trends shown in Figure A0.10 the SEM measured D50 can be corrected to 20 µm and the D99 to 93 µm for the 9 hour milled sample. The trend fits are slightly less good than those found with the Ti-Al-Nb particles but sufficient to calculate new D50 and D99 values. The corrections are also shown for the converted volumetric data from the SEM resulting in a D50 of 0.33 µm and D99 of 5.5 µm.

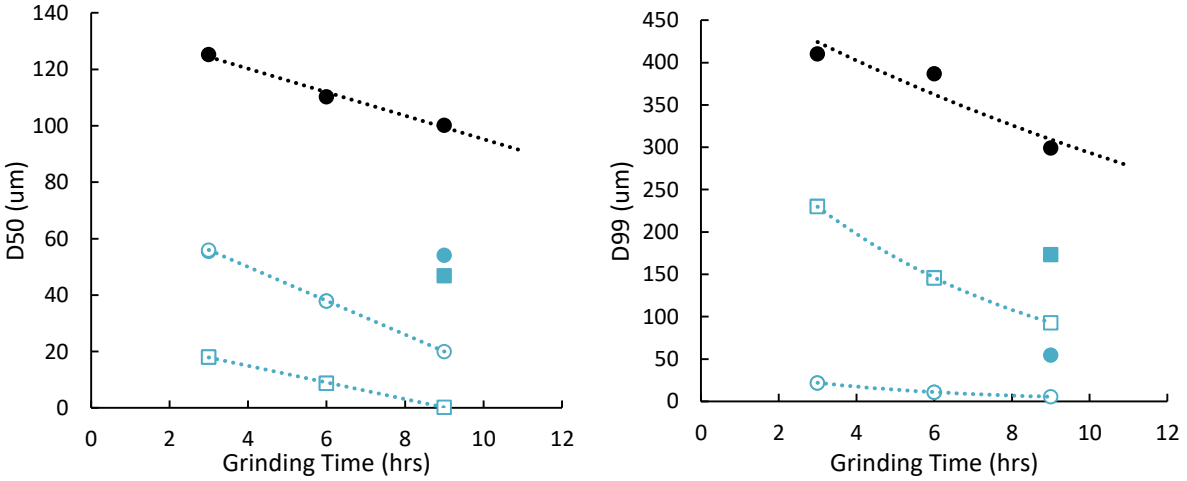

(A) (B)

Figure A0.10: Ti-Al-Ta (A) D50 and (B) D99 trends by SEM (blue) numerical (squares) and volumetric (circles) and DLS (Black).

A.3.3 Ti-Ta

As with the 9 hour Ti-Al-Nb particles expected D50 and D99 values can be found using the trends from the other distributions. In the case of the Ti-Ta particles the trend fits are power relations for both the D50 and D99, as seen in Figure A0.11. The expected D50 for the 9 hour powders is then 20 µm rather than 44 µm and the expected D99 is 108 µm rather than 195 µm.

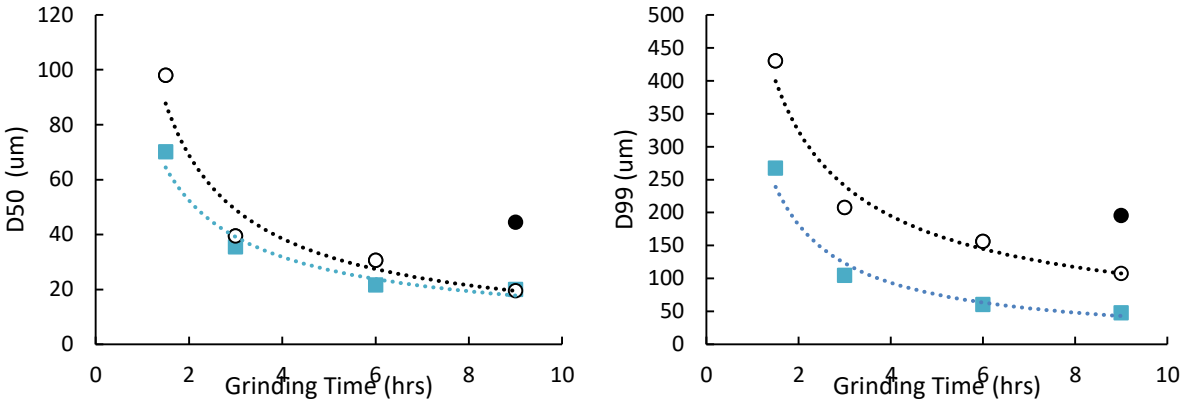

(A) (B)

Figure A0.11: Ti-Ta (A) D50 and (B) D99 evolution trends when measured by SEM (blue) and DLS (Black).

A.4 Comparison of SEM and DLS

In order to illustrate the differences between size distributions obtained by DLS and SEM image analysis the results of each for the 3 hour milled Ti-Al-Nb powder are shown in Figure A0.12. The distributions obtained by SEM or DLS are shown in Figure A0.12A and D respectively. The maximum size detected by DLS was 515 µm compared to 775 µm with the SEM. The numerical D50 obtained by SEM was 190 µm with a span of 1.7 compared to the volumetric D50 of 280 µm with a span of 1.0 obtained by DLS. The distributions look quite different with the DLS showing a slower increase in cumulative fraction as size increases than the SEM measurements, the reported D50s are also quite different. This is unsurprising as the DLS is measuring the distribution volumetrically while the SEM measures the distributions numerically. In order to compare the results between the SEM and DLS distributions they must be converted so they are reporting the same type of distribution (i.e. volumetric or numerical). The distributions were each converted from numerical to volumetric, or vise-versa, which can be seen in Figure A0.12B and C. It is known that conversion from a volumetric type distribution to numerical is not advisable as the results often do not represent the true distribution [**179**]. This is evident in Figure A0.12C where the calculated numerical distribution obtained from the DLS volumetric distribution reports nearly 100% of the particles by number being less than 2.5 µm. Even though, together, all the particles of this size have a small volume fraction, the small size of the particles means that such a volume contains a huge number of particles, conversely the ranges of larger particles contain very few particles even if the volume fraction is larger. This does not agree with the distribution obtained by SEM which had a D50 two orders of magnitude higher.

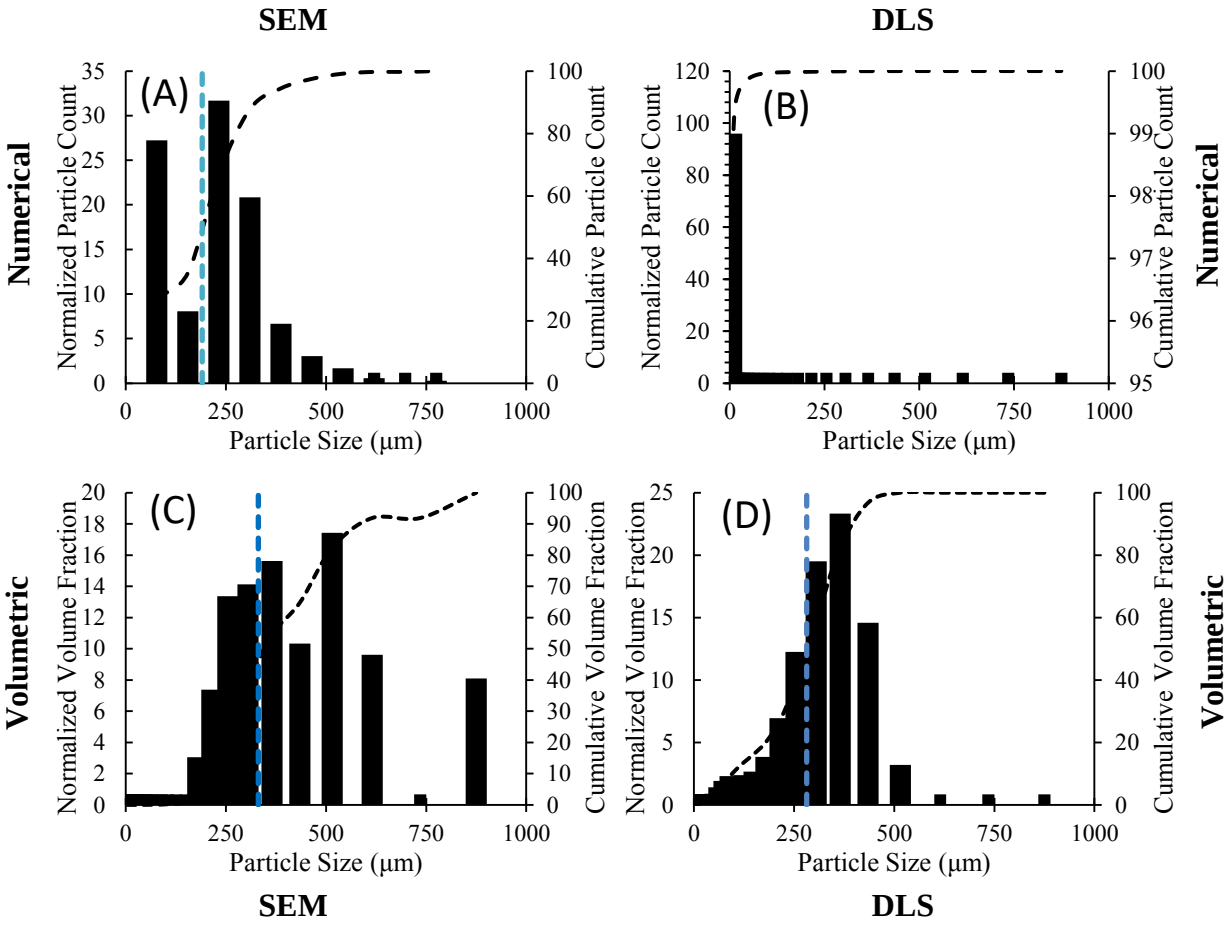

Figure A0.12: Particle size distributions for 3 hour milled Ti-Al-Nb powder (A) numerical size distribution obtained by SEM and (B) volumetric size distribution obtained by DLS.

Conversely the numerical distribution can be more easily converted to volumetric while maintaining physical meaning. In the case of Figure A0.12C the individual area measurements of each particle obtained by SEM were converted to equivalent spherical volumes and binned in the same manner as the DLS volumetric analysis. This resulted in a distribution with a D50 of 331 µm with a span of 1.2 which is on the same order as the values obtained directly from DLS (280 µm and 1.0). The increase in the D50 from the DLS measurement can be attributed to the few large particles detected by SEM which account for a relatively large volume fraction. If the particles detected by SEM which are larger than the largest detected by DLS (515 µm), which compromise 1% by number or 15% by volume of the distribution, are removed from the distribution the D50 and span are reduced to 310 µm and 0.9 respectively, much closer to the measured values from DLS. This indicates that the difference between the DLS and SEM measurements is likely due to sampling issues rather than a fundamental incompatibility between the measurement methods. Issues with sampling are to be expected since the size of the sample in either method is quite small, in this case ~15 mg by SEM and likely on the same order of magnitude by DLS, compared to a total of ~5 g of milled powder produced. It then appears that both methods give the same results: using the volumetric size distribution, D50 is around 300 µm and the span around 1.0.

Appendix B – Calculation of the Effect of Al Content on Grain Size

It is also important to consider the effects that slight changes in the aluminum content between the ingots has on their final grain size. Since the samples prepared all have compositions on the peritectic plateau small changes in the aluminium content can have larger than expected effects on the equiaxed grain size [**186**]. It is then important to separate the effect of the inoculants on the grain size from that of the changes in Al content.

The Ti-Al-Nb inoculations trials are the focus of the first analysis. Figure B0.1 shows the evolution of grain size with aluminum content for alloys processed in the same induction heated cold crucible apparatus, Ti-Al-2Cr-2Nb [**186**] and Ti-Al-O [**118**] alloys (shown as lines), along with the Ti-Al-Nb inoculated samples (points). The literature alloys were produced in a similar manner to the inoculated alloys, however their mass was lower (~20g) compared to the inoculant alloys (~40g), and the absence of the inoculant delivery system in the apparatus allowed the temperature of the melt to be measured directly (measured superheats of 20ºC for the Ti-Al-Cr-Nb samples and 100ºC for the Ti-Al-O samples). In both the Ti-Al-Cr-Nb and Ti-Al-O samples the trend can be seen that as the aluminum content in the alloy increases the grain size decreases. Of the inoculated samples tested, the reference sample has the highest aluminum content. The literature values then indicate that when using it as a reference for the inoculated samples it may have a smaller grain size than expected. It can also be noted that the sample inoculated with 6 hour milled particles had a larger grain size than the samples inoculated with unmilled or 3 hour milled particles contrary to expected This may be explained by the 6 hour sample having a smaller aluminum content than the others, and thus if the inoculation did not occur the sample would have a larger grain size than the others. In order to better evaluate how each inoculant distribution effects the final grain size it is important to take this into consideration and develop a method of calculating how much of the grain refinement can be attributed to the inoculants.

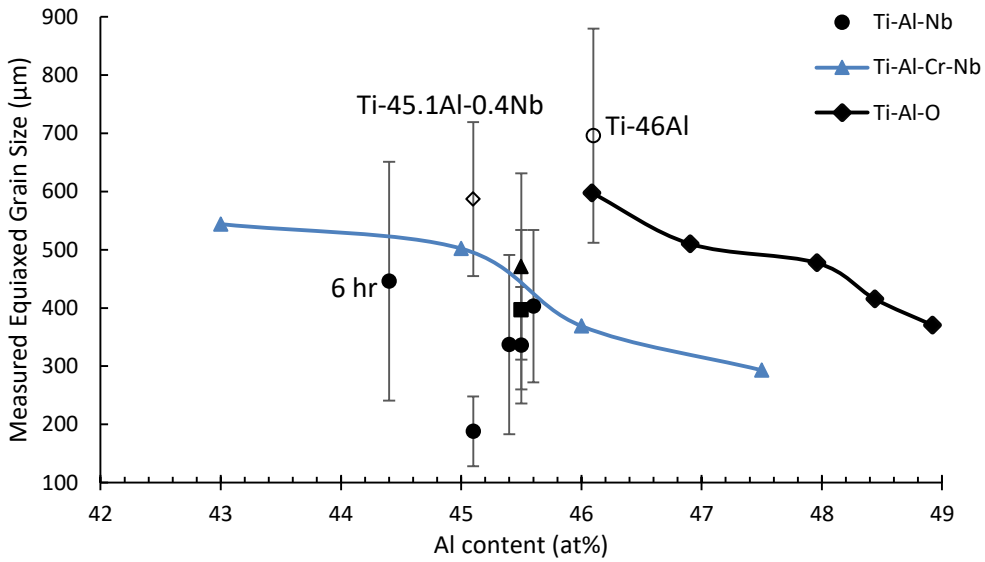

Figure B0.1: Grain size evolution with aluminum content

The samples used to produce the curves were processed in much the same manner as in this work, using the same apparatus but with different alloying compositions than in the inoculation trials, different sample masses and known superheats. The curves then must be adjusted to reflect these changes. The observed grain refinement on increasing aluminum content has been closely tied to the peritectic reaction and the amount of pro-peritectic primary phase [**186**]. Figure B0.2 shows the curves from literature along with the characteristics of their respective peritectic plateaus. It can be seen in Figure B0.2A that the peritectic points are shifted to higher Al contents in the Ti-Al-Nb-Cr alloy compared to the Ti-Al-(O) alloy (the binary Ti-Al values were used due to the small O contents). This also holds true when the pro-peritectic β fractions are considered, the Ti-Al-Nb-Cr alloy peritectic point is located at a higher pro-peritectic fraction. The onset and end of the peritectic plateau are located at 0 and 100% pro-peritectic β respectively.

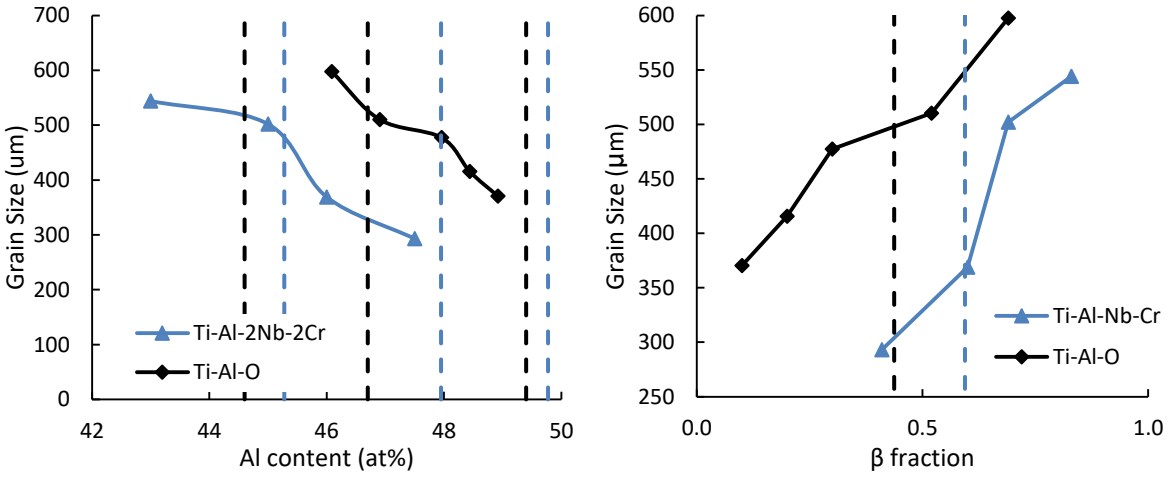

(A) (B)

Figure B0.2: Comparison of grain size with (A) aluminum content and (B) pro-peritectic β fraction. Vertical lines represent the onset, peritectic point, and end point of the peritectic plateau.

The pro-peritectic fractions were calculated for scheil solidification conditions using Thermocalc, the curves used can be found in Figure B0.3 for the 10 conditions possible assuming complete dissolution of the inoculant particles, i.e. the nominal composition of the ingot.

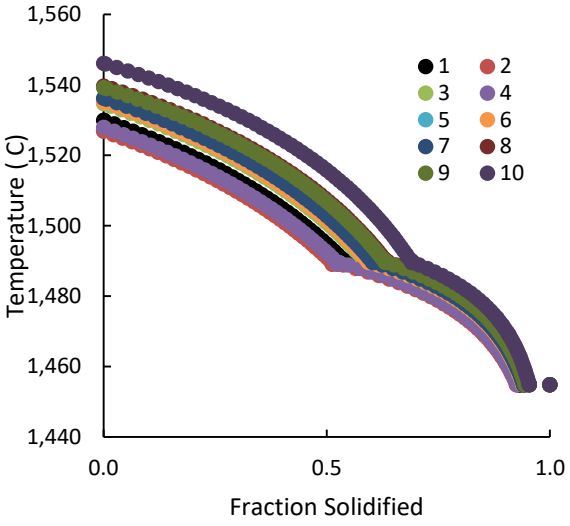

exp #	Ti (at%)	Al (at%)	Nb (at%)	β fraction
1	53.6	46	0.4	0.54
2	53.9	46.1	0	0.51
3	53.9	45.6	0.5	0.59
4	54	46	0	0.52
5	54	45.5	0.5	0.60
6	54.1	45.5	0.4	0.59
7	54.2	45.4	0.4	0.60
8	54.4	45.1	0.5	0.63
9	54.5	45.1	0.4	0.63
10	55.2	44.4	0.4	0.69

Figure B0.3: Scheil solidification curves for ingot conditions with nominal composition

The same can also be done assuming none of the inoculants dissolve and there is no Nb participating in the solidification. Curves of this type are shown in Figure B0.4

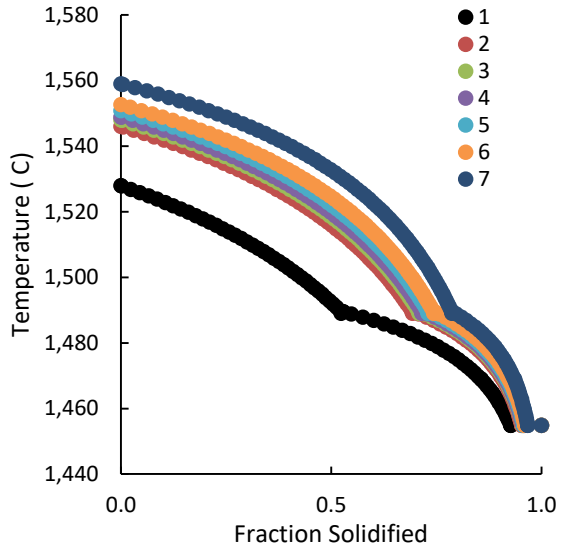

exp #	Ti (at%)	Al (at%)	β fraction
1	54.0	46.0	0.52
2	55.8	44.2	0.69
3	56.0	44.0	0.71
4	56.1	43.9	0.72
5	56.3	43.7	0.73
6	56.5	43.5	0.74
7	57.2	42.8	0.79

Figure B0.4: Scheil solidification curves for ingot conditions with no inoculant dissolution

In order to correct the curves so they can be used more accurately with the inoculated samples the change in the peritectic plateaus must be considered. The change in the location of the peritectic plateau points with increasing Nb content from the binary to 2% Nb can be seen in Figure B0.2A (calculated at equilibrium with Thermocalc) along with the Ti-Al-2Nb-2Cr and Ti-Al-O values. At 2% Nb it can be seen that the peritectic onset is at roughly the same Al content for both Ti-Al-2Nb and Ti-Al-2Nb-2Cr but the peritectic point is shifted to higher Al content and the end of the plateau shifted to lower. It is then necessary to not only transpose the curves to identical peritectic points but to transform them as well to represent the changing shape of the peritectic plateau i.e. changing hyper and hyo peritectic fractions. This

transformation was done on the Ti-Al-Nb-Cr (20° superheat) curve as shown in Figure B0.2B to the binary plateau, the compositions of the inoculated samples are also shown.

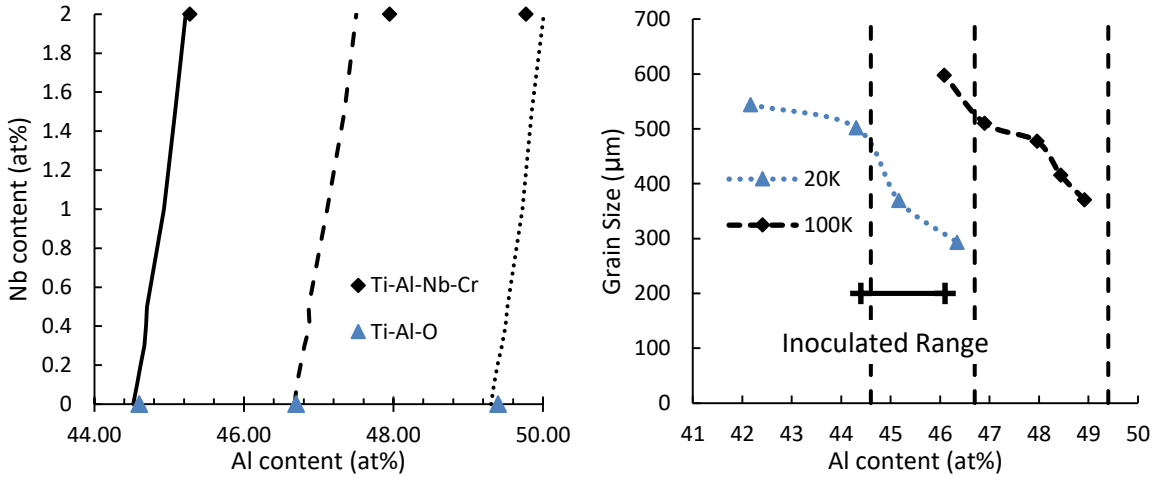

(A) (B)

Figure B0.5: (A) Change in peritectic plateau points (shown as lines, solid-onset, dashed peritectic point and dotted peritectic endpoint) with increasing Nb content and (B) grain size curves corrected to Ti-Al binary

Since the grain refinement on the peritectic plateau is linked to the fraction of pro-peritectic primary β formed [**186**] it was calculated for each inoculated alloy for two conditions encompassing the entirety of potential conditions, first using the nominal composition of the alloy, this supposes that all the Nb content added by inoculation is present in the liquid during solidification i.e. full dissolution of the particles, and secondly calculating the composition of the alloy if none of the Ti, Al or Nb present in the inoculant particles can participate in solidification i.e. zero dissolution of inoculant particles, however the Al added as a binder with the particles was considered to be present. In order to account for the change in hyper and hypo peritectic fractions these values were then converted to fractional distances from the peritectic point, i.e. the change in pro peritectic phase from the peritectic point to the sample relative to the change in pro peritectic phase from the peritectic point to the onset or end of the peritectic plateau. This can be seen in Figure B0.6 along with the value for the target condition of a binary Ti-46Al alloy.

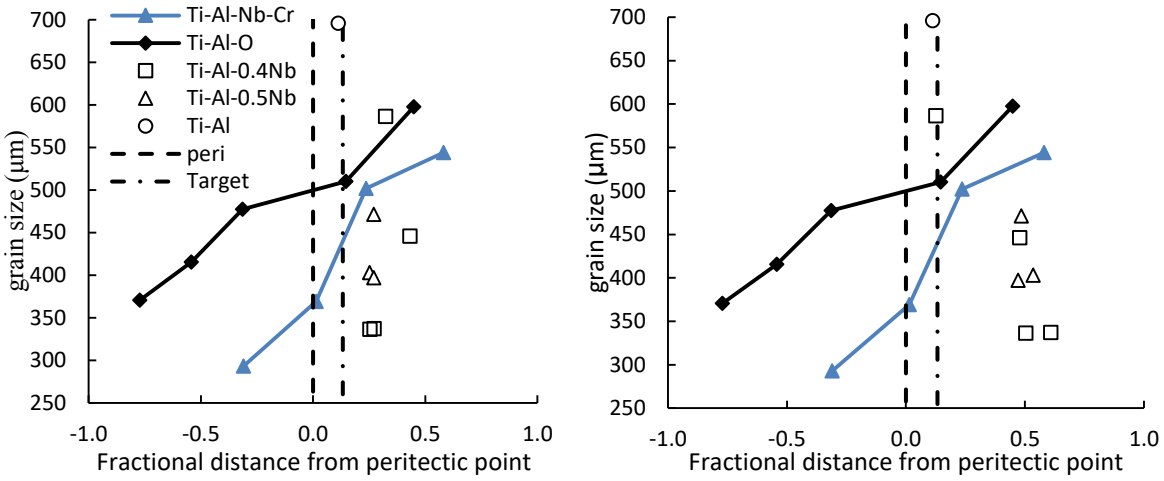

Figure B0.6: Fractional distances from the peritectic point for (A) full dissolution and (B) no dissolution of inoculant particles.

The curves could then be used to calculate the change in grain size depending on the fractional distance from the peritectic point as shown in Figure B0.7. The calculated grain size on either curve at the target composition of 46% Al (a fractional distance from the peritectic point of 0.13 for a binary alloy) was used as a reference to calculate how the grain size evolved on either curve as the fractional distance changed. These curves along with the calculated fractional distances at the nominal or zero-dissolution conditions and the measured reference grain size (696 µm at a fractional distance of 0.11) could then be used to calculate the expected reference grain size for each of the inoculated samples.

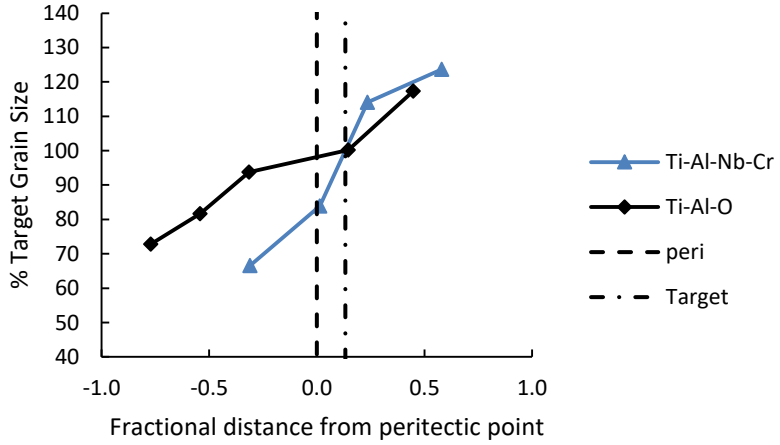

Figure B0.7: Effect of fractional distance from the peritectic point on grain size

Figure B0.8 shows the reduction of grain size for each Ti-Al-Nb inoculant distribution, isolated from the effect of the change in Al content between them. Four different conditions are considered for each distribution, superheats of 20° or 100° combined with the alloy conditions either at the nominal level (dissolution of all particles) or with no alloying effects from the particles (no particle dissolution). Grain size reductions were found to be greater when it was assumed that no particles dissolved and less when full particle dissolution was considered. This makes sense as the sample produced to see the solutal effect of the Nb addition had a smaller

grain size than the binary alloy. The largest reductions were found with an assumed 100° superheat and no particle dissolution while the smallest reductions were found with an assumed 100° superheat and complete particle dissolution. The range of possible grain size reductions is then greater as the superheat increases.

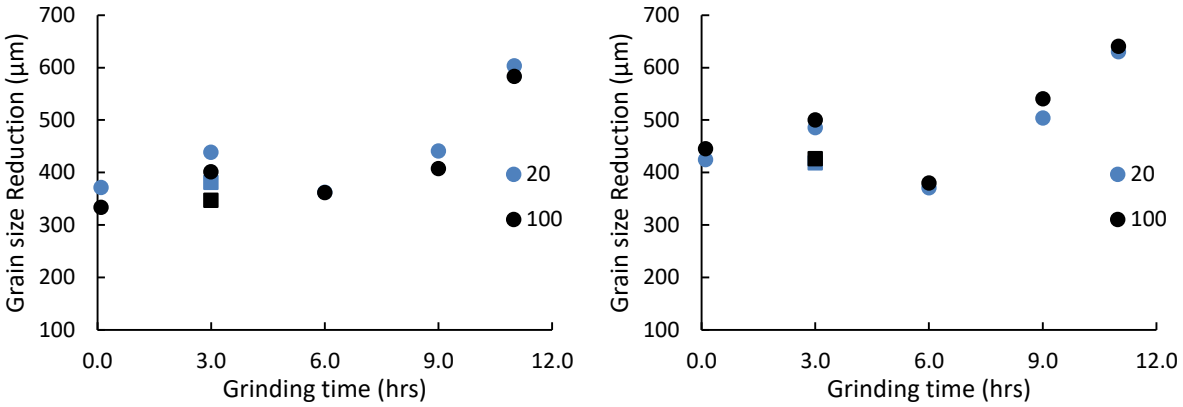

Figure B0.8: Grain refinement by inoculation as particle grinding time increases for (A) full dissolution and (B) no dissolution of inoculant particles.

The grain size reductions can also be compared to the size of the particles introduced (represented by the distribution numerical D50) and the number of particles introduced as shown in Figure B0.9. The reduction in grain size decreases as the particle size increases and number of particles introduced decreases. These are the same trends as seen before the effect of Al content was considered. The reduction in grain size in each case was greater taking into account the Al content than without. It can be seen that compared to the raw measured grain sizes that the 6 hour milled sample no longer appears so significantly different from the other trials. While it's measured grain size was greater than expected the grain size reduction observed was much closer to the observed trends from the other trials.

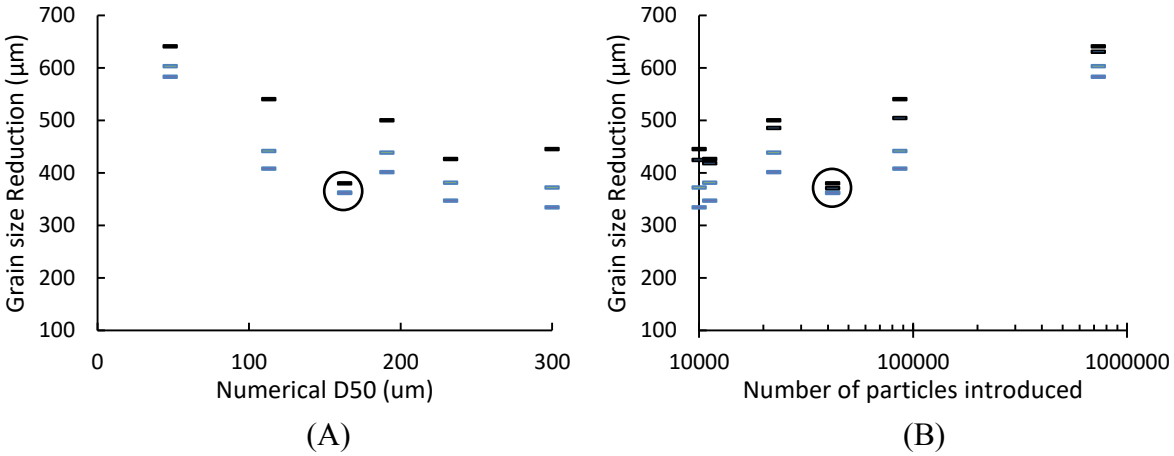

Figure B0.9: Influence of (A) particle size and (B) number of particles introduced on grain size reduction considering no particle dissolution (black) and full particle dissolution (blue) 6hr milled particle results circled

Using the grain size reduction from the inoculation the number of grains formed in the ingot by the inoculants can be calculated. This is shown in Figure B0.10 compared to the number of inoculants introduced to the melt. As when the Al content was not considered, in each case the number of particles formed was greater than the number of inoculants introduced to the melt. This further supports the idea that some form of particle breakup must occur since grain refinement due to Al content is then not a possible explanation for the degree of refinement.

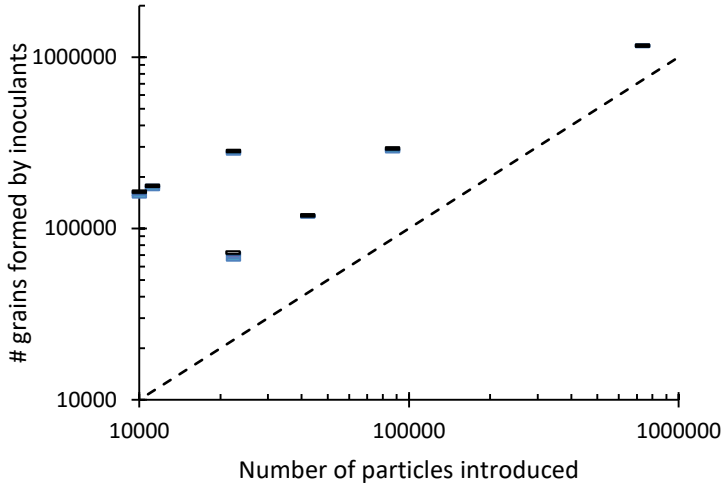

Figure B0.10: Number of grains formed by inoculants compared to number of inoculants introduced to the melt considering no particle dissolution (black) and full particle dissolution (blue). 1:1 ratio shown as dashed line.

T

Appendix C - Effect of interaction time on Unsuccessful Ti-Ta Trials

Particles found in the columnar zone of the TiTa inoculated ingots were investigated to see the effect of the interaction time (holding time at temperature) on the particles.

C.1 Nine Hour Milled Ti-Ta 20s Interaction Time

In the ingot inoculated with Ti-Ta many particles were found to have survived the melt and were found at the bottom of the ingot. A suitable particle was chosen as close to the equiaxed zone as possible to best approximate the behaviour of particles which would have been located within the equiaxed zone and helped form equiaxed grains. It was important to choose a particle not located within the semi-solid bottom cap of the ingot as the behaviour of these particles may be different than those which were in contact with just the melt before solidification. The particle of interest and the region of the ingot it was located in are shown in Figure C0.1. Since BSE images give atomic contrast the particle can be defined by two envelops, the exterior smooth region which appears darker in Figure C0.1B or the lighter coloured rough shape within the darker envelope. The darker envelop is the extent of the solid/liquid two phase region which would have existed between the solid particle and molten Ti-Al before solidification which the lighter region remained solid. The particle selected was 69 μm in diameter, using the solid dimensions, between the volumetric and numerical D99s (108 and 56 μm respectively), significantly larger than the distribution D50s (20 μm with both methods). It is also interesting that the solid shape is much less smooth than the exterior solid/liquid envelope. There are distinct regions of ingress into the solid between 2 and 8 μm in depth. Their average depth is 5.3 μm from the exterior of the solid and average 11.1 μm from one another. Not accounting the depth of these ingresses the average width of the solid/liquid region is 4 μm, this means the ingresses can more than double the solid dissolution length. The ingresses are likely preferential dissolution along the grain boundaries within the particle.

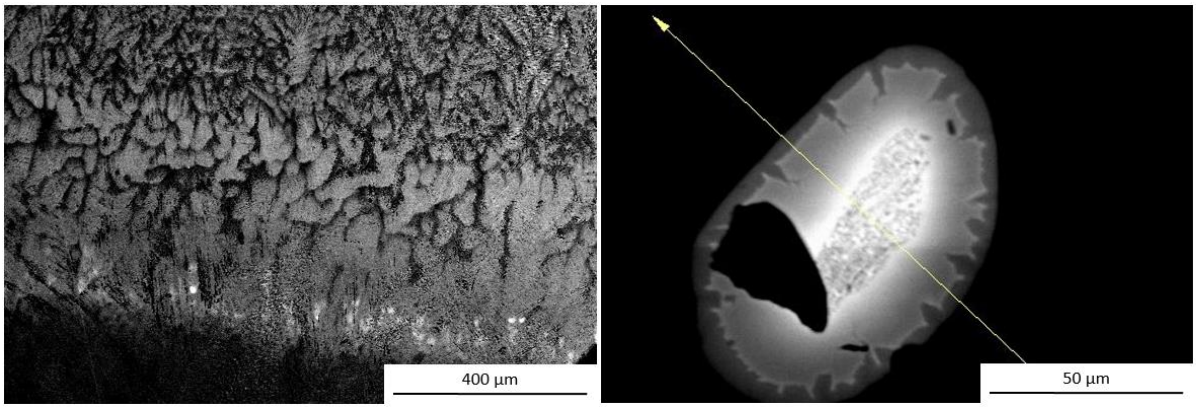

(A) (B)

Figure C0.1: SEM BSE images showing (A) region of columnar zone where the particle of interest was located and (B) 9 hr cryomilled TiTa particle after 20s interaction time

An EDX line scan was carried out across the particle to evaluate the composition through the particle and into the melt, as can be seen in Figure C0.2. The melt shows roughly the expected

composition of Ti-46Al while the center of the particle is also close to the expected composition of Ti-47Ta. It can be seen that the Al diffuses quite far into the particle, almost 25 µm from the solid, solid/liquid interface. In contrast the Ta diffuses less than 5 µm into the bulk from the liquid, solid/liquid interface. This makes sense as the Al diffusion into the particle occurs throughout the process, while the Ta which diffuses into the liquid will be mixed throughout the ingot and only any liquid which is trapped near the particle as solidification progresses will be Ta enriched. The diffusion of Ta seen here is likely then mostly occurring in the solid state, which, along with the slower diffusion rate of Ta, is why the distance is so short compared to the Al.

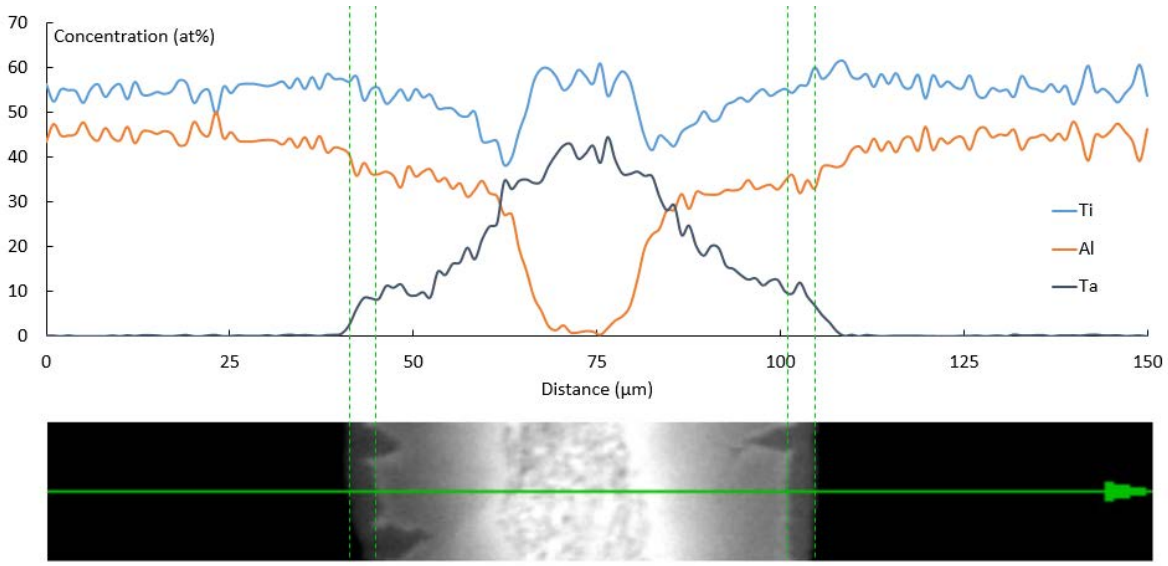

Figure C0.2: EDX line scan across 9 hr cryomilled TiTa particle after 20s interaction time

The EDX line scan can also be used to find the temperature at the interface between the particle and melt. The compositions along the scanning length are plotted as atomic fraction Ta and atomic fraction Al rather than composition vs. distance. This can then be compared to an isothermal section of the ternary phase diagram as shown in Figure C0.3. The locations of the interfaces are found using the profile in Figure C0.2, shown as dashed lines from the BSE image continuing to the profile. The compositions found in these regions are then distinguished from the others, shown as hollow points in Figure C0.3. Since these compositions are within the solid/liquid region of the profile they should also be located within the solid/liquid region of an isothermal section of the phase diagram. This can be seen in Figure C0.3A where the interface points from the composition profile are all located in the two phase solid/liquid region of the isothermal section at 1950K whereas in Figure C0.3B at 1856K the interface points are located well inside the one phase β region. This indicates that the temperature of the solid/liquid interface was 1950 K well above the melting temperature of the bulk.

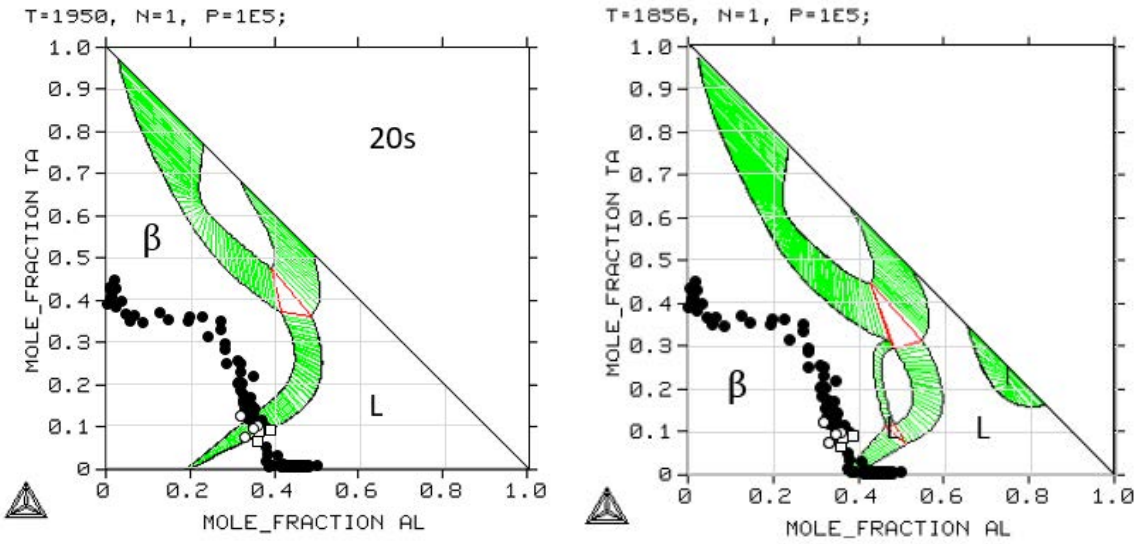

(A) (B)

Figure C0.3: EDX profile showing interface compositions (hollow points) of particle after 20s interaction time compared to isothermal section of the ternary Ti-Al-Ta phase diagram at (A) 1950 K and (B) 1856K.

C.2 6 Hour Milled Ti-Ta

A similar analysis was also carried out on the 6 hour milled particles used with a 10 s interaction time. The particle analyzed and the region of the ingot it came from can be seen in Figure C0.4. This particle was the sole particle located within a region of the ingot with equiaxed grains around it.

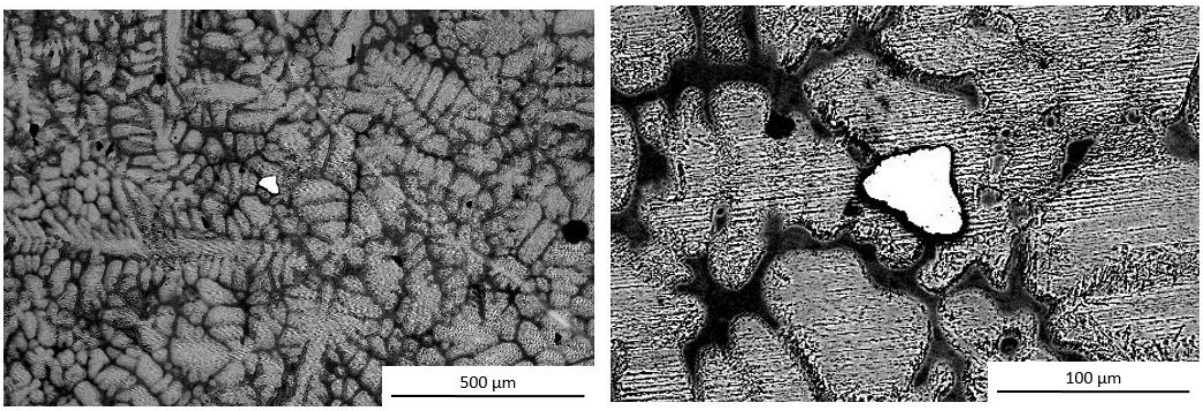

(A) (B)

Figure C0.4: SEM BSE images showing (A) region of ingot where the particle of interest was located and (B) 6 hr cryomilled TiTa particle after 10s interaction time

The BSE image of the particle does not show as clearly the two phase solid/liquid region as the other BSE images of particles. It does show some roughness at its border and inhomogeneity of contrast within it. Since the particle was harder to see than in previous cases a SE image was also taken as seen in Figure C0.5. When viewed by SE the particle appears much more

inhomogeneous with the melt and more homogeneous across its width. The interface between the particle and melt is much sharper than in previous cases.

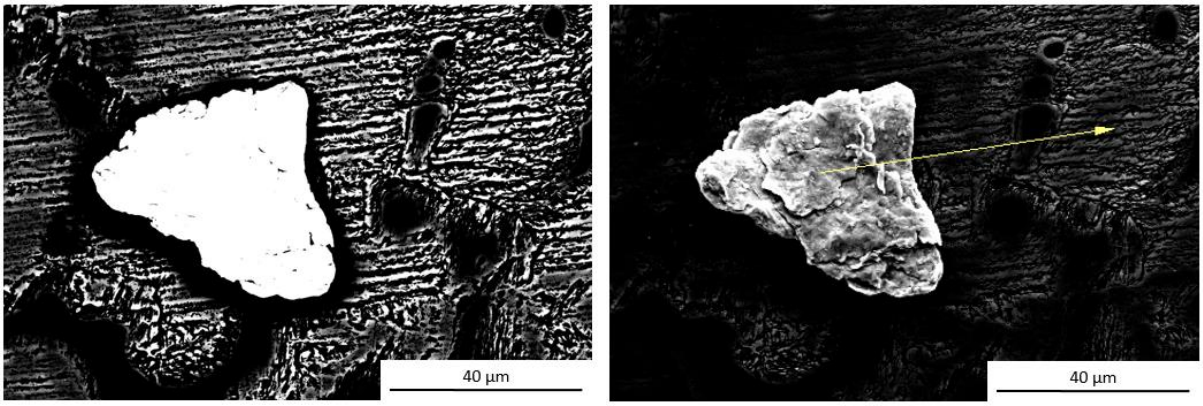

Figure C0.5: SEM (A) BSE and (B) SE image of 6 hr cryomilled TiTa particle after 10s interaction time

Once again an EDX composition was obtained across the interface as shown in Figure C0.6. As this line profile does not cross the entire particle the Al diffusion distance cannot be determined. However, the Ta concentration drops to zero directly at the interface between the particle and bulk material. This means that there is virtually no Ta diffusion from the particle into the bulk.

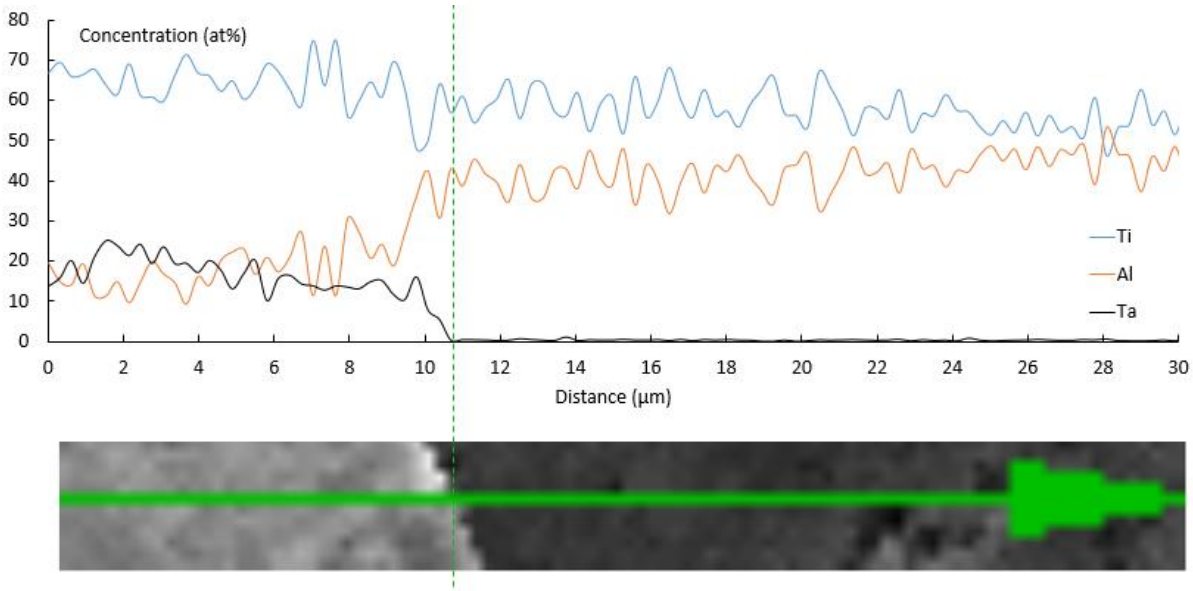

Figure C0.6: EDX line scan across 6 hr cryomilled TiTa particle after 10s interaction time

The interface temperature can once again be determined from the composition profile. However, since the interface is so sharp there is only one composition point from the line scan on the interface. Using isothermal sections of the phase diagram, shown in Figure C0.7, the interface can be estimated to be between 1925 and 1950K depending if the sharp interface corresponds to the liquidus, solidus or a point between them. The combination of the sharp interface with the possibility of the interface temperature being less than in the previous cases

indicates that the particle may not have yet reached thermal equilibrium with the melt. Since the 9 hour milled particle reached thermal equilibrium by 10s and the 6 hour did not it is likely that the time it takes for the particles to reach thermal equilibrium is very close to 10s.

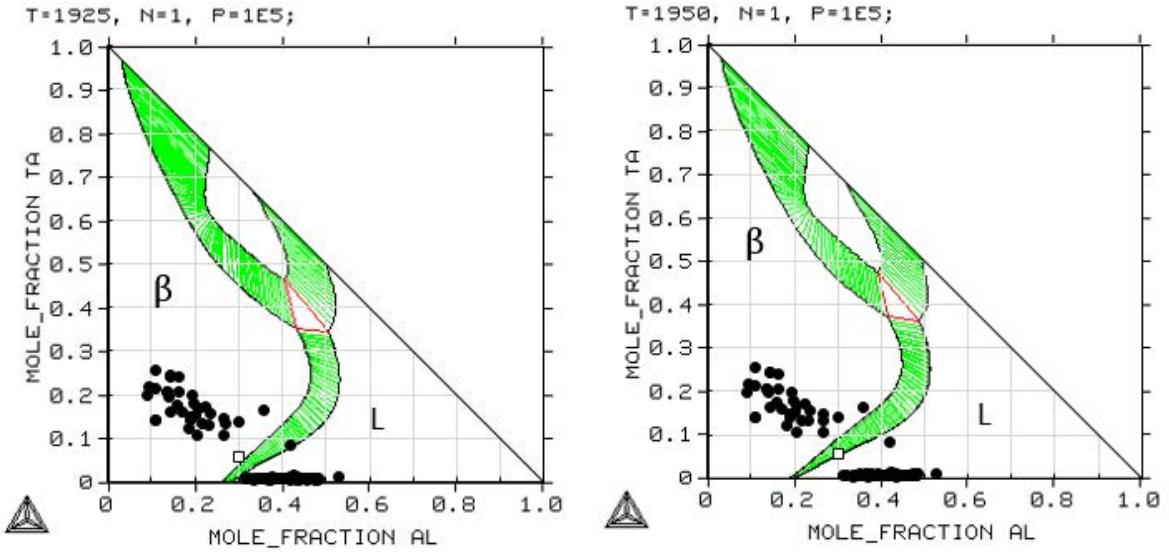

(A) (B)

Figure C0.7: EDX profile showing interface compositions (hollow points) of 6 hour milled particle after 10s interaction time compared to isothermal section of the Ti-Al-Ta phase diagram at (A) 1925 K and (B) 1950 K

C.3 Summary

Trials were conducted with Ti-Ta inoculant particles and bulk alloy obtained from the large ingot where the interaction time between the melt and particles was varied from 10 to 20 seconds. Using EDX composition profiles between remaining particles and the solidified melt and comparisons with phase diagrams the interface temperatures could be found. This temperature as determined to be 1950 K, a melt superheat of 137^{o}, for both interaction times. This indicates that the particles have reached thermal equilibrium with the melt after 10s as the temperature did not change between 10 and 20 seconds. The 6 hour milled particle found after 10s of interaction showed a sharp interface that corresponded to an interface temperature between 1925 and 1950 K. It is then likely that it takes approximately 10s for the particles to reach thermal equilibrium with the melt.

Z

Appendix D – Rod Manufacture and Further Analysis

This appendix address the manufacture of the Ti-Al-Nb rod and its testing along with microstructural analysis and dissolution without fluid flow.

D.1 Manufacturing of Ti-Al-Nb Rod

The rod was formed by vacuum pulling as shown in Figure D0.1. First a bulk alloy of Ti-10Al-25Nb was produced in the same manner as for the production of inoculant powders. Rather than drilling the ingot to produce powders the ingot was remelted a final time after homogenization. Once the ingot was fully molten a quartz tube with an internal diameter of 5 mm was inserted into the melt. The tube was exposed to a vacuum opposite the melt and the induction heating turned off. While the alloy was still molten the vacuum pulled it up the tube where it solidified as a rod. The insertion of the tube and application of the vacuum must occur near simultaneously with the deactivation of the heating or the alloy may ingress too far up the tube and damage the vacuum system.

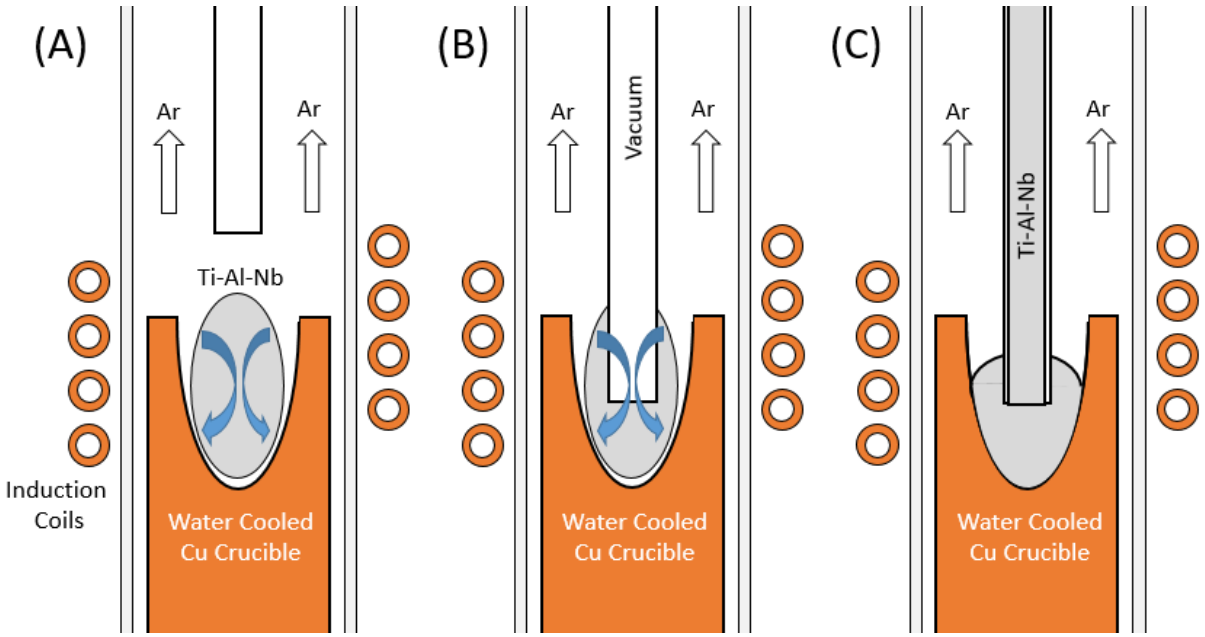

Figure D0.1: Schematic of vacuum pulling to fabricate Ti-Al-Nb rod

As the metal cools the tube often cracks from thermal stress. The pieces are then easily removed from the rod. The bottom of the rod remains in the bulk ingot along with the remainder of the tube, as shown in Figure D0.2A. The top of the rod may be hollow from solidification shrinkage and the molten metal falling back down the tube once the pressure has equalized. Both these ends were cut off and the rod acquired was approximately 15cm in length and 5mm in diameter. In order to introduce the rod to the melt in a controllable manner the rod was welded to a threaded steel rod. A tungsten electrode was used with Ar gas and no filler metal, the resulting weld, shown in Figure D0.2B was incredibly brittle but sufficient to hold the rod for the duration of the dipping experiment.

Figure D0.2: Ti-Al-Nb rod (A) as cast and (B) welded to threaded rod

Once the rod was assembly was prepared it could be used for the dipping experiment. A bulk Ti-46Al alloy was prepared in the same manner as for the inoculation experiments. The same procedure was used as in the inoculation trials but with the Ti-Al-Nb rod in place of the inoculating pellet. The rod was held away from the bulk alloy until it was fully molten, the rod was then inserted directly into the melt and held at temperature for 20 seconds before the furnace power was turned off and the melt allowed to solidify. This is shown schematically in Figure D0.3.

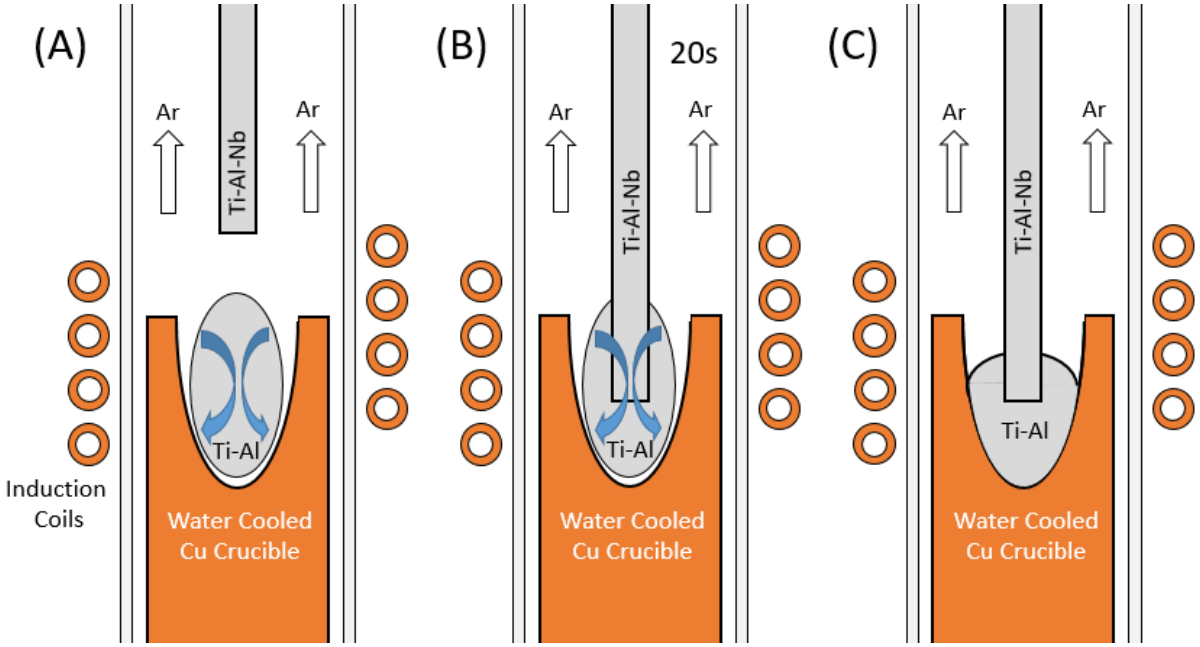

Figure D0.3: Schematic of procedure for Ti-Al-Nb rod dipping experiment

Once the apparatus was cooled to room temperature the ingot/rod assembly were removed. The weld connecting the Ti-Al-Nb rod to the steel threaded rod broke when the assembly was removed.

D.2 Rod Microstructure and Grain Size

Using the SEM the grain size inside the rod was also measured. As the grains could distinguished relatively easily compared to the dendritic grains observed in the ingots the line intercept method could be used to quickly evaluate the grain size. This is done by overlaying a circle of known circumference on a micrograph and counting the number of grain boundaries it intersects, the circumference divided by the number of intersections gives a value for the grain size. This was done in accordance with ASTM E112 - Standard Test Methods for Determining Average Grain Size.

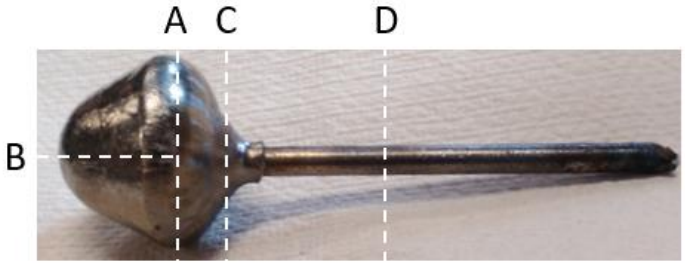

Figure D0.4: Ti-Al-Nb Rod in Ti-Al ingot and cutting planes, A, C and D used for grain size analysis

Representative micrographs of the rod after interaction with the melt, from section A of Figure D0.4 which was fully immersed in the melt and solidified ingot, imaged by secondary and backscattered electrons are shown in Figure D0.5. The microstructure appears similar when imaged with either detector. There is some Z contrast in the BSE image but the blocky β grains remain relatively obvious. The average grain size of the rod after interaction with the melt was found to be 212 μm.

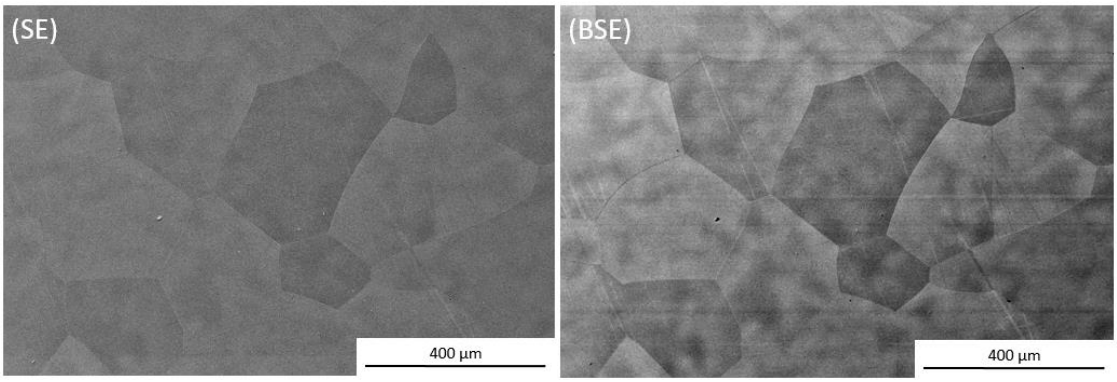

Figure D0.5: Microstructure of Ti-Al-Nb rod after interaction with the melt (section A) imaged with both secondary electrons (SE) and backscattered electrons (BSE)

The same procedure was carried out on section C of the ingot, representative micrographs are shown in Figure D0.6. This section of the rod was immersed in the melt for the 20s interaction time but when the melt fell into the crucible once the furnace power was turned off and the magnetic field could not hold the droplet shape only a thin <2mm thick layer of solidified Ti-Al remained around the rod. While the blocky grains can still be made out in the SE image, the

BSE image appears very dendritic. The dendrites are each roughly contained in a single blocky grain. The average blocky grain size measured for this section was 102 μm.

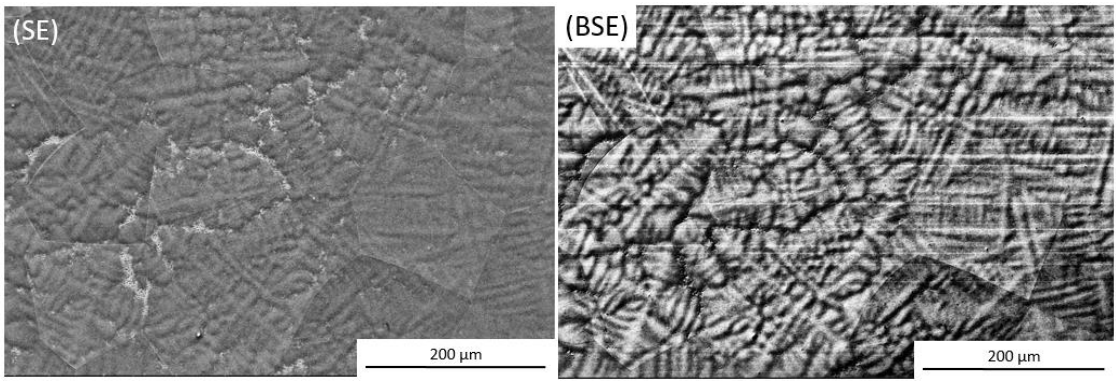

Figure D0.6: Microstructure of Ti-Al-Nb rod after some interaction with the melt (section C) imaged with both SE and BSE

The same appearance was also found in the micrographs obtained from section D which was not in contact with the melt, as shown in Figure D0.7. The measured blocky grain size for section D was 52 μm. Since only the section fully immersed in the ingot did not have a dendritic structure it is likely that the structure formed when the rod was vacuum cast and the heat from the melt and ingot as it cooled was sufficient to erase the dendritic structure. If the dendritic structure did not exist in both section D and C the change in grain size between them could be explained by the heat from interaction with the melt, however since they both retain their solidification structure the grain size difference is likely due to differences in the cooling rate of the rod when it was fabricated, the cooling rate being the fastest further from the bulk ingot. Since the rod was dipped in the same orientation as it was formed it makes sense that smaller dendrites were found further from the bulk ingot.

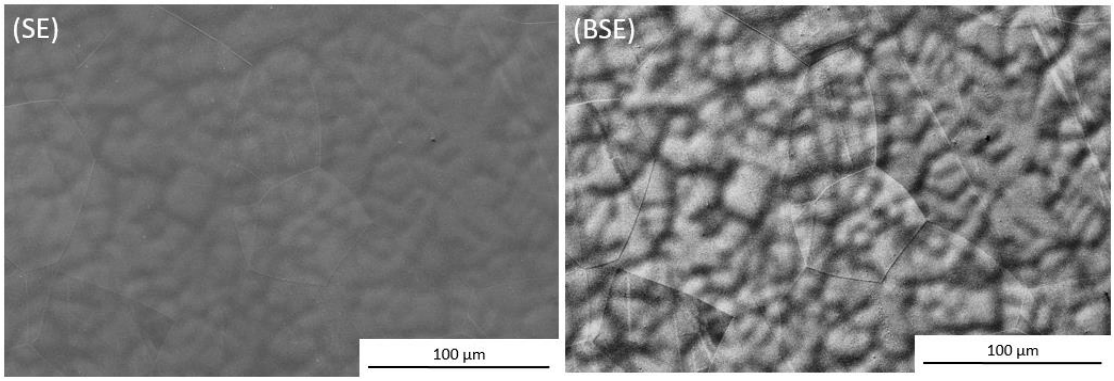

Figure D0.7: Microstructure of Ti-Al-Nb rod which did not interact with the melt (section D) imaged with both SE and BSE

The difference in grain size is roughly a factor of two both from section A to C and C to D, however the section D is located much further from section C than section A. This coupled with the erasure of the dendritic structure in section A alloys the supposition that the difference in grain size is due to the heat from the melt. If the initial grain size was similar in section C and A before interacting with the melt the interaction was then responsible for a grain size increase

by nearly a factor of 2. If this grain size increase occurred in the rod dipping trial it was likely also a phenomena in the inoculation trials. As preferential grain boundary dissolution was attributed to particle breakup in the inoculation trials this increase in grain size may play a critical role for inoculant efficiency since it would help determine the number of possible particles a single introduced particle may break apart into.

D.3 Chemical Analysis to Determine Interface Temperature

An EDX profile was obtained from the bulk ingot into the rod to see the composition across the interface. The composition gradients and BSE image of the region where they were taken are shown in Figure D0.8. The composition gradient was of roughly equal length for all three elements from the interface to the rod, 55 µm. The Ti and Al gradients were both roughly 80 µm from the interface into the bulk while the Nb gradient was only 25 µm. There is also an unexpected decrease in the Ti concentration approximately 30 µm into the rod.

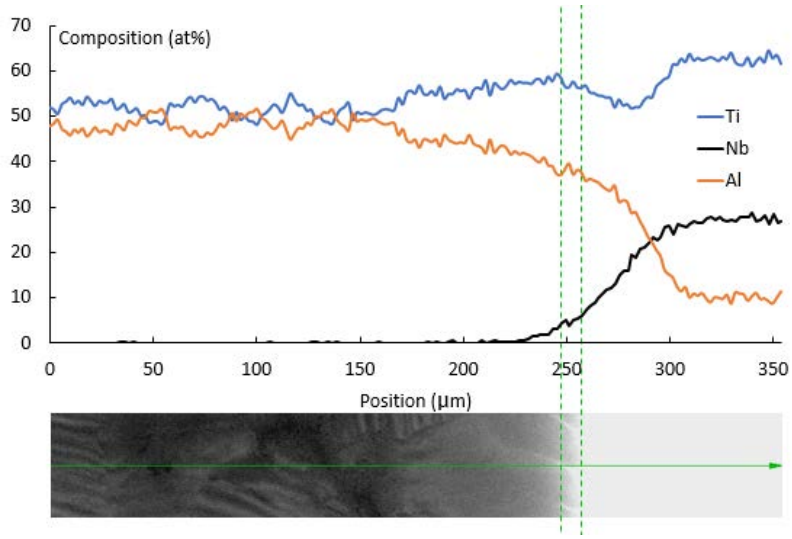

Figure D0.8: EDX profile from bulk alloy (left) into rod (right)

As with the profiles obtained from the TiTa inoculation trials the compositions at the interface could be used to find the temperature. The compositions were first compared to the temperature found for the TiTa particles, however the interface compositions did not match the solidus or liquidus temperatures. The interface points were all located between the solidus and liquidus lines of the ternary phase diagram at 1875K which corresponds to a superheat of 62^{o} above the meting temperature of the bulk alloy. The decrease in temperature can be explained by the increased mass of the rod introduced to the bulk compared to that of the inoculants. The calculated mass of rod just from the optical cross sections is 0.79g which does not include the rod volume above section A or the effect of the remaining rod outside of the melt on the temperature behaviour.

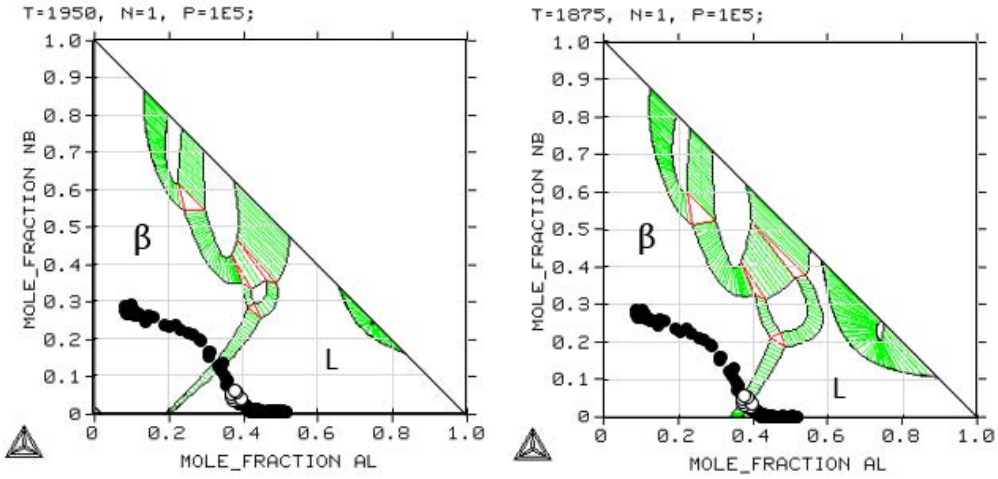

(A) (B)

Figure D0.9: EDX profile showing interface compositions (hollow points) of rod after 20s interaction time compared to isothermal section of the ternary Ti-Al-Nb phase diagram at (A) 1950 K and (B) 1875K.

D.4 Orientation Relationship Between Rod and Bulk

To further understand the relationship between the rod and the melt EBSD analysis was carried out on the rod/melt interfacial region as shown in Figure D0.10. The rod can be seen to be consisting of large β grains while the bulk is fine γ laths which were more difficult to index. The β grains at the edge of the rod are cut by an unindexed band approximately 30 μm from the phase change from β/α, the assumed solid/liquid interface. The α region continues another 30 μm into the bulk before the transition to a γ lamellar structure. The unindexed region corresponds well with the drop in Ti concentration seen in the edx profiles (Figure D0.8). The central β grain in the map is not well mapped after the unindexed region however the other two grains show the same orientation on either side of the unindexed region.

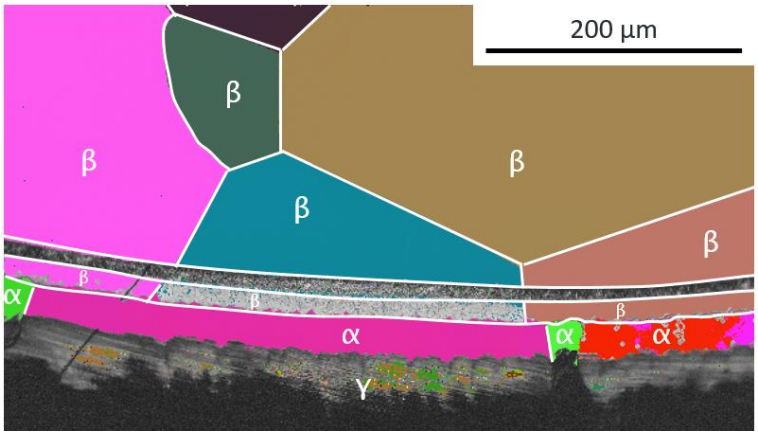

Figure D0.10: Low Resolution EBSD map of rod (top) / bulk (bottom) interface

In order to attempt to better index the band cutting the β grains near the interface a high resolution EBSD map was obtained of the banded region, shown in Figure D0.11. Both the brown and green β grains in Figure D0.11B are shown to have the same orientation on either

side of the band just as in Figure D0.10. The higher resolution EBSD was able to index the bands as α with a martensitic type morphology of very fine laths. The bottom section of the map did not index well, however all the indexed points were found to be γ.

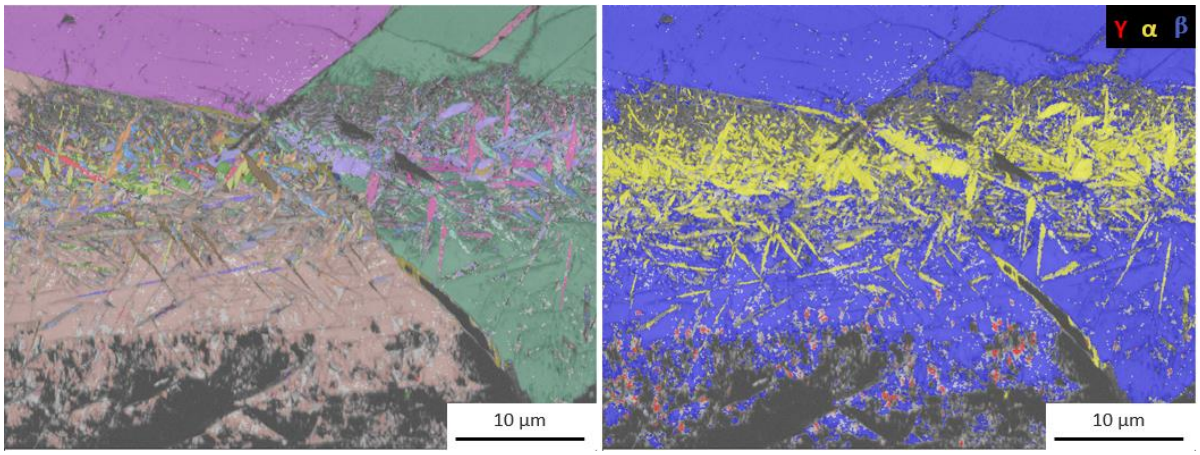

(A) (B)

Figure D0.11: High resolution EBSD maps of rod/bulk interface (A) orientation map (B) phase map

Of particular interest from the high resolution EBSD map were any regions where the β grains of the rod were in contact with α or γ to see if any orientation relationships existed between them. These interfaces were often unindexed, which is not unexpected due to the overlapping of the obtained Kikutchi patterns making indexing difficult. A location however was found where pixels identified as β from the rod were in direct contact with indexed pixels of α which contacted pixels of γ, the orientations of which are shown in Figure D0.12. The burgers and Blackburn orientation relationships are upheld between these regions, indicating that the bulk γ grew epitaxially from the β of the rod. It then stands to reason that the same phenomena would occur from the inoculant particles.

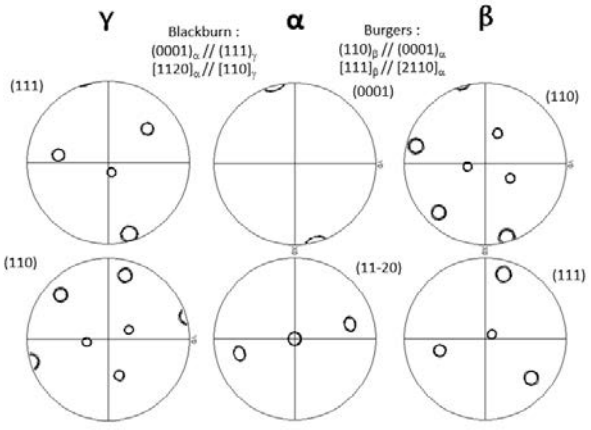

Figure D0.12: Orientation relationships between rod (β) and bulk (γ) showing epitaxial growth through intermediary α phase

HH

Appendix E - Particle Heat Treatment

This section details the particle heat treatment procedures used in chapter 6 for the long and short time period heat treatments as well as presenting chemical compositions to show the powders do not react with the CaF_2 salt.

E.1 Extended Time Heat Treatment Procedure

In order to evaluate the grain size within Ti-Al-Nb particles after extended time (5 minutes) at high temperature experiments were realized using a quenching directional solidification (TSD) apparatus, a schematic of which is shown in Figure E0.1. Such an apparatus is normally used for directional solidification experiments where a temperature gradient between the water cooled cold zone and hot point inside the induction coil is used to induce uni-directional solidification. In this case the apparatus is used rather to ensure the powders spend a controlled amount of time at high temperature. The central alumina tube can move up and down within the heated graphite susceptor. A crucible was placed within the tube, held in place by an alumina rod, such that it could be positioned at the temperature controlled hot point within the induction coil. The crucible was filled with Ti-Al-Nb powder and CaF2 salt in alternating layers. The weight, lid and top layer of Ti-Al-Nb powder were all used to prevent the contents of the crucible from emptying under the He gas flow, a problem observed in the initial trial using only CaF2. CaF2 was used both to protect the powders from oxidation as well as to more rapidly heat the powders. CaF2 was chosen as a medium since it has a melting point of ~1400ºC, and does not react with Ti. As well, the molten salt entraps the particles in a conductive matrix on solidification which assists with metallographic preparation and imaging/analysis with electron microscopy.

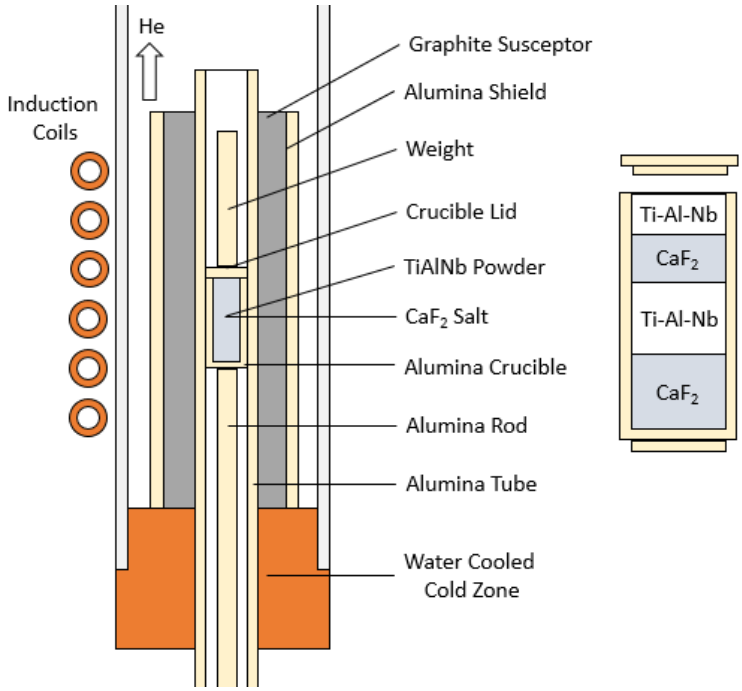

Figure E0.1: Schematic of TSD apparatus and crucible setup

The experiments began by positioning the alumina tube such that the crucible was ~10cm from the hot point of the furnace, as close to the cold point as possible. He gas was flown through the apparatus for a minimum of two hours to minimize the oxygen content of the atmosphere. The furnace was then heated slowly, necessary to prevent the alumina shield around the graphite susceptor from cracking, to 1600ºC over approximately one hour. This temperature was held for 10 minutes to ensure its stability, then the alumina tube moved rapidly up so that the crucible was located at the 1600ºC hot point. This position was maintained for five minutes before power was shut off to the induction coils and the crucible moved to the cold zone as fast as possible.

E.2 Short Time Particle Thermal Treatment

The five minute high temperature thermal treatment of the Ti-Al-Nb particles gives a good idea of the grain growth behaviour within the particles at 1600ºC, however the real interaction time of the particles during inoculation is significantly less than 5 minutes. Further experiments were carried out using the same molten salt and temperature, in this case with a high temperature casting furnace. CaF2 was heated to 1600ºC then mixed with Ti-Al-Nb particles, this is schematized in Figure E0.2. After 20s of interaction the crucible was removed from the furnace and quenched in a small portion of water to cool as quickly as possible without destroying the crucible. Since this procedure was done by hand there may be some variation from 20s in the real interaction time of the particles at 1600ºC, as such the values are presented with error bars in the time axis in chapter 6.

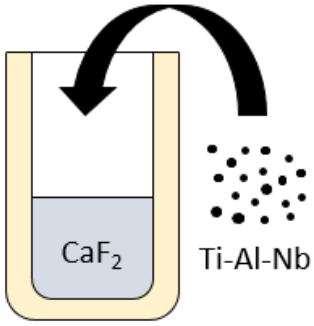

Figure E0.2: Short time high temperature particle treatment schematic

E.3 Chemical Analysis

Finally, the salt can be seen to not react chemically with the particle as shown by chemical analysis in Figure E0.3. Elements remain where expected, Ti and Nb within the particle, Ca and F outside. The CaF2 does react with the alumina crucible which is why there is also significant Al and O content outside of the particle. The points of Ca and F within the particle envelope are likely liquid salt ingress along a crack in the particle as the region appears black both by BSE image and Ti or Nb EDX analysis.

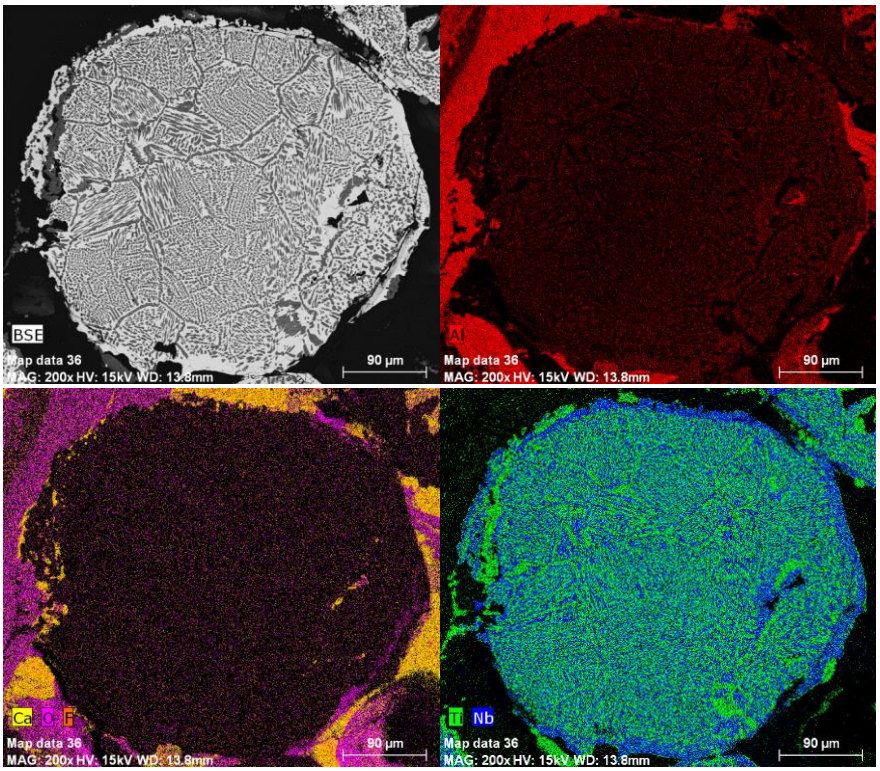

Figure E0.3: EDX chemical analysis of Ti-Al-Nb particle after 5 min interaction with molten CaF2 at 1600ºC including BSE image, Al content, Ca, O and F content and Ti and Nb content.

Abstract

Ti-Al alloys are an important material for aerospace applications. In order to implement them in more applications it is important to develop a method of grain refinement which can avoid precipitates. A new method of inoculation called isomorphic inoculation was developed where inoculant particles act as direct centers of growth rather than nucleation sites, avoiding the energy barrier required for nucleation. Three inoculant alloys were tested, two which balanced lattice matching between the inoculant and bulk alloy and the inoculant stability in the liquid melt, Ti-10Al-25Nb and Ti-25Al-10Ta, and one which prioritized stability, Ti-47Ta. Casting trials were carried out which showed the balanced alloys sucessfully grain refined the as-cast structure without leaving any heterogeneous particles in the structure. The binary Ti-Ta alloy was not successful due to its high density which caused the particles to settle to the bottom of the ingots where they could not participate in solidification. The inoculants were found to have an efficiency greater than one, meaning each particle was responsible for more than one new grain forming in the cast structure. This was attributed to the polycrystalline nature of the partciles which may break up into multiple particles by preferential dissolution or wetting of the grain boundaries during interaction with the melt. Calculations showed that taking into account particle break up and dissolution the efficiencies approached one, indicating this mechanism is responsible for the anomalously high efficiencies observed.

Keywords: Solidification, Inoculation, Ti-Al

Résumé

Les alliages Ti-Al sont depuis peu utilisés industriellement dans le domaine aéronautique. Il est nécessaire d'affiner les grains dans ces alliages en évitant la formation des précipités. Une nouvelle méthode d'inoculation appelée inoculation isomorphe a été développée où les particules agissent comme des sites de croissance plutôt que comme des sites de germination, évitant ainsi la barrière d'énergie pour la germination. Trois alliages inoculants ont été développés, les deux premiers, Ti-10Al-25Nb et Ti-25Al-10Ta, allient une bonne cohérence du paramètre de maille avec l'alliage de base et une bonne stabilité dans le liquide. Le troisième, Ti-47Ta, met en avant l'aspect stabilité. Les coulées ont montré que les premiers deux alliages ont affiné les grains sans laisser de particules hétérogènes. L'alliage binaire Ti-Ta a une densité trop importante et les particules ont sédimentées dans le lingot où elles n'ont pas pu jouer leur rôle. L'efficacité des inoculants est supérieure à l'unité, chaque particule étant responsable de la formation de plus d'un nouveau grain. Ce dernier effet est attribué à la polycristallinité des inoculants qui peuvent se fragmenter par dissolution préférentielle aux joints de grains. Les calculs prenant en compte la fragmentation et la dissolution indiquent des efficacités proches de l'unité, ce qui confirme les valeurs expérimentales d'efficacité anormalement élevées.

Mots Clés: Solidification, Inoculation, Ti-Al